GRID MODERNIZATION LABORATORY CONSORTIUM
U.S. Department of Energy

Duke-RDS Final Report

GMLC 1.5.03: Increasing Distribution System Resiliency using Flexible DER and Microgrid Assets Enabled by OpenFMB

September 2021

KP Schneider (PNNL)
S Laval (Duke Energy)
B Ollis (ORNL)
K Prabakar (NREL)
L Tolbert (UTK)
S Essakiappan (UNCC)
R Tucker (SEPA)
W Du (PNNL)
J Xie (PNNL)
L Marinovici (PNNL)
B Bhattarai (PNNL)
DC Lawrence (Duke Energy)
J Hambrick (ORNL)
N Shepard (ORNL)
M Ferrari (ORNL)
C Murphy (NREL)
V Yaswanth (NREL)
Y Liu (UTK)
P Kritprajun (UTK)
Y Liu (UTK)
L Zhu (UTK)
J Dong (UTK)
Q Dong (UTK)
M Manjrekar (UNCC)
PR Chowdhury (UNCC)

PNNL-32075

Duke-RDS Final Report

1.5.03: Increasing Distribution System Resiliency using Flexible DER and Microgrid Assets Enabled by OpenFMB

KP Schneider (PNNL)
S Laval (Duke Energy)
B Ollis (ORNL)
K Prabakar (NREL)
L Tolbert (UTK)
S Essakiappan (UNCC)
R Tucker (SEPA)
W Du (PNNL)
J Xie (PNNL)
L Marinovici (PNNL)
B Bhattarai (PNNL)
DC Lawrence (Duke Energy)
J Hambrick (ORNL)
N Shepard (ORNL)
M Ferrari (ORNL)
C Murphy (NREL)
V Yaswanth (NREL)
Yilu Liu (UTK)
P Kritprajun (UTK)
Yunting Liu (UTK)
L Zhu (UTK)
Q Dong (UTK)
J. Dong (UTK)
M Manjrekar (UNCC)
PR Chowdhury (UNCC)

September 2021

PACIFIC NORTHWEST NATIONAL LABORATORY
operated by
BATTELLE
for the
UNITED STATES DEPARTMENT OF ENERGY
under Contract DE-AC05-76RL01830

Printed in the United States of America

Available to DOE and DOE contractors from the
Office of Scientific and Technical Information,
P.O. Box 62, Oak Ridge, TN 37831-0062;
ph: (865) 576-8401
fax: (865) 576-5728
email: reports@adonis.osti.gov

Available to the public from the National Technical Information Service
5301 Shawnee Rd., Alexandria, VA 22312
ph: (800) 553-NTIS (6847)
email: orders@ntis.gov <https://www.ntis.gov/about>
Online ordering: http://www.ntis.gov

Summary

This is the final project report for the Grid Modernization Laboratory Consortium (GMLC) Resilient Distribution System (RDS) project titled "Increasing Distribution System Resiliency using Flexible DER and Microgrid Assets Enabled by OpenFMB". The primary goal of this project was to increase the resiliency of distribution systems at utilities around the nation by deploying flexible operating strategies that engage end-use assets as a resource. The primary goal was successfully achieved. The primary goal was divided into three areas:

- Develop the architectures and controls to accelerate the deployment of resilient and secure distribution concepts through the flexible operation of traditional assets, DERs, and Microgrids;

- Integrate the operations of switching devices, DERs, and microgrids to implement a flexible segment-based approach for operating distribution systems;
- Develop a scheme of flexible operations that will be applicable to a wide range of technology combinations.

This project addressed the increasingly common challenge of coordinating the operations of distributed field devices with centralized utility systems. While there are numerous examples of this class of challenge, this project focused on a specific operational challenge at Duke Energy. The specific operational challenge was to coordinate the operation of centralized self-healing systems (deployed to address increasingly severe weather events) with distributed generation resources (primarily in the form of non-utility solar PV). For Duke Energy, the specific challenge was to ensure proper protection coordination at the distribution level when the system is reconfigured by centralized self-healing systems, or other centralized systems. Without proper coordination, Duke has had instances of not being able to deploy self-optimizing grid (SOG) technologies in regions of modern to high penetration of solar PV. To achieve the necessary coordination, the project utilized Open Field Message Bus (OpenFMB) to implement a layered control system that increased operational flexibility by facilitating a level of control at the system "edge". The work conducted as part of this project, in collaboration with other industry and DOE efforts, has advanced the state-of-the-art for distributed control on the industrial control systems utilized by electric distribution utilities. Specific outcomes of the project included:

- The Duke-RDS project was a proof of concept that successfully demonstrated that coordination of distributed assets, using existing commercially off-the-shelf relays and open-source software, can produce a more flexible system.
- Using distributed control, via OpenFMB, it is possible to coordinate the operation of centralized and distributed systems to increase operational flexibility, meeting all operational requirements. This project focused on ensuring protection coordination in a dynamic system, but the work is extensible to a range of other operational issues.
- The work performed in the RDS project provided Duke Energy additional confidence to move forward with future SOG technologies in regions with moderate to high penetration of grid-tied distributed energy resources.
- As described by Duke Energy in their 2020 Sustainability Report: "an innovative microgrid setup is being planned at the Anderson County Civic Center. A 5-MW battery will be grid-connected and will provide backup power at the facility, which supports several emergency service agencies and serves as the state's largest hurricane evacuation shelter."
- Pursuant to docket no. E-2 sub 1219 and 1193, Duke Energy will spend $302 million on expanding the deployment of self-optimized grid (SOG). As quoted in the PUC filing, the new SOG system must address the fact that "…when privately owned roof-top solar becomes widespread, a dynamic, automated, capacity-enabled two-way power flow grid will be essential". The Duke-RDS project, and the concepts developed as part of it, provides Duke-Energy with new technical capabilities to complement and enhance the coordination of SOG in regions with medium to high penetration of grid-tied distributed energy resources.

Acknowledgments

Contributions to this project were achieved through the Grid Modernization Laboratory Consortium (GMLC), a strategic partnership between the U. S. Department of Energy and the National Laboratories. The GMLC was established as part of the U.S. Department of Energy Grid Modernization Initiative (GMI) to accelerate the modernization of the U.S. electricity infrastructure. The views expressed in the report do not necessarily represent the views of the U.S. Department of Energy or the United States Government.

This work was supported in part by the U.S. Department of Energy under contract DE-AC05-76RL01830.

Acronyms and Abbreviations

AMQP	Advanced Message Queuing Protocol
ANSI	American National Standards Institute
BEMS	Building Energy Management System
BESS	Battery Energy Storage System
C&I	Commercial and Industrial
CB	Circuit Breaker
CF	Criticality Factor
CHIL	Control Hardware-In-the-Loop
CONOPS	Concept of Operations
DDS	Data Distribution Service
DER	Distributed Energy Resource
DMS	Distribution Management System
DNP3	Distributed Network Protocol 3
DOE	Department of Energy
DRTS	Digital Real-Time Simulator
D-SCADA	Distribution Supervisory Control and Data Acquisition
DSO	Distribution System Operator
EENS	Expected Energy Not Served
EERE	Energy Efficiency & Renewable Energy
EMI	Electromagnetic Interference
EOD	Expected Outage Duration
EPI	Expected Probability of Interruption
FFT	Fast Fourier Transform
FLISR	Fault Location, Isolation, and Service Restoration
FMB	Field Message Bus
GE	General Electric
GMI	Grid Modernization Initiative
GMLC	Grid Modernization Laboratory Consortium
GOOSE	Generic Object Oriented Substation Event
GUI	Graphical User Interface
HIL	Hardware-In-the-Loop
IAP	Integrated Assessment Plan
IED	Intelligent Electronic Device
IEEE	Institute of Electrical and Electronics Engineers
IGBT	Insulated Gate Bipolar Transistor
IoT	Internet of Things
IT	Information Technology

LoR	Loss of Revenue
LRC	Load Restoration Curve
LTE	Long-Term Evolution
LVAT	Laboratory Value Analysis Team
MCS	Monte-Carlo Simulation
MG	Microgrid
MOSFET	Metal Oxide Semiconductor Field Effect Transistor
MPPT	Maximum Power Point Tracking
MQTT	Message Queuing Telemetry Transport
NREL	National Renewable Energy Laboratory
OE	Office of Electricity
OES	Open Energy Solutions
OpenFMB	Open Field Message Bus
ORNL	Oak Ridge National Laboratory
OS	Operating System
PCB	Printed Circuit Board
pf	Power Factor
PHIL	Power Hardware-In-the-Loop
PLC	Power Line Carrier
PNNL	Pacific Northwest National Laboratory
PUC	Public Utility Commission
PV	Photovoltaic
QSTS	Quasi Static Time Series
RCL	Recloser
REopt	Renewable Energy Integration & Optimization
RHIL	Remote Hardware-In-the-Loop
RTAC	Real-Time Automation Controller
SAIDI	System Average Interruption Duration Index
SAIFI	System Average Interruption Frequency Index
SCADA	Supervisory Control and Data Acquisition
SEL	Schweitzer Engineering Laboratory
SEPA	Smart Electric Power Alliance
SOG	Self-Optimizing Grid
SPOT	System Placement Optimization Tool
TEA-1	Transactive Energy Algorithm-1
TEA-2	Transactive Energy Algorithm-2
TCC	The Civic Center
TES	Transactive Energy System
TTF	Time to Failure
TTR	Time to Repair
UNCC	University of North Carolina Charlotte

UTK	University of Tennessee, Knoxville
UUID	Universally Unique Identifier
VA	Volt Ampere
var	Volt Ampere Reactive
W	Watt

Table of Contents

Contents

Figures

Tables

1.0 Introduction

As part of the Department of Energy Grid Modernization Laboratory Consortium (GMLC), Pacific Northwest National Laboratory (PNNL) was tasked with leading the project titled "GMLC 1.5.03: Increasing Distribution System Resiliency using Flexible Distributed Energy Resources (DERs) and Microgrid Assets Enabled by OpenFMB". This GMLC funded effort was a joint collaboration between the Office of Electricity Delivery & Energy Reliability, now the Office of Electricity (OE), and the Office of Energy Efficiency & Renewable Energy (EERE). The objective of this GMLC project was to accelerate the deployment of resilient and secure distribution concepts through the flexible operation of traditional assets, non-utility DERs, and microgrids. Centralized distribution management system (DMS) functions were coordinated with decentralized DERs and microgrid using Open Field Message Bus (OpenFMB), a reference architecture for security and interoperability. This represents a change in the operational paradigm from treating DERs and microgrids as boundary conditions to leveraging them as active system assets with distributed controls, enabling system flexibility to address all hazards. Interoperability was supported using open standards such as distributed network protocol 3 (DNP3), C37.118, and generic object oriented substation events (GOOSE) in the operational system.

The primary goal of this project was to increase the resiliency of distribution systems at utilities around the nation by deploying flexible operating strategies that engage end-use assets as a resource. The primary goal was divided into three areas:

- Develop the architectures and controls to accelerate the deployment of resilient and secure distribution concepts through the flexible operation of traditional assets, DERs, and Microgrids,
- Integrate the operations of switching devices, DERs, and microgrids to implement a flexible segment-based approach for operating distribution systems,
- Develop a scheme of flexible operations that will be applicable to a wide range of technology combinations.

The operational use-case at Duke Energy sought to develop a "segment" based self-healing distribution system that can actively engage DERs through a transactive control system. The segment-based self-healing system is designed to operate four distribution circuits as a collection of individual segments that have been designed to have the ability to operate connected in a wide range of topologies, well in excess of legacy technologies. During a resiliency event, the system has the ability to reconfigure based on local control and on centralized controls to increase "optimality". To increase the flexibility of the system, DERs are engaged through a transactive control signal which can incentivize the DERs to operate in a manner that increases the number of available reconfiguration options. Specifically, a signal incentivizes DERs to adjust active and/or reactive power output to change power flows and voltage so that additional switching operations are available for the system to respond to the resiliency event. In addition to engaging the DERs as active elements in the segment-based operations, the framework can be extended to also engage end-use loads.

The developed flexibility scheme is applicable to a wide range of technology combinations, but the use-cases in this report will focus on a specific example of fault location, isolation, and service restoration (FLISR), solar photovoltaic (PV), and a microgrid. The developed capabilities are applicable to technologies deployed across of all of Duke's service territory, in six states, as well as utilities across the nation. Specifically, the generalized framework for coordinating the operation of centralized and decentralized systems, enabled by OpenFMB, is applicable to the various combinations of technologies deployed across the nation. To support the project goals, PNNL engaged a number of team members which include: Duke Energy, Oak Ridge National Laboratory (ORNL), National Renewable Energy Laboratory

(NREL), Smart Electric Power Alliance (SEPA), University of North Carolina – Charlotte (UNCC), and University of Tennessee, Knoxville (UTK).

This project was executed over a four-year period, from 10/1/2017 to 9/30/2021. The initial work focused on developing a generalized architecture for the coordination of centralized and decentralized systems [1]. Building on the generalized architecture, a specific control system to coordinate the operation of FLISR, PV, and microgrids was developed, including a transactive control system to engage DERs as an operational asset. To validate the developed control systems, hardware in the loop (HIL) testing was conducted to ensure proper operation of both centralized (at NREL) and decentralized (at ORNL) systems. A HIL platform (at Duke's Mount Holly facility) was used to test the control of the coordinated centralized and decentralized systems. In parallel with the HIL testing, work was conducted to ensure that there are planning and operational structures in place for the new control systems. For planning, integrated co-simulations were conducted to ensure that there is a planning process in place to replicate the deployment of the developed control system in other regions. The project developed a Concept of Operations (CONOPS) document that detailed the use-cases and procedures for operating the segment-based system. While the final field validation was not completed, an event-based Integrated Assessment Plan (IAP), which outlines the procedure for executing a field demonstration, was developed. It is expected that Duke Energy will use the developed IAP as part of the full system commissioning once the public utility commission (PUC) interconnection process is approved and completed.

In the final commissioning, there will be a microgrid operating at the civic center (TCC) as well as deployed G&W Viper-S® reclosers and Schweitzer Engineering Laboratory (SEL) Real-Time Automation Controller (RTACs) as part of the self-optimizing grid (SOG). Despite the lack of a field demonstration, the work completed as part of this DOE-funded effort provided Duke Energy with a better understanding, and increased confidence, in the coordination of centralized and distributed systems. Two documented examples of this are:

- As described by Duke Energy in their 2020 Sustainability Report: "an innovative microgrid setup is being planned at the Anderson County Civic Center. A 5-MW battery will be grid-connected and will provide backup power at the facility, which supports several emergency service agencies and serves as the state's largest hurricane evacuation shelter."
- Pursuant to docket no. E-2 sub 1219 and 1193, Duke Energy will spend $302 million on expanding the deployment of self-optimized grid (SOG). As quoted in the PUC filing, the new SOG system must address the fact that "…when privately owned roof-top solar becomes widespread, a dynamic, automated, capacity-enabled two-way power flow grid will be essential". The Duke-RDS project, and the concepts developed as part of it, provides Duke Energy with new technical capabilities to complement and enhance the coordination of SOG in regions with medium to high penetration of grid-tied distributed energy resources.

This report outlines the work that supported these outcomes and is organized as follows. An overview of OpenFMB is presented in Section 2.0 and is intended to provide a general background. Section 3.0 presents the Duke Energy electrical distribution infrastructure that was used as part of this project. The control architecture that the project developed is presented in Section 4.0 and is intended to give a high-level overview of the operational structure to be developed. Section 5.0 presents the OpenFMB Harness, which is the physical instantiation of the OpenFMB references architecture and the control architecture from Section 4.0. Operational use-cases are developed in Section 6.0, based on the architecture of Section 4.0 and the OpenFMB Harness in Section 5.0. Section 7.0 presents calculation of reliability metrics for the use-case in Section 6.0, quantifying the change in reliability for direct operations. In Section 8.0, the foundation for quantifying the degradation in power electronic inverter life-tim is presented, to support the transactive energy system presented in Section 9.0. The transactive energy system in Section 9.0 presents how distributed non-utility assets are coordinated to supported centralized utility systems, and the work

presented in Section 8.0 can be used to quantify the impact to inverter life-time. Co-simulation of the use-cases, including the architecture and controls, is presented in Section 10.0. In coordination with the co-simulation work of Section 10.0, Section 11.0 presents the hardware in the loop (HIL) testing that was used to verify and validate performance of hardware sub-systems. Extending the HIL work of Section 11.0, Section 12.0 details the power system emulation work that was conducted to integrate device unit testing with centralized controls. Section 13.0 presents the lessons learned and concluding comments for the project. This includes specific technical lessons learned from the project as well as identifying the impacts the project work will continue to have after the completion of the project.

Additional contents are provided as appendices: 1) Appendix A includes the detailed operational steps of closing a recloser for load transfer; 2) Appendix B shows the simulation results of Transactive Energy Algorithm (TEA) TEA-2 in Use-Case #1, Scenario 3; 3) Appendix C provides simulation results of the Scenario 2 of all use-cases; and 4) The valuation analysis for the full technology suite is reported in Appendix D. Appendix E is a complete list of all publications prepared as part of the project.

2.0 Overview of OpenFMB

OpenFMB is a framework and reference architecture which enables the coordination of grid edge devices through interoperability and distributed controls [2]. The framework reduces the need for a centralized intelligence or control and allows management of distribution systems at the circuit level. Additionally, OpenFMB can be deployed on environmentally hardened hardware, i.e., intelligent electronic devices (IEDs), that electric distribution utilities commonly use. For this reason, OpenFMB was selected for this project.

OpenFMB adapters enable communication between such varied protocols as: distributed network protocol 3 (DNP-3), Modbus, American National Standards Institute (ANSI) C12, message queuing telemetry transport (MQTT), data distributed service (DDS), IEC 61850, GOOSE messages, advanced message queuing protocol (AMQP), and the NATS protocol. The OpenFMB adapters have been developed, tested, and placed in the open-source [2].

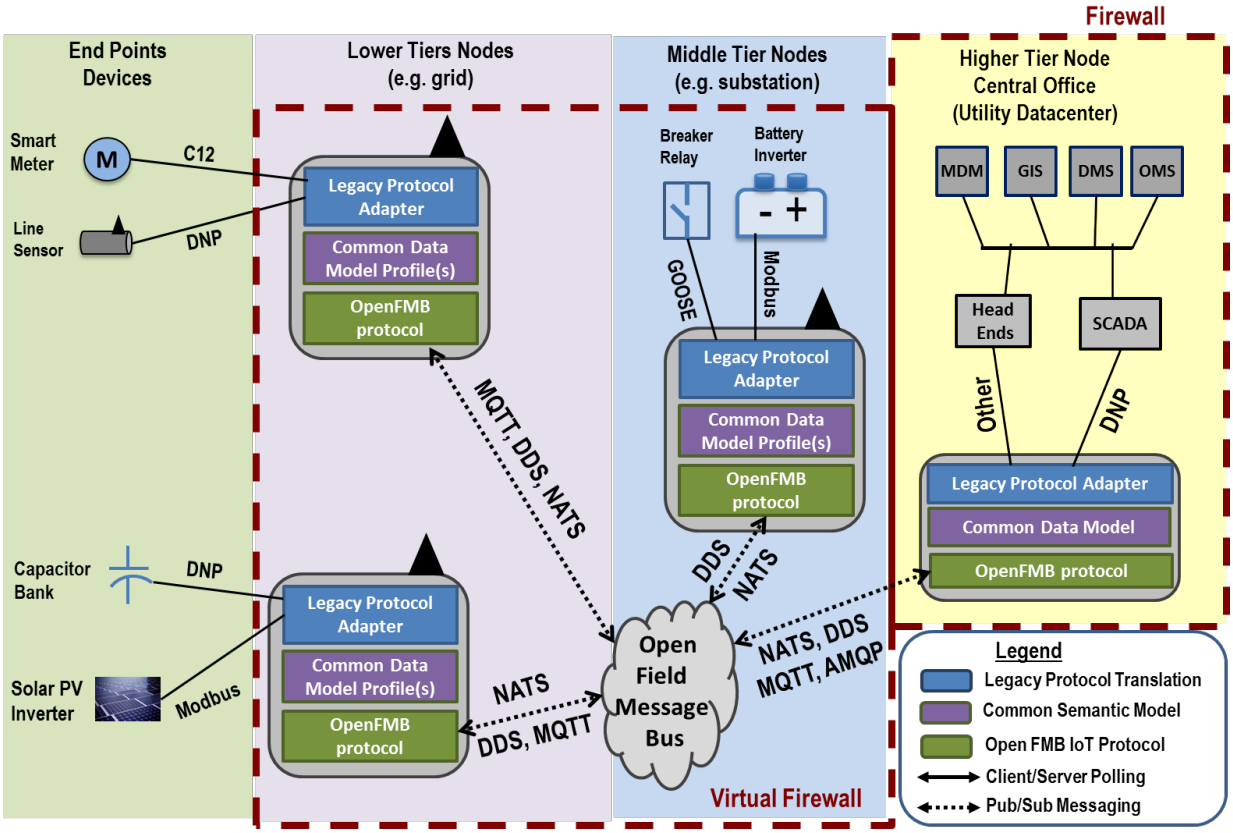

Figure 2.1: Layered architecture of OpenFMB control system.

In Figure 2.1, it is shown that the OpenFMB framework allows the simultaneous use of multiple protocols across multiple devices. This is essential in distributed control systems since multiple protocols are often used because of the range of device types. For example, electric distribution utilities in North America use DNP-3 for end-point devices, such as line sensors and shunt capacitors. However, the majority of PV and battery energy storage system (BESS) controllers use Modbus, and smart meters commonly use ANSI C12. As a result, the interoperability challenges associated with coordinating these devices can be significant [3]. Early implementations of OpenFMB-based distributed controls provided a number of lessons learned [4]:

- Open-source, lightweight message bus protocols are not difficult to implement on static embedded telemetry and have the following advantages:
    - Portability, reusability, and modularity,
    - Significant reduction in time and effort to deploy,
    - Greater interoperability between different vendors.
- A publish and subscribe (pub/sub) messaging pattern enables interoperability between different protocols, disparate legacy assets, and information technology (IT) enterprise systems, and has multiple advantages:
    - Agnostic of programming language, operating system (OS), and protocol(s),
    - Agnostic of physical communications medium: Wi-Fi, Cellular, or power line carrier (PLC),
    - Decoupling of physical, network, and logic layers.

3.0 Overview of Duke Distribution Infrastructure

For the purposes of this project, the system considered is constrained to four distribution circuits operated by Duke Energy in South Carolina. The four distribution circuits are operated at a nominal voltage of 12.47 kV and are of a standard four-wire grounded wye design. Because of the sensitivities of utility operations, the descriptions of systems (Section 3.0) and use-cases (Section 6.0) will be based on a reduced order one-line diagram. The simulation, analysis, and research were conducted using full-detail planning model information.

The following subsections provide the details for three scenarios that will be used within each of the use-cases. Scenario 1 is the base case operations. Scenario 2 builds on Scenario 1 but includes the operation of an inverter-based microgrid, and Scenario 3 builds on Scenario 2 and includes a transactive control system.

3.1 Duke Energy System for Scenario 1 (Pre-RDS Project)

The reduced order one-line diagram of the Duke Energy circuits, and substation considered for this project, which was in operation as of December 2017, is shown in Figure 3.1. These distribution circuits are supplied from two substations. Circuits F-1, F-2, and F-3 are supplied by the substation #1, and circuit F4 is supplied by the substation #2. This system is used for Scenario 1 of all use-cases.

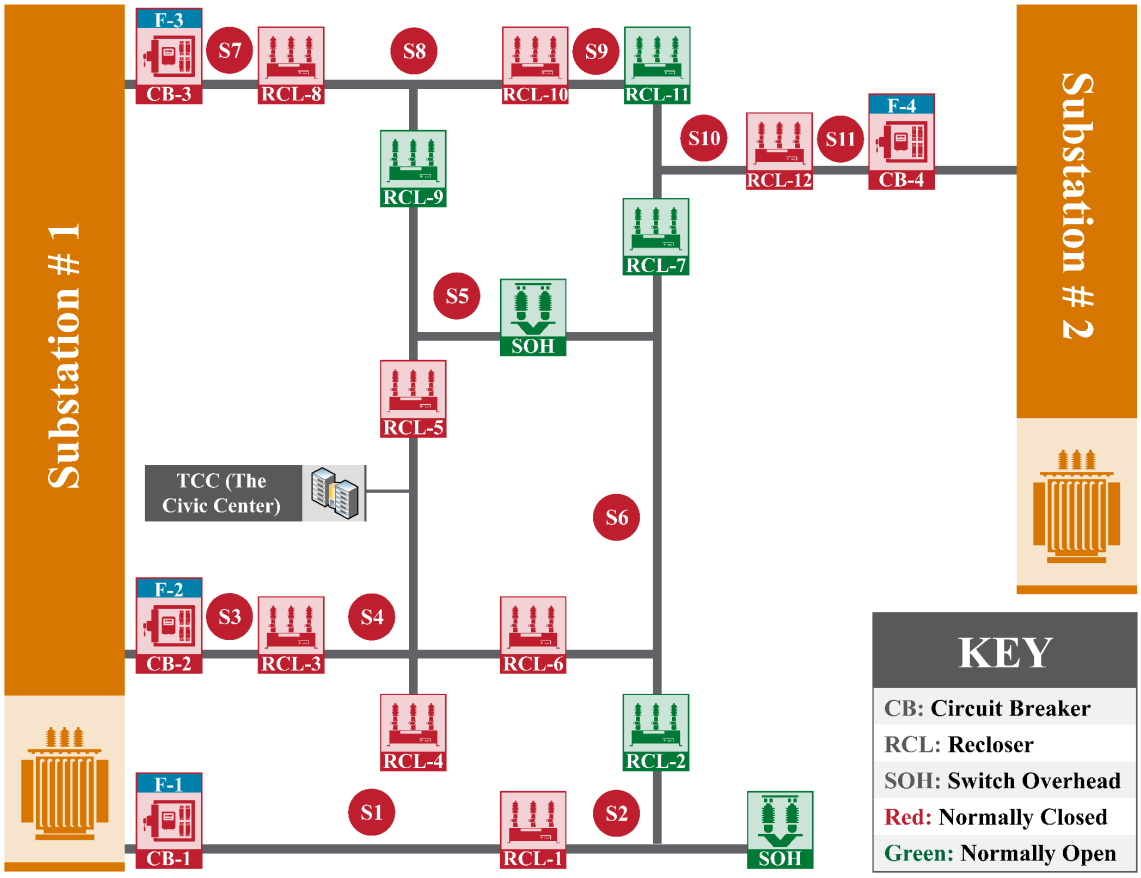

Figure 3.1: Reduced order one-line diagram of Duke Energy system for this project.

3.1.1 Critical End-Use Load

The Civic Center (designated TCC in segment 4, S4, of Figure 3.1) is considered to be a critical load in the distribution circuits, because it supports several emergency service agencies and serves as the state's largest hurricane evacuation shelter [5]. As of December 2017, power was typically supplied from circuit F-2, with the ability to manually reconfigure and supply from circuit F-1, F-3, or F-4. Because most switches were manually operated by field crews, transferring TCC to a circuit other than circuit F-2 could take several hours and would require customer outages because manual switches are not designed to perform on energized lines. The time required to manually switch TCC to another circuit could be significantly increased if an extreme weather event delayed line crews, either because of higher priority tasking or transportation delays.

Because of these reasons, TCC was extremely dependent on the operation of circuit F-2 to support normal operations. Any disruption in supply to circuit F-2 caused TCC to lose power for an extended period. To increase the resiliency of TCC, Duke Energy examined several options to increase the number of available supplies.

3.1.2 System Operators and Other Involved Personnel

Under normal operations in Scenario 1, circuits are monitored and controlled from the regional control center using a General Electric (GE) distribution management system (DMS). In addition, a legacy Yukon Feeder Automation system is in operation with circuits F-3 and F-4. A number of switches can be remotely operated via the DMS [6]. The distribution operator (DO) interacts with the distribution system via the DMS, the Yukon Feeder Automation system, and workflow management systems to dispatch line crews. Field crews physically interact with the system by executing switching operations and maintenance tasks coordinated with the system operator.

Other Duke Energy personnel interact with the system, but typically not on the operational time frame. Personnel involved include, but are not limited to, distribution system planners, protection engineers, customer service agents, and meter technicians. For the legacy system used in Scenario 1, owners of non-utility assets such as photovoltaic systems are electrically interconnected to the Duke Energy circuits but are not active participants in the normal operations.

3.2 Updated System with Microgrid for Scenario 2

In Figure 3.2, the updated system with an inverter-based microgrid is shown. This is the system, as operated, after the deployment of the microgrid at TCC and the SOG equipment, which include the G&W Viper-S® reclosers and SEL RTACs. This microgrid can be used to restore critical loads, e.g., TCC. This system is used for the Scenario 2 of all use-cases.

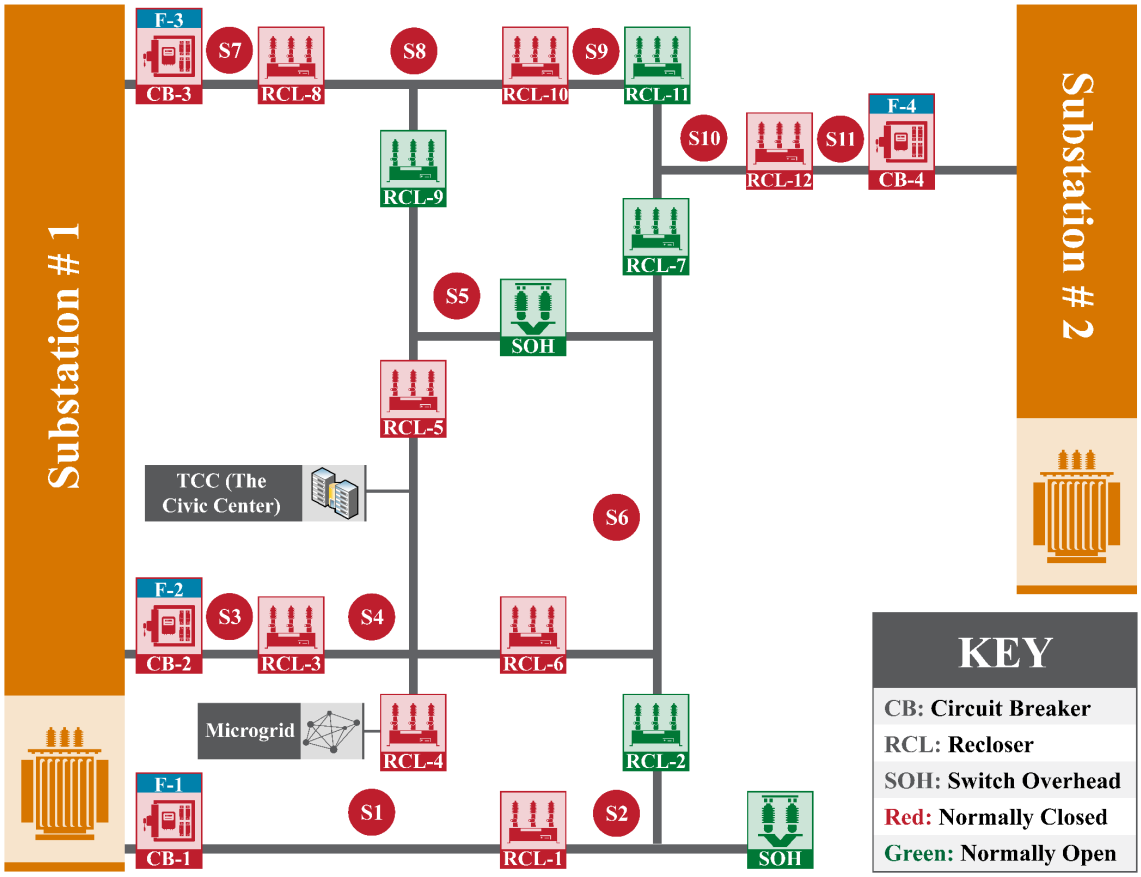

Figure 3.2: Reduced order one-line diagram of Duke Energy circuits with a Microgrid.

3.3 Updated System with DERs and Transactive Energy for Scenario 3

In Figure 3.3, the updated system is presented with DERs, which can participate in the transactive energy. This system is used for the Scenario 3 of all use-cases. In this study, a set of solar PV objects are modeled in the GridLAB-D simulation environment for each of all 11 segments. However, the solar PV objects/symbols can be replaced by different types of DERs and/or microgrid systems. All DERs of a microgrid can be aggregated for generating the bidding curve of this microgrid. Therefore, the transactive algorithms that will be presented in Sections 9.3 and 9.4 can be applied directly.

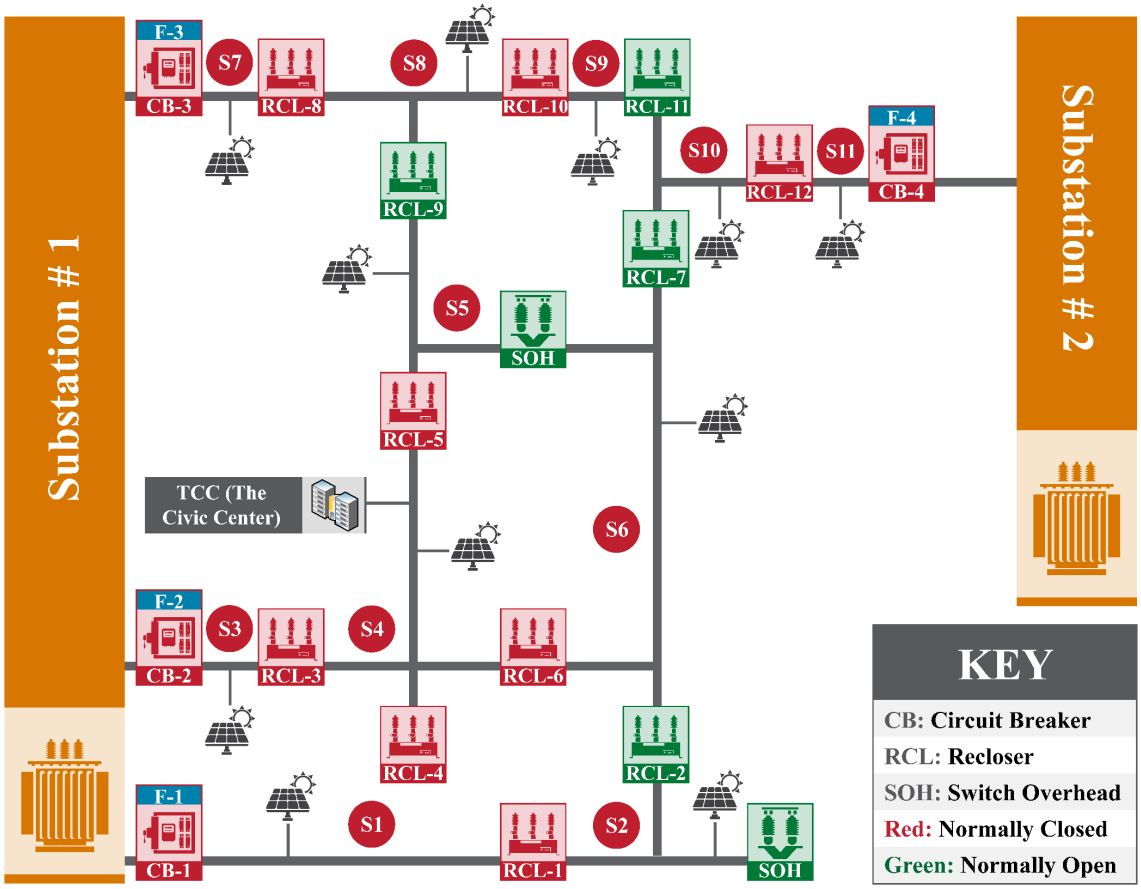

Figure 3.3: Reduced order one-line diagram of Duke Energy circuits with DERs and transactive energy.

4.0 Control Architecture

This section outlines the control architecture that was used in this project The conceptual architecture is shown in Figure 4.1. It aggregates information from the more detailed diagrams associated with the operational use-cases, which are discussed in Section 6.0. The inclusion of a transactive system is covered separately in Section 9.0.

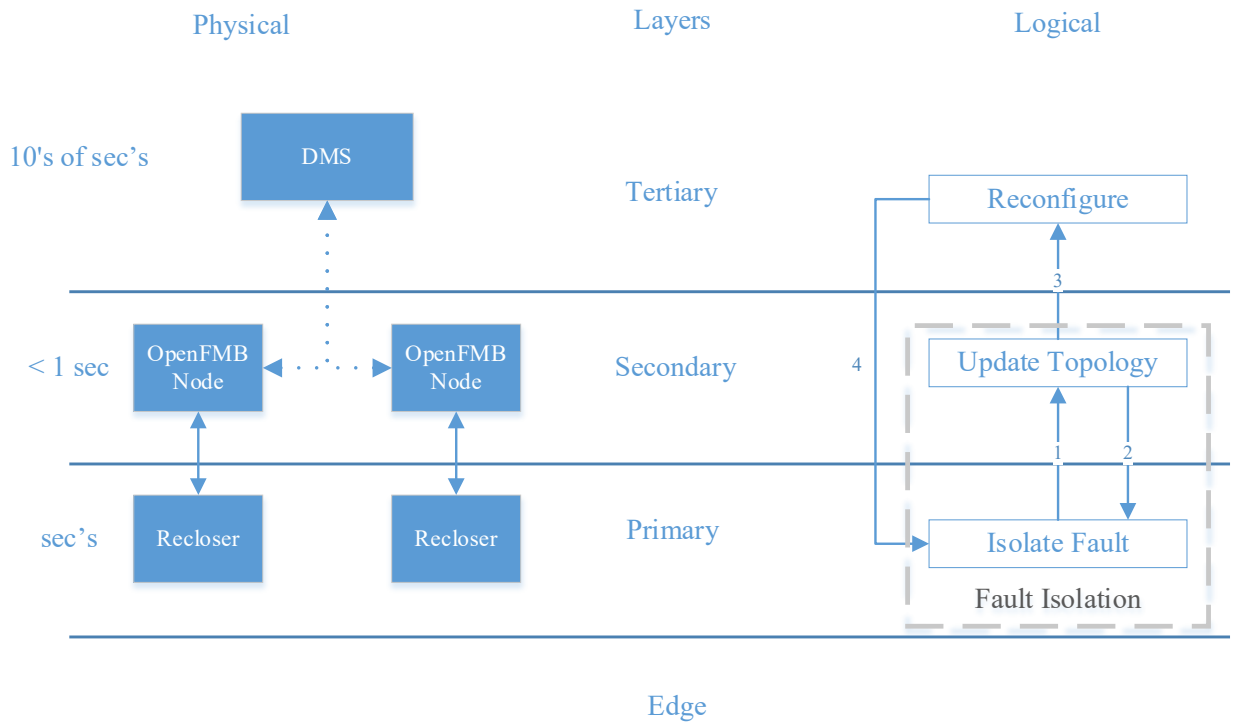

Figure 4.1: Conceptual control architecture.

As shown on the left portion of Figure 4.1, there are four layers to the architecture. For consistency with electric power system control conventions, these are the DER/Premises, primary, secondary, and tertiary layers (moving from edge to central control). The time-scale of action for the three upper layers also is shown: Primary being sub-second, secondary on the order of seconds, and tertiary being on the order of tens of seconds to minutes.

The left portion of the figure also illustrates communications pathways. There are two classes of communication shown: general, broad paths from the DMS to Open Field Message Bus (OpenFMB) nodes and from OpenFMB nodes to DER or premises devices; and tightly coupled direct communication from the OpenFMB nodes to the recloser devices. The right side of the figure shows the baseline logical structure and interactions associated with automated reconfiguration.

The sequence of actions for a typical line-to-ground fault is illustrated via the numbered arrows in Figure 4.2, and is provided as an example of how the architecture operates.

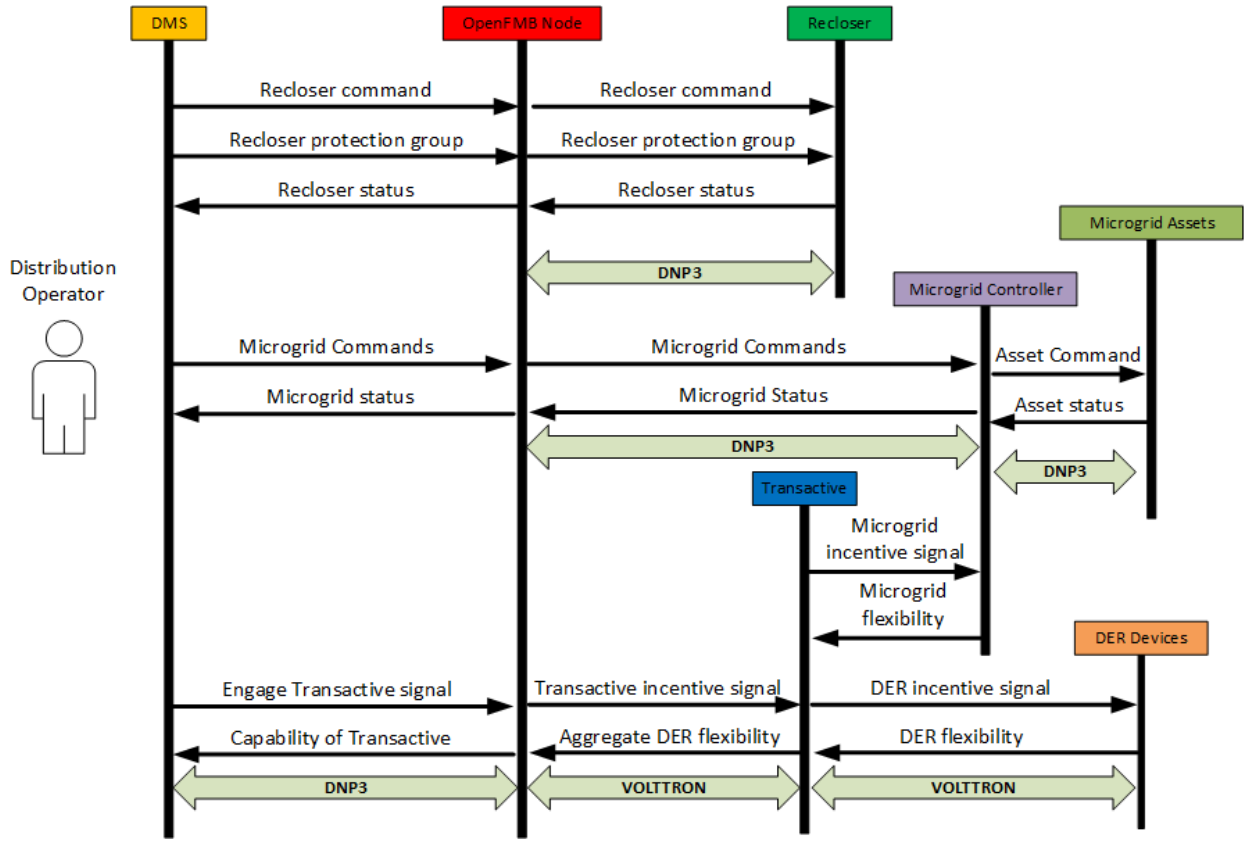

Figure 4.2: Sequence of actions for a typical line-to-ground fault.

The sequence and layers are listed as follows:

- Layer 1: Locally, the fault is detected and isolated by individual reclosers.
- Layer 2: Using the OpenFMB Harness, any status changes which occur are detected by each recloser, using the publish and subscribe (pub/sub) system.
- Layer 1: Each recloser updates its protection group settings based on the information obtained via the pub/sub-system.
- Layer 3: Centrally at the DMS, the optimal switching plan is determined based on the current reclosers' status values, from the pub/sub-system, and based on the customers who are not being served.

5.0 OpenFMB Harness

The Architecture shown in Section 4.0 shows operations at a conceptual level, but it still needs to be implemented in physical equipment, supported by software. The work presented in this final project report was conducted OpenFMB as a reference architecture, using an OpenFMB Harness. The "Harness" is the distributed command and control structure that the project developed as shown in Figure 5.1, and is the physical instantiation of the OpenFMB architecture.

The Harness can be accessed by utility and non-utility assets to share information in the pub/sub-system; control signals are not sent over the OpenFMB Harness. The communications infrastructure for the Harness uses the leased LTE network that Duke Energy uses for its operations. For utility assets, the connection to the Harness is made using SEL RTACs. The assets include multiple G&W Viper-S® reclosers through SEL 651R relays, the GE DMS through a DNP3 connection, and a microgrid controller.

For non-utility assets, the connection to the Harness is made using VOLTTRON™ nodes [7]. VOLTTRON is an open-source technology developed by the Department of Energy to be a flexible, scalable, economical, and secure solution to operate the Internet of Things (IoT). The assets that may interact via a VOLTTRON node include inverters and potentially the Building Energy Management System (BEMS) of TCC. While it would be technically possible to interconnect this equipment with an IED, it would not be cost effective. This is why VOLTTRON nodes are used. It is not expected that the non-utility inverters will be engaged in the field deployment/commissioning, but laboratory testing was conducted to evaluate the engagement of non-utility assets as part of the Harness.

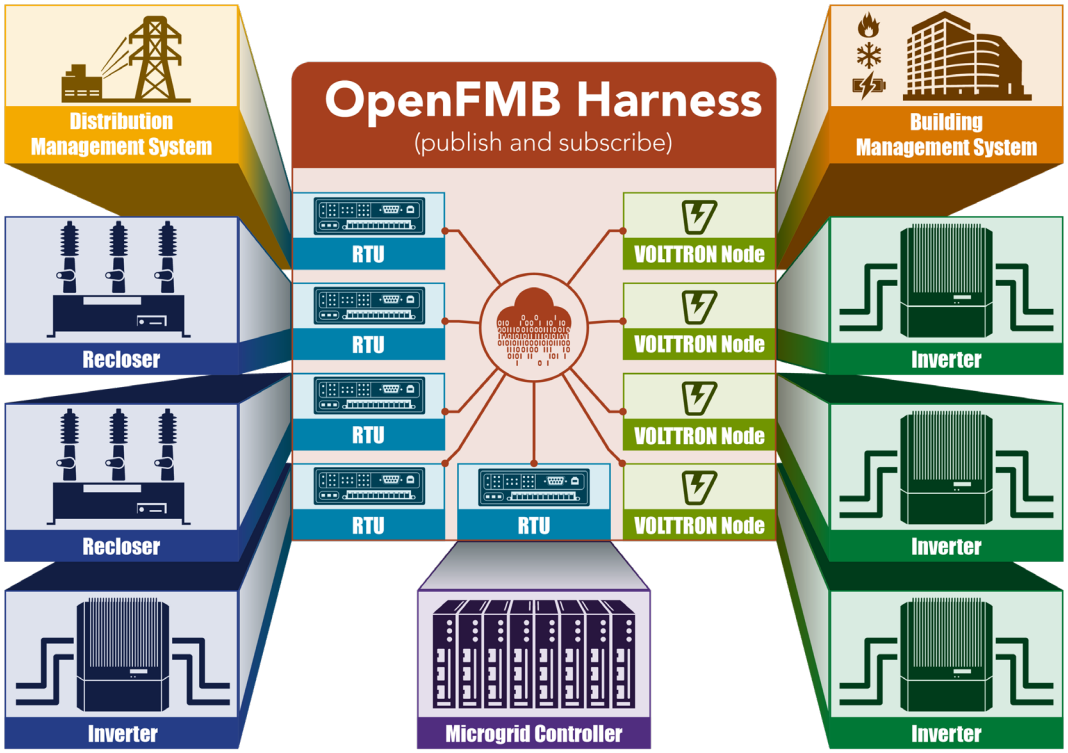

Figure 5.1: Structural view of the OpenFMB Harness being deployed on the Duke Energy circuits.

To enable communication between non-utility DERs and OpenFMB, a connection between each system is required. VOLTTRON as an open-source platform [9] is used to form the connection between the Harness and the non-utility DERs. The VOLTTRON node is designed to send the inverter's data to the Harness and to receive the control signal from the Harness in order to determine how, and if, to change set points of the inverter. In addition, the VOLTTRON node is also designed to interact with the Transactive Energy System (TES) for demonstrating the participation of the inverter to bid into a reactive power market [10]. A VOLTTRON node is required to communicate with both inverters and the Harness by using Modbus and NATS, respectively. The developed VOLTTRON node framework is shown in Figure 5.2.

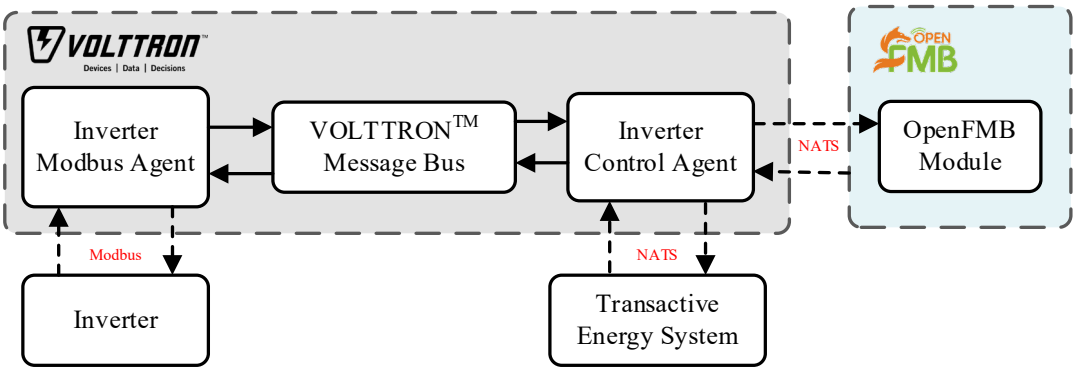

Figure 5.2: VOLTTRON node framework.

An agent is defined as a system that is situated in an environment that is capable of autonomous actions to meet its design objectives [11]. The agents in a VOLTTRON node, including inverter Modbus agent and inverter control agent, are developed to handle tasks separately. The inverter Modbus agent is the connection between the VOLTTRON node and inverter for monitoring and controlling. PyModbus, a Python package [12], is implemented in the agent to enable the communication between the VOLTTRON node and the inverter via Modbus TCP/IP. The inverter Modbus agent contains addresses of measured parameters of interest, including voltage magnitude, current magnitude, active power, and reactive power. For control, setpoints are written into active and reactive power addresses for changing the operating point of the inverter based on the setpoint data. For monitoring, the inverter Modbus agent reads data from registers to provide the data of voltage, current, active, and reactive power from the inverter.

The inverter control agent is designed to be the connection between a VOLTTRON node and the Harness, enabling communications between the inverter and the TES. Since the TES is not currently a part of the OpenFMB model, the detail of the VOLTTRON node and TES will be provided in the Transactive Energy section of this report, Section 9.0. The inverter control agent can send the inverter data to the OpenFMB model using the NATS protocol, and it can receive control signals directly from the OpenFMB model to change set points of the inverter. The VOLTTRON node framework was tested to verify the capabilities of communicating with the Harness by using the solar control profile and solar reading profile of the OpenFMB model. The VOLTTRON node is able to map the data points in terms of operating points from the inverter to the solar reading profile and is able to receive the control signals in terms of ramp rate of active power and reactive power from the solar control profiles. The data points of parameters from the solar reading profile and the solar control profiles are shown in Table 5.1 and Table 5.2, respectively.

Table 5.1: Data Points of Parameters in Solar Reading Profile

Parameters	OpenFMB Data Point
Va (V)	solarReading.readingMMXU.PhV.phsA.cVal.mag.f.value
Vb (V)	solarReading.readingMMXU.PhV.phsB.cVal.mag.f.value
Vc (V)	solarReading.readingMMXU.PhV.phsC.cVal.mag.f.value
Active power (kW)	solarReading.readingMMXU.W.net.cVal.f.mag.value
Reactive power (kvar)	solarReading.readingMMXU.Var.net.cVal.mag.f.value

Table 5.2: Data Points of Parameters in Solar Control Profile

Parameters	OpenFMB Data Point
Active power setpoint	SolarControlScheduleFSCH.ValDCSG.crvPTs.add() 1) rampRates.positiveRealpowerKWPerMin.value 2) rampRates.negativeRealpowerKWPerMin.value
Reactive power setpoint	SolarControlScheduleFSCH.ValDCSG.crvPTs.add() 1) rampRates.positiveReactivepowerKVarPerMin.value 2) rampRates.negativeReactivepowerKVarPerMin.value

For demonstrating the capability of a VOLTTRON node to communicate to with the OpenFMB model, a test scenario was developed under the case that the control signal is sent directly from the OpenFMB model to the inverter that has an agreement to provide the support to the system when it is needed. The control signal in this test scenario is sent via NATS through the Harness to the inverter. The mapping between the Harness and the particular inverter is done by using universally unique identifiers (UUIDs) to guarantee that the control signal will be sent to the desired inverter. Inverter control agents in VOLTTRON nodes detect the control signal from the subscribed topic, which contains an amount of requested reactive power and time duration for providing the support. The agent publishes a control signal to the VOLTTRON message bus by using a specific topic which is subscribed to by inverter Modbus agents. After the inverter Modbus agent receives the control signal and sets the new setting points to the inverter, the new operating points will be read from the inverter and sent back to the OpenFMB reading profile for updating the current status of the inverter. The results of inverter dispatch based on OpenFMB's direct control approach and the updated operating points of the inverter to OpenFMB are shown in Figure 5.3 and Figure 5.4, respectively. The results show that the developed VOLTTRON node can be used as the connection between the OpenFMB Harness and non-utility assets such as inverters. The VOLTTRON node is able to subscribe to the control signal from the Harness and it can send the inverter parameters to the OpenFMB profile for updating the operating point of the inverter.

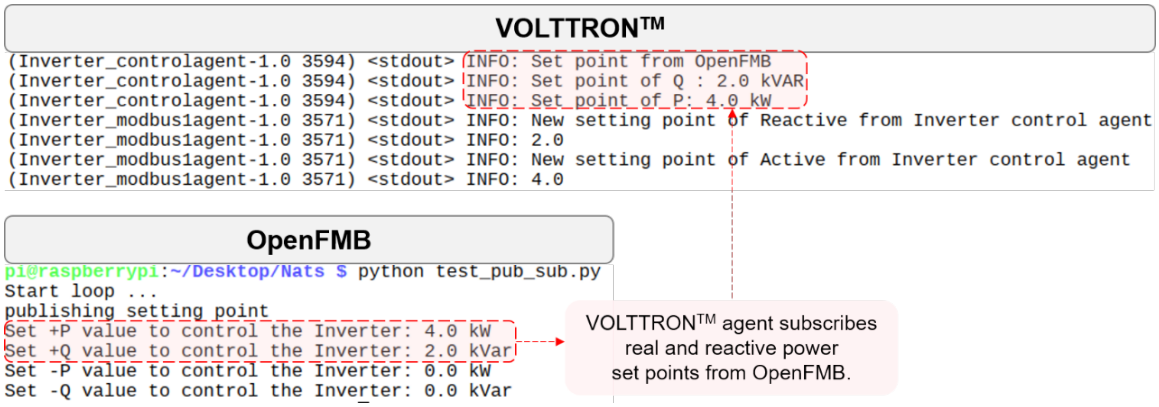

Figure 5.3: Inverter control agent subscribes active and reactive power set points from OpenFMB.

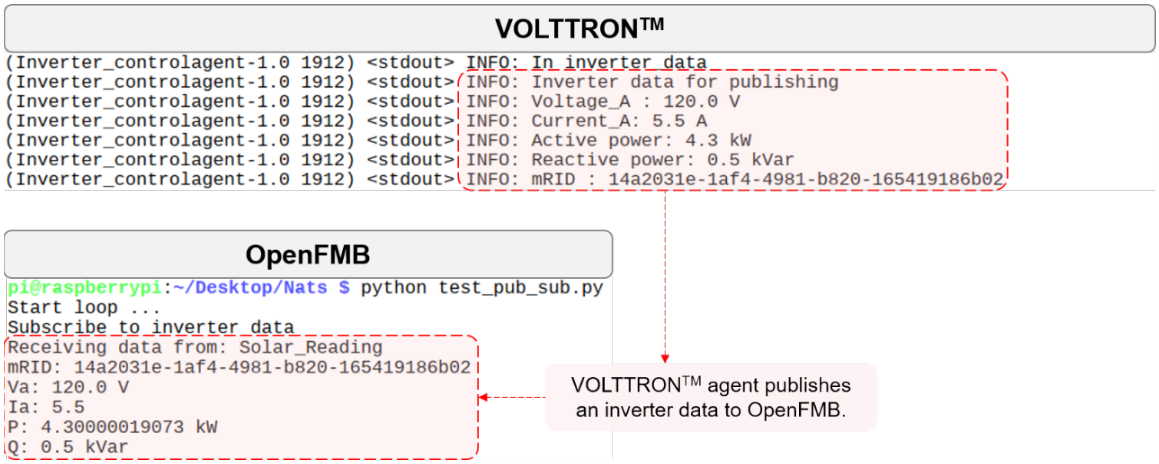

Figure 5.4: Inverter control agent publishes inverter data to update in OpenFMB.

The Harness demonstrates the ability of a VOLTTRON node to act as the connection that enables the communication between both systems. NATS has been used as the pub/sub communication protocol between the OpenFMB and the non-utility DERs, which enables peer to peer communication among the devices. Each device can receive data based on the subscription topics. This peer-to-peer idea reduces the latency of direct communication between the system and devices. So that the controlling and monitoring of non-utility inverters can be done locally by using the OpenFMB with the VOLTTRON node as a connection to the customer's devices.

6.0 Operational Use-Cases

The OpenFMB Harness described in Section 5.0 is a control system that enables a wide range of communications and operations. This section describes four use-cases detailing how the OpenFMB Harness enables operations that coordinate the centralized and distributed resources. These use-cases were used as the basis for the project and were the framework for the execution of work by the team members. This includes the reliability and resiliency metrics, inverter aging, simulations, transactive energy systems, and the HIL modeling. Each use-case provides a sequence of operations for various events to represent how the electrical system, and operators are expected to respond to various conditions. All work conducted in the project is traceable to one or more elements in the use-cases.

Within the following use-case discussions, there are many operations that are not fully expanded. For example, the closing of a recloser that requires paralleling between two sources involves multiple procedural steps. Instead of detailing all of the procedural steps, the use-cases will simplify this to a statement such as "close RCL-5." This is done so that the same description of complex actions is not continuously repeated. The detailed procedural steps for these operations can be found in Appendix A.

Each of the four use-cases presented in this section has three associated scenarios. The first scenario assumes that only the self-healing system is in operation. The second scenario assumes that the self-healing system and the microgrid are in operation. The third scenario assumes that the self-healing system, the PVs, and the TES are all in operation. An overview of these use-cases and their scenarios is shown in Table 6.1. The simulation results of all scenarios are presented in Section 10.2, Appendix B, and Appendix C.

Table 6.1: List of Use-Cases and Scenarios

Use-Case	Scenario
Use-Case#1 Blue-Sky Operations	Use-Case #1-S1: Self-Healing System Only
	Use-Case #1-S2: Self-Healing and Microgrid
	Use-Case #1-S3: Self-Healing, DERs, and Transactive Energy
Use-Case#2 Grey-Sky Operations	Use-Case #2-S1: Self-Healing System Only
	Use-Case #2-S2: Self-Healing and Microgrid
	Use-Case #2-S3: Self-Healing, DERs, and Transactive Energy
Use-Case#3 Grey-Sky Operations	Use-Case #3-S1: Self-Healing System Only
	Use-Case #3-S2: Self-Healing and Microgrid
	Use-Case #3-S3: Self-Healing, DERs, and Transactive Energy
Use-Case#4 Dark-Sky Operations	Use-Case #4-S1: Self-Healing System Only
	Use-Case #4-S2: Self-Healing and Microgrid
	Use-Case #4-S3: Self-Healing, DERs, and Transactive Energy

6.1 Use-Case#1 Blue-Sky Operations

Use-case #1 examines operations for normal switching/reconfiguration activities under blue-sky conditions. Blue-sky conditions are defined as normal operations when all controls are in operation, and a small number of uncorrelated faults or scheduled maintenance activities may occur. Descriptions of use-case #1 scenarios follow.

6.1.1 Use-Case #1-S1: Self-Healing System Only

In the first scenario for use-case #1, it is assumed that only the self-healing system is in operation and that there are no manual field operations performed. For this scenario, the DO decides to "pre-condition" the system prior to an event to place the distribution system in a more resilient configuration such as possibly before a major storm. In this scenario, there are no system faults, and the DO is executing a series of switching operations. The decision is to move two segments so that load is transferred between feeders: Segment #9 is moved from circuit F-3 to circuit F-4, and Segment #5 is moved from circuit F-2 to circuit F-3. The final configuration for this scenario is depicted in Figure 6.1.

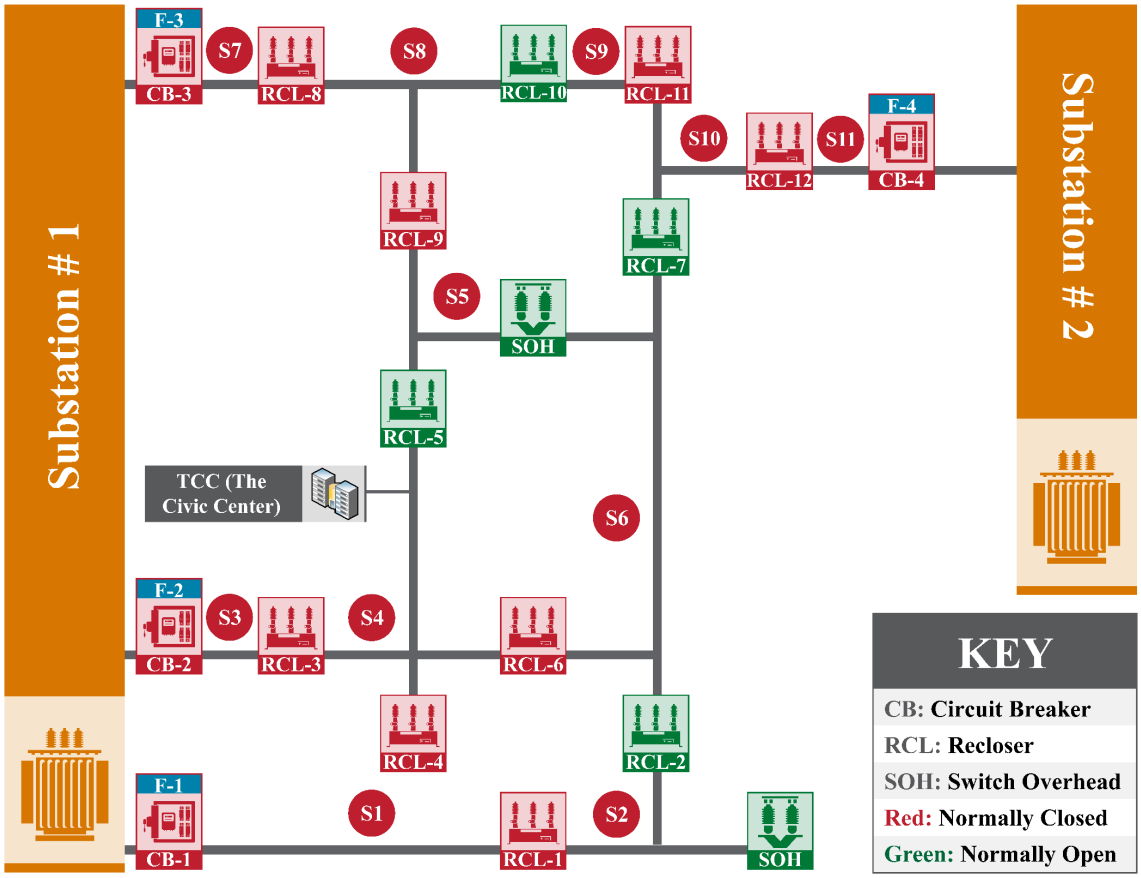

Figure 6.1: Use-Case #1-S1 final configuration.

The associated DO switching plan is detailed as follows:

- DO decides to pre-condition the system prior to a storm (only self-healing system in operation).
- Develop a switching plan (grid engineer involved, couple of hours, includes selection of protection settings). For this use-case scenario, two segments will be moved:
    - Segment #9 is moved from circuit F-3 to circuit F-4.
    - Segment #5 is moved from circuit F-2 to circuit F-3.
- The DO executes the switching plan:
    - Close RCL-11 (parallel circuit F-3 and circuit F-4).

- Open RCL-10 (move Segment #9 from circuit F-3 to circuit F-4).
- Close RCL-9 (parallel circuit F-2 and circuit F-3).
- Open RCL-5 (move Segment #5 from circuit F-2 to circuit F-3).

- DO informs Grid Engineer that the switching plan is complete.

6.1.2 Use-Case #1-S2: Self-Healing and Microgrid

In the second scenario for use-case #1, it is assumed that the self-healing system and the microgrid are in operation and no manual field operations are performed. For this scenario, the DO decides to "pre-condition" the system prior to an event to place the distribution system in a more resilient configuration by intentionally islanding the microgrid. The DO may choose to do this because of an anticipated loss of the transmission supply due to an extreme weather event. In this scenario, there are no system faults, and the DO is executing a series of switching operations, including a signal to the microgrid controller. The DO decides to move two segments so that load is transferred between feeders: Segment #5 is moved from circuit F-2 to circuit F-3, Segment #6 is moved from circuit F-2 to circuit F-1, and Segment #4 is established as a microgrid. The final configuration for this scenario is depicted in Figure 6.2.

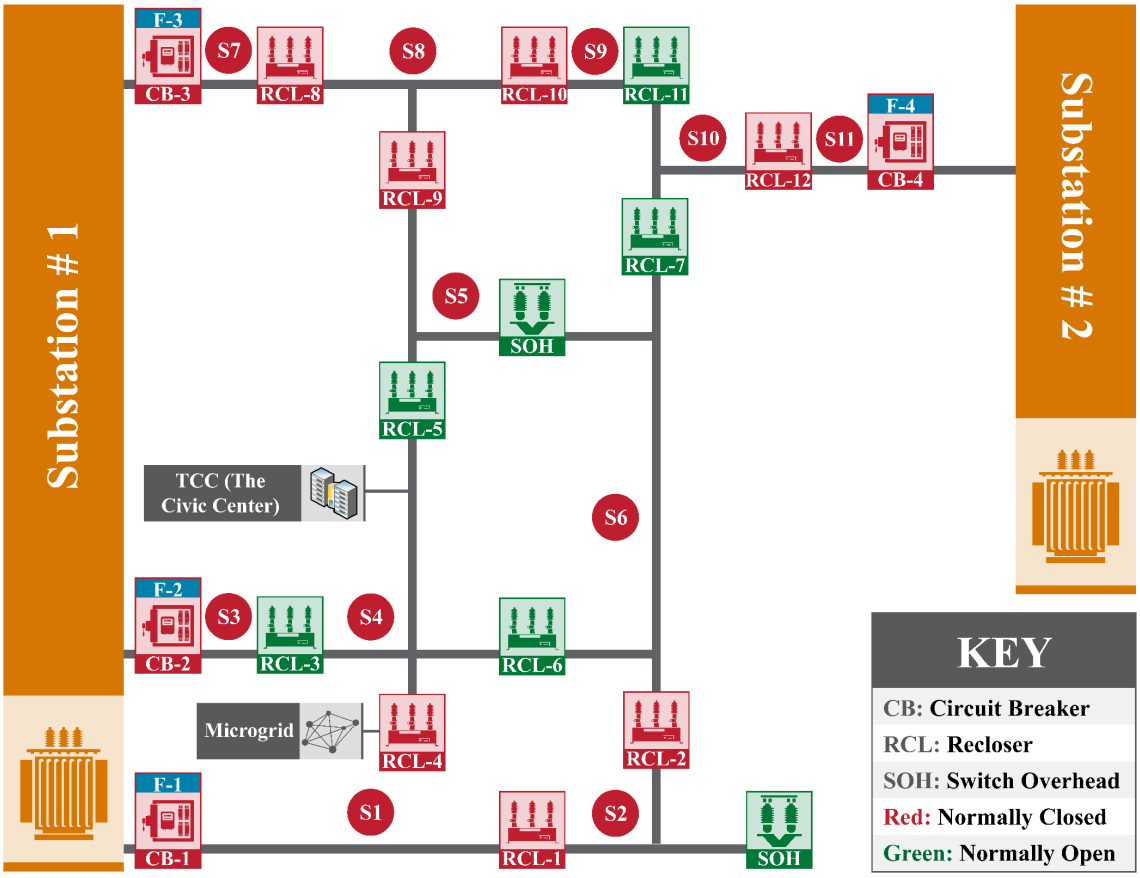

Figure 6.2: Use-Case #1-S2 final configuration.

The associated DO switching plan is detailed as follows:

- DO decides to pre-condition the system prior to a storm (self-healing system and microgrid are in operation).
- Develop a switching plan to intentionally island the microgrid (grid engineer involved, couple of hours, selection of protection setting initiates islanding of the microgrid). For this plan:
    - Energize Segment #5 from circuit F-3, Segment #6 from circuit F-1, and Segment #4 from the microgrid.
        - Segment #5 moved from circuit F-2 to circuit F-3.
        - Segment #6 moved from circuit F-2 to circuit F-1.
        - Segment #4 will become an islanded microgrid.
- The DO executes the switching plan:
    - Energize Segment #5 from circuit F-3, Segment #6 from circuit F-1, and Segment #4 from the microgrid:
        - Close RCL-9 (parallel circuit F-2 and #12010).
        - Open RCL-5 (move Segment #5 from circuit F-2 to circuit F-3).
        - Close RCL-2 (parallel circuit F-1 and circuit F-2).
        - Open RCL-6 (move Segment #6 from circuit F-2 to circuit F-1).
        - Direct microgrid controller to island with Segment #4:
            - The microgrid controller ensures that it will be able to support all load on Segment #4.
            - If it is necessary to discharge energy storage to meet the load requirements the microgrid controller will estimate for how long the segment can be supported before the energy storage is fully discharged.
            - It is assumed that the microgrid can support operations for the desired length of time.
            - DO sends block command to RCL-4 using DMS/Distribution-Supervisory Control and Data Acquisition (D-SCADA).
            - Open RCL-3 (isolate the microgrid area).
            - The microgrid control switches from grid following to grid forming and parallels all assets and forms a stable island.
            - DO manually removes block on RCL-4 via DMS/D-SCADA.
            - Segment #4 is a stable island with the microgrid controlling frequency and voltage.
- DO informs Grid Engineer that the switching plan is complete.

6.1.3 Use-Case #1-S3: Self-Healing, DERs, and Transactive Energy System

In the third scenario for use-case #1, it is assumed that the self-healing system, the DERs, and the TES are in operation, and no manual field operations are performed. The switching operations are the same to the ones of use-case #1-S1. However, DERs and the transactive energy system are engaged to improve the voltage profiles. See Section 10.2.2 for details.

6.2 Use-Case#2 Grey-Sky Operations

Use-case #2 examines operations when an isolated event occurs under blue-sky conditions. An example is a single line-to-ground fault.

6.2.1 Use-Case #2-S1: Self-Healing System Only

In the first scenario for use-case #2, it is assumed that only the self-healing system is in operation and there are no manual field operations performed. For this scenario, there is a bolted single line-to-ground fault on Segment #3. The segment-based system operates to restore the maximum number of end-use customers after the reclosers have isolated the fault. The final configuration for this scenario is depicted in Figure 6.3.

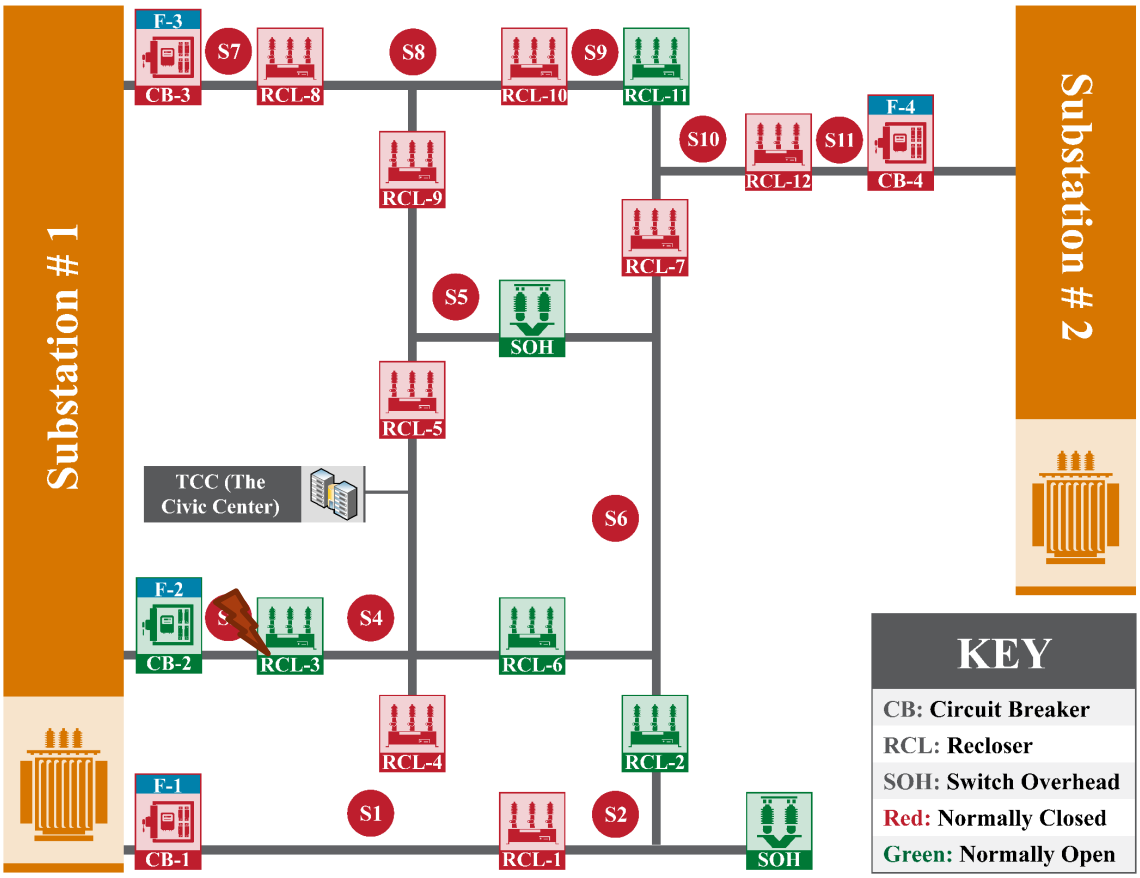

Figure 6.3: Use-Case #2-S1 final configuration.

The associated DO switching plan is detailed as follows:

- A bolted fault occurs on Segment #3. It is assumed that this fault is caused by a tree falling across the line, resulting in multiple damaged poles and phase conductor on the ground.
- Because of the fault location, CB-2 is the only protective device to see fault current and operates based on local protection settings, opening CB-2.
- With the opening of CB-2, Segments #3, #4, #5, and #6 lose power.

- The centralized self-healing system evaluates the current system condition and determines a switching plan to reenergize Segments #4, #5, and #6. There are multiple options for reenergizing these segments, and the self-healing system develops the following switching plan which is automatically executed:
  - Energize Segments #4 and #5 from circuit F-3:
    - Open RCL-3.
    - Open RCL-6.
    - Close RCL-9.
  - Energize Segment #6 from circuit F-4:
    - Close RCL-7.
- The self-healing system indicates to the DO that a self-healing switching plan has been executed, and that service has been restored to Segments #4 and #6.

6.2.2 Use-Case #2-S2: Self-Healing and Microgrid

In the second scenario for use-case #2, it is assumed that the self-healing system and microgrid are in operation and no manual field operations are performed. For this scenario, there is a bolted fault on Segment #3. The segment-based system operates to restore the maximum number of end-use customers after the reclosers have isolated the fault. The final configuration for this scenario is depicted in Figure 6.4.

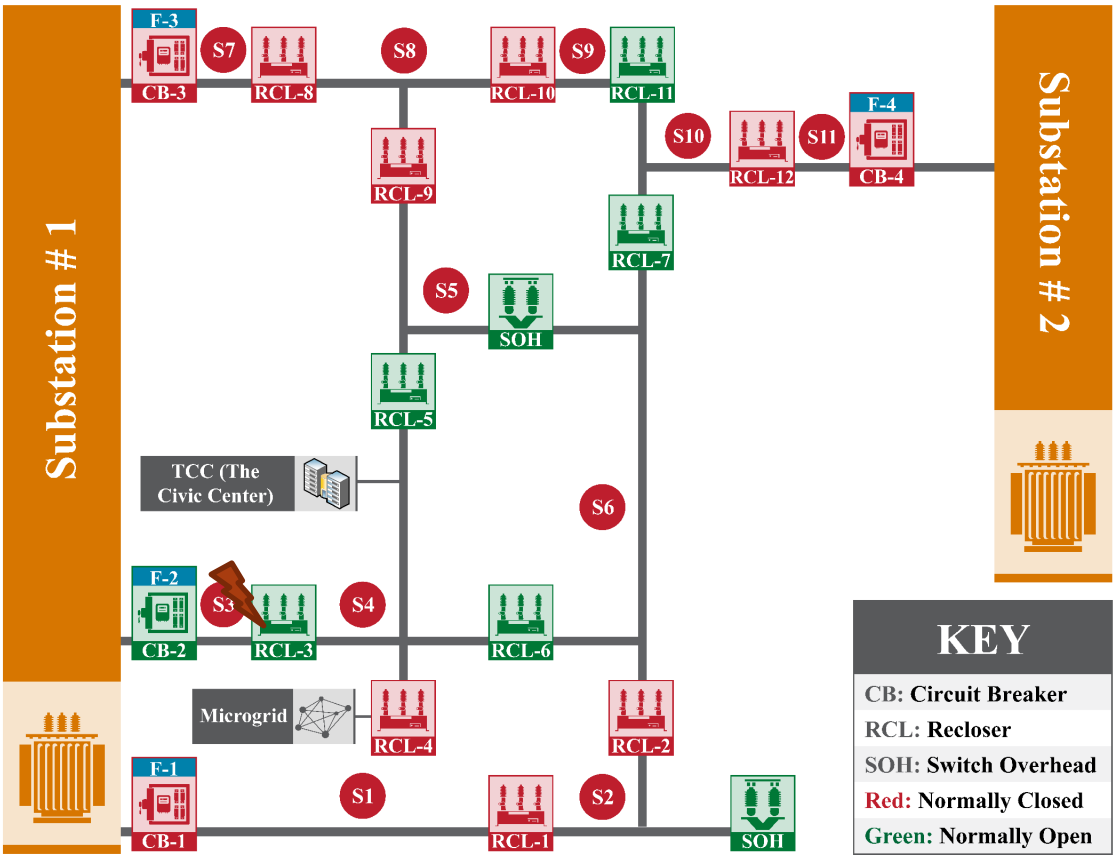

Figure 6.4: Use-Case #2-S2 final configuration.

The associated DO switching plan is detailed as follows:

- A bolted fault occurs on Segment #3. The cause is assumed to be a tree that fell across the line, resulting in multiple damaged poles and a phase conductor on the ground.
- Because of the fault location, CB-2 is the only protective device to see fault current and operates based on local protection settings, opening CB-2. In addition, RCL-4 opens in accordance with IEEE 1547 anti-islanding requirements.
- With the opening of CB-2, Segments #3, #4, #5, and #6 lose power.
- The centralized self-healing system evaluates the current system condition and determines a switching plan to reenergize Segments #4, #5, and #6. There are multiple options for reenergizing these segments, and the self-healing system develops a switching plan that involves the microgrid, and is automatically executed:
    - Energize Segment #4 from the microgrid:
        - The microgrid controller determines that it can supply power to Segment #4 at its current load for 4.5 hours, which is more than the time required.
        - The microgrid controller reports this to the centralized self-healing systems.
        - The centralized self-healing system re-evaluates the switching plan and determines that the use of the microgrid is desired.
        - The self-healing system instructs the microgrid controller to island and supply power to Segment #4.
        - The microgrid controller determines that it can supply the load on Segment #4 for the required time and executes the islanding operation.
    - Energize Segments #4 from the microgrid:
        - Open RCL-3 (isolate the fault).
        - Open RCL-6 (isolate Segments #4 from Segment #6).
        - Open RCL-5 (isolate Segments #4 from Segment #5).
        - Form a microgrid behind RCL-4 with a stable frequency and voltage.
        - Close RCL-4 (energize Segment #4).
    - Energize Segment #6 from circuit F-1:
        - Close RCL-2 (energize Segment #6).
    - Energize Segment #5 from circuit F-3:
        - Close RCL-9 (energize Segment #5).

6.2.3 Use-Case #2-S3: Self-Healing, DERs, and Transactive Energy System

In the third scenario for use-case #2, it is assumed that the self-healing system, the DERs, and the TES are in operation, and no manual field operations are performed. The switching operations are the same as the ones of use-case #2-S1. However, DERs and the transactive energy system are engaged to improve the voltage profiles. See Section 10.2.2 for details.

6.3 Use-Case#3 Grey-Sky Operations

Use-case #3 examines operations when multiple events occur under grey-sky conditions. A grey-sky condition assumes that all control systems are in operation; however, there are multiple uncorrelated simultaneous faults. An example is a single line-to-ground fault.

6.3.1 Use-Case #3-S1: Self-Healing System Only

In the first scenario for use-case #3, it is assumed that only the self-healing system is in operation and no manual field operations are performed. For this scenario, there are two line-to-ground faults that are not related; they occur on Segments #3 and #7. The segment-based system operates to restore the maximum number of end-use customers after the reclosers have isolated the fault. The final configuration for this scenario is depicted in Figure 6.5.

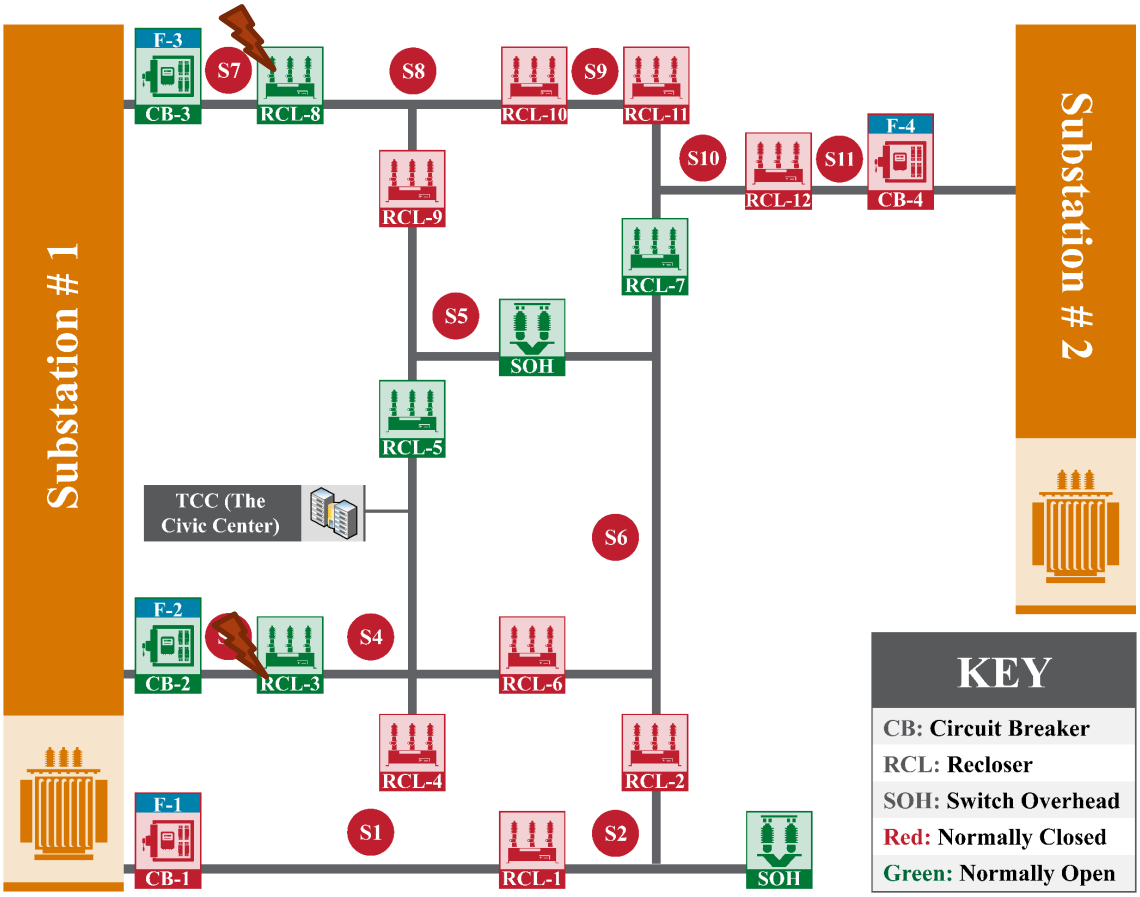

Figure 6.5: Use-Case #3-S1 final configuration.

The associated DO switching plan is detailed as follows:

- Bolted faults occur on Segments #3 and #7 at approximately the same time. The cause is assumed to be trees falling across the lines, each resulting in multiple damaged poles and phase conductors on the ground.
- For the fault on Segment #3, CB-2 is the only protective device to see fault current and operates based on local protection settings, opening CB-2.

- With the opening of CB-2, Segments #3, #4, #5, and #6 lose power.
- For the fault on Segment #7, CB-3 is the only protective device to see fault current and operates based on local protection settings, opening CB-3.
- With the opening of CB-3, Segments #7, #8 and #9 lose power.
- The centralized self-healing system evaluates the current system condition and determines a switching plan to reenergize Segments #4, #5, #7, #8, and #9. There are multiple options for reenergizing these segments, and the self-healing system develops the following switching plan, which is automatically executed:
    - Energize Segment #5, #8,and #9 from circuit F-4:
        - Open RCL-8 (Isolate the fault).
        - CLOSE RCL-11.
        - CLOSE RCL- 9.
    - Energize Segment #4 and #6 from circuit F-1:
        - Open RCL-3 (Isolate the fault).
        - OPEN RCL-5.
        - CLOSE RCL-2.
- The self-healing system indicates to the DO that a self-healing switching plan has been executed, and that service has been restored to Segments #4, #5, #6, #8, and #9.

6.3.2 Use-Case #3-S2: Self-Healing and Microgrid

In the second scenario for use-case #3, it is assumed that the self-healing system and microgrid are in operation and no manual field operations are performed. For this scenario, there are two line-to-ground faults that are not related; they occur on Segments #3 and #7. The segment-based system operates to restore the maximum number of end-use customers after the reclosers have isolated the fault. The final configuration for this scenario is depicted in Figure 6.6.

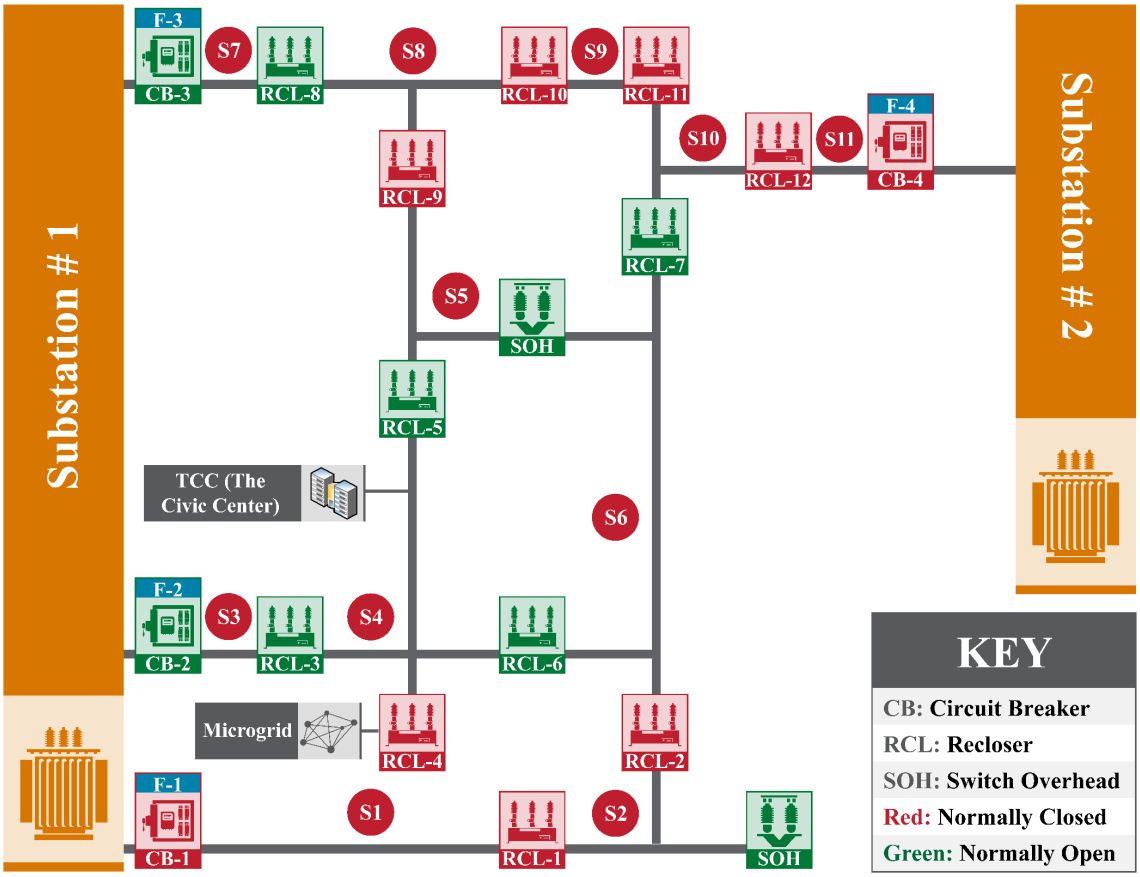

Figure 6.6: Use-Case #3-S2 final configuration.

The associated DO switching plan is detailed as follows:

- Bolted faults occur on Segments #3 and #7 at approximately the same time. The cause is assumed to be trees falling across the lines, each resulting in multiple damaged poles and phase conductors on the ground.
- For the fault on Segment #3, CB-2 is the only protective device to see fault current and operates based on local protection settings, opening CB-2. In addition, RCL-4 opens in accordance with IEEE 1547 anti-islanding requirements.
- With the opening of CB-2, Segments #3, #4, #5, and #6 lose power.
- For the fault on Segment #7, CB-3 is the only protective device to see fault current and operates based on local protection settings, opening CB-3.
- With the opening of CB-3, Segments #7, #8, and #9 lose power.
- The centralized self-healing system evaluates the current system condition and determines a switching plan to reenergize Segments #4, #5, #6, #8, and #9. There are multiple options for reenergizing these segments, and the self-healing system develops the following switching plan which is automatically executed:
    - Energize Segment #4 from the microgrid:
        - The microgrid controller ensures that it will be able to support all load on Segment #4.

        - If it is necessary to discharge energy storage to meet the load requirements, the microgrid controller will estimate for how long the segment can be supported before the energy storage is fully discharged.
        - Open RCL-3 (Isolate the fault).
        - Open RCL-6 (Isolate the segment).
        - Open RCL-5 (isolate the fault).
        - The microgrid control parallels all assets and forms a stable island.
        - Close RCL-4 (energize Segment #4).
        - Segment #4 is a stable island with the microgrid controlling frequency and voltage.
    - Energize Segments #5, #8 and #9 from circuit F-4:
        - Open RCL-8 (isolate the fault).
        - Close RCL-11 (energize Segments #8 and #9).
        - Close RCL-9 (energize Segment #5).
    - Energize Segment #6 from circuit F-1.
        - Close RCL-2 (energize the segments).
- The self-healing system indicates to the DO that a self-healing switching plan has been executed, and that service has been restored to Segments #4, #5, #6, #8, and #9.

6.3.3 Use-Case #3-S3: Self-Healing, DERs, and Transactive Energy System

In the third scenario for use-case #3, it is assumed that the self-healing system, the DERs, and the TES are in operation, and no manual field operations are performed. The switching operations are the same to the ones of use-case #3-S1. However, DERs and the transactive energy system are engaged to improve the voltage profiles. See Section 10.2.2 for details.

6.4 Use-Case#4 Dark-Sky Operations

Use-case #4 examines operations when multiple events occur under dark-sky conditions. A dark-sky condition assumes that one or more failures in communications or controls occur, and there are multiple uncorrelated simultaneous faults. The primary difference between use-case #4 and use-case #3 is that failures also occur in the various control systems, at the same time as the line-to-ground faults. The failures include:

- Two simultaneous faults occur—a single-phase fault to ground and a three-phase fault to ground. (i.e., represents a large storm with potentially correlated faults).
- RCL-2 fails to close (e.g., because of a sensor malfunction).
- Because of damage in the communications infrastructure, breaker status values are not properly updated via OpenFMB. (This leads to potentially miss-coordinated protection, and the DMS will not receive accurate information.)

6.4.1 Use-Case #4-S1: Self-Healing System Only

In the first scenario for use-case #4, it is assumed that only the self-healing system is in operation and no manual field operations are performed. For this scenario, there are two unrelated line-to-ground faults; they occur on Segments #3 and #10. The segment-based system operates to restore the maximum number of end-use customers after the reclosers have isolated the fault. The final configuration for this scenario is depicted in Figure 6.7.

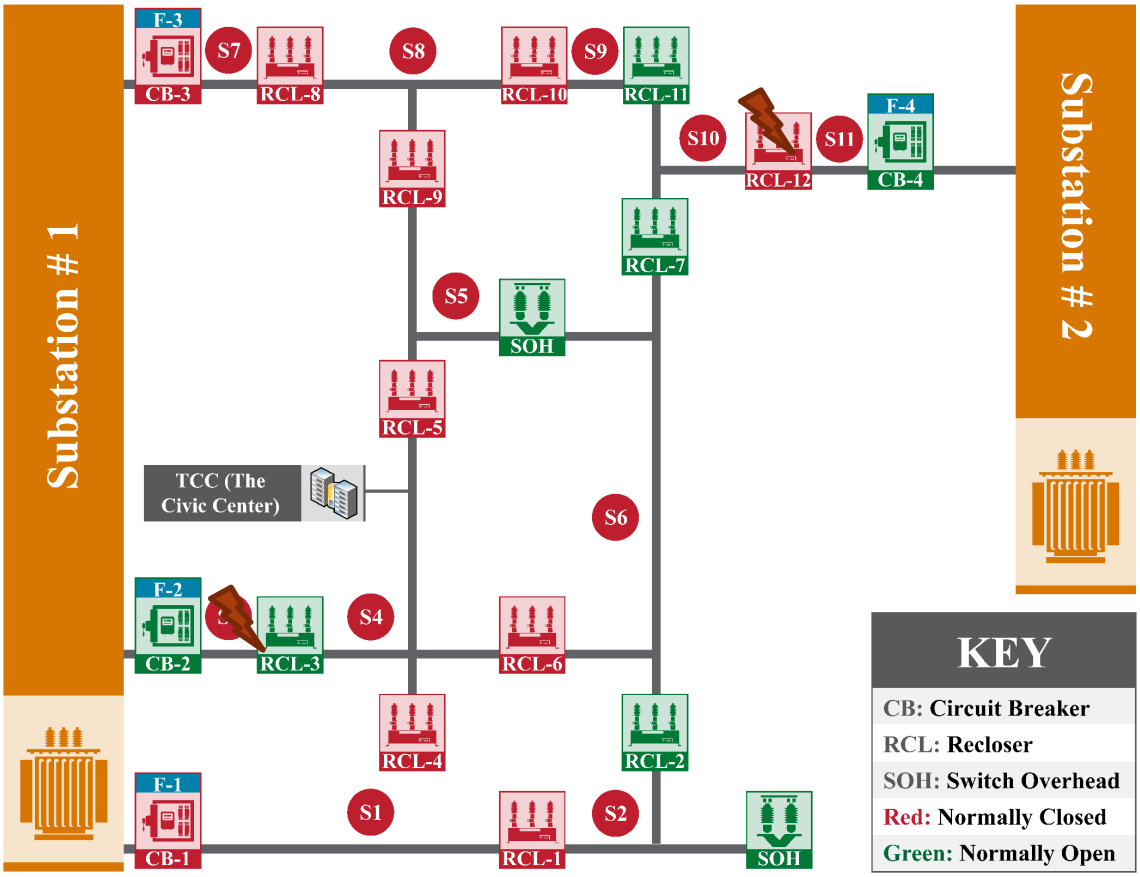

Figure 6.7: Use-Case #4-S1 final configuration.

The associated DO switching plan is detailed as follows:

- Bolted faults occur on Segments #3 and #10 at approximately the same time. The cause is assumed to be trees that have fallen across the lines, each resulting in multiple damaged poles and phase conductors on the ground.
- For the fault on Segment #3, CB-2 is the only protective device to see fault current and operates based on local protection settings, opening CB-2.
- With the opening of CB-2, Segments #3, #4, #5, and #6 lose power.
- For the fault on Segment #10, RCL-12 and CB-4 both see the fault current, and RCL-12 should operate first based on local protection settings.
- Because of a failure within the control logic of RCL-12, the recloser does not operate, thus remaining closed.

- With the continued presence of the fault resulting from failure of RCL-12 to open, CB-4 should operate next based on local protection settings.
- With the opening of CB-4, Segments #10 and #11 lose power.
- The centralized self-healing system evaluates the current system condition and determines a switching plan to reenergize Segments #4 and #6. There are multiple options to reenergize these segments, and the self-healing system develops the following switching plan that it attempts to execute:
    - Energize Segment #4 and #5 from circuit F-3:
        - Open RCL-3 (isolate the fault).
        - Open RCL-6 (isolate the Segment #6 from circuit F-2).
        - Close RCL-9 (energize Segments #4 and #5).
    - Energize Segment #6 from circuit F-1:
        - Attempt to close RCL-2 (energize the segment).
        - RCL-2 fails to indicate a change in status.
- When RCL-2 fails to indicate a change in status, the self-healing system develops the following alternate switching plan, which it executes:
    - Energize Segment #6 from circuit F-3:
        - Close RCL-6 (energize the segment).
- The self-healing system indicates to the DO that a self-healing switching plan has been executed, and that service has been restored to Segments #4 and #6.
- The self-healing system indicates to the DO that there was a failure with the operation of RCL-2.

6.4.2 Use-Case #4-S2: Self-Healing and Microgrid

In the second scenario for use-case #4, it is assumed that the self-healing system and microgrid are in operation and no manual field operations are performed. For this scenario, two unrelated line-to-ground faults occur on Segments #3 and #10. The segment-based system operates to restore the maximum number of end-use customers after the reclosers have isolated the fault. The final configuration for this scenario is depicted in Figure 6.8.

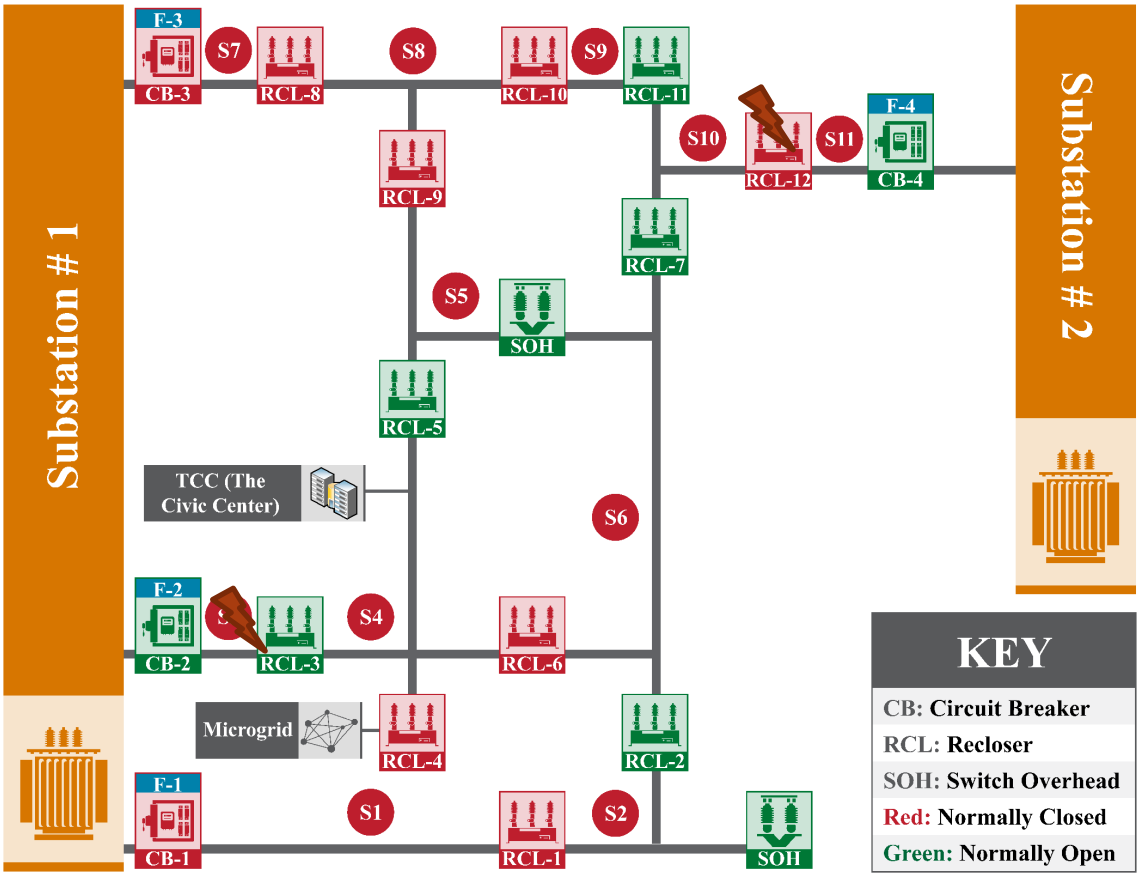

Figure 6.8: Use-Case #4-S2 final configuration.

The associated DO switching plan is detailed as follows:

- Bolted faults occur on Segments #3 and #10 at approximately the same time. The cause is assumed to be trees that have fallen across the lines, each resulting in multiple damaged poles and phase conductors on the ground.
- For the fault on Segment #3, CB-2 is the only protective device to see fault current and operates based on local protection settings, opening CB-2. In addition, RCL-4 opens in accordance with IEEE 1547 anti-islanding requirements.
- With the opening of CB-2, Segments #3, #4, #5, and #6 lose power.
- For the fault on Segment #10, RCL-12 and CB-4 both see the fault current, and RCL-12 should operate first based on local protection settings.
- Due to a failure within the control logic of RCL-12, it does not operate, and remains closed.
- With the continued presence of the fault, due to RCL-12 failing to open, CB-4 should operate next based on local protection settings.
- With the opening of CB-4, Segments #10 and #11 lose power.
- The centralized self-healing system evaluates the current system condition and determines a switching plan to reenergize Segments #4 and #6. There are multiple options for reenergizing these segments, and the self-healing system develops the following switching plan, which is automatically executed:

- Energize Segment #4 from the microgrid:
  - The microgrid controller ensures that it will be able to support all load on Segment #4.
  - If it is necessary to discharge energy storage to meet the load requirements, the microgrid controller will estimate for how long the segment can be supported before the energy storage is fully discharged.
  - Open RCL-3 (isolate the fault).
  - Open RCL-6 (isolate the segment).
  - Open RCL-5 (isolate the segment).
  - The microgrid control parallels all assets and forms a stable island.
  - Close RCL-4 (energize Segment #4).
  - Segment #4 is a stable island with the microgrid controlling frequency and voltage.
- Energize Segment #6 from circuit F-1:
  - Attempts to close RCL-2 (energize the segment).
  - RCL-2 fails to indicate a change in status.

- When RCL-2 fails to indicate a change in status, the self-healing system develops the following alternate switching plan, which it executes:
  - Energize Segment #6 from the microgrid:
    - The microgrid controller ensures that it can support all load on Segments #4 and #6.
    - If it is necessary to discharge energy storage to meet the load requirements, the microgrid controller will estimate for how long the segment can be supported before the energy storage is fully discharged.
    - Close RCL-6 (energize the segment).
- The self-healing system indicates to the DO that a self-healing switching plan has been executed and service has been restored to Segments #4 and #6.
- The self-healing system indicates to the DO that there was a failure with the operation of RCL-2.

6.4.3 Use-Case #4-S3: Self-Healing, DERs, and Transactive Energy

In the third scenario for use-case #4, it is assumed that the self-healing system, the DERs, and the TES are in operation, and no manual field operations are performed. The switching operations are the same to the ones of use-case #4-S1. However, DERs and the transactive energy system are engaged to improve the voltage profiles. See Section 10.2.2 for details.

7.0 Reliability/Resilience Metrics

The use-cases in Section 6.0 outlined a range of operations that were the basis for project research. In this section, the reliability and resilience of Duke Energy distribution systems has been evaluated considering the optional use-cases of Section 6.0. The use-cases are, self-healing system/SOG, the microgrid, and TES. The analysis was conducted using a time-sequential Monte Carlo simulation method. The reliability analysis function in the sensor placement optimization tool (SPOT) is leveraged and enhanced by integrating the three advanced technologies [13]. With the input of the system circuit models and other parameters from the Duke Energy distribution systems, the reliability evaluation method generates a series of fault events in a 10-year time period, performs fault location, isolation and service restoration using FLISR for each fault event, calculates the outage history of each load point, and finally calculates the reliability and resilience indices of the critical loads and the whole system. In this process, three-phase unbalanced power flow is performed for each restoration strategy to ensure the voltage operation constraints are satisfied. A detailed operational sequence is designed and implemented to coordinate the non-utility owned DERs and utility owned assets such as self-healing system and microgrids in service restoration. Results show that the reliability indices for both the whole system and the critical loads are improved using the self-healing control, microgrid, and transactive energy. The engagement of non-utility owned DERs through a TES plays a significant role in improving the reliability of both the whole system and the critical load.

7.1 Evaluation Methodology

The following sections outline the methodology that was used to evaluate the reliability and resiliency of the new system, using the technologies developed as part of the project.

7.1.1 Overview of Sensor Placement Optimization Tool

To quantitatively evaluate the reliability and resilience considering the three advanced technologies, this project leverages the SPOT that was developed in a former GMLC funded project [13]. As shown in Figure 7.1, the SPOT has a module-based structure with several applications. For example, meter placement for improving the distribution state estimation accuracy, and the recloser placement for enhancing distribution system reliability.

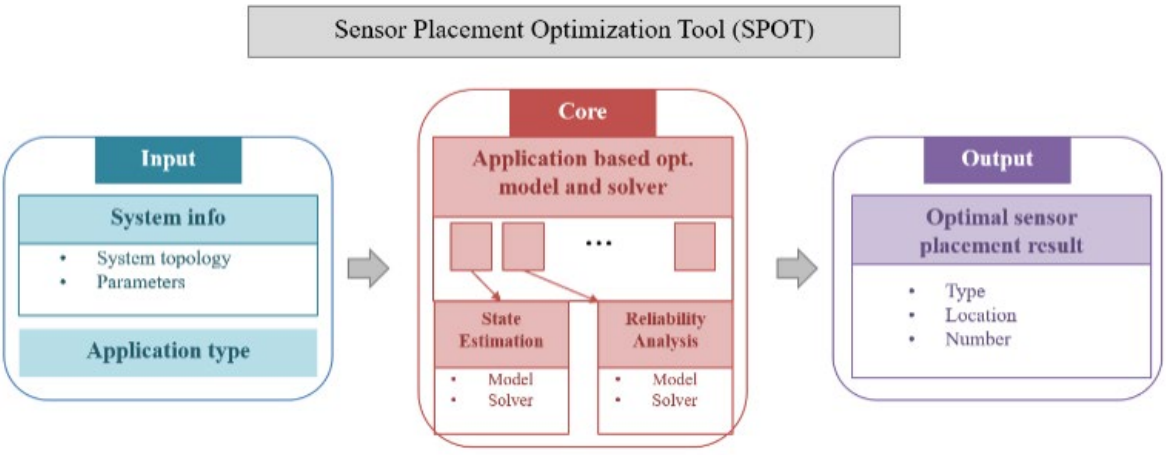

Figure 7.1: Conceptual structure of SPOT.

For the recloser placement module, the main purpose is to optimize recloser locations to improve distribution system reliability. A conceptual structure of the recloser placement module is shown in Figure 7.2. The input contains network topology, historical reliability indices, existing recloser locations, the location and territory of distributed generators, and the number of reclosers to be placed. After this data is supplied to the algorithm, the sensor placement program is used to update the sensor strategies and each strategy is evaluated in the reliability analysis program. This process is repeated until the optimal solution is found.

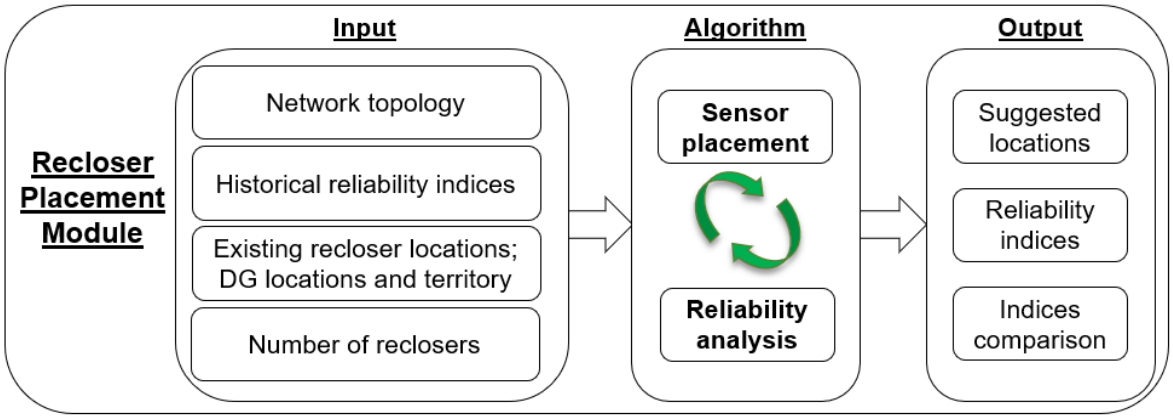

Figure 7.2: Conceptual structure of recloser placement module.

In this project, the reliability program is leveraged and modified to integrate the three advanced technologies, i.e., self-healing control, microgrid, and transactive energy.

7.1.2 Method for Reliability Evaluation

Given the input of the system circuit model and other parameters such as the failure rate and repair time of each component, the reliability evaluation method can calculate the reliability indices of the whole system and the critical loads. For this work, the impedances of the overhead lines and underground cables are used to compute the three-phase unbalanced power flow [14] to ensure the voltage constraints are satisfied during all operations.

The historical reliability indices in the utility are used to calibrate the failure rate and repair time of the overhead lines and underground cables. The microgrid locations and territories are needed for the service restoration using the microgrids. The locations and capacities of the non-utility DERs are also needed to capture the additional load restoration when engaging the transactive energy.

The reliability evaluation procedure is shown in Figure 7.3. The event history of each component is first generated using a time sequential Monte Carlo simulation [15] after importing the system parameters. Momentary faults are not considered in this report. For each fault event k in $\{1, 2, \ldots, K\}$, where K is the total number of events, fault isolation and service restoration are performed to identify the interrupted load sections during the event. The faults happening at a lateral branch are isolated by a fuse, and the customers are restored after the fuse is replaced. The faults happening at the main trunk are isolated by reclosers, and the restoration process is described below. The reliability indices are then calculated from the customer interruptions of all generated events.

The operational sequence of the service restoration using the three advanced techniques is designed. First, a three-phase to ground fault happens at fault k. An example of this type of fault would be a tree falling

across the line and contacting the ground. Based on the fault location, the adjacent protective devices (e.g., reclosers, circuit breakers, etc.) sense the fault current and operate based on the local protection settings. The faulted segment will remain in a non-energized (isolated) state until the faulted line is repaired. The centralized self-healing control evaluates the current system condition and designs several restoration paths that satisfy the voltage operational constraints. There are several algorithms to design service restoration strategies in the existing literature with details described in a review paper [16].

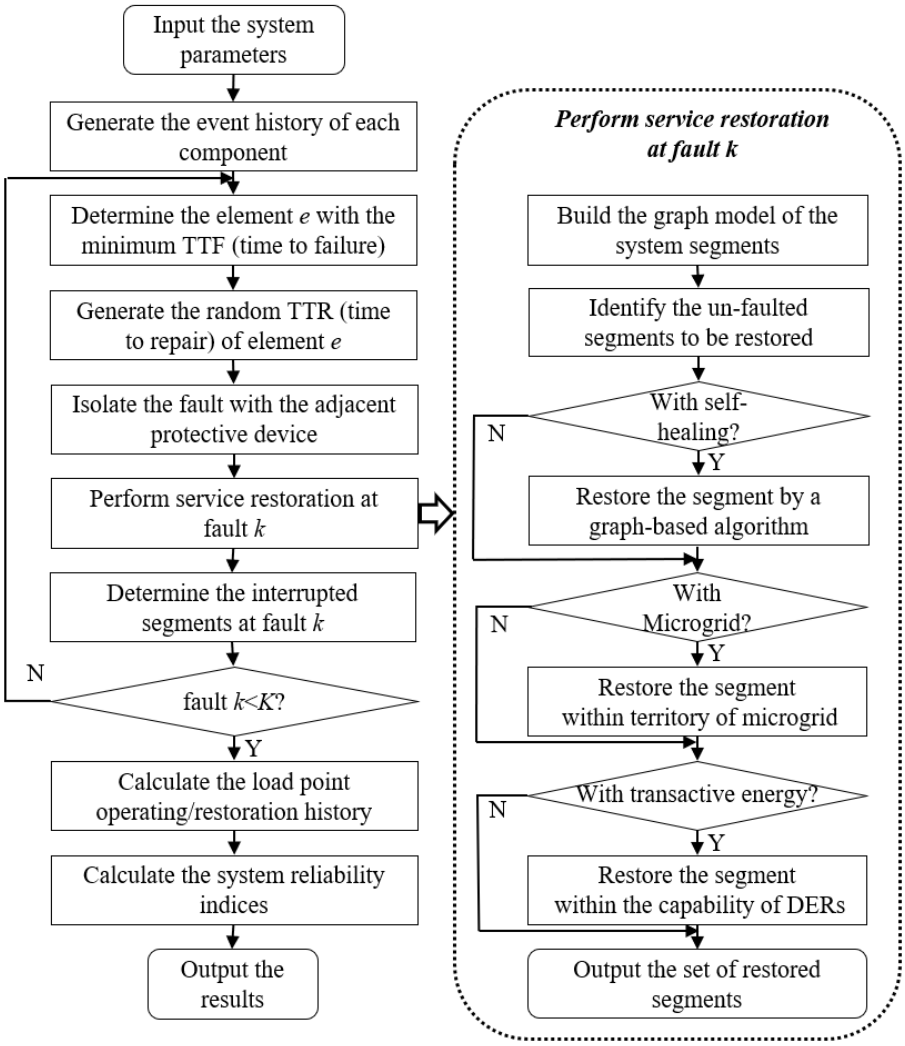

Figure 7.3: Procedure of the distribution system reliability evaluation.

The microgrid controller also checks its available power and energy and evaluates if it can support the territory for a required time period. The microgrid will report it to the distribution system operator (DSO) and wait for islanding signals to switch to the island mode if it can support its territory during the fault. It should be noted that the DSO is the operating entity and not necessarily the human operator, i.e., the DO.

Furthermore, if the non-utility DERs are available, the transactive energy control is engaged. A double auction market is established with the demand curve submitted by the DSO and the supply curves by the DERs. With market clearing, the additional switching option is determined and sent back to the DSO to restore additional load segments. With these three advanced techniques, both the restored and interrupted load segments are determined for the reliability calculation.

The most common set of indices to evaluate the system reliability by electric utilities are the System Average Interruption Frequency Index (SAIFI) and System Average Interruption Duration Index (SAIDI) [17]. SAIFI shows the frequency that the average customer experiences a sustained interruption over a predefined time period, where N_i is the number of interrupted customers for each sustained interruption event during the reporting period, and N_T is the total number of customers served for the area. The SAIDI shows the total duration of interruption for the customers during a predefined period, where r_i is the restoration time for each interruption event. It is usually calculated in minutes or hours of customer interruption.

$$SAIFI = \sum_i N_i / N_T \tag{7-1}$$

$$SAIDI = \sum_i r_i N_i / N_T \tag{7-2}$$

7.1.3 Method for Resilience Evaluation

Natural disasters, such as thunderstorms, hurricanes, and manmade attacks, are an increasing threat to electric power systems. They have the potential to cause wide-scale power outages, damage the infrastructure, and result in significant economic losses. The ability of a system to withstand such high-risk, low-probability events is system resilience. This work uses a method to evaluate the impact of the three techniques, i.e., self-healing control, microgrid, and transactive energy systems, individually and collectively on the distribution system resilience.

The procedures of resilience evaluation [18] are shown in Figure 7.4. First, the sequential Monte-Carlo simulation (MCS) is used to generate a series of events over a long period to show the stochastic nature of the resilience evaluation process. The random parameters include the number of failures, time-to-repair (TTR) and time-to-failure (TTF), etc. Second, for each event the selected fault isolation and service restoration strategies which consider self-healing control, microgrid and transactive energy are tested. Customer interruptions data are collected. Third, after all the events are analyzed, the operating history of all the loads are calculated. Resilience indices of both the system and the critical load are calculated as output.

Expected probability of interruption (EPI), expected outage duration (EOD), and expected energy not served (EENS) [19] are the three selected resilience indices adopted in this work for resilience evaluation. EPI quantifies the vulnerability of load point to the extreme events. EOD the average outage duration due to interruption a load point experiences. EENS reflects the average curtailed energy of the load point whenever the load point experiences an interruption because of an extreme event.

$$EPI_l = \frac{\sum_{s=1}^{Ns} OF_l(s)}{Ns} \tag{7-3}$$

$$EOD_l = \frac{\sum_{s=1}^{Ns} OD_l(s)}{N_s^o} \tag{7-4}$$

$$EENS_l = \frac{\sum_{s=1}^{Ns} ENS_l(s)}{N_s^o} \tag{7-5}$$

where N_s denotes the total number of fault events. N_s^o represents the number of simulated events in which a load point experiences an interruption. The system resilience profile is weighted on the peak MVA demand of the load points.

$$EPI_{sys} = \frac{\sum_{l \in LP} EPI_l(l) \times CF_l \times MVA_l}{\sum_{l \in LP} CF_l \times MVA_l} \tag{7-6}$$

$$EOD_{sys} = \frac{\sum_{l \in LP} EOD_l(l) \times CF_l \times MVA_l}{\sum_{l \in LP} CF_l \times MVA_l} \tag{7-7}$$

$$EENS_{sys} = \frac{\sum_{l \in LP} EENS_l(l) \times CF_l}{\sum_{l \in LP} CF_l} \tag{7-8}$$

where CF is the criticality factor that differentiates critical loads and non-critical loads.

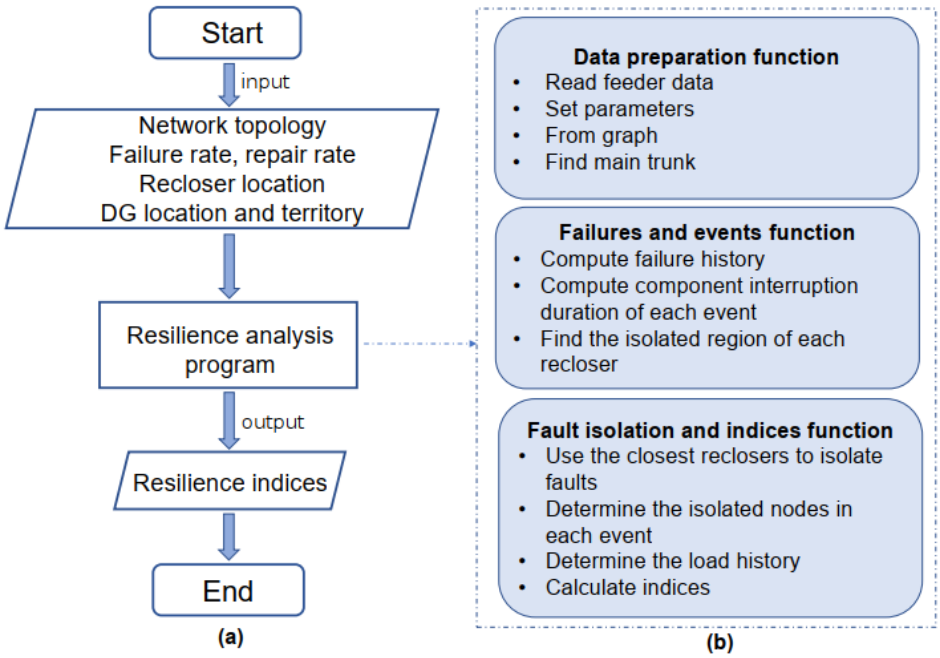

Figure 7.4: Procedure of resilience evaluation.

7.2 Results on Reliability Evaluation

The following sections discuss the service restoration strategy and the results of the reliability evaluation that was conducted.

7.2.1 Service Restoration Strategy

For all the possible fault locations, Table 7.1 summarizes the restoration results with different scenarios' settings. For Scenario 3 with transactive energy, different penetration levels of DERs that can participate in the transactive energy control are examined. It was shown that with higher penetration of DERs, more reactive power can be provided, supporting the voltage profile, and enabling the restoration of additional load segments. By gradually increasing the DER penetration level, which is the percentage of total DER capacity in the total load of the four feeders, the following results were obtained: 1) when the DER penetration level reaches 10%, S4 can be restored by transactive energy, even without the microgrid; 2) when the DER penetration level reaches 20%, S8 can be further restored; and 3) when the DER penetration level reaches 60%, S10 can also be restored.

Table 7.1: Summary of Service Restoration in All Scenarios

Scenario	Restoration	
	Not restored	Details
Base Case	S4, S8, S10	--
Scenario 1	S4, S8, S10	--
Scenario 2	S8, S10	S4 by MG
Scenario 3: 10% DER	S8, S10	S4 by TE
Scenario 3: 20% DER	S10	S8 by TE
Scenario 3: 60% DER	--	S10 by TE

The service restoration strategy for Scenario 3 with reactive power support from transactive energy is discussed in detail in the following sections. Additional details can be found in [20]-[22].

Assuming a fault happens on S11, it is isolated by opening CB4 and RCL12. The faulted segment S11 will be in an outage state until the faulted line is repaired. Also, S10 will lose power and need to be restored by adjacent feeders. Since the loading of S10 is relatively high, it cannot be restored by any of the other three feeders if only using utility-owned assets since the voltage constraints will be violated after picking up S10. Therefore, non-utility DERs need to be engaged to enable the restoration of S10. For illustration, Feeder 3 is selected to pick up S10.

Figure 7.5 through 7.9 shows the detailed operation of the transactive energy. From the load restoration curve in Figure 7.5**Error! Reference source not found.**, the demand curve in Figure 7.6 is calculated by the marginal benefit that the DSO can receive from reactive power support. Then, from the supply curve of each DER in Figure 7.7 the aggregated supply curve in Figure 7.8 is calculated. Both the demand curve and the supply curve are inputs to the double-auction market. Figure 7.9 shows the market clearing point for this case is (2,791 kvar, 0.048 $/kvar), computed by the intersection of the demand curve and aggregated supply curve. It means the DSO and DERs are willing to trade reactive power for 2,791 kvar at the price of 0.048 $/kvar. The cleared reactive power is mapped on the load restoration curve to calculate the actual amount of the load that can be restored for the given cleared reactive power value. From Figure 7.5 this reactive power support can help restore an additional 6,670 kW of load, which is larger than the load amount of S10. Therefore, S10 could be fully restored after engaging the non-utility DERs through transactive energy. The additional restored load segment S10 is 25.96% of the total load in the whole system, and the total load in Feeder 3 under this new configuration is increased by 95.41%.

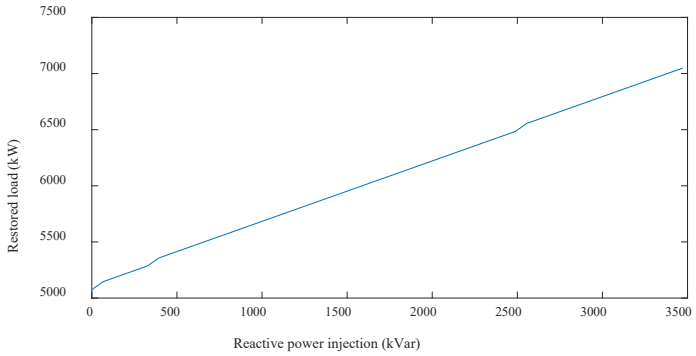

Figure 7.5: Voltage profile of Feeder 3 when restoring S10, load restoration curve.

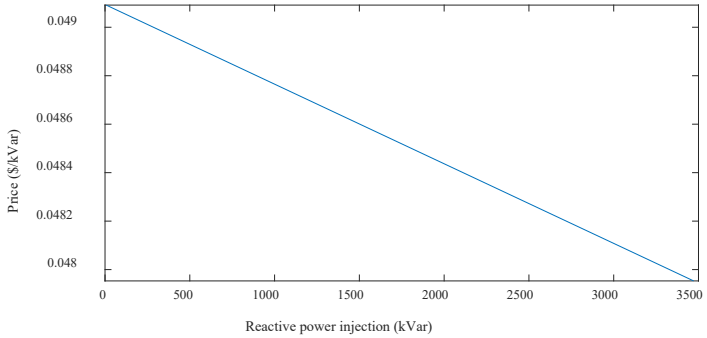

Figure 7.6: Voltage profile of Feeder 3 when restoring S10, demand curve.

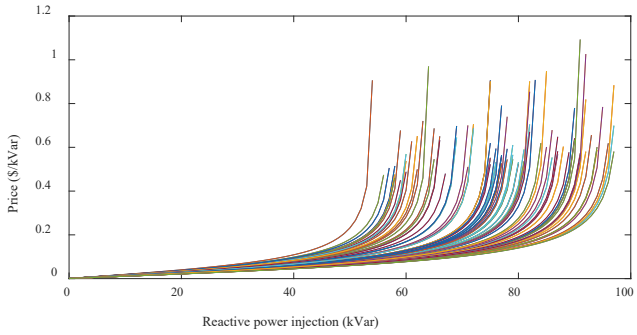

Figure 7.7: Voltage profile of Feeder 3 when restoring S10, supply curve of each DER.

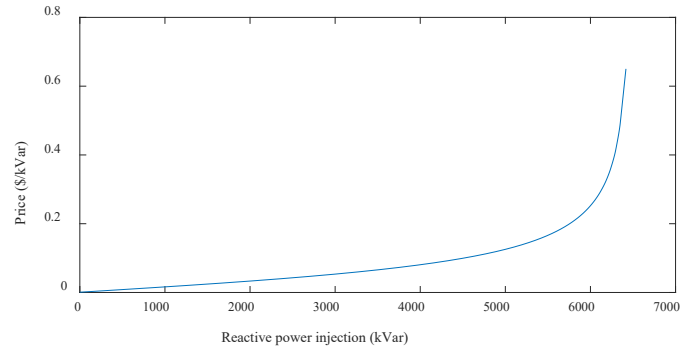

Figure 7.8: Voltage profile of Feeder 3 when restoring S10, supply curve of each DER, aggregated supply curve.

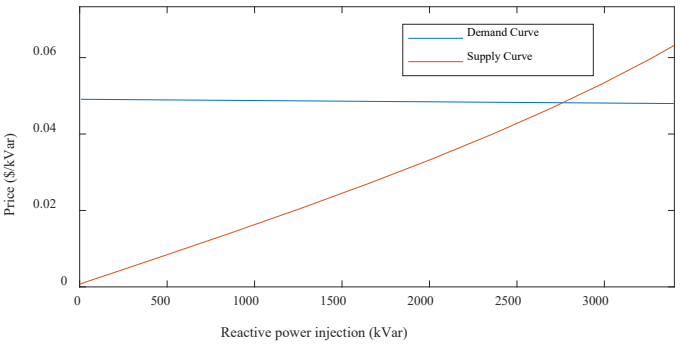

Figure 7.9: Voltage profile of Feeder 3 when restoring S10, supply curve of each DER, double auction market clearing.

Figure 7.10 shows the voltage profile for the new configuration of Feeder 3 before and after engaging the non-utility owned DERs through transactive energy. Before using transactive energy, Feeder 3 has a low-voltage issue after picking up the large load in segment S10, and the minimum voltage magnitude is around 0.92 p.u. But after using the transactive energy, the voltage is within the limit (0.95 p.u.) because the non-utility DERs are used to provide reactive power support and improve the voltage profile.

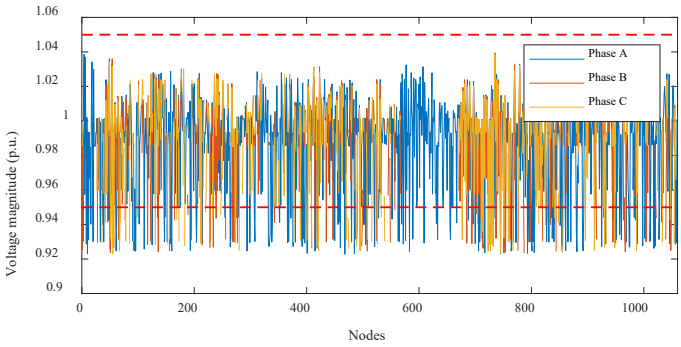

(a) Without transactive energy

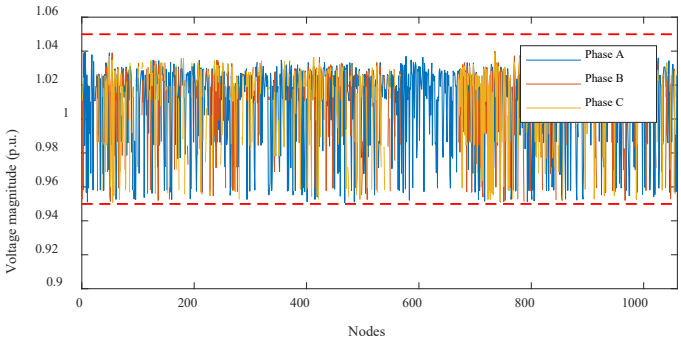

(b) With transactive energy

Figure 7.10: Voltage profile of Feeder 3 when restoring S10.

7.2.2 Example of Reliability Evaluation Procedure

After the service restoration strategies are designed and evaluated for each possible fault location in the three scenarios, the reliability is evaluated using the time-sequential Monte-Carlo simulation method. An example of the reliability evaluation using Scenario 1 with a self-healing system is illustrated below.

First, to represent the behavior of the practical distribution system operation, a sequence of events in a 10-year time period (or 10 yrs. * 365 days/yr. * 24 hrs./day = 87,600 hours) is generated by time sequential Monte Carlo simulation. From the historical reliability indices provided by Duke Energy, the failure rate and repair time of overhead lines and underground cables are calibrated. Using the calibrated data, the history of time to failure (TTF) and time to repair (TTR) in the 10 year-period for each component in the system is obtained, including all the overhead lines and underground cables, etc. As an example, Table 7.2 shows the failure history of a randomly selected overhead line.

Table 7.2: Failure History of a Randomly Selected Overhead Line

Event No.	Start of TTR (hour)	End of TTR (hour)	Event No.
1	15,239	15,244	1
2	40,415	40,419	2
⋮	⋮	⋮	⋮

Then, the obtained failure records of all components in the system are combined together, and all these events are ordered chronologically. As a result, a sequence of events is obtained as shown in Table 7.3. The failed component in each event is converted to its located segment, and the fault duration of each event is calculated. In total, there are 1,510 events that occur in the 10-year simulation period.

Table 7.3: Simulated Sequence of Events in a 10-Year Time Period

Event No.	Fault segment	Fault duration (hours)
1	S1	4
2	S5	3
⋮	⋮	⋮

After that, the fault detection, isolation, and service restoration processes are conducted for each of the 1510 events to determine the affected segments during each event and the interruption duration. Table 7.4 and Table 7.5 respectively show the interruption duration of each segment before and after deploying the self-healing system where the number zero means the segment is not interrupted.

Table 7.4: Interruption Duration before Deploying Self-Healing System

Event No.	S1	S2	S3	S4	S5	S6	…
1	4	1.5	0	0	0	0	…
2	0	0	0	0	3	0	…
⋮	⋮	⋮	⋮	⋮	⋮	⋮	⋮

Table 7.5: Interruption Duration after Deploying Self-Healing System

Event No.	S1	S2	S3	S4	S5	S6	…
1	4	0	0	0	0	0	…
2	0	0	0	0	3	0	…
⋮	⋮	⋮	⋮	⋮	⋮	⋮	⋮

In event 1, the fault occurs at an overhead line in S1 and needs 4 hours to repair the faulted line as shown in Table 7.4. As a result, S1 and S2 are interrupted. For S1, its interruption time is 4 hours since it has to be restored after the faulted line is repaired. But for S2, it can be restored to other feeders using the designed service restoration strategy, and its interruption time depends on how quickly the service restoration strategy is executed. Before deploying the self-healing system, the service restoration strategy needs to be executed by operating the manual switches, which is assumed to take 1.5 hours in the simulation. So, the interruption time of S2 is 1.5 hours before deploying the self-healing system. But after deploying the self-healing system, operating the automated reclosers is much faster so the interruption time of S2 is treated as negligible in the reliability analysis. In event 2, the fault occurs at an overhead line in S5 and needs 3 hours to repair the faulted line as shown in Table 7.4. In this case, only S5 is interrupted, and its interruption time is 3 hours whether deploying the self-healing system or not. This is because S5 contains a faulted line and it needs to be restored after the faulted line is repaired. Similarly, the customer interruption duration for all the 1,510 simulated events can be determined.

Finally, the interrupted customers and interruption duration in all the simulated 1,510 events are integrated to calculate the system reliability indices.

7.2.3 Reliability Improvement in Three Scenarios

Table 7.6 shows the reliability indices of the whole system, as well as the reliability improvement compared with the base scenario. It shows that Scenario 1 with self-healing control can reduce the SAIFI by 11.85%, since the deployment of reclosers and self-healing control can enable the capability of autonomous service restoration after an outage. Furthermore, Scenario 3 with transactive energy can greatly improve the system reliability, for example, the SAIFI and SAIDI can be reduced by 38.72% and 31.59% from the base case respectively if the DER penetration levels reaches 60%. These results demonstrate the great potential of transactive energy combined with self-healing control in improving the whole system level reliability. For Scenario 2 with microgrid, the reliability indices of the whole system do not have significant improvement compared with Scenario 1 with self-healing control only. This is because the size of the microgrid is relatively small and is mainly used to serve the critical load. Therefore, the microgrid will greatly improve the reliability of the critical load as intended but would only have a small impact on the whole system.

Table 7.6: Reliability of the Whole System

Scenario	SAIFI (interruptions/customer)	SAIDI (minutes)	SAIFI Reduction	SAIDI Reduction
Base Case	12.99	63.06	--	--
#1	11.45	61.24	11.85%	2.89%
#2	11.42	61.10	12.09%	3.11%
#3: 10% DER	11.42	61.10	12.09%	3.11%
#3: 20% DER	10.05	54.97	22.64%	12.83%
#3: 60% DER	7.96	43.14	38.72%	31.59%

Table 7.7 shows the reliability indices of the critical load as well as the reliability improvement compared with the base scenario. It shows that Scenario 1 with self-healing control does not improve the critical load reliability due to the lack of available service restoration path. For all other scenarios, there exists a path to restore the critical load segment S4, either by the microgrid in Scenario 2 or by the transactive energy in Scenario 3, so the reliability indices of the critical load segment are greatly improved by the microgrid or the transactive energy.

Table 7.7: Reliability of the Critical Load

Scenario	SAIFI (interruptions/customer)	SAIDI (minutes)	SAIFI Reduction	SAIDI Reduction
Base Case	6.59	30.50	--	--
#1	6.59	30.50	--	--
#2	4.02	16.38	39.00%	46.30%
#3: 10% DER	4.02	16.38	39.00%	46.30%
#3: 20% DER	4.02	16.38	39.00%	46.30%
#3: 60% DER	4.02	16.38	39.00%	46.30%

7.3 Results of Resilience Evaluation

With the selected restoration strategy, the system resilience can be evaluated under four scenarios. Different scenarios are developed to show the engagement of different technologies, including a centralized self-healing system, an inverter-based microgrid, and a transactive energy scheme. From the results listed in

Table 7.8 and Table 7.9, self-healing control, microgrid and transactive energy system contribute to improving the resilience of both the system and the critical load, shown by the decrease in the outage indices EPI, EOD and EENS.

Comparing results in Scenario 0 and Scenario 1, the system resilience is increased as indicated by the decrease of 10% for EPI and 3% for EOD and EENS. This means the replacement of manual switches with reclosers improves the system resilience. On the other hand, the critical load resilience remains unchanged. This is because, with self-healing control, the critical load cannot be restored. Whether using manual switches or reclosers does not affect the resilience of the critical load S4. The simulation results correspond to the theoretical analysis. Comparing results in Scenario 2 (microgrid + self-healing control) with the base scenario (Scenario 0) and Scenario 1 (self-healing system), the resilience indices further decrease, and the resilience improvement is much more desirable at both the system level and the critical load level. At the system level, the resilience improvement is around 26% (EPI) to 15% (EOD, EENS). At the critical load level, the resilience improvement can reach as high as 42.15% with the microgrid and self-healing control. This shows self-healing control and microgrid are useful techniques for enhancing the resilience of a distribution system. Having a microgrid back up the critical load is particularly effective in improving the resilience of the critical load.

Comparing results in Scenario 3 with the other scenarios, self-healing, microgrid and transactive energy collectively can help improve the resilience of the distribution system to the most extent. At the system level, resilience is improved by around 31%-40%. At the critical load level, resilience is improved by around 42.15%. This figure remains unchanged compared to Scenario 2, since with microgrid alone it has been restored. The additional incorporation of a transactive energy system does not affect the critical load's operation.

Table 7.8: Summary of System Resilience Improvement in All Scenarios

Scenario	**Resilience Indices of the System**					
	EPI	**EOD**	**EENS**	**EPI Reduction**	**EOD Reduction**	**EENS Reduction**
Base Case	14.55	73.79	731.76	-	-	-
#1	13.07	71.41	708.14	10.17%	3.22%	3.22%
#2	10.83	62.60	620.76	25.57%	15.16%	15.17%
#3	8.79	51.12	506.92	39.59%	30.72%	30.64%

Table 7.9: Summary of Critical Load Resilience Improvement in All Scenarios

Scenario	**Resilience Indices of the System**					
	EPI	**EOD**	**EENS**	**EPI Reduction**	**EOD Reduction**	**EENS Reduction**
Base Case	7.83	44.90	437.72	-	-	-
#1	7.83	44.90	437.72	0%	0%	0%
#2	4.53	30.82	300.34	42.15%	31.36%	31.39%
#3	4.53	30.82	300.34	42.15%	31.36%	31.39%

8.0 Inverter and Semiconductor Aging

The use-cases in Section 6.0 included the engagement of non-utility DERs using a transactive energy system. However, the engagement of inverters for functions other than their primary use has the potential to impact the life-time of the equipment, due to increased thermal loading. In this section, the impact of reactive power on the PV inverter aging is investigated. This fills the gaps in the literature by systematically analyzing the thermal stress of PV inverter semiconductors, when the inverters provide reactive power during support of ancillary services that require the production/absorption of reactive power. In addition, the simulation results of semiconductor aging are presented. A fast semiconductor fatigue simulation approach that can be extended to QSTS simulations is reported.

8.1 Reactive Power Impact on PV Inverter Aging

The TES engages non-utility PVs to generate/absorb reactive power in support of ancillary services to increase microgrid resiliency during extreme events. Many publications in the literature have reported that the inverter's power electronic devices and passives (capacitors) have shorter lifetime compared to its associated PV panels [23], [24]. For example, in a PV system, the lifetime of the PV panels is normally warrantied at 20–30 years, whereas the PV inverter lifetime is usually less than 15 years [23]. Due to the short lifetime of inverters, more than one half of the maintenance cost of a PV system is consumed by inverters [25]. In addition, the utility power industry usually expects a long lifetime of the inverters so that the inverters could retire from the power grid at the same time as the whole PV system [26].

An industry-wide survey presented in [26] indicates that semiconductors and capacitors are the most vulnerable components that lead to inverter failure. The power losses of semiconductors and capacitors are dissipated as heat, and this heat dissipation increases the mean junction temperature and the temperature variation of semiconductors and capacitors. Literature have shown that the thermal stress (both mean junction temperature and junction temperature variation) may drastically reduce the lifetime of electrolytic capacitors [27] and semiconductors [28]-[30].

In addition to active power generation, PV inverters are requested to provide reactive power support in distributed systems and microgrids that adopt TES. The TES is a concept to engage more distributed energy resources (DERs), especially non-utility owned DERs, to participate in the operation of the power grid [31], [32], [33]. The work in [32] and [33] proposed a transactive approach to engage DERs to provide ancillary services.

TES can incentivize customers to provide ancillary services from the customer-owned DERs to improve the reliability and quality of the grid's power. The TES controller could publish low reactive power demand level when the utility reactive power generation is sufficient, which would discourage customers from generating reactive power [31], [32], [34]-[36]. The customer DERs could also publish low reactive power generation capability if the reactive power generation would decrease the profit of the customers [37]-[44] because it might require decreasing their active power output.

Some publications in the literature have indicated that the engagement of DERs to provide ancillary services may have a negative effect on the lifetime of DER inverters due to increasing thermal stress [45], [46]. The reactive power may change the current distribution among inverter semiconductors. In addition, different current distribution may change the power loss distribution among the individual semiconductors. The impact of reactive power on other major components, such as dc capacitors and filtering inductors, is not as significant as that on semiconductors. Therefore, this report selects inverter semiconductors as the objective of the ancillary services aging effect analysis.

Work in the power electronic literature has proposed solutions to extend the lifetime of inverters. The method presented in [47] proposed a maximum-power-point-tracking (MPPT) control for PV systems which limits the maximum junction temperature of the power semiconductors. Yang *et al*. [48], [49] also proposed a MPPT methodology to limit the maximum operating point which will limit the temperature indirectly. Also, PV inverter manufacturers design their products by derating the output power as ambient temperature increases [50]-[52]. However, none of the existing literature systematically study the mechanism of reactive power impact on PV inverter semiconductor aging.

This section aims to fill these gaps in the literature by systematically analyzing the thermal stress of PV inverter semiconductors when the inverters provide reactive power during support of ancillary services that require the production/absorption of reactive power. A brief review on the lifetime estimation of PV inverter semiconductors is presented followed by the electrothermal model of the semiconductors. The analysis of the thermal model reveals that the reactive power generation will increase both the mean junction temperature and the junction temperature variation of the inverter diodes. This increased junction temperature will lead to a shorter inverter lifetime. The power losses of PV inverter semiconductors derived in this section provide a support analysis for the calculation of junction temperature. The theoretical analysis is supported by simulation results. The main body of this subsection was published in [53] and partly presented at the 2020 IEEE PES General Meeting [54].

8.1.1 Electrothermal Model of PV Inverter

The following sections detail the basis for thermal modeling of an inverter. This includes device level characteristics and how they can be represented in larger system models.

8.1.1.1 Background of Semiconductor Lifetime Expectation

The lifetime model of semiconductors can be formulated as follows [55],

$$N_f = A \times \left(\Delta T_j\right)^{\alpha} \times (ar)^{\beta_1 \Delta T_j + \beta_0} \times \left[\frac{C+(t_{on})^{\gamma}}{C+1}\right] \times exp\left(\frac{E_a}{k_b \times \bar{T}_j}\right) \times f_d \tag{8-1}$$

where N_f is the number of cycles to failure. This parameter indicates that a new semiconductor device is going to fail after N_f cycles of use for a given operating condition. $\bar{T}_j$ is the mean junction temperature of a semiconductor. ΔT_j is the junction temperature variation in the time period of t_{on}. t_{on} is the thermal cycle period, which is typically the same as the electrical line period. The other parameters are given in Table 8.1 [55].

Table 8.1: Parameters of the Lifetime Model of an IGBT Module

Parameter	Value	Experimental condition
A	3.4368×10^{14}	
α	– 4.923	5 K ≤ ΔT_{junc} ≤ 80 K
β_1	9.012×10^{-3}	
β_0	1.942	0.19 ≤ ar ≤ 0.42
C	1.434	
γ	– 1.208	0.07 s ≤ t_{on} ≤ 63 s
f_d	0.6204	
E_a	0.06606 eV	32.5 °C≤ T_{junc} ≤ 122 °C
k_B	8.6173324×10^{-5} eV/K	

From (8-1), the semiconductor lifetime is related to the mean junction temperature $\bar{T}_j$ and the junction temperature variation ΔT_j. When $\bar{T}_j$ and/or ΔT_j increase, the number of cycles to failure N_f will decrease.

8.1.1.2 Foster Thermal Model

The insulated-gate bipolar transistor (IGBT) type and metal-oxide-semiconductor field-effect transistor (MOSFET) type PV inverter have similar electrothermal models. This section focuses on IGBT-type PV inverters since IGBT-based PV inverters are more common especially for high power ratings (>5 kW) [56]. The electrothermal model of a typical discrete IGBT with anti-parallel diode with thermal management is shown in Figure 8.1 [57]. IGBT and diode chips are the heat source in the inverter system. The heat generated in the IGBT's junction will flow to the case of the IGBT module through several layers of materials, such as solder, metal, ceramic, etc., and finally results in a case temperature, T_c. The case of an IGBT normally will be attached to a heat sink by thermal paste. The resulting heat sink temperature is T_h. The heat sink dissipates the heat to the ambient by convection. Other types of thermal management systems include fans, cold plate, and water cooling.

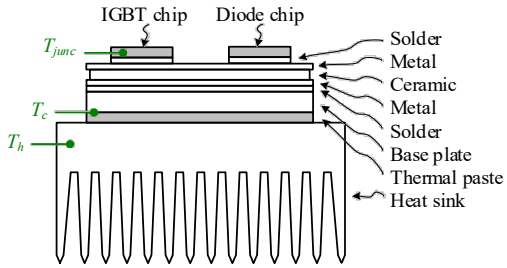

Figure 8.1: Typical IGBT module with thermal management.

The Foster thermal model presented in [46] is used in this research work to estimate the thermal stress of a PV inverter. The Foster thermal model describes the temperature transient of an object by a branch-based RC network. The detailed thermal model of a PV inverter composed of IGBTs with anti-parallel diode pack is shown in Figure 8.2. The switching loss (P_{sw}) and conduction loss (P_{con}) are the heat source for each IGBT and diode. In a two-stage PV inverter, it normally contains five (single-phase) to seven (three-phase) IGBTs depending on the topology.

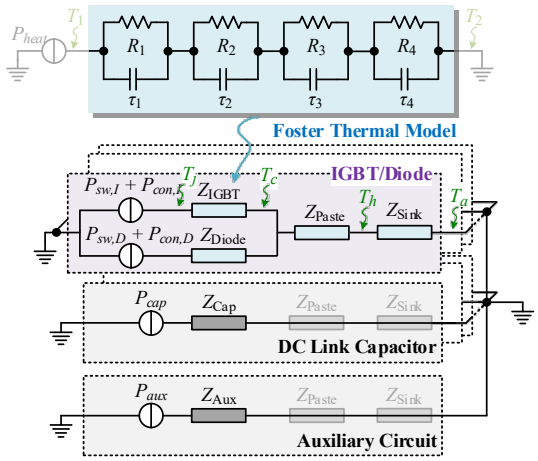

Figure 8.2: Detailed thermal model of PV inverter using discrete IGBT-diode pack.

Each IGBT module is attached to a heat sink by thermal paste. The capacitor power loss (due to current flowing through its own parasitic resistance) is the heat source for each capacitor. Each PV inverter normally contains several capacitors on the dc link, and their thermal resistances are thermally in parallel. The capacitors and other auxiliary circuits such as printed circuit boards (PCBs), filtering inductors, and electromagnetic interference (EMI) filters may not have active thermal management or dedicated heat sinks depending on inverter design. The common IGBT-diode packages and their thermal models are summarized in Table 8.2.

Table 8.2: Common IGBT-Diode Packages and Thermal Model

Type	IGBT	Diode	Heatsink	Thermal Model
1	Discrete	Discrete	Independent heatsink for each IGBT and diode	Figure 8.3(a)
2	Discrete	Discrete	Shared by IGBT and diode	Figure 8.3(b)
3	Bridge Module	Built-in IGBT module	Shared by multiple bridge modules	Figure 8.3(c)
4	Discrete	Built-in IGBT module	Independent heatsink for each IGBT-diode pair	Figure 8.3(d)

Several possible thermal models shown in Figure 8.3 can be used to calculate junction temperature. For example, the junction temperature of the IGBT and diode of Figure 8.3(a) can be formulated as (8-2) and (8-3),

$$T_{j,I} = \left(P_{sw,I} + P_{con,I}\right)\left(Z_{IGBT} + Z_{Paste} + Z_{Sink}\right) + T_{amb} \tag{8-2}$$

$$T_{j,D} = \left(P_{sw,D} + P_{con,D}\right)\left(Z_{Diode} + Z_{Paste} + Z_{Sink}\right) + T_{amb} \tag{8-3}$$

where subscript D indicates the variable associated with the diode, and subscript I indicates the variable associated with the IGBT. Z_{Paste} is the thermal paste thermal impedance. Z_{Sink} is the heatsink thermal impedance. T_{amb} is the ambient temperature. Other types of thermal models shown in Figure 8.3 can also be formulated similar to (8-2) and (8-3). The derivation is omitted in this subsection.

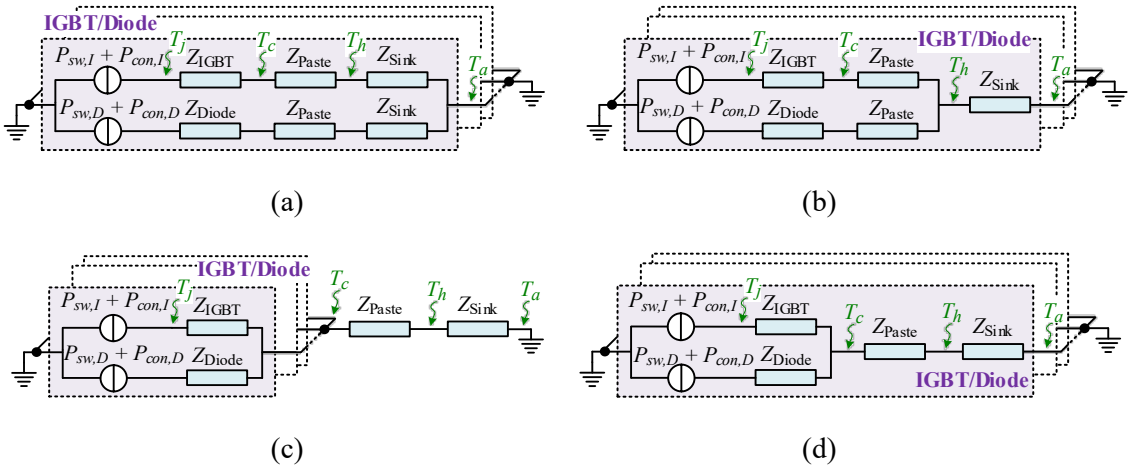

Figure 8.3: Semiconductor thermal model. (a) Independent IGBT and diode package. Each IGBT/diode is attached to an independent heatsink. (b) Independent IGBT and diode package. The IGBT and diode are sharing a heatsink. (c) Half/full bridge module that contains more than two IGBT-diode pairs in one

package. The bridge module is attached to a heatsink. (d) IGBT packaged with anti-parallel diode in single package. Each IGBT-diode module is attached to an independent heatsink.

Each thermal impedance Z can be represented by

$$Z = \sum_n^l R_n \left(1 - e^{-\frac{t}{\tau_n}}\right) \tag{8-4}$$

where l is the number of terms in the Foster thermal model. R is the thermal resistance, and τ is the thermal time constant.

The Foster thermal model generally neglects the nonlinearities by modeling the thermal properties with a RC network. The superposition theorem can be applied to the semiconductor Foster model to calculate the semiconductor junction temperature. The mean junction temperature $\bar{T}_j$ is determined by the average power loss ($\bar{P}_{con}$ and $\bar{P}_{sw}$) of the semiconductors. And the thermal cycle ΔT_{junc} is determined by the power loss variation (ΔP_{con} and ΔP_{sw}) of the semiconductors which is due to the switching of the IGBTs and the variation of the ac current provided by the inverter.

8.1.2 Semiconductor Power Loss Formulation

The power losses of semiconductors consist of two parts: 1) switching loss and 2) conduction loss. A typical two-stage single-phase PV inverter topology is shown in Figure 8.4. The following power loss evaluation is based on the PV inverter topology shown in Figure 8.4. The semiconductors on the dc-dc side will not be analyzed in this section because dc-dc stage operation is only affected by active power generation. The reactive power generation would slightly increase the current stress of dc-dc stage semiconductors due to the increasing power loss of the reactive power generation. Therefore, the semiconductors of the dc-dc stage will not be discussed in this section.

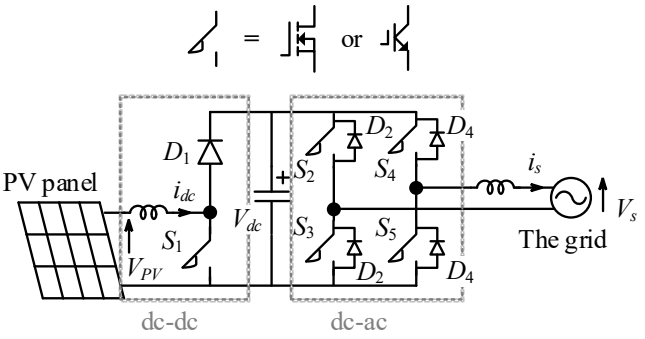

Figure 8.4: Typical PV inverter topology.

8.1.2.1 Switching Loss

For a given IGBT, the switching loss is determined by the turn-on and turn-off energy, and the turn-on loss could be formulated as follows [58],

$$E_{on,I} = V_{dc} i_s \cdot \frac{1}{2} t_{on} \tag{8-5}$$

where t_{on} is the total time of current rising and voltage falling when power switches turn on. t_{on} is a fixed value once a specific switching device and its associated gate drive are selected. V_{dc} is the dc-link voltage; i_s is the load current. The switching loss during the IGBT's turn-on state is shown in Figure 8.5 (a) [58].

The average value of $E_{on,I}$ for each dc-ac side IGBT (S_2 - S_5) during the sinusoidal period of the inverter output current can also be calculated as [59],

$$E_{on,I} = \frac{\sqrt{2}}{2\pi} V_{dc} I_s \cdot t_{on} \tag{8-6}$$

where I_s is the rms value of the inverter output current. Similarly, each IGBT's (S_2 - S_5) turn-off loss can be calculated as [59],

$$E_{off,I} = \frac{\sqrt{2}}{2\pi} V_{dc} I_s \cdot t_{off} \tag{8-7}$$

Each IGBT's total (S_2 - S_5) switching loss is calculated as,

$$P_{sw,I} = (E_{on,I} + E_{off,I}) \cdot f_{sw} \tag{8-8}$$

where f_{sw} is the switching frequency.

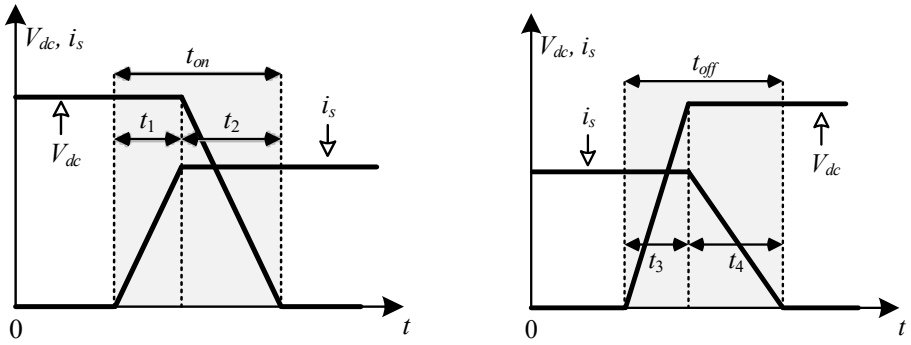

(a) (b)

Figure 8.5: Switching loss during IGBT's (a) turn-on time; and (b) turn-off time.

For a given MOSFET, the switching loss is similar to that for an IGBT and also follows (8-5)-(8-8).

Diode switching loss is generated by the reverse recovery during the turn-off transition. Normally, diode datasheets provide the value of reverse recovery energy loss $E_{rr,D}$ under the manufacturer's specified test conditions. The actual diode switching loss needs to be rescaled by the actual current and blocking voltage. The diode (D_2 - D_5) switching loss during the sinusoidal period of the inverter output current is calculated as [59],

$$P_{sw,D} = (\frac{\sqrt{2}}{\pi} \frac{I_s V_{dc}}{I_{ref} V_{ref}} E_{rr,D}) \cdot f_{sw} \tag{8-9}$$

where I_{ref} and V_{ref} are the testing current and voltage condition provided from the datasheet.

8.1.2.2 Conduction Loss

The conduction loss of an IGBT can be modeled by two components connected in series, a resistor and a dc voltage source as shown in Figure 8.6 (a). The dc voltage source represents the built-in voltage of the device p-n junction. The power losses in both the resistor and dc voltage source contribute to the IGBT conduction losses [59].

$$P_{con,IGBT} = I_{rms,IGBT}^2 R_{IGBT} + I_{avg,IGBT} V_{0,IGBT} \tag{8-10}$$

where $I_{rms,IGBT}$ and $I_{avg,IGBT}$ are the rms value and average value of the current flowing through the IGBT collector to emitter. The details for determining $I_{rms,IGBT}$ and $I_{avg,IGBT}$ are summarized in [53]. $V_{0,IGBT}$ and R_{IGBT} are typically given by IGBT datasheets.

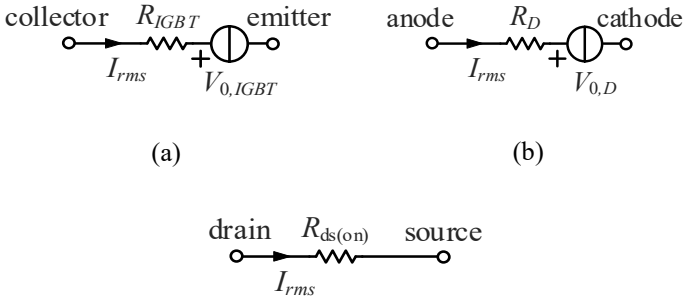

Figure 8.6: Semiconductor conduction loss model. (a) IGBT; (b) diode; (c) MOSFET.

The conduction loss of a diode is similar to an IGBT and can be modeled as shown in Figure 8.6 (b). The power losses in both the resistor and dc voltage source contribute to the diode conduction losses.

$$P_{con,D} = I_{rms,D}^2 R_D + I_{avg,D} V_{0,D} \tag{8-11}$$

where $I_{rms,D}$ and $I_{avg,D}$ are the rms value and the average value of the current flowing through the diode anode to cathode. The details of $I_{rms,D}$ and $I_{avg,D}$ are summarized in [53]. $V_{0,D}$ and R_D are typically given by diode datasheets.

For the MOSFET, the conduction loss is formulated as follows [59],

$$P_{con,M} = I_{rms,M}^2 R_{ds(on)} \tag{8-12}$$

where $R_{ds(on)}$ is the drain-source on-resistance of a MOSFET as shown in Figure 8.6 (c). $I_{rms,MOSFET}$ is the MOSFET current rms value. The details of the $I_{rms,MOSFET}$ for a MOSFET-based dc-ac inverter is included in [53].

The complete semiconductor switching loss and conduction loss for a PV inverter's possible devices are summarized in Table 8.3.

Table 8.3: Semiconductor Power Loss

	Switching Loss	Conduction Loss
IGBT	$P_{sw,I} = (E_{on,I} + E_{off,I}) \cdot f_{sw}$	$P_{con,IGBT} = I_{rms,IGBT}^2 R_{IGBT} + I_{avg,IGBT} V_{0,IGBT}$
MOSFET	$P_{sw,M} = (E_{on,M} + E_{off,M}) \cdot f_{sw}$	$P_{con,M} = I_{rms,M}^2 R_{ds(on)}$
Diode	$P_{sw,D} = (\frac{\sqrt{2}}{\pi} \frac{I_s V_{dc}}{I_{ref} V_{ref}} E_{rr,D}) \cdot f_{sw}$	$P_{con,D} = I_{rms,D}^2 R_D + I_{avg,D} V_{0,D}$

8.1.3 Reactive Power Impact on Power Loss

To evaluate the reactive power impact on the semiconductor power loss, the IGBT-diode type of PV inverter is selected in the following analysis. Assume that the output voltage and current follow,

$$v_s = \sqrt{2} V_s \sin(\omega t + \varphi) \tag{8-13}$$

$$i_s = \sqrt{2} I_s \sin \omega t \tag{8-14}$$

Assuming a fixed apparent output power $S = V_s I_s$ for the PV inverter, then the modulation function follows

$$m = \frac{M \sin(\omega t + \varphi) + 1}{2} \tag{8-15}$$

The modulation index M is typically 0.8~1.0 for PV inverters. The current conducted by S_2 IGBT can be formulated as

$$i_{S2} = \begin{cases} \sqrt{2} I_s \sin \omega t \cdot \frac{M \sin(\omega t + \varphi) + 1}{2} & i_s \geq 0 \\ 0 & i_s < 0 \end{cases} \tag{8-16}$$

The current conducted by D_2 diode can be formulated as

$$i_{D2} = \begin{cases} -\sqrt{2} I_s \sin \omega t \cdot \frac{M \sin(\omega t + \varphi) + 1}{2} & i_s < 0 \\ 0 & i_s \geq 0 \end{cases} \tag{8-17}$$

8.1.3.1 Average Power Loss

The power loss distribution among inverter semiconductors varies with respect to output power factor (*pf*). In general, a lower power factor will reduce the conduction loss of IGBTs and increase the conduction loss of diodes. Thus, the reactive power negatively impacts the diode thermal stress. The equivalent current that flows through the diode increases as the *pf* decreases. Figure 8.7 shows the rms current $I_{rms,D}$ and average current $I_{avg,D}$, from [53], and maximum current $I_{max,D}$ from (8-17) of the diode.

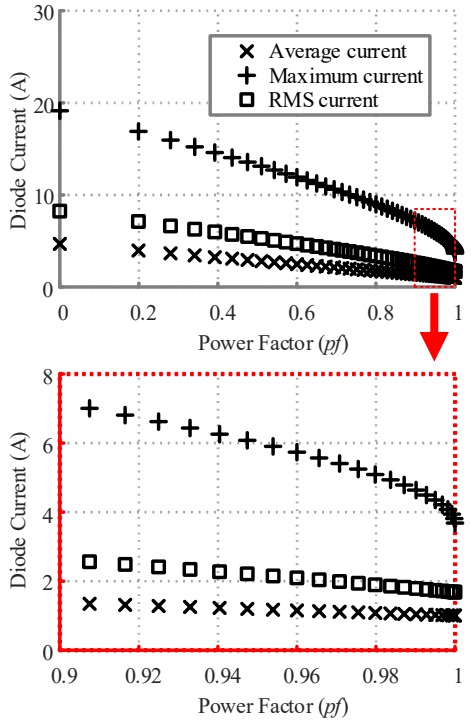

Figure 8.7: Equivalent current rms, average, and maximum value through diodes.

More current flowing through diodes will increase the conduction loss of the diode. From (8-11), the conduction loss of diode can be formulated as

$$P_{con,D} = \left(\frac{I_S^2}{4}R_D + \frac{I_S}{\sqrt{2}\pi}V_{0,D}\right) - \left(\frac{I_S^2}{4}\cdot\frac{8M}{3\pi}R_D + \frac{I_S}{\sqrt{2}\pi}\cdot\frac{\pi M}{4}V_{0,D}\right)pf \tag{8-18}$$

where *pf* is the power factor of the PV inverter output power. The diode conduction loss increases as the *pf* decreases.

As the power factor decreases, more current flows through diodes, and less current flows through the IGBTs (for a fixed apparent power). From (8-10), the conduction loss of an IGBT can be formulated as

$$P_{con,IGBT} = \left(\frac{I_S^2}{4}R_{IGBT} + \frac{I_S}{\sqrt{2}\pi}V_{0,IGBT}\right) + \left(\frac{I_S^2}{4}\cdot\frac{8M}{3\pi}R_{IGBT} + \frac{I_S}{\sqrt{2}\pi}\cdot\frac{\pi M}{4}V_{0,IGBT}\right)pf \tag{8-19}$$

The IGBT conduction loss decreases as the *pf* decreases.

8.1.3.2 Power Loss Cycling

Since the ac current and voltage cycle periodically (60 Hz in this section), the semiconductor losses are also typically cycling in this fundamental cycle. In addition to the average conduction loss, the power loss variation during a fundamental cycle also varies with power factor. The average losses determine the mean junction temperature (T_j). The power loss variation in a fundamental cycle determines the junction temperature variation (ΔT_j).

Eq. (8-17) formulates the D_2 diode current. Figure 8.8 shows the D_2 diode current for one half of one fundamental cycle (from π to 2π). The D_2 diode current has less variation at unity *pf*. Compared to the

current at unity power factor, the current variation during one of the two half cycles doubles when the *pf* decreases to 0.9. Other diodes in the inverter will also have similar current variation as D_2 diode.

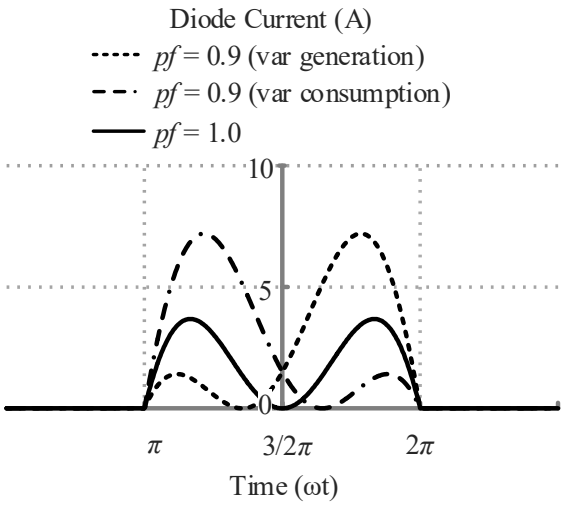

Figure 8.8: Full-bridge single phase inverter diode current variation in a fundamental cycle.

8.1.3.3 Effect of Filtering Inductor

The inverter's filtering inductor is normally deemed an integral part of a PV inverter. However, from a semiconductor point of view, the filtering inductor is part of the load. Assume that the PV inverter midpoint voltage vector is V_c. The PV inverter's midpoint voltage contains a wide spectrum of harmonics, especially the switching frequency harmonics. V_c denotes the fundamental component of the midpoint voltage. The voltage drop on the filtering inductor is V_L. The grid voltage vector is V_s. The voltages should follow

$$V_c = V_s + V_L \tag{8-20}$$

The polarities of V_c, V_s, and V_L are shown in Figure 8.9 (a). The phase angle between V_s and I_s is θ_s. The phase angle between V_c and I_s is θ_c. The *pf* of fundamental output current is defined as $\cos\theta_s$. The *pf* of bridge circuit current is defined as $\cos\theta_c$. $\cos\theta_c$ is the actual power factor that determines the current distribution among the semiconductors.

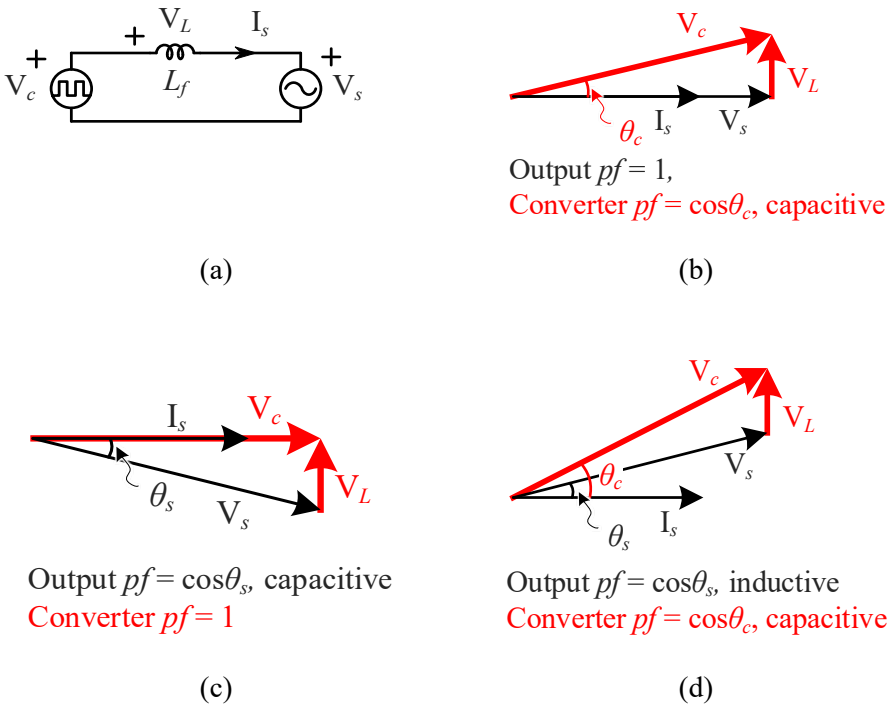

Figure 8.9: (a) Equivalent circuit of PV inverter connected to the grid. Phasor diagram of PV inverter with (b) unity power factor; (c) capacitive output; and (d) inductor output.

If the output power is at unity *pf* as shown in Figure 8.9 (b), the bridge circuit *pf* will be lagging because of the filter inductor and has a value of $\cos\theta_c$. The inverter needs to generate a reactive power to compensate the reactive power consumed by the filtering inductor. If the output power is slightly capacitive with a *pf* of $\cos\theta_s$ as shown in Figure 8.9 (c), the small reactive power consumed by the filtering inductor may result in the bridge circuit *pf* being unity.

If the output power is inductive as shown in Figure 8.9 (d), the filtering inductor will further reduce the bridge circuit *pf*. The filtering inductors of PV inverters are typically 0.01 to 0.05 p.u. The filtering inductors do not significantly affect the bridge circuit *pf* in typical cases. However, some PV inverters may have relatively large filtering inductors/transformers that are up to 0.15 p.u. In this case, the filtering inductors will significantly affect the bridge circuit *pf* and hence the amount of current through the individual semiconductors in these cases.

8.1.3.4 Total PV Inverter Power Loss

The current distribution among semiconductors can be influenced by the *pf*. If the on-resistance and the built-in voltage of the IGBT and diode have significant difference, the current distribution will change the overall conduction loss of the PV inverter. For example, the majority of the current flows through IGBTs rather than diodes at unity *pf*. If the on-resistance of the IGBT is larger than that of diode, the conduction loss of the PV inverter at unity *pf* will become larger than that at non-unity *pf*. If the on-resistance and the built-in voltage of the IGBT is similar to that of diodes in a PV inverter, the conduction loss of the PV inverter at unity *pf* will be similar to that at non-unity *pf*.

In typical PV inverter design, the selection of IGBTs and diodes often have similar conduction loss characteristics. Therefore, the total power loss of the inverter normally remains the same regardless of the *pf*. The total PV inverter power loss is typically determined by the apparent power.

Typically, the active power generation has higher priority than the reactive power generation in customer owned PV inverters. PV inverters are unlikely to sacrifice active power generation for reactive power because the compensation for active power greatly exceeds that for reactive power in today's markets. Since the active power and reactive power are in quadrature with each other, the increase of apparent power is not linearly proportional to the increase in reactive power.

Figure 8.10 shows the phasor diagram of the PV inverter power with reactive power generation. When the active power generation is 0.2 p.u., the apparent power increment is 0.247 p.u. (to 0.447 p.u.) when generating 0.4 p.u. reactive power. When the active power generation is 0.8 p.u., the apparent power increment is 0.094 p.u. (to 0.894 p.u.) to generate 0.4 p.u. reactive power. In these two cases, to generate 0.4 p.u. reactive power, the additional apparent power (ΔS) of the PV inverter is quite different. In general, the ΔS of the PV inverter at larger active power generation level is less than that at smaller active power generation level. Similarly, the increment of power loss of the PV inverter at larger active power generation level is less than that at smaller active power generation level. Figure 8.11 illustrates the apparent power with respect to reactive power.

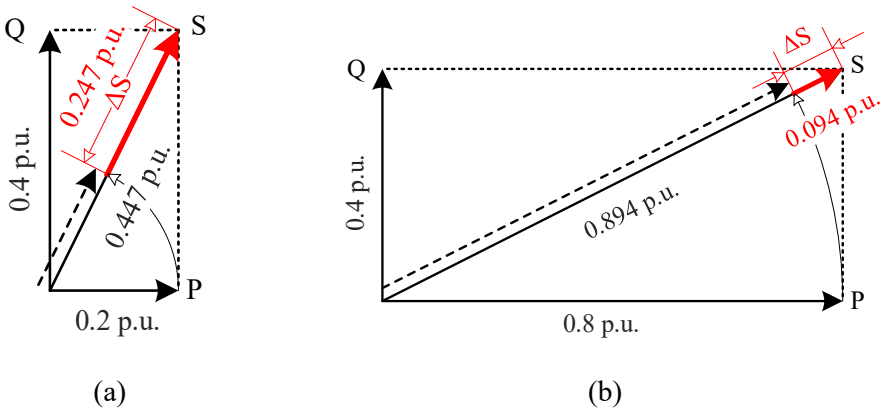

Figure 8.10: Phasor diagram of PV inverters with reactive power generation.

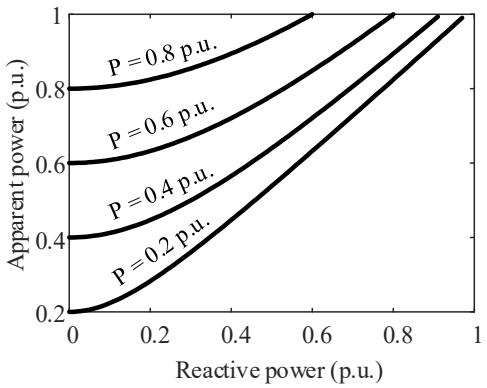

Figure 8.11: Apparent power curve with respect to reactive power.

8.1.4 Simulation Results

The following sections provide the details of the simulation results which examine the inverter aging due to thermal loading.

8.1.4.1 Scenario Definition

The single-phase PV inverter topology shown in Figure 8.4 is simulated in PLECS. The key parameters used in the simulation are summarized in Table 8.4. The semiconductor thermal models used in the simulation are from commercial device datasheets. The information of the devices used in this simulation is summarized in Table 8.5. The PV inverter is connected to a 120 V ac voltage source. The output current is controlled to follow the power generation reference. The ambient temperature utilized in the simulation is 25 °C. A group of power loss simulations with different active-reactive power combinations are conducted. In this simulation study, the PV inverter is assumed to have the reactive power generation settings follow IEEE Standard 1547 [60] with maximum reactive power support to be 0.44 p.u.

Table 8.4: PV Inverter Key Parameters

Parameters	Values
PV voltage, V_{PV}	50-70 V
DC link voltage, V_{dc}	200 V
Grid voltage, V_s	120 V
Power rating, P	2,500 W
Switching frequency, f_{sw}	10 kHz
Fundamental frequency, f_0	60 Hz

Table 8.5: Semiconductor Device Information

Part No.	Manufacturer Part No.	Manufacturer	Package
S_1	IGP50N60T	Infineon	TO-220
D_1	C4D20120D	Wolfspeed	TO-247
S_2, S_3, S_4, S_5	IKW50N60H3	Infineon	TO-247
D_2, D_3, D_4, D_5	IKW50N60H3	Infineon	TO-247

8.1.4.2 Inverter Aging Results

Figure 8.12 shows the output voltage and current waveforms from the PV inverter simulation. Figure 8.12 (a), (b), and (c) all have apparent power to be 2,500 VA. A group of power loss simulations with different active-reactive power combinations are conducted. The total power loss results are summarized in Figure 8.13. Figure 8.14 is the contour of Figure 8.13. Figure 8.13 shows the PV inverter total power loss in a 3-D plot. The *x*-axis is the active power, *y*-axis is the reactive power, and *z*-axis is the power loss. The traces in Figure 8.14 are the power loss contours projected on the *xy*-plane. Figure 8.14 shows that the power loss contour is in a circle. The total power loss of the PV inverter remains the same with different power factors.

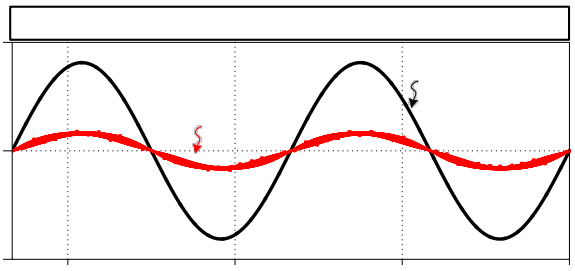

(a)

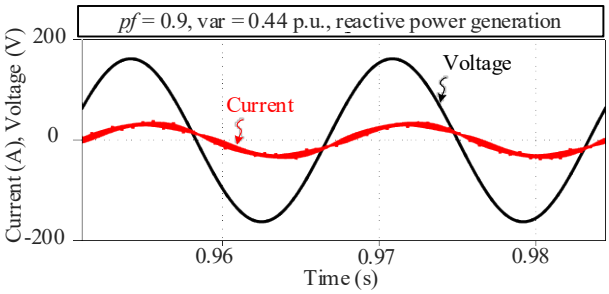

(b)

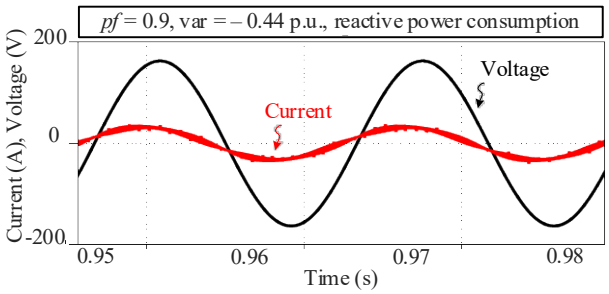

(c)

Figure 8.12: Sample waveforms from PV inverter simulation. (a) *pf* = 1.0, var =0; (b) *pf* = 0.9, var = 0.44 p.u.; and (c) *pf* = 0.9, var = – 0.44 p.u.

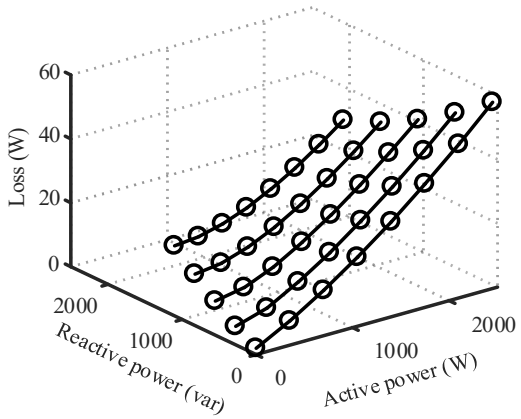

Figure 8.13: PV inverter power loss results for different combinations of active and reactive power.

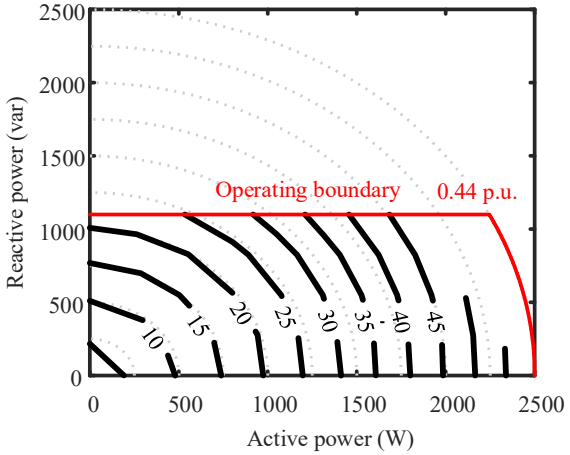

Figure 8.14: Power loss contour of the PV inverter simulation.

8.1.4.3 Semiconductor Power Loss

Figure 8.15 shows the individual IGBT and diode power loss results. Note that the second stage of the PV inverter has four IGBTs and four diodes. Each semiconductor has power losses and switching losses. Figure 8.15 selects one set of IGBTs and diodes to visualize the power loss contour so that the thermal stress of the diodes and IGBTs can be discriminated. In particular, Figure 8.15 (c) shows the diode conduction loss. The diode conduction loss increases as the *pf* decreases because more power flows through the diode instead of the IGBT. 2,250 W active power for the converter can generate 1.8-W diode conduction loss, whereas only 1,000-var reactive power generation can lead to 1.8-W diode conduction loss. From Figure 8.15 (a), the conduction loss of the IGBT is slightly decreased as the *pf* decreases. From Figure 8.15 (b) and (d), the switching loss of the IGBT and the reverse recovery loss of the diode do not have significant correlation with the power factor.

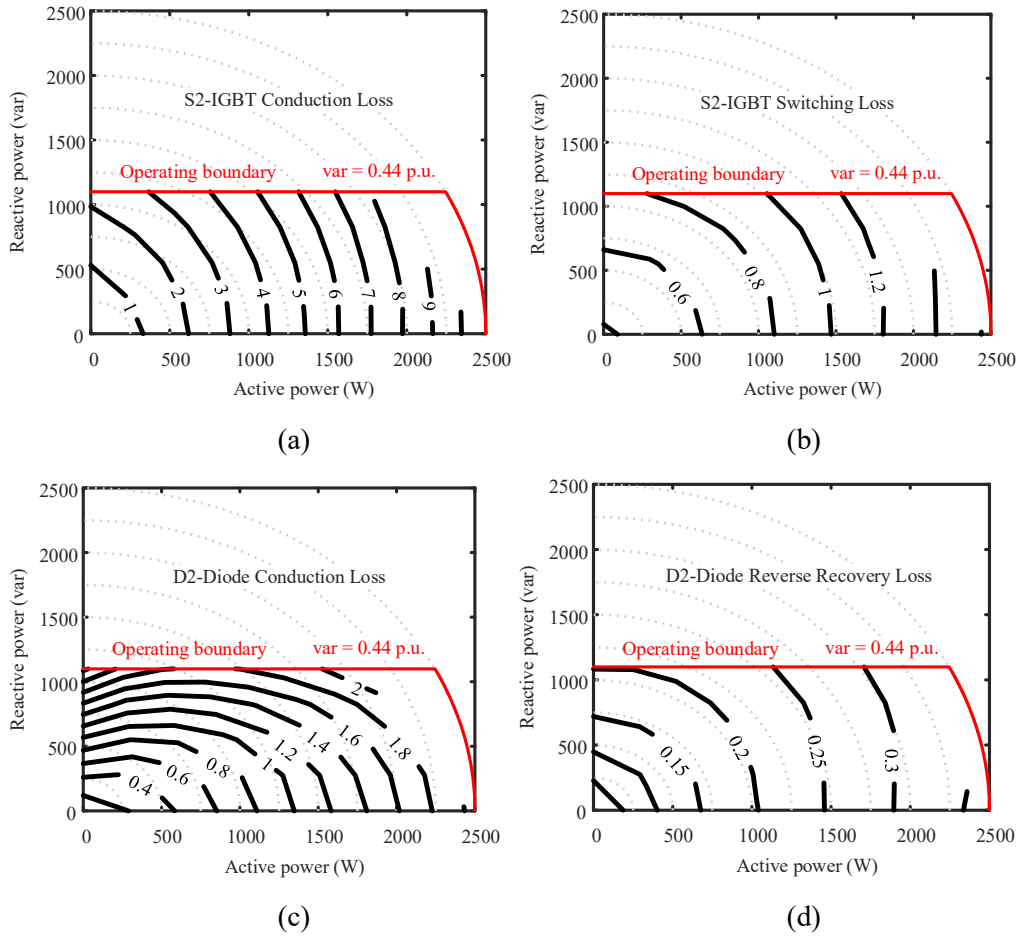

Figure 8.15: Semiconductor power loss contour with respect to different loading conditions. (a) IGBT conduction loss; (b) IGBT switching loss; (c) diode conduction loss; and (d) diode reverse recovery loss.

8.1.4.4 Thermal Cycle

Figure 8.16 shows the junction temperature of the IGBT and diode at the location S_2 D_2 in Figure 8.4. The filtering inductor used in this simulation is 0.2 mH (1.3% p.u.). Figure 8.16 presents three operating points: a) pf = 1.0, var = 0.00; b) pf = 0.9, var = 0.44 p.u.; and c) pf = 0.9, var = – 0.44 p.u. The thermal model in Figure 8.3(d) is used in this simulation study. The IGBT junction temperature ($T_{j,I}$ and $\Delta T_{j,I}$) for these three cases remains the same. On the other hand, the diode junction temperature variation ($\Delta T_{j,D}$) shows a significant difference among the three cases. As discussed in Section 8.2.3.2, the diode current variation in a fundamental cycle may double when the pf = 0.9. This will lead to larger diode junction temperature variation in a fundamental cycle.

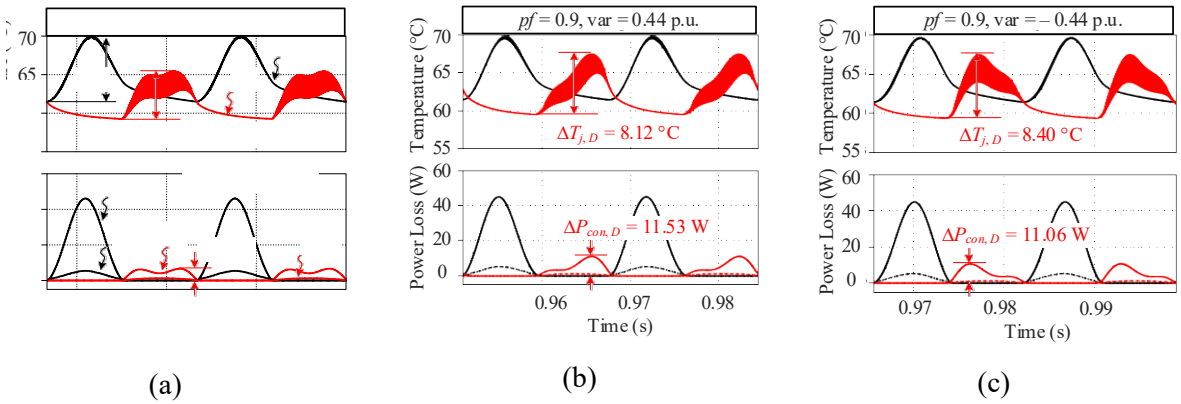

Figure 8.16: Junction temperature of IGBT and diode.
(a) pf = 1.0, var = 0.00 (b) pf = 0.9, var = 0.44 p.u. (c) pf = 0.9, var = – 0.44 p.u.

Figure 8.16 (b) and (c) show that the diode junction temperature variation ($\Delta T_{j,D}$) is more than 8 °C when pf = 0.9, whereas Figure 8.16 (a) shows that the junction temperature variation ($\Delta T_{j,D}$) is 6.3 °C when pf = 1. A higher junction temperature will significantly influence the lifetime of the diode.

8.1.4.5 Filtering Inductor Effect

Figure 8.17 shows the junction temperature of the PV inverter's IGBT and diode when the filtering inductor is relatively large (5 mH, 32.7% p.u.). Figure 8.17 presents three operating points: a) pf = 1, var = 0; b) pf = 0.9, var = 0.44 p.u.; and c) pf = 0.9, var = – 0.44 p.u.. The IGBT junction temperature ($T_{j,I}$ and $\Delta T_{j,I}$) of these three cases remains the same. On the other hand, the diode junction temperature variation ($\Delta T_{j,D}$) has a significant difference for the three cases.

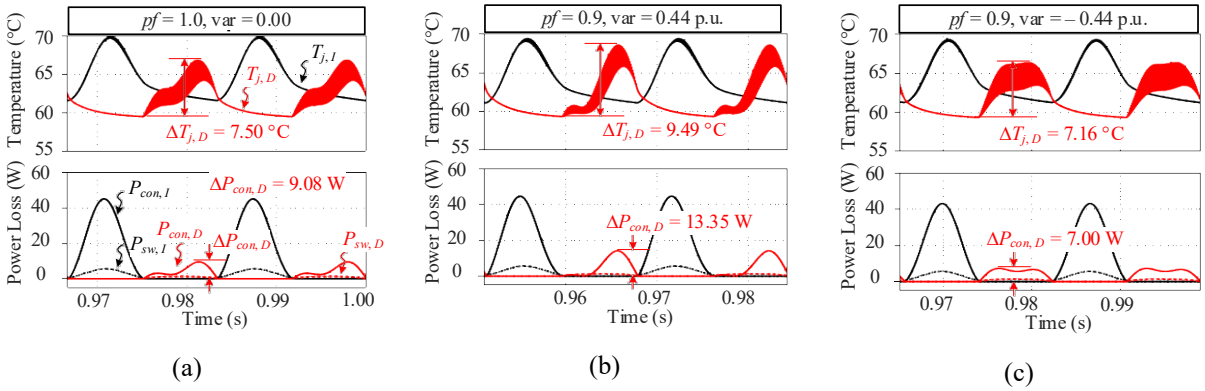

Figure 8.17: Junction temperature of IGBT and diode with 50-mH (32.7% p.u.) filtering inductor.
(a) pf = 1.00, var = 0.00 (b) pf = 0.9, var = 0.44 p.u.. (c) pf = 0.9, var = – 0.44 p.u.

As discussed in Section 8.1.3.3, the bridge circuit pf needs to include the filtering inductor as part of the load. When the output pf is 1 as shown in Figure 8.17 (a), the bridge circuit pf is slightly inductive. Hence, the diode junction temperature waveform in Figure 8.17 (a) is similar to that in Figure 8.16 (b). When the load is inductive as shown in Figure 8.17 (b), the bridge circuit pf is more inductive. This leads to even greater diode junction temperature variation. When the load is capacitive as shown in Figure 8.17 (c), the

filtering inductor can be compensated by the load. The bridge circuit *pf* is close to unity. Therefore, the diode junction temperature variation is the least among the three cases.

8.1.4.6 Semiconductor Aging Analysis

To assess the aging effect of the reactive power generation, a theoretical-model-based assessment platform is established. The workflow of the theoretical-model-based assessment is shown in Figure 8.18. This platform calculates the cycles to failure N_f of inverter semiconductors (IGBTs and diodes) using the theoretical models discussed in Section 8.1.1 and 8.1.2. The PV inverter under analysis is the same as Section 8.1.4.1. The input of the platform is the power generation of the two-stage PV inverter. The junction temperatures of inverter diodes and IGBTs are calculated accordingly.

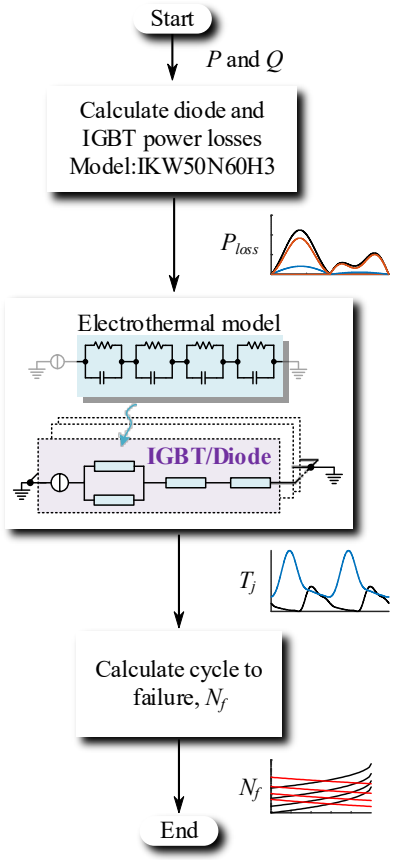

Figure 8.18: Workflow of semiconductor aging effect assessment platform.

Figure 8.19 shows the junction temperature results from the theoretical models in comparison with that from simulations conducted in the PLECS simulation environment. From Figure 8.19, the diode junction temperature variation from the theoretical models is less than that of the PLECS simulation, whereas the IGBT junction temperature variation from the theoretical models is larger than that of the PLECS simulation. This is because the theoretical model linearizes the semiconductor power loss model by using a built-in voltage source ($V_{0,D}$ or $V_{0,IGBT}$) and an on-resistor (R_D or R_{IGBT}). The theoretical models of the diodes and the IGBTs of this section are linearized from the 175-°C data from the device datasheets. A more accurate model can be obtained by using interpolation to find the corresponding power loss of a semiconductor at a certain junction temperature. This requires at least two sets of semiconductor thermal data.

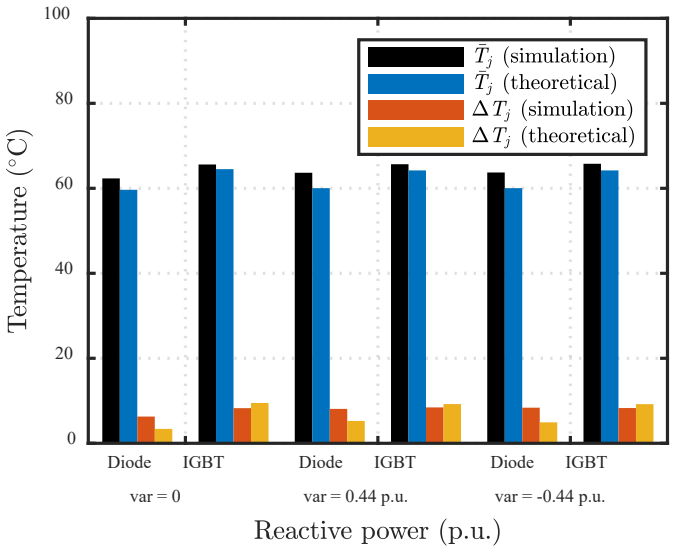

Figure 8.19: Junction temperature results from the theoretical models and PLECS simulation.

From Figure 8.19, the average temperatures of inverter diodes and IGBTs from the theoretical model is slightly smaller than that of the PLECS simulation. The average temperature is largely determined by the sum of the IGBT and diode power losses. The overall power loss from the theoretical model is less than that of the PLECS simulation. This leads to the small differences in average junction temperatures between the theoretical model and PLECS simulation. Despite the discrepancies in absolute values between the theoretical model and the PLECS simulation, the theoretical model can properly track the trends of junction temperature given different levels of PV generation.

The junction temperature profiles of PV inverter semiconductors are used for calculating the cycle-to-failure (N_f) from (8-1). The aging analysis of this section is based on the theoretical model. Figure 8.20 shows the N_f of PV inverter diodes and IGBTs with respect to different PV generation. When the active power generation is small (less than 1.5 kW), a small amount of reactive power generation/absorption will drastically reduce the semiconductor N_f. When the active power generation is large (more than 1.5 kW), extra reactive power generation/absorption will only slightly reduce the semiconductor N_f. In general, the additional reactive power generation/absorption reduces the semiconductor N_f. However, the N_f reduction effect depends on the PV inverter active power production. The reduction of N_f at small active power generation levels is more than that at large active power generation levels.

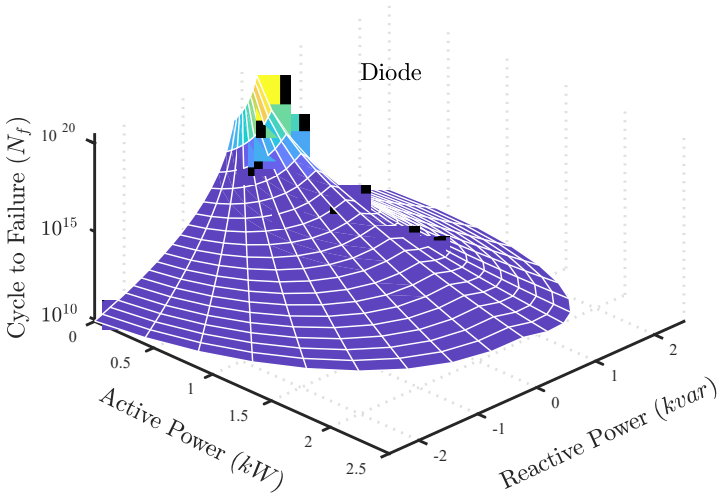

(a)

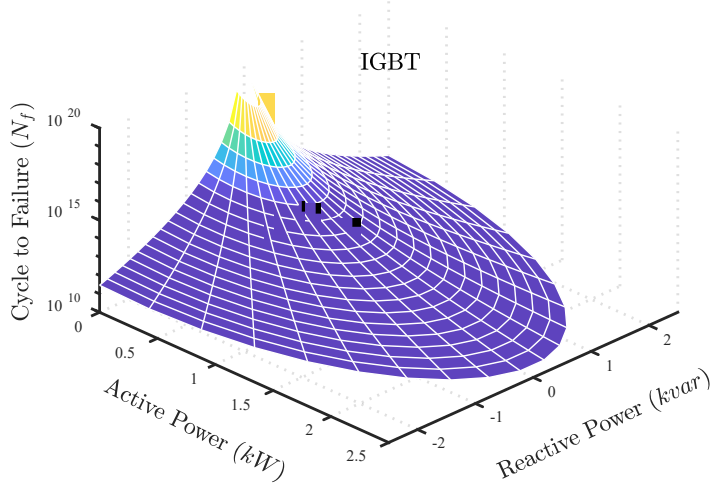

(b)

Figure 8.20: (a) Number of cycles to failure for the PV inverter diodes. (b) Number of cycles to failure for the PV inverter IGBTs.

Figure 8.21 shows the N_f of PV inverter diodes and IGBTs with respect to different power factors. As discussed in Sections 8.1.4.3 and 8.1.4.4, the power loss of diodes increases as the *pf* decreases. Also, the junction temperature variation for diodes increases as the *pf* decreases. Larger thermal cycle will accelerate the failure of diodes. The diode N_f decreases as the *pf* decreases. This can be seen from Figure 8.21. Similarly, the power loss of IGBTs decreases as the *pf* decreases. Also, the junction temperature variation for IGBTs decreases as the *pf* decreases. Smaller thermal cycle (ΔT_j) will lead to longer IGBT lifetime. The IGBT N_f increases as the *pf* decreases. Low *pf* will help extend the IGBT lifetime. This can be seen from Figure 8.21.

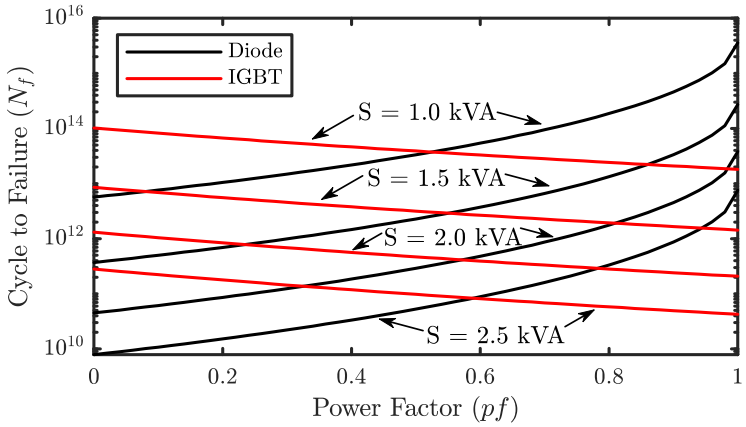

Figure 8.21: N_f of PV inverter diodes and IGBTs with respect to power factors.

Figure 8.22 shows the N_f of PV inverter diodes and IGBTs with respect to different reactive power generation levels. In the ancillary services market, the PV inverter is typically requested to provide reactive power in addition to the maximum active power point, thus extra reactive power generation leads to extra power loss. Both the diodes and IGBTs will suffer from the extra heat. This can be seen from Figure 8.22. Both diode N_f and IGBT N_f decrease as the reactive power increases. However, the reactive power aging effects on the IGBTs and diodes are slightly different. The diode N_f is much more sensitive to the reactive power than the IGBT N_f. Diode N_f decreases more than 100 times when the reactive power increases from 0.00 p.u. to 0.44 p.u., whereas the IGBT N_f decreases less than 10 times when the reactive power increases from 0.00 p.u. to 0.44 p.u.

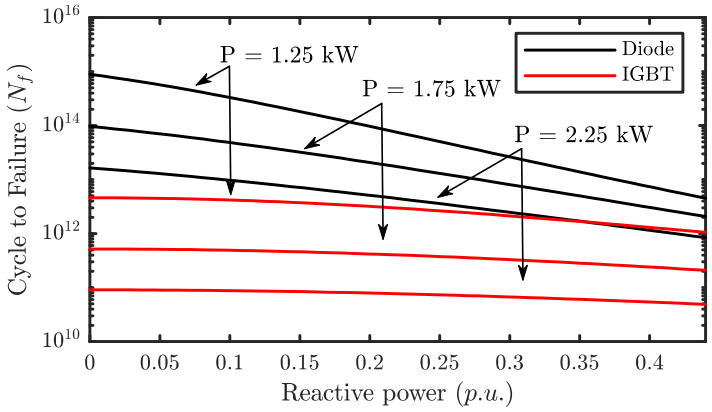

Figure 8.22: N_f of PV inverter diodes and IGBTs with respect to different var generation.

Figure 8.23 shows the N_f of PV inverter diodes and IGBTs with respect to different filter inductances. In general, the filtering inductor will accelerate the semiconductor aging for both diodes and IGBTs. However, the filter inductor aging effects on the IGBTs and diodes are slightly different. The diode N_f is much more sensitive to the filter inductor value than the IGBT N_f. Diode N_f decreases more than 10 times when the filter inductance increases from 0.0 p.u. to 0.3 p.u., whereas the IGBT N_f decreases less than 10 times when the reactive power increases from 0.0 p.u. to 0.3 p.u.

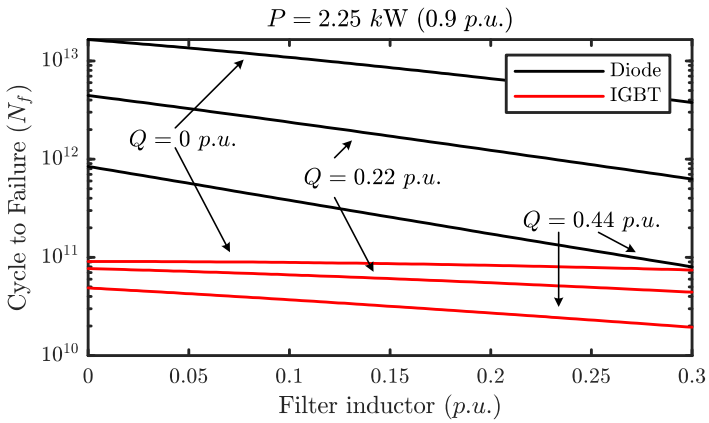

Figure 8.23: N_f of PV inverter diodes and IGBTs with respect to different filter inductances.

8.1.5 Reactive Power Impact on PV Inverter Aging Conclusions

This section develops the lifetime model of the semiconductors in a PV inverter by integrating the semiconductor electrothermal model and the PV inverter modulation. The lifetime model formulates the inverter semiconductors' thermal stress under the scenarios where the PV inverter is engaged in reactive power support. Both the analysis and the simulation results show that the average conduction loss of inverter diodes increases when the output current *pf* decreases. In addition to the average conduction loss of diodes, the conduction loss variation of the diodes doubles when the *pf* decreases to 0.9. The aging effect of the extra thermal stress on diodes also shows that the diodes suffer from accelerated aging during reactive power support.

The filtering inductor impact on semiconductor current distribution also has to be considered because of its effect on the power factor of the output current and resulting current distribution among the inverter's IGBTs and diodes. The analysis and simulation results show that the filtering inductor can increase the conduction loss variation of diodes when the load is inductive. The extra power losses in diodes lead to shorter lifetime expectation of PV inverter diodes.

PV inverter manufacturers will need to account for the provision of ancillary services, and in particular reactive power support, in the design of future products in order to ensure that provision of ancillary services does not negatively impact the lifetime of their products. This may include needing to use higher current ratings in the anti-parallel diodes and more closely examining the parasitics in their dc link capacitors and filter inductors.

8.2 Semiconductor Aging Simulation

To extend the lifetime of PV inverters, many methods have been tested on a simulation-based aging analysis to evaluate the performance of the proposed methods. The work in [61] presented a lifetime model to predict the fatigue level of the semiconductor bond wires. Similar lifetime models are also used in [62], -[64]. This lifetime model of semiconductors has the potential to be extended to grid-level simulations and incorporated into reliability studies.

Simulation-based aging analysis typically involves three steps [65]-[70]: 1) an electrothermal model to calculate the semiconductor junction temperature; 2) a rainflow-counting algorithm to assess the temperature profile; and 3) a semiconductor aging model to estimate the degradation. Among the three steps, the junction temperature calculation and rainflow-counting (thermal cycles) can be time consuming

because the junction temperature profile is strongly related to the converter switching actions. The corresponding time step of the junction temperature calculation is around 100 μs if the conventional Euler-Maruyama method is applied to the simulation [71]. To accelerate the fatigue simulation, multiple solutions have been proposed in the literature. Several look-up-table based methods are proposed to eliminate the junction temperature calculation [67]-[69]. The work in [66] proposed a reduced-order thermal model to accelerate the junction temperature calculation. Most existing acceleration methods have focused on the junction temperature calculation. Some material in the literature has proposed replacing the semiconductor aging model with indirect measurements, such as IGBT turn-on losses [72] and case temperature [73], to estimate the health of the semiconductor. Few items in the literature have reported acceleration methods for calculating reliability by focusing on rainflow counting.

This section leverages the quasi-static time series concept to simulate the fatigue of inverter semiconductors over longer periods of time. The simulation-based aging analysis for semiconductors can be incorporated with power systems simulations, so that a specific grid code can be tested for its aging effect on grid-connected inverters. Power systems simulations typically adopt a quasi-static time series (QSTS) approach to evaluate a system with the data ranging from several days to several years [74], [75]. QSTS simulations provide a good representation of time-varying characteristics in grid objects that incorporate various control systems, such as voltage regulators and shunt capacitors [76].

This section presents a fast semiconductor fatigue simulation approach that can be extended to QSTS simulations. The semiconductor fatigue simulation incorporates the PV inverter solar irradiance and load profiles as the input and estimates the lifetime remaining of the inverter semiconductors as the output. In addition, small thermal cycling during switching and the fundamental frequency is neglected to further accelerate the rainflow counting. A 7-day simulation and a 2-year simulation are provided to evaluate the proposed fatigue simulation. The computation speed and accuracy of the proposed simulation are benchmarked with a quasi-static time series fatigue simulation with complete thermal cycling profile. A PV inverter that responds to a TES is simulated to demonstrate the use of the proposed fatigue simulation. The proposed simulation can be incorporated with semiconductor lifetime model and predict the lifetime expectancy. The main body of this section has been submitted to IEEE Open Journal of Power Electronics for review [77] and was partly presented at the 2021 IEEE PES General Meeting [78].

8.2.1 Fast Electrothermal Simulation

Electrothermal simulation is a calculation to map PV generation to a semiconductor junction temperature profile. To evaluate the junction temperature of a semiconductor, the power loss of the semiconductor needs to be calculated. The power losses modeled by the semiconductor conduction loss and switching loss are the heat source for each semiconductor. The power loss will be dissipated into ambient as heat. This section develops a Fast Fourier Transform (FFT) based approach to calculate the steady-state junction temperature so that the junction temperature can be used in fatigue analysis.

8.2.1.1 Semiconductor Power Loss Formulation

A typical two-stage single-phase PV inverter topology is shown in Figure 8.4. The power switches of a PV inverter could be either MOSFETs or IGBTs. The complete semiconductor switching loss and conduction loss for both MOSFET-based and IGBT-based PV inverters are summarized in Table 8.6 [70], where E_{on} is the device turn-on energy; E_{off} is the device turn-off energy; f_{sw} is the switching frequency; I_{rms} is the rms value of the current that flows through a semiconductor; I_{avg} is the average value of the current that flows through a semiconductor; R_{IGBT} is the equivalent ON-resistance of the IGBTs; R_{D} is the equivalent ON-resistance of the diodes; $R_{ds(\mathrm{on})}$ is the equivalent ON-resistance of the MOSFETs; V_{dc} is the dc-link voltage; i_s is the load current; V_0 is the built-in voltage of the device p-n junction; I_{ref} and V_{ref} are the testing current

and voltage condition provided from the device datasheets; and $E_{rr,D}$ is the reverse recovery energy loss of diodes. The derivation of the semiconductor power loss formulation can be found in Section 8.1.2.

Table 8.6: Semiconductor Power Loss

Semiconductor Type	Loss Type	Equation
IGBT	Switching Loss	$(E_{on,I} + E_{off,I}) \cdot f_{sw}$
	Conduction Loss	$I_{rms,IGBT}^2 R_{IGBT} + I_{avg,IGBT} V_{0,IGBT}$
MOSFET	Switching Loss	$(E_{on,M} + E_{off,M}) \cdot f_{sw}$
	Conduction Loss	$I_{rms,M}^2 R_{ds(on)}$
Diode	Switching Loss	$(\frac{\sqrt{2}}{\pi} \frac{I_s V_{dc}}{I_{ref} V_{ref}} E_{rr,D}) \cdot f_{sw}$
	Conduction Loss	$I_{rms,D}^2 R_D + I_{avg,D} V_{0,D}$

An IGBT-based PV inverter is selected as the model for the fatigue simulation in this section since IGBT based PV inverters are more common especially for high power ratings (>5 kW) [79]. The key parameters of the IGBT/diode pair are summarized in Table 8.7 and Table 8.8.

Table 8.7: IGBT Key Parameters

Part No.	IKW60N60H3
Manufacturer	Infineon
$V_{0,IGBT}$	1.06 V
R_{IGBT}	0.024 Ω
T_j	175 °C
V_{GE}	0/15 V
V_{CE}	400 V
I_C	60 A
E_{on}	2.63 mJ
E_{off}	1.46 mJ

Table 8.8: Diode Key Parameters

Part No.	IKW60N60H3
Manufacturer	Infineon
$V_{0,IGBT}$	0.76 V
R_{IGBT}	0.025 Ω
T_j	175 °C
V_{GE}	2.8 µC
V_{CE}	400 V
I_C	60 A

8.2.1.2 Electrothermal Model

The electrothermal model of a semiconductor can be represented by a branch of an *RC* network (Foster model) as shown in Figure 8.24 [80]. The Foster model uses linear components (*RC*) to capture the linear properties of the thermal behavior and eliminate the nonlinearities. The accuracy of a Foster model is acceptable for steady-state analysis; thus, the electrothermal model for the semiconductors in this section adopts the Foster model. The power losses will be passed through the device Foster model and result in the device junction temperature. The parameters of the Foster models of the diodes and IGBTs of this section are summarized in Table 8.9. The Foster model for the semiconductors of this section contains five *RC* branches to maintain consistency with the original data from manufacturers.

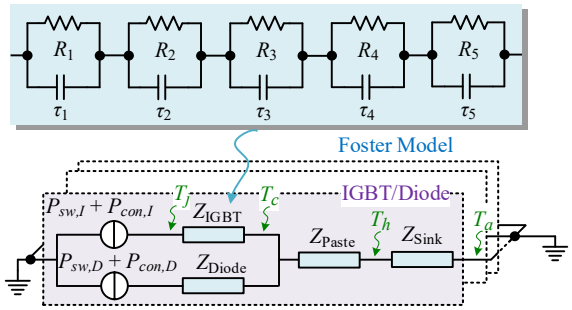

Figure 8.24: Detailed thermal model of PV inverter using discrete IGBT-diode pack.

Table 8.9: Diode and IGBT (IKW60N60H3) Foster Model

	Thermal Resistance (K/W)				
	R1	**R2**	**R3**	**R4**	**R5**
Diode	0.049	0.23	0.31	0.27	0.2
IGBT	0.003	0.072	0.082	0.196	0.009
	τ1	**τ2**	**τ3**	**τ4**	**τ5**
Diode	7.5×10^{-6}	2.2×10^{-4}	2.3×10^{-3}	1.55×10^{-2}	0.108
IGBT	3.0×10^{-5}	2.7×10^{-4}	3.0×10^{-3}	1.6×10^{-2}	0.228

The electrothermal model of this section adopts a typical discrete IGBT module with an on-chip anti-parallel diode, which is commonly used in PV inverter designs. The detailed electrothermal model of the IGBT modules with anti-parallel diode packs is shown in Figure 8.24. The switching loss (P_{sw}) and conduction loss (P_{con}) are the heat sources for each IGBT and diode. The thermal impedance of thermal paste is typically small, and hence neglected in this section. The Foster model for the heatsink used in this section is summarized in Table 8.10.

Table 8.10: Heatsink Thermal Parameters

Parameters	**Values**
Heatsink Part Number	C247-025
Manufacturer	Ohmite
Surface Area	7312 mm^2
Thermal Resistance	3~9 °C/W (5 °C/W for this report)
Thermal Capacitance	1000 sec.

8.2.1.3 Fast Junction Temperature Calculation

Common simulation algorithms such as Euler-Maruyama method can be adopted to find the junction temperature. The power loss of semiconductors typically cycles at a frequency of 60 Hz [81]. Euler-Maruyama method requires the time step to be much smaller than 1/60 s (a value of around 100 μs is typically used in simulation) in order to achieve an acceptable accuracy [71]. Such small time-steps are computationally burdensome for long-term simulations.

Quasi-static simulations are widely adopted for long-term power system simulations [74]. The basic idea of the quasi-static simulation is to calculate the steady-state of the system and use the steady-state to represent the system during the whole period of a time step. The time step of a quasi-static simulation varies from a second to several minutes depending on the simulation data and accuracy requirements. Also, quasi-static time-series simulations compute the network states depending on past states, which is useful for modeling control system interactions. This section leverages the quasi-static time series concept to simulate the fatigue of inverter semiconductors over longer periods of time. The proposed simulation has the potential to co-simulate with any simulation which also adopts the quasi-static concept. The results of the simulation can be used for grid control design or reliability studies.

The quasi-static concept can effectively avoid the small-time step computational-intensive issue typically seen when employing the Euler-Maruyama method. For example, suppose a PV dataset has a sampling rate of one measurement per 15 minutes. To use the Euler-Maruyama method, the simulation needs to adopt a time step of 100 μs in order to obtain the junction temperature waveform. This will lead to 9 million-time steps to simulate a 15-minute time slot. In contrast, to use quasi-static concept, the simulation only calculates the junction temperature once every sample. This means the simulation only computes once in a 15-minute simulation. The accuracy of the simulation is typically limited by the data resolution. For instance, the dataset of this section has a one-sample-per-15-minute resolution. The accuracy of the Euler-Maruyama method and the quasi-static method will be the same in this case since both methods can obtain the same junction temperature profile in this case.

To find the steady-state of semiconductor thermal stress, the heat source (device power loss) can be decomposed into several sinusoids by FFT. The steady-state response of the electrothermal model for each sinusoid can be calculated using phasors. Then, the inverse Fourier transform will be applied to the phasor forms of the junction temperature to find the time-domain waveforms. Thus, the junction temperature waveform from the inverse FFT can be recorded and sent to the rainflow-counting algorithm. Figure 8.25 shows the FFTs of the sample IGBT and diode power loss waveforms.

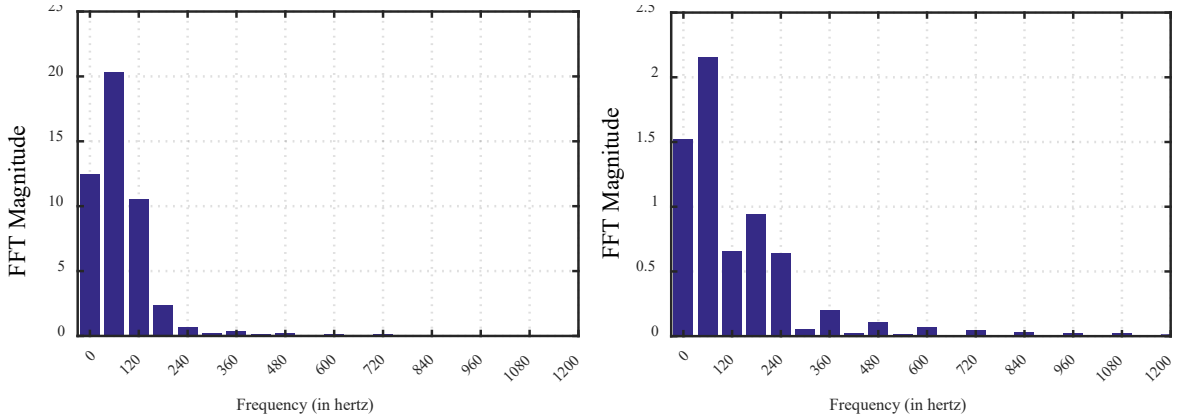

(a) (b)

Figure 8.25: PV inverter (a) typical IGBT power loss FFT; and (b) typical diode power loss FFT.

From Figure 8.25, the magnitudes of the harmonics over 240 Hz are relatively small, and therefore, can be neglected. The recovered power loss waveform from the inverse Fourier transform of the selected harmonics is shown in Figure 8.26, which contains the waveforms recovered from 1) dc to third harmonic; 2) dc to fourth harmonic; and 3) dc to fifth harmonic. The recovered time-domain waveform with the dc to fourth-order harmonics has already achieved an acceptable accuracy. Hence, this section selects the spectrum from DC to 4th harmonics as the heat source for the junction temperature.

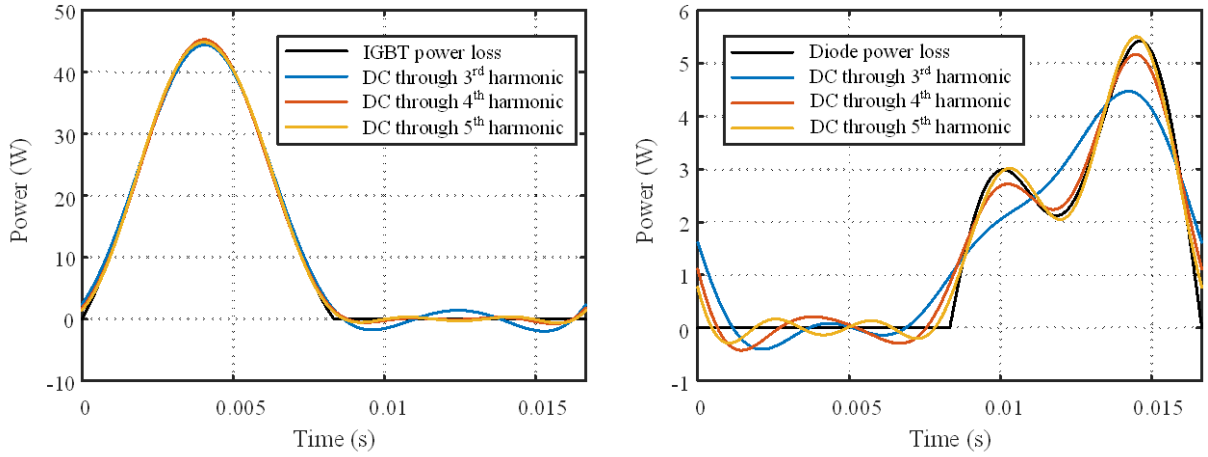

(a) (b)

Figure 8.26: Inverse Fourier transform of (a) IGBT power loss;
and (b) diode power loss in a PV inverter.

The selected harmonics from the power loss FFT are then applied to the Foster model of the semiconductors to calculate the corresponding steady-state junction temperature in frequency-domain. The junction temperature phasors are then inverted back to the time domain to find the junction temperature waveform. A sample of recovered time-domain junction temperature is shown in Figure 8.27.

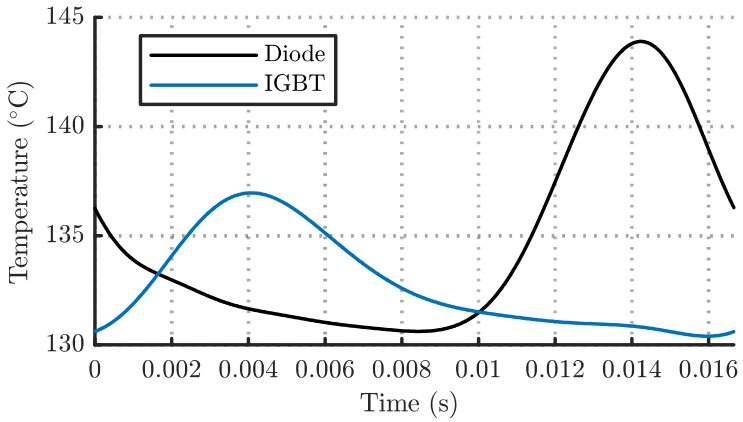

Figure 8.27: Recovered time-domain diode and IGBT junction temperature for one electric cycle (60 Hz) in a PV inverter.

8.2.2 Fatigue Analysis

The fatigue analysis of PV inverter semiconductors contains two parts. The first part is to evaluate the junction temperature profile by using a rainflow-counting algorithm. The rainflow-counting algorithm will count the number of thermal cycles and group the thermal cycles by their average value and magnitude. The second part is to map the rainflow counting results into semiconductor degradation. A semiconductor aging model will be used to map each thermal cycle from the rainflow counting into semiconductor degradation.

8.2.2.1 Rainflow Counting

Rainflow counting is a standard algorithm to evaluate the fatigue data of a system [82]. The basic idea of rainflow-counting algorithms is to count the strain cycle over a certain period of time. Each strain cycle is described with three key parameters: the peak value, valley value, and the stress duration. For the rainflow-counting algorithm of the inverter semiconductors, the strain is the junction temperature of each device. The peak and valley refer to the local maximum and minimum value of the junction temperature profile. The stress duration is the time duration that starts with the valley of the cycle and ends with the peak of the cycle.

The rainflow-counting algorithm of this section follows the standard algorithm described in [82]. Figure 8.28 (a)-(c) shows the thermal profile preparation for the rainflow counting. The junction temperature is calculated from the PV generation based on the procedure established in Section 8.2.1.3. Then, the peaks and valleys are recorded from the junction temperature profile. The transitions between the peaks and valleys are not of interest in the fatigue simulation and, therefore, are removed. The complete peak-valley profile can be fed into the rainflow-counting algorithm. However, considering the massive data the complete peak-valley profile might contain, the complete peak-valley profile will not be computationally efficient for long-term simulation.

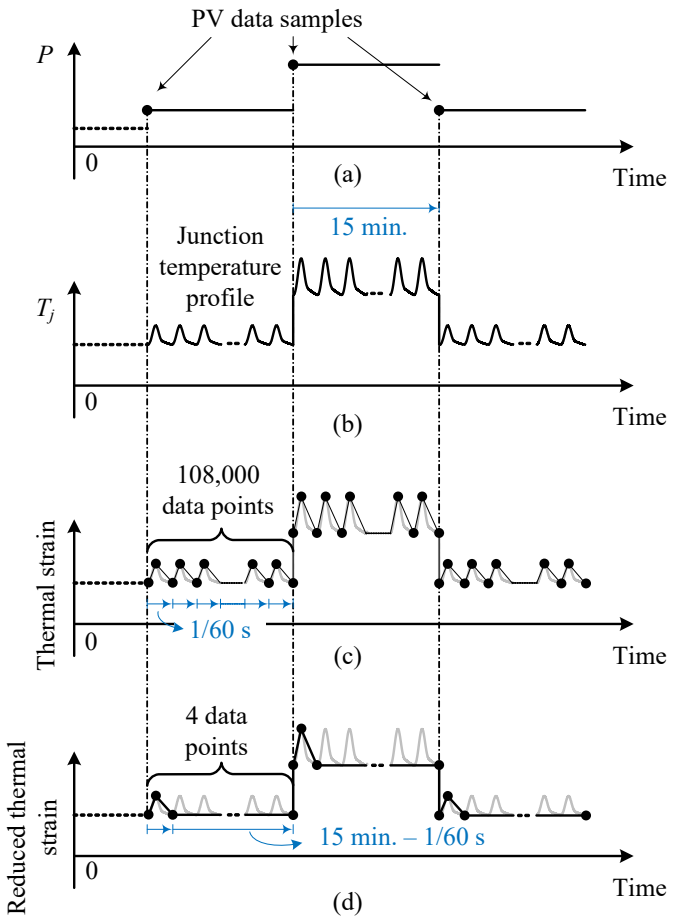

Figure 8.28: Thermal profile preparation for rainflow counting. (a) PV solar incidence data; (b) IGBT/diode junction temperature; (c) complete peak-valley profile; and (d) reduced peak-valley profile.

8.2.2.2 Reduced Thermal Profile

The complete peak-valley profile typically contains a massive amount of data. Semiconductor junction temperature typically cycles in a fundamental frequency (60 Hz or 50 Hz, depending on the region) as shown in Figure 8.28. Each fundamental period contains one peak and one valley. If all peaks and valleys are recorded, a 15-minute peak-valley profile will contain 108,000 data points, and a 3-year peak-valley profile will contain over one billion data points.

Literature have shown that the low frequency large thermal cycling is the leading factor in semiconductor aging [62], [83], [84]. The 60 Hz thermal cycling contributes little to semiconductor aging [62], [83], [84]. This is because the 60 Hz thermal cycling typically involves small strains (ΔT_j), which fall into the elastic region of the stress-strain curve [62]. In the elastic region, it is assumed that no damage is occurring during cycling [83]. Similar results are also observed in [84].

The complete strain profile is typically reduced to a smaller profile by discarding small stress cycles before applying to the rainflow-counting algorithm [85]. The 60 Hz thermal cycling is neglected in this section to accelerate the rainflow counting algorithm. In this section, only the first 60 Hz fundamental thermal cycling is kept for each PV sampling period. For example, if the PV sampling rate is one data per 15 minutes, then

only the first peak and valley will be recorded in a 15-minute simulation. The remaining peaks and valleys will be disregarded. The peak-valley profile reduction can be explained with the aid of Figure 8.28(d). The reduced thermal profile will greatly reduce the number of data if the sampling rate of the PV generation is much slower than 60 Hz.

8.2.2.3 Accumulated Fatigue Model

The rainflow-counting result can be mapped to a fatigue level by using the semiconductor aging model. The aging model of semiconductors is an empirical equation to associate aging factors to a lifetime expectation. For instance, the semiconductor aging model of this simulation follows [86],

$$N_f = A \times \left(\Delta T_j\right)^{\alpha} \times (ar)^{\beta_1 \Delta T_j + \beta_0} \times \left[\frac{C+(t_{on})^{\gamma}}{C+1}\right] \times exp\left(\frac{E_1}{k_b \times \bar{T}_j}\right) \times f_d \tag{8-21}$$

where N_f is the number of cycles to failure. This parameter indicates that a new semiconductor device is going to fail after N_f cycles of use for a given operating condition. $\bar{T}_j$ is the mean junction temperature of a semiconductor. ΔT_j is the junction temperature variation in a thermal cycle. t_{on} is the time from the valley to the peak. The other parameters are related to the semiconductor material physics and are given in Table 8.1 in Section 8.1.1.1 [86]. The aging model is tested in a way that a periodic thermal stress is applied to a semiconductor until it fails. The thermal stress is applied during 0 to t_{on} of each period, and then the thermal stress is released during t_{on} to the end of this period. The applied thermal stress has a variation of ΔT_j and a mean temperature of $\bar{T}_j$. The semiconductor is expected to fail after N_f cycles under this test condition.

There are various cumulative damage models in the literature for reliability assessment [87]-[89]. The accumulated damage model of this section follows Miner's rule, which is a linear cumulative damage model [24]. The assumption of Miner's rule is that the damage of the IGBT modules is independent of the stresses experienced during its life cycle, which means each cycle from the rainflow counting will create a separate independent damage. The sum of the damages from all rainflow cycles will be the accumulated damage of the device. The accumulated fatigue can be expressed as follows,

$$AF = \sum_i \frac{n_{f,i}}{N_{f,i}} \tag{8-22}$$

where $N_{f,i}$ is the number of cycles to failure given the condition i, and $n_{f,i}$ is the number of cycles that the device is exposed under the condition i. $n_{f,i}$ is obtained from the rainflow-counting algorithm.

8.2.3 Case Study

The proposed fatigue simulation was developed in MATLAB. The flow chart of the proposed fatigue simulation is shown in Figure 8.29. The PV generation profile is provided to the simulation, and the power loss of each semiconductor then is calculated accordingly. The power loss is fed into the FFT based junction temperature calculation. Then, the semiconductor thermal profile is fed into the rainflow-counting algorithm to determine the device stress profile. The stress profile from the rainflow counting is mapped to the accumulated fatigue result. A two-year PV inverter generation dataset is provided to the fatigue simulation. The data are from a sampled MPPT profile of a PV inverter in Chattanooga, Tennessee from Aug. 1st, 2014 to July. 31st, 2016. The time step of the dataset is 15 minutes. The complete dataset is shown in Figure 8.30. In the following case study, the first seven-day data from the two-year dataset are tested using both complete thermal profile and the reduced thermal profile. The complete two-year dataset is tested using the reduced thermal profile only.

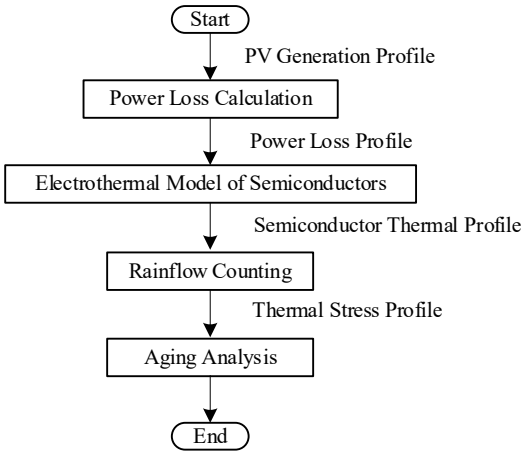

Figure 8.29: Flowchart of the proposed fatigue simulation.

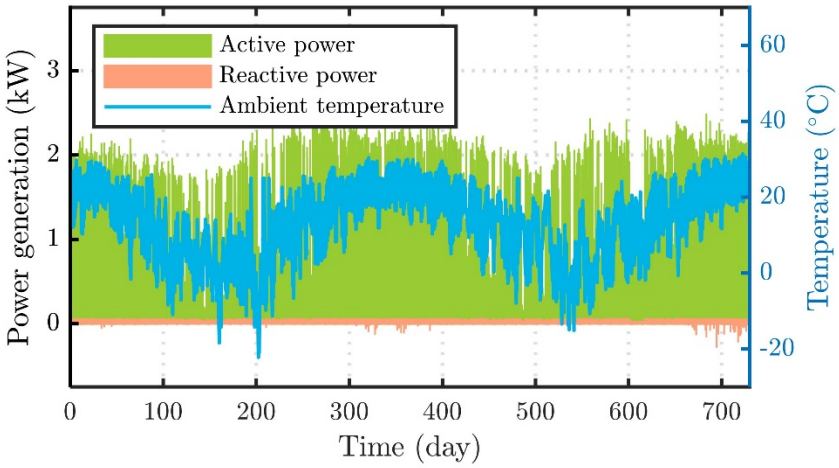

Figure 8.30: Two-year PV inverter generation profile for the case study.

8.2.3.1 Junction Temperature Profile

Both the complete and reduced peak-valley plot of the semiconductor junction temperature are formed in this section. As discussed in Section 8.2.2.2, the complete peak-valley profile may contain 108,000 data points in a 15-min simulation, whereas the reduced peak-valley profile contains 4 data points. The complete and reduced peak-valley profiles from the simulation are shown in Figure 8.31. The zoom-in figure for the complete peak-valley profile shows the 60 Hz cyclic junction temperature. The reduced peak-valley profile only keeps the first 60 Hz cyclic junction temperature and removes the rest. The overall picture for both complete and reduced peak-valley plots are similar because of the low resolution once the peak-valley plots are zoomed out.

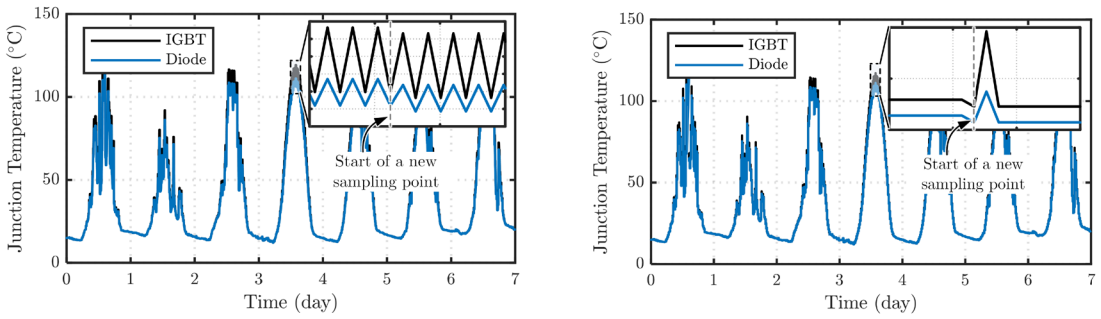

(a) (b)

Figure 8.31: IGBT and diode junction temperature profile for a PV inverter with 7-days of insolation data. (a) complete peak-valley profile; and (b) reduced peak-valley profile.

8.2.3.2 Rainflow Counting

The rainflow-counting algorithm is tested with a) 7-day complete peak-valley profile, b) 7-day reduced peak-valley profile, and c) 2-year reduced peak-valley profile. The rainflow-counting results are displayed in Figure 8.32. Figure 8.32 (a) and (b) shows the 7-day rainflow counting results using complete peak-valley profile and reduced peak-valley profile, respectively. The rainflow counting results in Figure 8.32 (a) and (b) are similar. Both results show that the thermal cycles can be categorized into three groups. Group 1 refers to the cycles with low frequency. Group 1 cycles are caused by solar irradiance variation, which typically varies from a few seconds to a few hours. The main causes of the solar irradiance change are solar angle change, cloud cover, and temporary bird (or other object or animal) shading. The diurnal temperature variation also contributes to the low-frequency cycles in Group 1. Group 2 refers to the cycles with a 60 Hz frequency during the time the PV inverter generates active power (daylight). Group 3 refers to the cycles with a 60 Hz frequency while the PV inverter is idling (night).

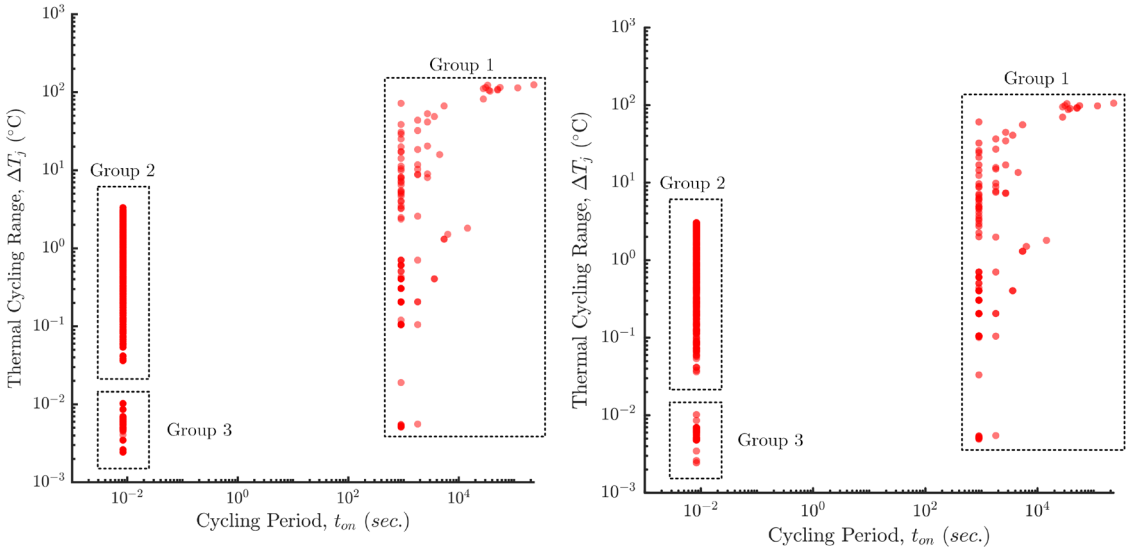

(a) (b)

Figure 8.32: Rainflow-counting results of the diode junction temperature profile for (a) 7-day complete peak-valley profile; and (b) 7-day reduced peak-valley profile.

The number of cycles for each group is summarized in Table 8.11. The complete peak-valley profile shows that Group 1 data are large in ΔT_j (greater than 5 °C) but the number of cycles is small (125 cycles). Group 2 data are relatively small in ΔT_j (between 0.02 to 5 °C) and the number of cycles is relatively large (in the order of 10^7). Group 3 data are extremely small in ΔT_j (less than 0.02) and the number of cycles is large (in the order of 10^7).

Table 8.11: Accumulated Fatigue Results from the 7-Day Simulation

	Complete Thermal Profile				
		IGBT		**Diode**	
Fatigue Type	**t_{on} (s)**	**Number of Cycles**	**Accumulated Fatigue**	**Number of Cycles**	**Accumulated Fatigue**
Low Frequency Cycling	> 1/120	125	0.4882%	125	0.3228%
60 Hz Cycling	1/120	2.0304×10^{7}	7.9904×10^{-4}%	2.0304×10^{7}	9.0085×10^{-6}%
Inverter Idling	1/120	1.5984×10^{7}	2.8396×10^{-18}%	1.5984×10^{7}	6.4579×10^{-19}%
		Total Fatigue	0.4890%	**Total Fatigue**	0.3228%
	Reduced Thermal Profile				
		IGBT		**Diode**	
Fatigue Type	**t_{on} (s)**	**Number of Cycles**	**Accumulated Fatigue**	**Number of Cycles**	**Accumulated Fatigue**
Low Frequency Cycling	> 1/120	127	0.4882%	127	0.3228%
60 Hz Cycling	1/120	323	1.0103×10^{-8}%	323	1.1447×10^{-10}%
Inverter Idling	1/120	222	4.6369×10^{-23}%	222	9.5791×10^{-24}%
		Total Fatigue	0.4882%	**Total Fatigue**	0.3228%

8.2.3.3 Accumulated Fatigue

The accumulated fatigue results from the 7-day simulation are summarized in Table 8.12 The total fatigue level of the IGBT is 0.4890% from the complete thermal profile, whereas the total fatigue level of the IGBT is 0.49% from the reduced thermal profile. The error of the reduced thermal profile is 0.16% which is acceptable in fatigue simulation. The error in the diode fatigue result is not significant. The total fatigue level of the diode is 0.3228% for both the complete and reduced thermal profile.

The accumulated fatigue result shows that the low frequency thermal cycling is the leading factor of the PV inverter semiconductor aging. The 60 Hz thermal cycling (Groups 2 and 3) only contributes to a minor aging effect.

The accumulated fatigue results from the two-year simulation is summarized in Table 8.12. The two-year simulation shows that the total fatigues of the IGBT and diode are 20.85% and 13.98%, respectively. This means the remaining lifetime of the IGBT and diode are 79.15% and 86.02%, respectively. The IGBT and diode are expected to have a lifetime of 9.59 years and 14.31 years, respectively, given the simulated condition. Thus, the IGBTs will determine the overall lifetime of the PV inverter instead of diodes in this case.

Table 8.12: Accumulated Fatigue Results from the Two-Year Simulation

Fatigue Type	IGBT		Diode	
	Number of Cycles	Accumulated Fatigue	Number of Cycles	Accumulated Fatigue
Low Frequency Cycling	12,898	20.8543%	12,887	13.9768%
60 Hz Cycling	28,524	4.5591×10^{-7}%	28,677	5.0886×10^{-9}%
Inverter Idling	28,650	4.8181×10^{-21}%	28,508	2.6372×10^{-21}%
	Total Fatigue	20.8543%	**Total Fatigue**	13.9768%

8.2.3.4 Computation Time

The computation time of each stage of the fatigue simulation is recorded. The computation time is summarized in Table 8.13. The rainflow counting takes 120 seconds to process the 7-day data using the complete peak-valley profile, whereas it only takes 0.0044 seconds to process the same dataset using the reduced thermal profile. The total computation time of the 2-year simulation is 77 seconds using the reduced thermal profile. The junction temperature calculation would take most of the computation time in the 2-year simulation, whereas the rainflow counting only takes 0.13 seconds. The reduced thermal profile mainly focuses on reducing the peak-valley profile for the rainflow counting, whereas the junction temperature calculation remains the same as the complete thermal profile. Therefore, the junction temperature calculation speed of the reduced thermal profile is similar to that of the complete thermal profile. This leads to the result that the junction temperature calculation takes most of the computation time for the 2-year simulation.

Table 8.13: Computation Time Comparison

		Junction Temperature Calculation	Rainflow Counting
Complete thermal profile	7-day data	3.27 s	120.27 s
Reduced thermal profile	7-day data	1.15 s	0.0044 s
	2-year data	77.02 s	0.13 s

8.2.4 Semiconductor Aging Simulation Conclusion

This section proposes a quasi-static time series fatigue simulation for PV inverter semiconductors. This capability is necessary to determine the impact of using inverters to support power system operations. Specifically, to quantify the degradation in inverter lifetime if the inverter has to output power in addition to the active power for which it was initially intended.

The proposed fatigue simulation is suitable for degradation evaluation with long-term data and co-simulation with other quasi-static simulation platforms for power systems. The proposed simulation increases the time step from 100 μs (as used in conventional Euler-Maruyama based simulation tools) to 15 minutes, so that the simulation time step is consistent with the solar data time step. The small junction temperature cycling is disregarded to accelerate the rainflow counting. The simulation results show that the small thermal cycling contributes to insignificant aging effects on semiconductors. The reduced thermal profile can correctly predict the fatigue level. The error of the reduced thermal profile is 0.16% which is acceptable in fatigue simulation. The simulation using the reduced thermal profile completes the 7-day simulation within 1.16 seconds, where 0.0044 seconds are consumed by rainflow counting. In contrast, the complete thermal profile takes 123.54 seconds to finish, where 120.27 seconds are consumed by rainflow counting. The proposed simulation approach can greatly reduce the computation time for rainflow counting. The total computation time of the 2-year simulation is 77 seconds. The proposed simulation can potentially be used for developing new system control strategies and evaluating inverter semiconductor degradation given a certain grid code.

9.0 Transactive Energy System

As discussed in the Section 6.0 use-cases, a transactive energy system can be used to increase operational flexibly. Additionally, the impact to inverter life-time for engaging them in his way was quantified in Section 8.0. Based on this work, this section presents the VOLTTRON agents discussed in Section 3.0, and how they can be integrated into a transactive energy system. Additionally, this section details two transactive algorithms: transactive energy algorithm-1 (TEA-1) and transactive energy algorithm-2 (TEA-2) that a DSO can deploy, individually, as an added DMS functionality to incentivize and engage non-utility DERs during resiliency events. While both approaches engage inverter-based non-utility DERs during resiliency events to increase load restoration by incentivizing the reactive power input/output of non-utility DERs, their design, and most importantly the application, is different. In Section 9.1 and 9.2, the VOLTTRON connection and transactive operational framework are presented, respectively. Sections 9.3 and 9.4 detail the transactive process to engage non-utility DERs during resiliency events.

9.1 Transactive Energy System - VOLTTRON Connection

Transactive energy is the approach to engage non-utility assets to support the voltage in the system by injecting or absorbing the reactive power of customer-owned inverters based on an incentive signal that will be sent from a Transactive Energy System [31], [32]. Based on this approach, the customer receives an economic benefit by providing the reactive power support from available capacity of an inverter, and the utility receives reactive power support without installing new equipment and/or systems which would require substantial capital investment. Engaging non-utility DERs requires communication between the customer devices and TES. Coordination between these systems is required in order to perform the bidding of reactive power based on the transactive energy approach.

In this project, a VOLTTRON node is used as a connection of non-utility DERs and the TES, and the VOLTTRON node is able to respond to transactive signals from the TES. The communication between the VOLTTRON node and TES is also NATS, which is similar to the communication used in the OpenFMB platform. The transactive energy approach is integrated into the VOLTTRON node through an inverter control agent. This inverter control agent is designed to subscribe to the transactive signal and to publish required data to perform the bidding between a non-utility owned inverter and the TES [10]. To coordinate with the TES, a state machine is designed and implemented into the inverter control agent in the VOLTTRON node. The steps of the coordination between the two systems are shown in Figure 9.1.

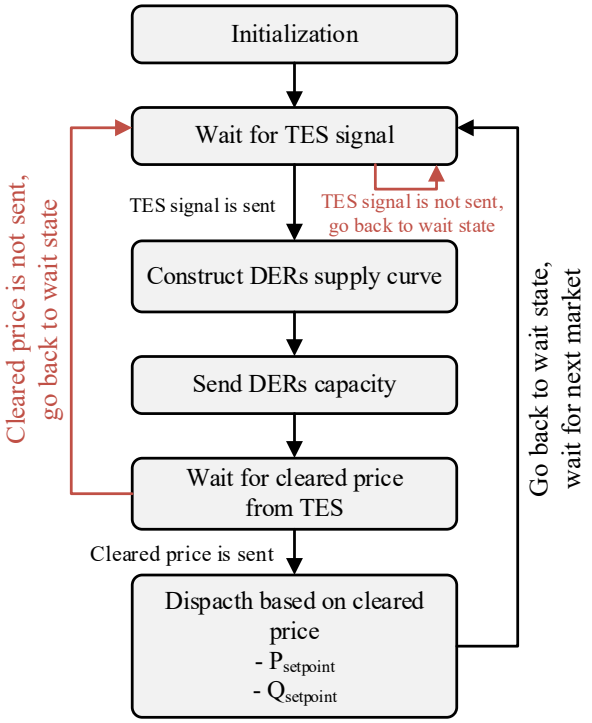

Figure 9.1: State machine implementation in VOLTTRON agents.

The coordination between two systems begins with the inverter control agent in the waiting state until the agent receives a TES signal, which indicates the system needs the support from the non-utility inverters. In the case when the agent waits for an extended period of time (30 seconds), the agent will flag the timeout error and close the connection between the VOLTTRON node and the TES, and it will then wait for participating in the next market opportunity. After the agent receives the TES signal, the agent moves to construct the DER's supply curve and send the DER's supply curve back to the TES to participate in the market. After the market is cleared, the agent will receive the cleared price from the TES, and the price will determine the amount of reactive power the inverter should supply to the system. After the amount of reactive power is determined, the set point of active and reactive power will be calculated in the agent and sent to the VOLTTRON message bus, and the inverter Modbus agent will subscribe the set points for setting new operating points of the inverter.

A Raspberry Pi with an installed VOLTTRON agent is used in the demonstration of this work. The framework is illustrated in Figure 9.2 with multiple agents performing with different inverters of various power ratings [10]. After the TES signal is sent by the TES for requesting the support from customers, multiple DERs will submit their own DER's supply curve for participation in bidding. When the market is cleared, each inverter will dispatch the power based on its individual supply curve.

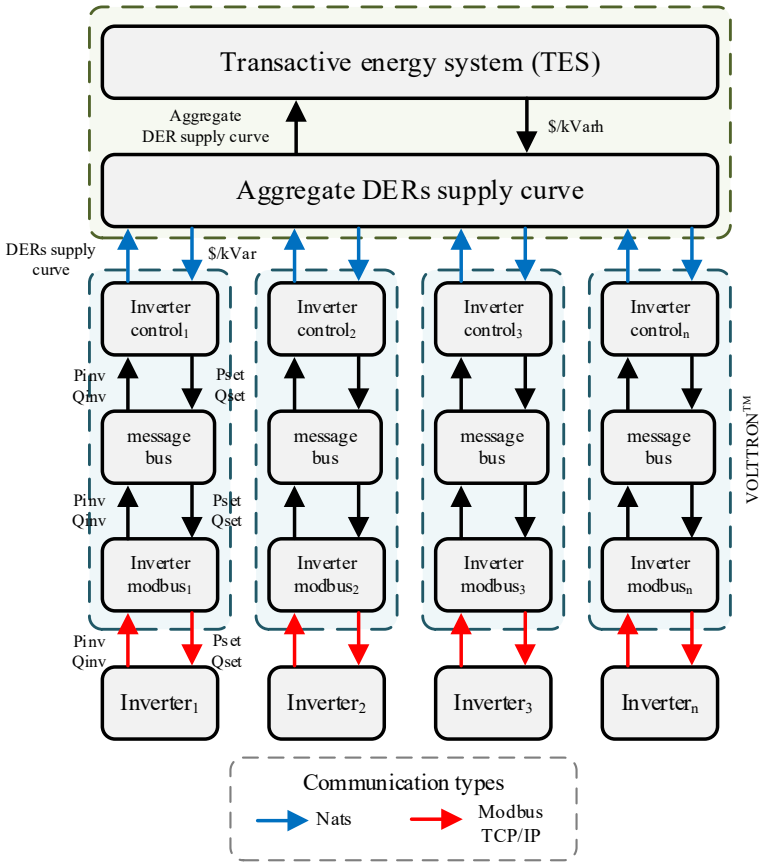

Figure 9.2: Framework of VOLTTRON nodes and TES.

In order to respond to a transactive energy signal for participating in reactive power bidding, each DER has to provide its reactive power capability in the form of inverter/DER's supply curve, which presents the price of reactive power per kvar-h ($/kvar-h) and reactive power capability of the inverter, based on its active power operating point. The DER's supply curve of the inverter can be constructed based on its loading condition which can be categorized into three conditions including: 1) Full load, 2) No load, and 3) Partial load. For demonstrating the participation of DERs in the reactive power market, the DERs' parameters as presented in Table 9.1 are used to construct each DERs' cost curve and DERs' supply curve in this study.

Table 9.1: Inverter Parameters for Each DER

DER ID	S (kVA)	Efficiency (%) at Power Levels						Model
		10%	20%	30%	50%	75%	100%	
DER1	5	93.6	95.9	96.5	96.7	96.6	96.3	ABB PVI-5000
DER2	10	95.4	96.6	96.8	96.8	96.7	96.3	Fronius Symo Advanced 10.0
DER3	15	95.5	97.2	97.8	97.8	97.8	97.8	SMA America STP15000TL

A test scenario was established to demonstrate the implementation of reactive power support from non-utility inverters by using the transactive energy approach. DERs' supply curves for different ratings of inverters are presented in Figure 9.3 (a). When considering these inverters are all operated at their full load condition, the curves for 5 kVA inverters (lowest power) have the highest cost for providing the reactive power followed by 10 kVA and 15 kVA units, respectively. Figure 9.3 (b) shows the aggregated curve of these inverters which can be determined by the sequence of price per kvar-h ($/kvar-h) based on DERs'

supply curves from the lowest to the highest value. The aggregated curve and demand curve are used to determine a cleared price of a market. After the market is cleared, the cleared price is sent to the participating DERs for dispatching active and reactive power to support the system based on their own individual DER's supply curves.

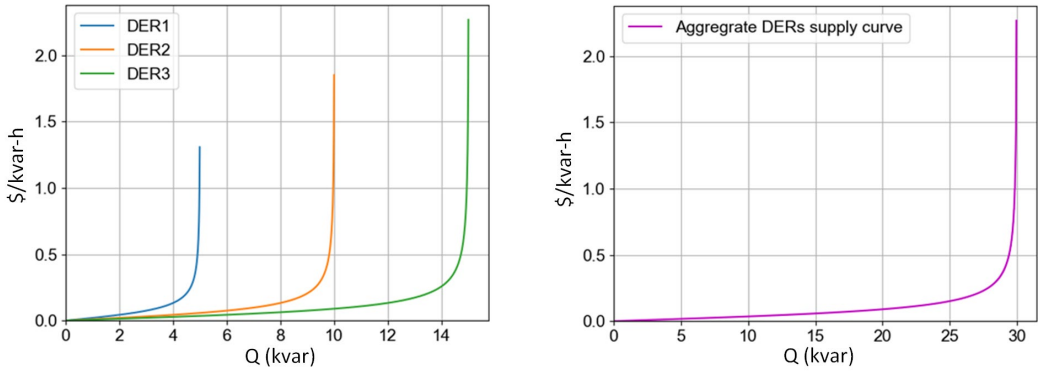

(a) (b)

Figure 9.3: DER's supply curves of (a) DER1 (blue curve), DER2 (orange curve), and DER3 (green curve). (b) Aggregate DER's supply curve of these three DERs.

Figure 9.4, Figure 9.5, and Figure 9.6 show simulation results from the agents when TES requests 10 kvar and cleared price = 0.0316 $/kvar-h is sent out to invite non-utility DERs to participate in the market. Upon receipt of the cleared price, output of reactive power dispatch of each DER is equal to 2 kvar, 3 kvar, and 5 kvar for DER1, DER2, and DER3, respectively.

```
(Inverter_controlagent-1.0 1909) <stdout> INFO: Cleared price: 0.0316403790611
(Inverter_controlagent-1.0 1909) <stdout> INFO: leaving subscribe cleared price,
(Inverter_controlagent-1.0 1909) <stdout> INFO: Q support: 2
(Inverter_controlagent-1.0 1909) <stdout> INFO: Entering update dispatch
(Inverter_controlagent-1.0 1909) <stdout> INFO: Set point of Q : 2 kVAR
(Inverter_controlagent-1.0 1909) <stdout> INFO: Set point of P: 4.58257569496 kW
(Inverter_controlagent-1.0 1909) <stdout> INFO: End of loop
```

Figure 9.4: VOLTTRON agent result of DER1.

```
(Inverter_control2agent-1.0 1929) <stdout> INFO: Cleared price: 0.0316403790611
(Inverter_control2agent-1.0 1929) <stdout> INFO: leaving subscribe cleared price,
(Inverter_control2agent-1.0 1929) <stdout> INFO: Q support: 3
(Inverter_control2agent-1.0 1929) <stdout> INFO: Entering update dispatch
(Inverter_control2agent-1.0 1929) <stdout> INFO: Set point of Q : 3 kVAR
(Inverter_control2agent-1.0 1929) <stdout> INFO: Set point of P: 9.53939201417 kW
(Inverter_control2agent-1.0 1929) <stdout> INFO: End of loop
```

Figure 9.5: VOLTTRON agent result of DER2.

```
(Inverter_control3agent-1.0 1949) <stdout> INFO: Cleared price: 0.0316403790611
(Inverter_control3agent-1.0 1949) <stdout> INFO: leaving subscribe cleared price,
(Inverter_control3agent-1.0 1949) <stdout> INFO: Q support: 5
(Inverter_control3agent-1.0 1949) <stdout> INFO: Entering update dispatch
(Inverter_control3agent-1.0 1949) <stdout> INFO: Set point of Q : 5 kVAR
(Inverter_control3agent-1.0 1949) <stdout> INFO: Set point of P: 14.1421356237 kW
(Inverter_control3agent-1.0 1949) <stdout> INFO: End of loop
```

Figure 9.6: VOLTTRON agent result of DER3.

Regarding the idea of reactive power support from non-utility DERs by integrating the transactive energy approach, the developed VOLTTRON node demonstrates the capability of the DERs to participate in the reactive power market by coordinating with the TES. The coordination framework between VOLTTRON nodes and TES is able to engage the support from the customers by using an incentive signal. The non-utility DERs would provide the support based on their DER's supply curves, which depend on the rating and loading condition of the DERs. Based on the transactive energy approach, both the utility and customer can receive tangible benefits. The customer can earn money based on the available capacity of an inverter for providing reactive power to the system, and the utility receives system operational benefit from voltage support, which can be done without the need of expensive capital investment.

9.2 Transactive Operational Framework

This subsection presents a framework for the proposed transactive approaches to be deployed in the field. The transactive approaches are envisioned to be deployed as an added DMS functionality to engage and incentivize non-utility-owned DERs during resiliency events. The transactive algorithms compute transactive signals to engage non-utility DERs such that local grid constraints are alleviated and thus, more switching options are enabled to allow for resilience actions. In this work, the proposed framework focuses on engaging non-utility solar PV systems to provide reactive power to support the load restoration and switching operations to utility. However, the framework can be applied to any DER type. The following considerations are made in this study:

- Electric utility may not have direct visibility of the non-utility DERs and may not be able to directly control them;
- Electric utilities first utilize utility-owned resources in response to resiliency events and call for transactive only if they could not restore the entire loads;
- Transactive algorithm is called by DMS with their targeted performance improvement, such as reducing the voltage across the normally open recloser to an acceptable level for closing; and
- When called, the transactive algorithm collects the bid information (from DERs and DSO) and computes the incentive signals to engage non-utility resources.

A conceptual framework illustrating the operational deployment of the proposed transactive approaches with utility DMS is shown in Figure 9.7. The numbers in Figure 9.7 represent the sequence of operations in terms of executing the transactive approach during grid outage conditions. When there is a resiliency event such as a bulk power outage, the resiliency plan starts with the DMS computing the optimal reconfiguration plan considering utility-owned resources. If the utility is able to restore the entire load by utilizing their own resources, only the actions defined through interface '1' (as shown in Figure 9.7) are performed. DMS makes the optimal reconfiguration decision utilizing the monitored status of the network intelligent electronic devices and utility-owned DERs. Those optimal decisions are executed by DMS using their own infrastructure.

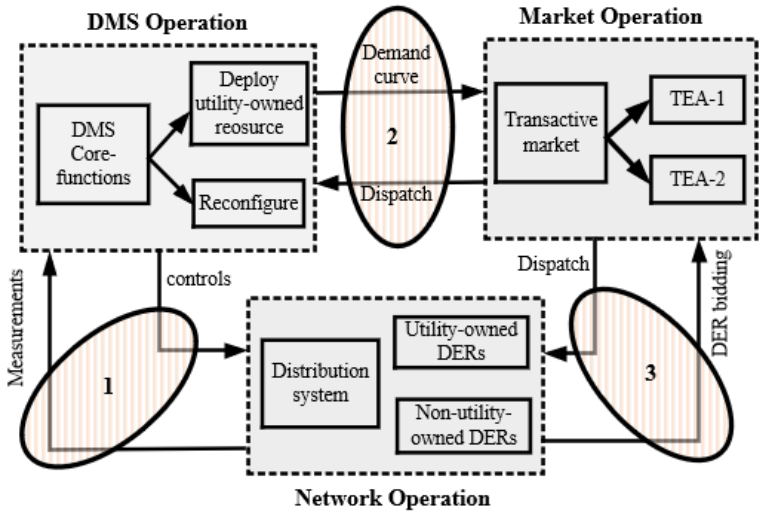

Figure 9.7: Conceptual framework for deploying transactive.

However, if utility-owned resources are not enough to restore the entire loads, DMS activates the transactive algorithm to engage non-utility DERs (shown by interface '2' in Figure 9.7). DSO expresses its requirement in the form of its demand curve. Then, the transactive framework runs a distribution-level transactive market to calculate incentive signals to engage non-utility DERs to meet the DSO demand (shown by interface '3' in Figure 9.7). DSO may express its demand in the form of marginal benefits from the participation of non-utility DERs or simply in terms of the technical requirements (e.g., demand to improve voltage by *x*% at the weakest node in the network). Similarly, non-utility DERs express their willingness to participate in the market by submitting their marginal cost. After running the market, the transactive approach dispatches the incentive signals to all market participants to enable additional switching option to DMS for restoring additional loads. Finally, the DMS executes the additional switching options that were feasible due to contributions from the non-utility DERs.

9.3 Transactive Energy Algorithm -1

Conceptual process of TEA-1 is illustrated by a flowchart in Figure 9.8. The following subsections detail the key components and the overall transactive mechanism for TEA-1, including the demand curve generation, supply curve generation, transactive market process, and control/operation implementation.

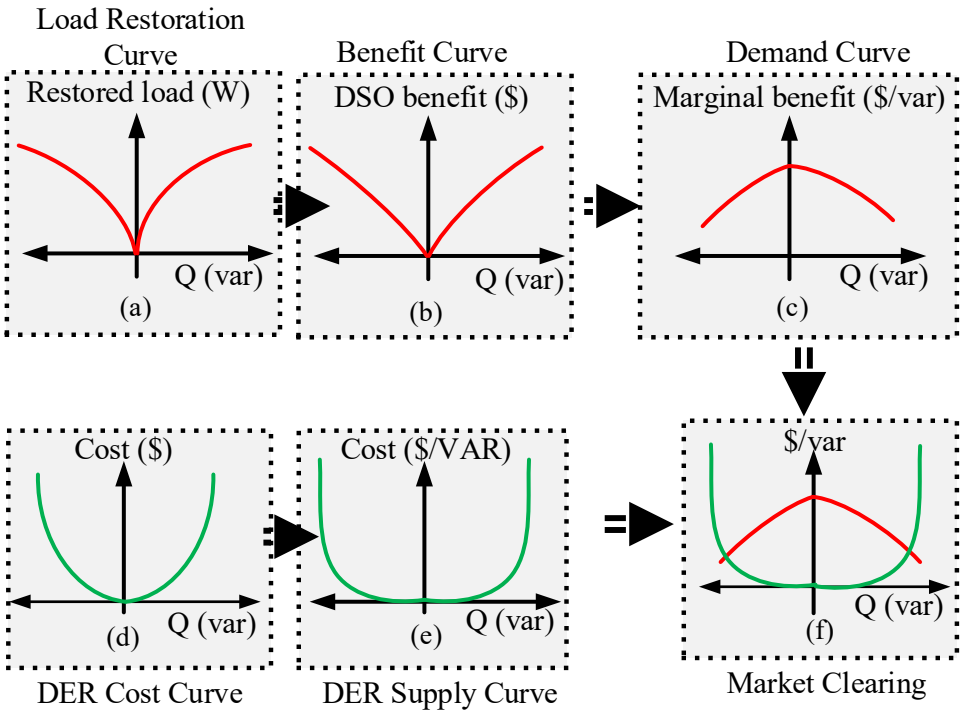

Figure 9.8: High-level transactive market mechanism for TEA-1.

9.3.1 TEA-1 Supply Curve Generation

Supply curve reflects the marginal cost of providing reactive power to the supplier. Therefore, each participating DER prepares its supply curve by reflecting its cost of providing reactive power. The cost may include combination of: 1) loss of revenue (LoR) due to active power curtailment requirement to provide the reactive power, 2) increased losses in the system to provide reactive power, and 3) wear-and-tear cost of the system to provide the additional reactive power, as discussed in Section 8.0. Since the LoR depends heavily on the DER operating points, the supply curve is also greatly influenced by the loading level of the DERs. For example, if the DER is operating at no load, the cost of providing reactive power is very small because there is no need to curtail active power. However, the cost of providing reactive power can be significant if the DER is operating at full load because a DER cannot provide reactive power without curtailing its active power. As presented in a recent technical work [32], the cost of providing reactive power is computed as follows:

$$C_{Curt}^{Q} = C_{RT} \cdot \left(\sqrt{S_{INV}^2 - Q_{INV}^2} - P_{INV}\right) - C_{RT} \cdot \left(\sqrt{S_{INV}^2 - (Q_{INV} + Q_{OFR})^2} - P_{INV}\right) \quad (9\text{-}1)$$

where, C_{Curt}^{Q} is the cost to DERs for providing reactive power, C_{RT} is the retail price of electricity, S_{INV} is the rated apparent power of the inverter, P_{INV} and Q_{INV} are the current operating points of the inverter, and Q_{OFR} is the offered reactive power from DER. Differentiating the reactive power cost with respect Q_{OFR} yields the marginal cost of providing reactive power, that is, the supply curve of the DER.

9.3.2 TEA-1 Demand Curve Generation

During resilience actions, the DSO would require the DERs' flexibility in order to make decisions on how to restore the loads and enable additional switching options. Therefore, DSO calculates a demand curve to reflect the marginal benefit it would get as a function of reactive power from the DERs. First, DSO

expresses the additional loads that can be restored as a function of reactive power from DERs, hereafter called load restoration curve (LRC). The LRC is computed iteratively by increasing the reactive power contribution from DERs in small steps and calculating the corresponding additional load that can be restored.

Utilities may include the targeted resiliency metrics to convert the LRC into the monetary benefit to the DSO. The metrics are chosen such that they properly value the additional restored load. In this study, the LRC is converted into a benefit curve by using a) LoR to DSO due to not being able to serve the loads, b) energy not served (ENS) cost to DSO, and c) demand not served (DNS) cost to DSO. LoR is used based on the assumption that DSO makes some profit from the difference between the wholesale electricity price where it purchases energy and the retail electricity price where it sells the electricity. Similarly, ENS and DNS are used based on the assumption that DSO may need to pay some penalties for not serving loads to certain critical customers. The DSO benefit curve is calculated as follows:

$$B_{DSO} = \Delta P_L \cdot (\Delta T \cdot (C_{WL} - C_{RT}) + \Delta T \cdot C_{ENS} + C_{DNS}) \quad (9\text{-}2)$$

where B_{DSO} is the benefit to the DSO (\$), ΔP_L is the additional restored load (kW), ΔT is the outage duration (h), C_{WL} is the wholesale electricity price (\$/kWh), C_{RT} is the retail price of electricity (\$/kWh), C_{ENS} is the ENS cost (\$/kWh) to DSO, and C_{DNS} is the DNS cost (\$/kW) to DSO. The demand curve for the DSO is then computed from the DSO benefit curve by taking the first-order differentiation of the benefit curve with respect to the reactive power quantity offered by the DERs.

9.3.3 TEA-1 Market Resolution Process

The market collects supply curves from all participating customers and demand curves from DSO. First, all the supply curves from the participating customers are aggregated. A double auction market strategy (shown in Figure 9.8 (f)) is used to clear the demand curve from DSO and the aggregated supply curves from the participating DERs. The intersection between the aggregated supply curve and demand curve maximizes social welfare and gives market clearing. It is worth mentioning that the market-clearing process provides the cleared quantity and prices.

While DSO is interested in the cleared price and quantity, they are more concerned about the overall load that can be restored as a result of the transactive engagement of the DERs. Therefore, the cleared reactive power needs to be mapped on LRC to compute additional load that can be restored. After computing the additional load that can be restored for the cleared reactive power, the algorithm checks whether additional switching is possible for the predefined switching sequence. Moreover, the switch for a given distribution segment can only be closed if the load that can be restored from reactive power is greater than the total load of that segment.

9.4 Transactive Energy Algorithm -2

TEA-2 incorporates network voltage sensitivity in the market process to provide voltage support to targeted weak points in distribution systems as well as to capture the locational value of spatially distributed DERs. For instance, utilities can use TEA-2 to close their “normally open” switches during service restoration that they would not normally be able to do due to larger voltage differences across the terminals. TEA-2 provides a transactive mechanism to engage DERs to reduce the voltage difference across those switching devices and enables the utilities to achieve more switching operations, and hence restores additional network segments and loads. One of the key novelties of TEA-2 is the incorporation of the network voltage sensitivity into the transactive process to capture the locational value of spatially distributed DERs. For instance, the DERs located closer to the weak point in the network may be more impactful than the DERs

located farther from the weak point for supporting voltage. The simulation results of TEA-2 in Use-Case #1-S3 are reported in Appendix B.

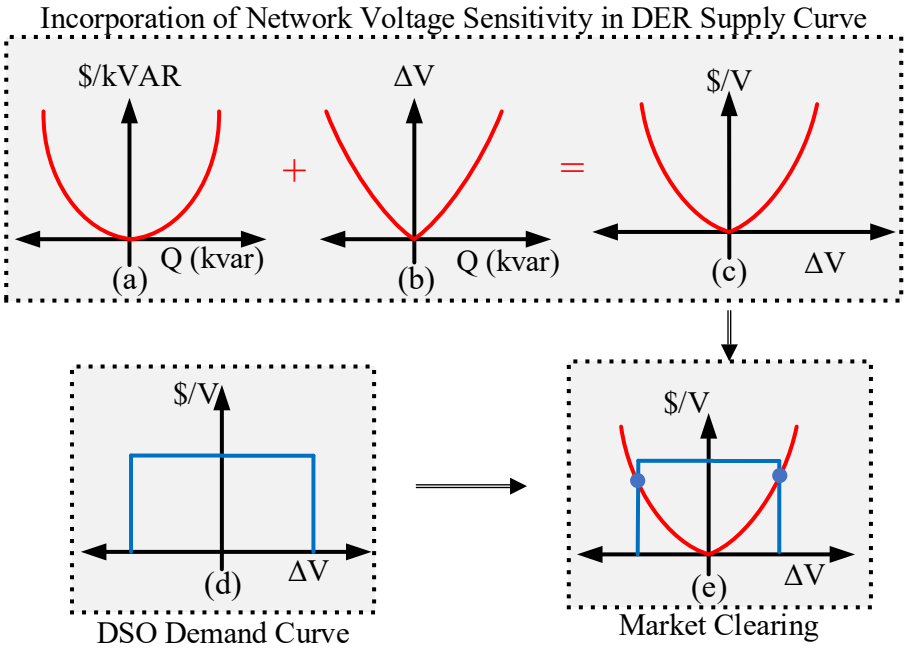

Figure 9.9: High-level market mechanism for TEA-2.

9.4.1 TEA-2 DER Supply Curve

The DER supply curve indicates the marginal cost of injecting and absorbing reactive power to the system. The process of constructing the supply curve is the same as the process described in TEA-1 (Section 9.3.1), except for one difference where the supply curve generated by the participating DERs are modified to integrate network voltage sensitivity. Since TEA-2 is applied to reduce the voltage difference across a switch, the DER supply curve should express how much voltage support is available at the given node. However, DER connected to a node usually does not have the system-level information therefore they cannot integrate the voltage sensitivity into their bid curve. Moreover, bus voltages can change with respect to the network topology and other operational conditions. Therefore, DERs cannot express their supply curves by incorporating the network voltage sensitivity. Consequently, DERs submit their marginal supply curves ($/kvar vs kvar) and DSO converts the marginal supply curves into ($ vs V) using the voltage sensitivity at the node, to which these DERs are connected. Details of the calculation are shown as follows:

$$C_{INV}^{Q} = C_{RT} \times \left(\sqrt{S_{INV}^2 - Q_{INV}^2} - \sqrt{S_{INV}^2 - (Q_{INV} + Q_{OFR})^2}\right) \tag{9-3}$$

$$A_{INV}^{Q} = C_{INV}^{Q} \times \Delta t,\ B_{INV}^{Q} = A_{INV}^{Q}/Q_{OFR},\ D_{INV}^{Q} = A_{INV}^{Q}/|\Delta v_n| \tag{9-4}$$

where C_{INV}^{Q} is the cost to the DER owner for producing Q_{OFR} in unit $/h. Q_{INV} is zero for all inverters. Q_{OFR} is the offered reactive power from this inverter. S_{INV} is the rated apparent power of the inverter. A_{INV}^{Q} is the cost in dollars and Δt is the operation duration in hours. B_{INV}^{Q} is the cost in unit $/var. D_{INV}^{Q} is the cost in $/V, $|\Delta v_n|$ is the voltage magnitude changes at node n by solving power flow with respect to the Q_{OFR}.

9.4.2 TEA-2 Demand Curve

The demand curve is designed to reflect the need of the DSO. As the application of TEA-2 is to reduce the voltage difference across a switch, the demand curve represents the voltage magnitude of a selected node which the DSO intends to increase or decrease. Whenever there is a need to close a switching device, of which the voltage difference is higher than the acceptable level, DSO prepares its demand curve to express how much voltage it needs to increase or decrease so as to be able to close the switch. In IEEE Std C50.13-2014, the synchronizing limit of the generator side voltage difference is provided. For distribution systems and microgrids, the tolerance and settings may vary among different utilities. In this study, 2% is selected for a strict limit. One of the two nodes connected via the switch is selected as the targeted point where the utility needs to increase or decrease the voltage.

Since the need of the DSO is simply expressed in terms of the amount of voltage required to be increased or decreased at the targeted node in the system, the demand curve is a straight line as shown in Figure 9.9 (d), the demand curve can be used either to increase the voltage or decrease the voltage at given nodes. The horizontal lines on both positive and negative sides in the demand curve Figure 9.9 (d) represent the price-cap, the maximum price DSO is willing to pay.

9.4.3 TEA-2 Market Clearing Process

The market-clearing process includes two parts. First, the intersection point of the demand and the aggregated supply curve is identified. It is shown in Figure 9.9 (e). The blue point (labeled as “A”) represents the intersection point. This part is similar to the market-clearing process of TEA-1. That is, a double auction market is used. When a buyer’s price and a seller’s asking price match, the trade proceeds at that price. Auction markets do not involve direct negotiations between individual buyers and sellers. The second part of the process is depicted using the green dashed arrow lines and blue points. In Figure 9.9 (e), the point “B” that indicates the price in $\$/V$ can be determined using the point “A”. As a result, the ΔV of each DER can be determined using point “B” and the supply curve of that DER. See Figure 9.9 (c). With the ΔV needed from each DER, the reactive power amount (marked as point “F”) of the DER can be determined. See Figure 9.9 (b). In addition, the $/kvar price of the DER can be determined, which is marked as point “H” in Figure 9.9 (a). This price may vary among DERs, as the network voltage sensitivity is considered with respect to the DER locations.

10.0 Power and Communications Co-Simulation

In order to evaluate the performance of the transactive energy system presented in Section 9.0, it is necessary to simulate the full scale system with large numbers of transactive agents. To study the performance of the TEA-1 methods presented in Section 9.0, the use-cases are examined in a co-simulation of the power system model with the utility control running the transactive algorithm and a communication network to carry the control signals to the electric switches such as reclosers. For the co-simulations, the Hierarchical Engine for Large-scale Infrastructure Co-Simulation (HELICS) is used [90].

10.1 Co-Simulation Framework

A HELICS-based co-simulation framework has been employed to federate the distribution system simulation in GridLAB-D [8] a representative DMS, and transactive algorithms in a Python emulator operated by the DO, and the communication system in ns-3. Figure 10.1 graphically depicts the interaction between the involved federates realizing each scenario. HELICS allows the time synchronization between the simulators. HELICS also enables the network reconfiguration signals to be transferred through an appropriately-modeled long-term evolution (LTE) communication infrastructure between the DMS federates, with the network communications simulated in ns-3.

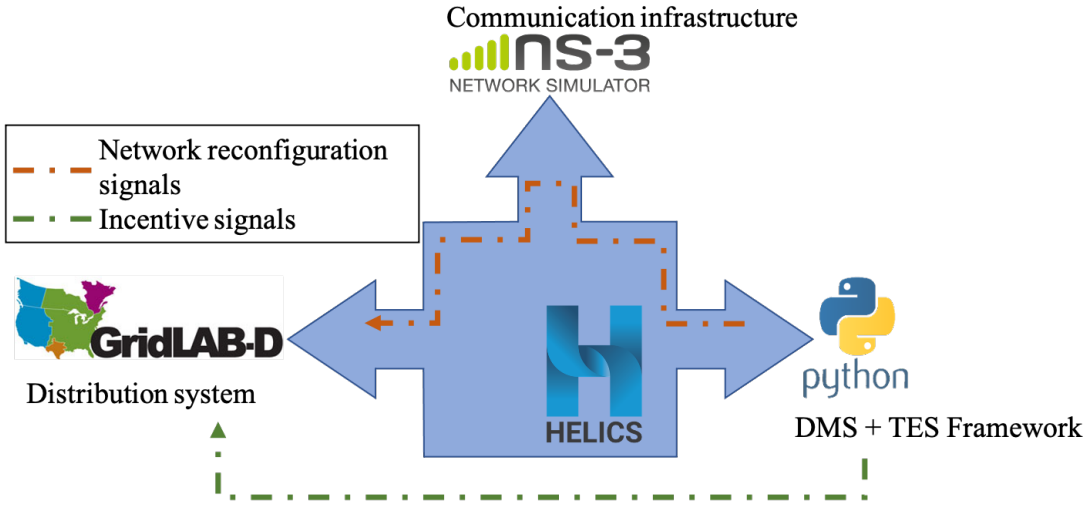

Figure 10.1: Co-simulation framework.

The DMS decision making procedure on switching control has not been modeled explicitly in this study, but rather the pre-defined reconfiguration path has been integrated as a separate function in the transactive algorithm federate. These switching control actions are sent sequentially through the ns-3 modeled communication network from the DMS to the corresponding node location of the recloser.

The incentive signals calculated by TEA-1 as the amount of the reactive power injected in the system by the PV resources are transferred through HELICS to the corresponding inverter-based resource in the power system.

10.2 Co-Simulation Results

This subsection presents the co-simulation results of the S1 and S3 (with TEA-1) of each use-case.

10.2.1 Co-simulation Results for Use-Case #1-S1

As detailed in Section 6.1.1, under Blue-sky conditions the systems operate normally with all controllers active and a slight chance of uncorrelated faults occurrence and/or scheduled maintenance activities. Scenario 1 assumes that only the self-healing system is operational and no manual field maneuvers are performed. The system is "pre-conditioned" prior to an event to automatically reconfigure and adjust into a more resilient configuration able to overcome a possible incident, such as a major storm. The DO executes a series of switching operations on the system configuration in Figure 3.1 to specifically move two segments such that the load is transferred between feeders. The final configuration of the system is presented in Figure 6.1.

As the DO executes the switching plan, the effects of generation taking over serving extra loads can be observed at the level of segments voltages. Plots in Figure 10.2 through Figure 10.6 show how the voltage level changes for each segment of the system as the sequential reconfiguration steps are performed. Starting with the system in Figure 3.1 exhibiting normal voltage levels, the DO closes RCL-11 to parallel circuits F-3 and F-4. That affects the levels of voltages in segments S-8, S-9, and S-10, as observed in Figure 10.3. The next step of the switching plan is to open RCL-10 to move segment S-9 from F-3 to F-4, which leads to the increased voltage levels in S-9 and S-10 in Figure 10.4. Paralleling circuits F-2 and F-3 by closing RCL-9 helps with better voltage stability as seen in Figure 10.5. However, once RCL-5 is switched open to complete the required recloser reconfiguration as part of the self-healing process, the system exhibits under-voltage problems in segment S-8, according to the ANSI C84.1 Range standard for voltage tolerance (between 0.95 and 1.05 p.u.), as seen in Figure 10.6.

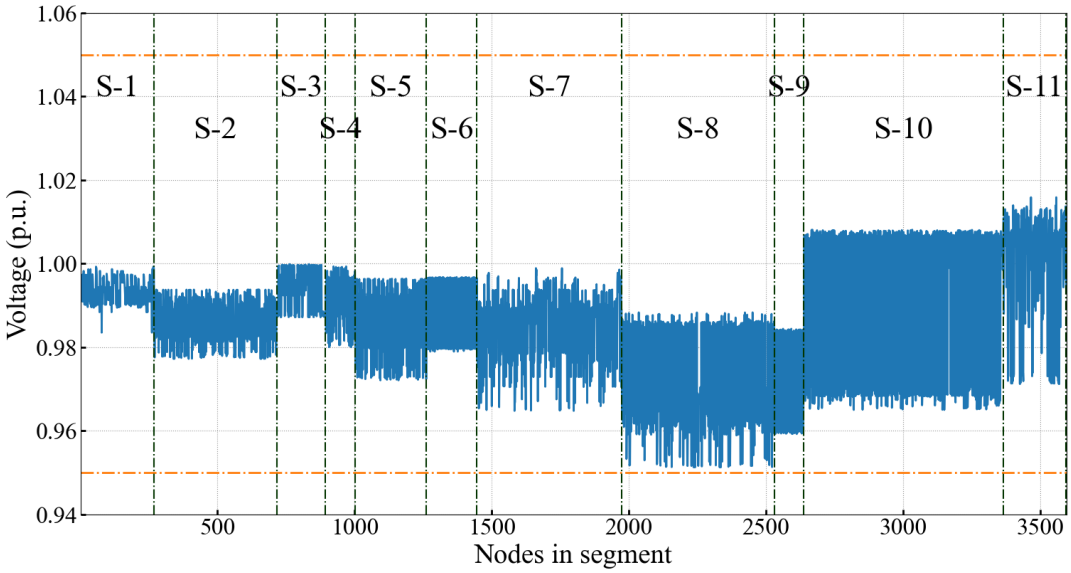

Figure 10.2: Use-Case #1-S1 – initial voltage magnitudes.

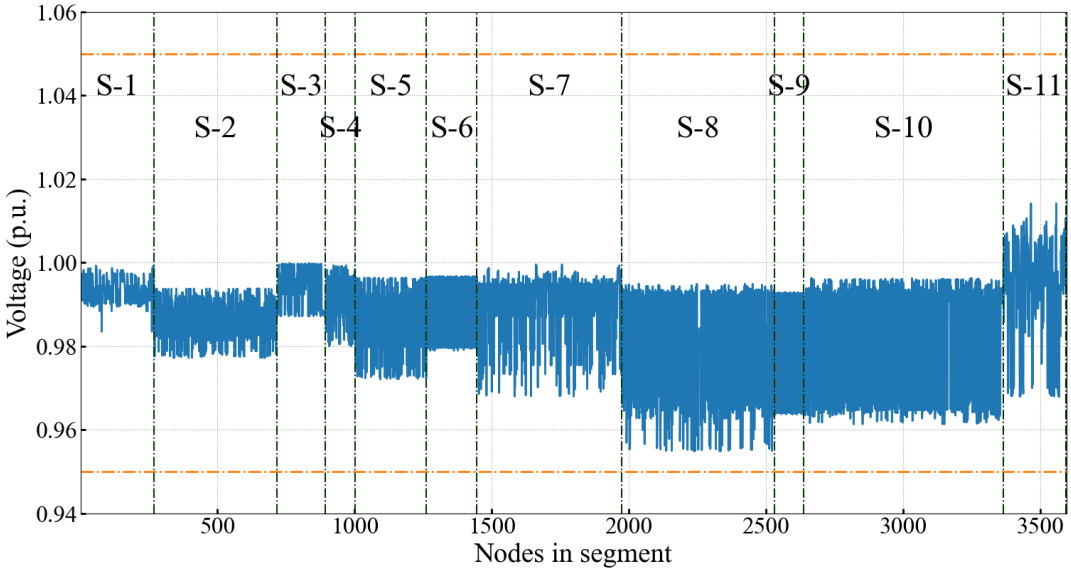

Figure 10.3: Use-Case #1-S1 – voltage magnitudes after closing RCL-11.

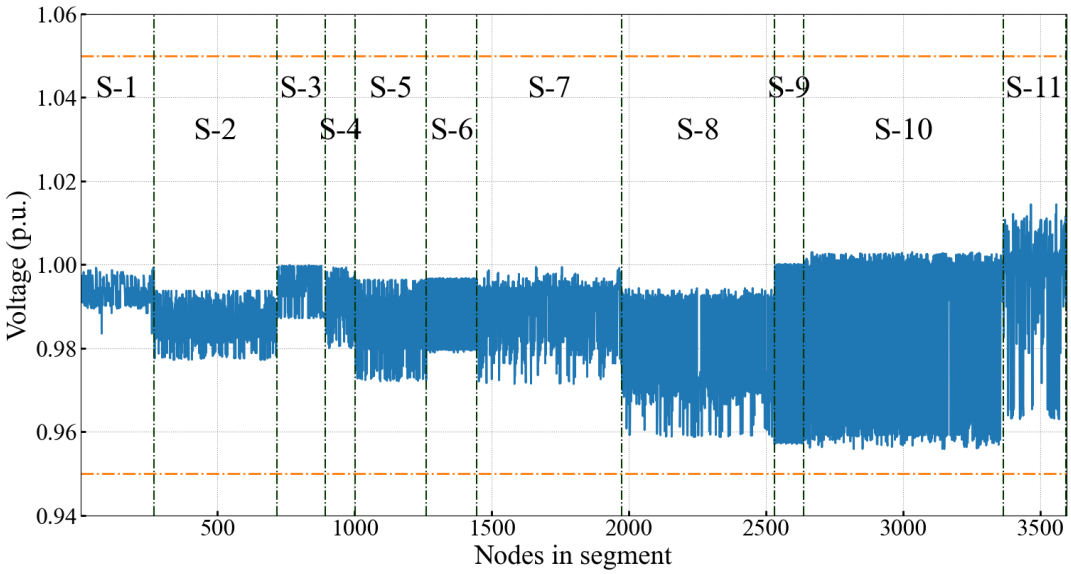

Figure 10.4: Use-Case #1-S1 – voltage magnitudes after opening RCL-10.

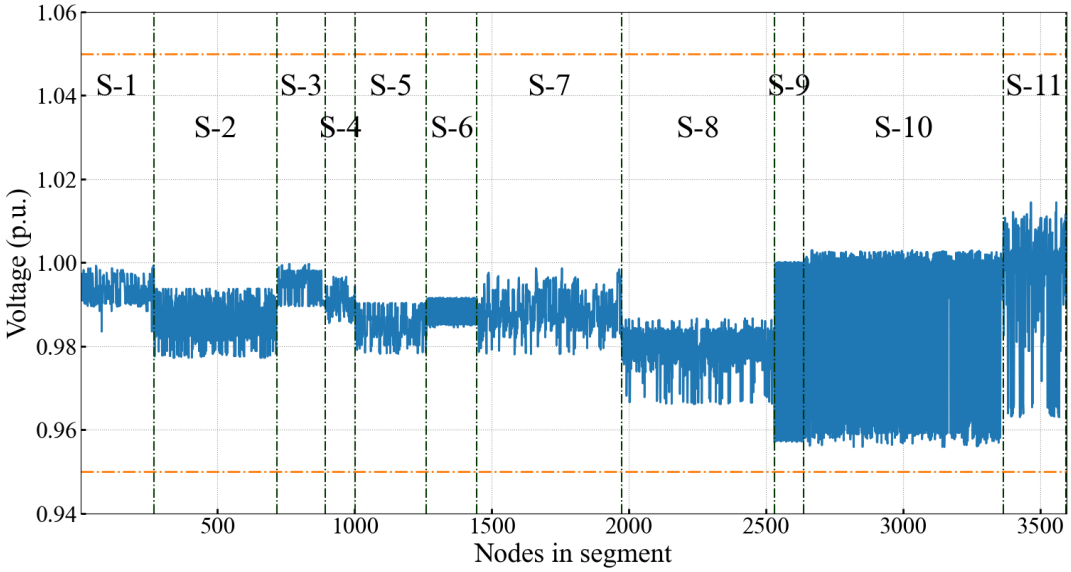

Figure 10.5: Use-Case #1-S1 – voltage magnitudes after closing RCL-9.

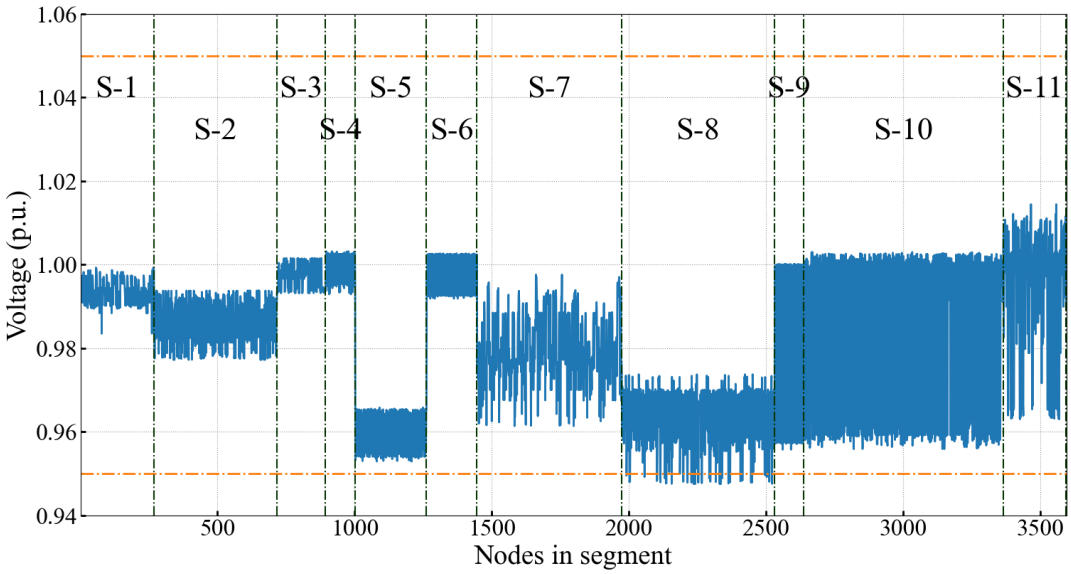

Figure 10.6: Use-Case #1-S1 – voltage magnitudes after opening RCL-5.

10.2.2 Co-simulation Results Use-Case #1-S3 using TEA-1

TEA-1 supports the load transfer and switch reconfiguration increasing system resiliency by engaging customer-owned DERs to provide their reactive power. Specifically, in this scenario, the TEA-1 will engage the PV assets shown in the system configuration in Figure 10.7 to inject reactive power in the system to regulate the voltage magnitude across the segments affected by under-voltage events.

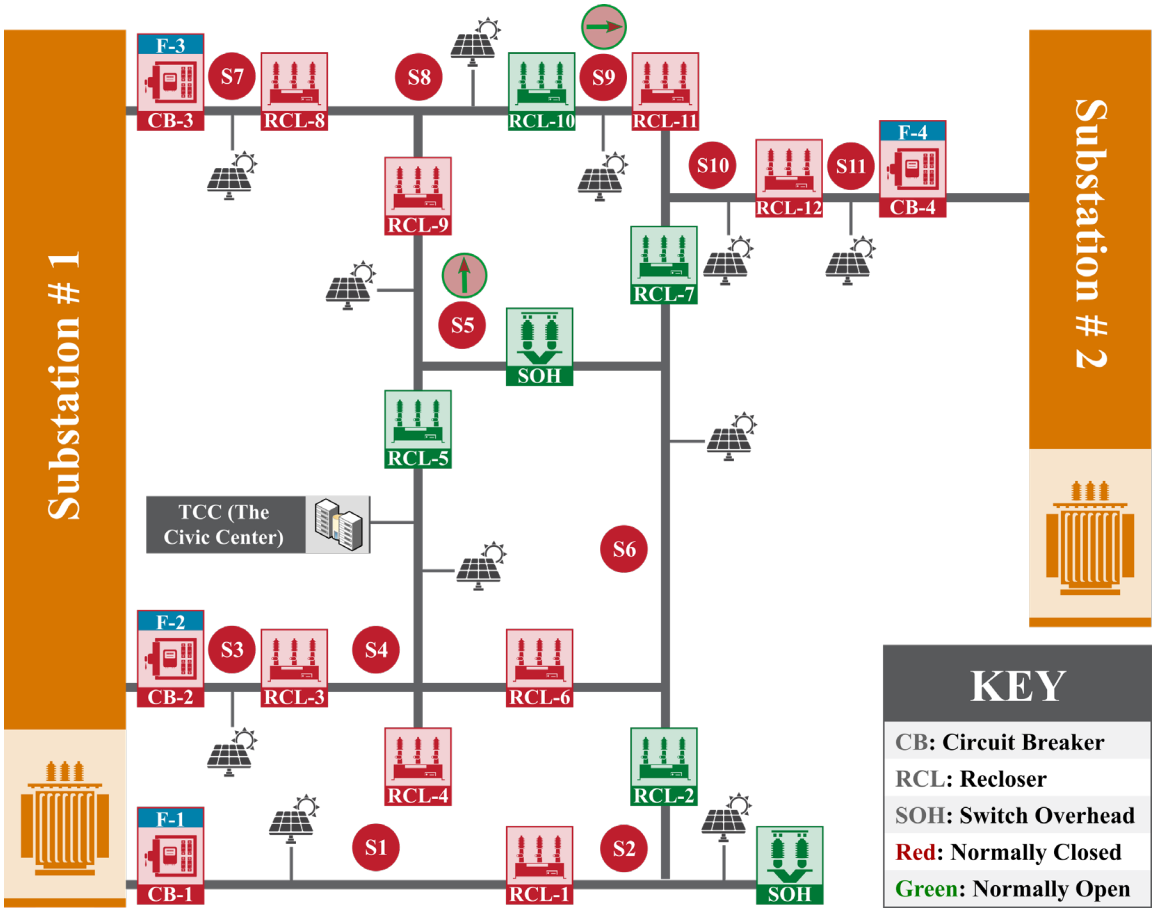

Figure 10.7: Use-Case #1-S3 – final configuration.

Following the steps in Section 9.3, the double auction market clears based on the demand curve from DO and the aggregated supply curves from DERs, as shown in Figure 10.8. For Use-Case #1-S3, the market clears 967 kvar at 1.95 ¢/kvar, as detailed in the bottom plot of Figure 10.8. Subsequently, LRC calculates the additional 619 kW load that can now be transferred when RCL-5 is open. This new load represents approximately 15% of the total load that is being transferred between serving distribution circuits within the system, that is the 4,128 kW shown in Figure 10.9.

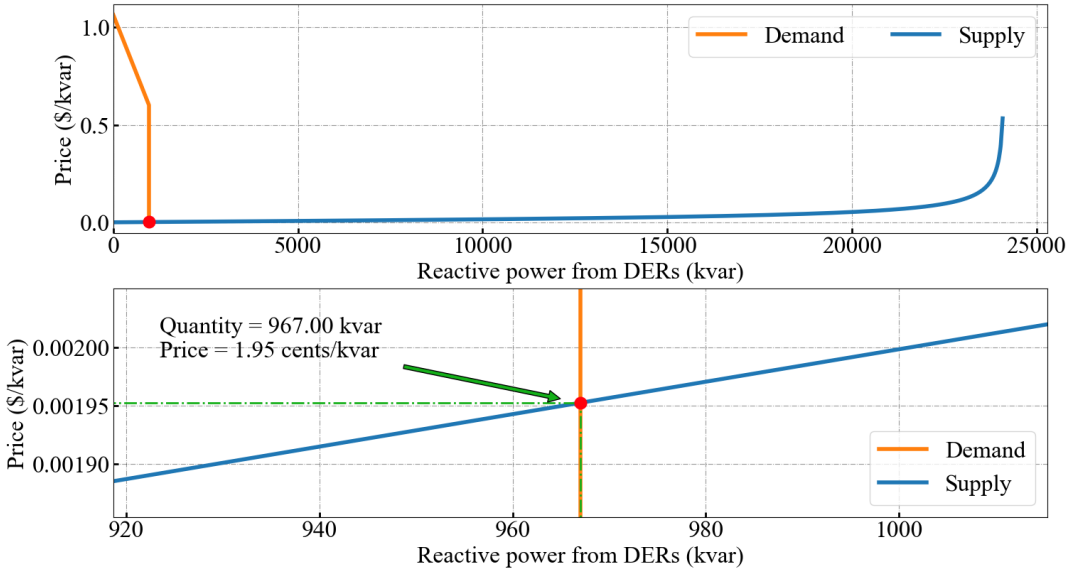

Figure 10.8: Use-Case #1-S3 – market clearing.

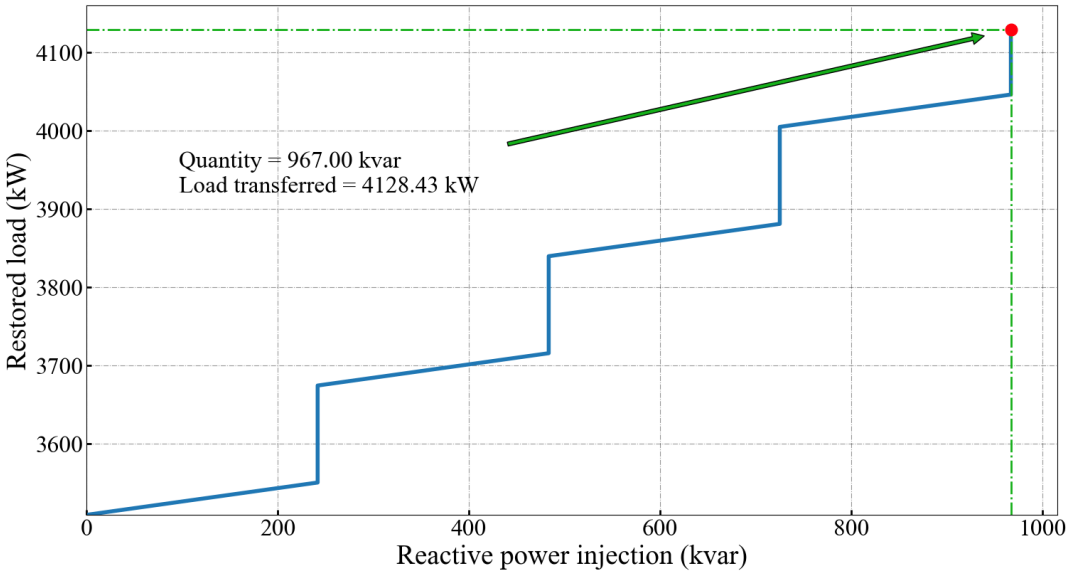

Figure 10.9: Use-Case #1-S3 – additional load transferred.

As a consequence of transferring the extra load to be serviced by F-3, opening RCL-5 could safely be performed for reconfiguration purposes, without causing the self-healing system to experience the under-voltage events in Figure 10.6, but rather stay within the required limits, as seen in Figure 10.10.

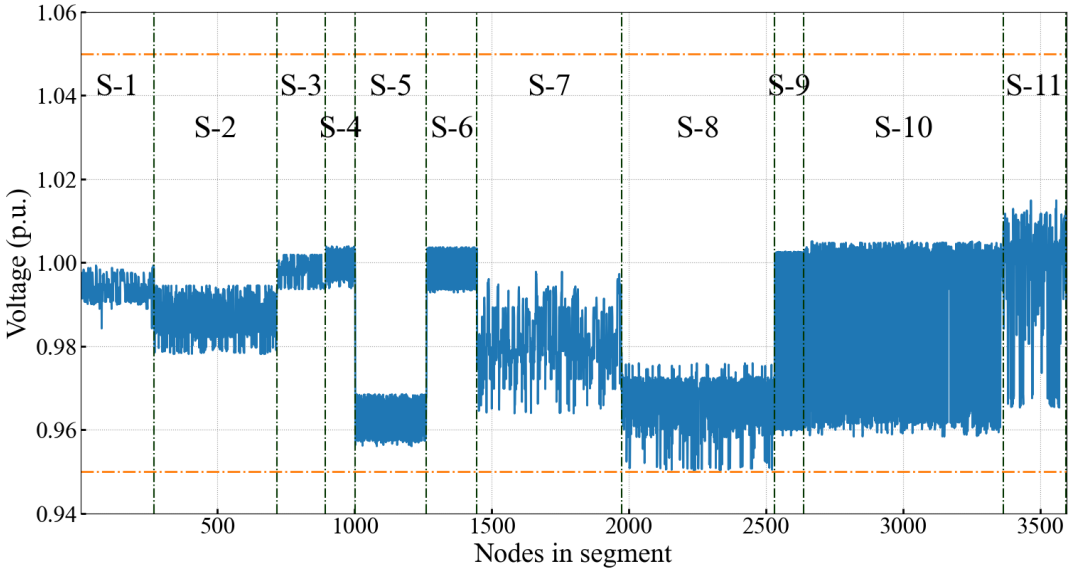

Figure 10.10: Use-Case #1-S3 – voltage magnitudes when TEA-1 is employed.

10.2.3 Co-simulation Results Use-Case #2-S1

The details of this use case scenario are shown in Section 6.2.1. The self-healing system determines and executes the switching plan to reenergize the impacted segments in the system. However, only 3,260 kW of the load can be served without under-voltage problems. If the switching operations are continued according to the self-healing plan, some segments will experience under-voltage problems, as shown in the sequential stages in Figure 10.11 through Figure 10.13.

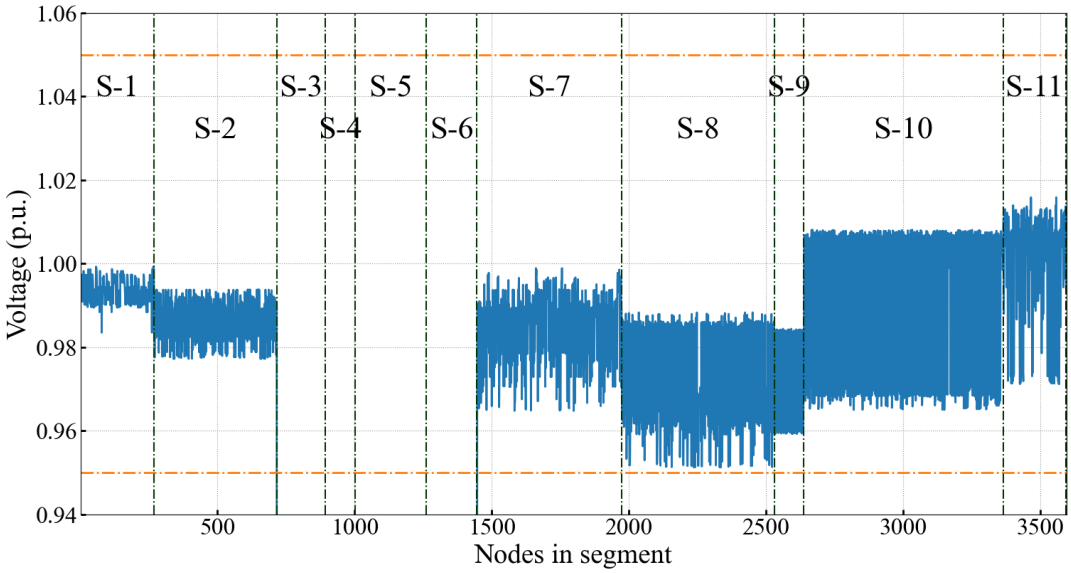

Figure 10.11: Use-Case #2-S1 – voltage magnitudes after opening RCL-3 and RCL-6.

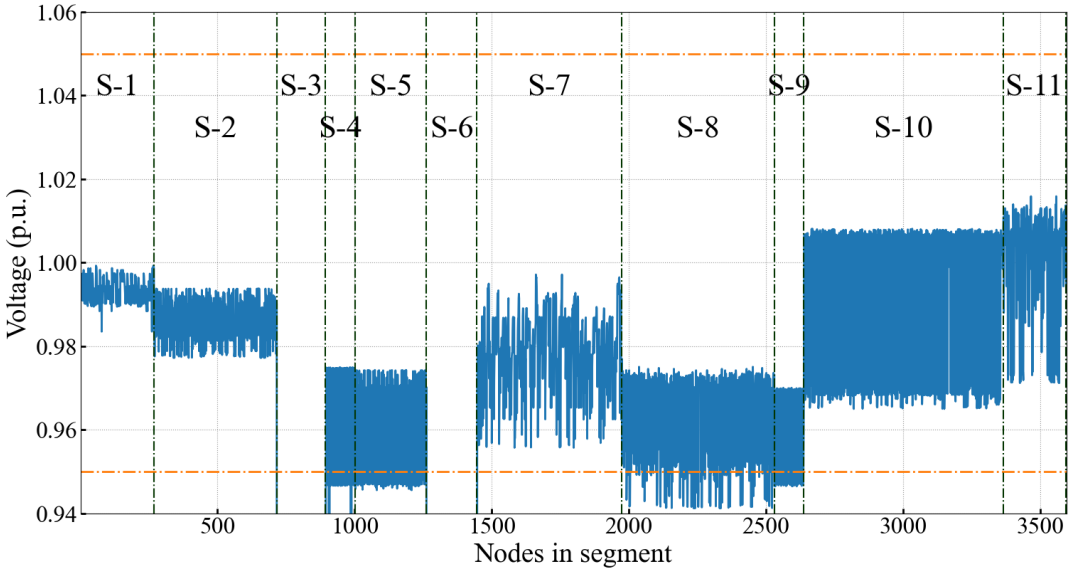

Figure 10.12: Use-Case #2-S1 – voltage magnitudes after closing RCL-9.

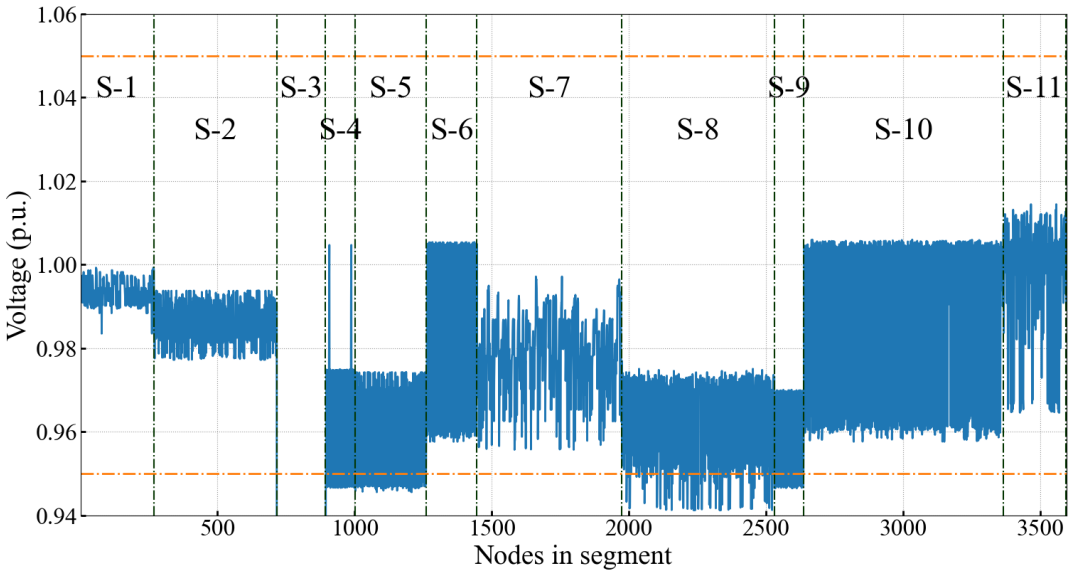

Figure 10.13: Use-Case #2-S1 – voltage magnitudes after closing RCL-7.

10.2.4 Co-simulation Results Use-Case #2-S3 using TEA-1

Similar to the steps in Section 10.2.2, the TEA-1 algorithm engages the PVs in the system to inject reactive power for voltage control. Thus, as shown in Figure 10.14, the market clears 1,934 kvar at 3.29 ¢/kvar.

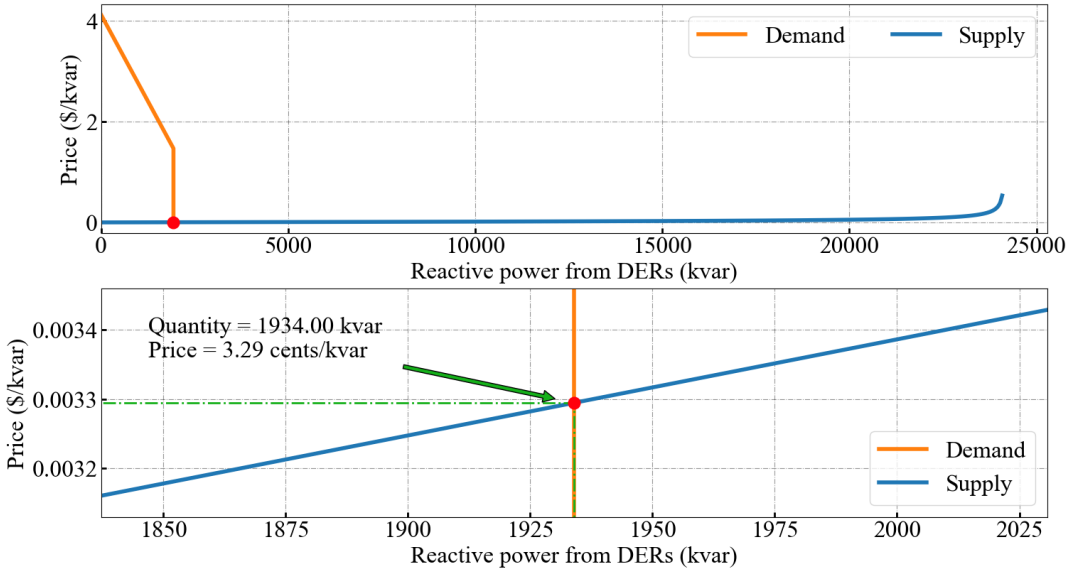

Figure 10.14: Use-Case #2-S3 – market clearing.

LRC maps the 1,934 kvar of injected reactive power into 5,176 kW of total load restored (Figure 10.15), that is adding extra 1,915 kW (~37%) to be restored while the entire switching sequence is performed without under-voltage events (Figure 10.16).

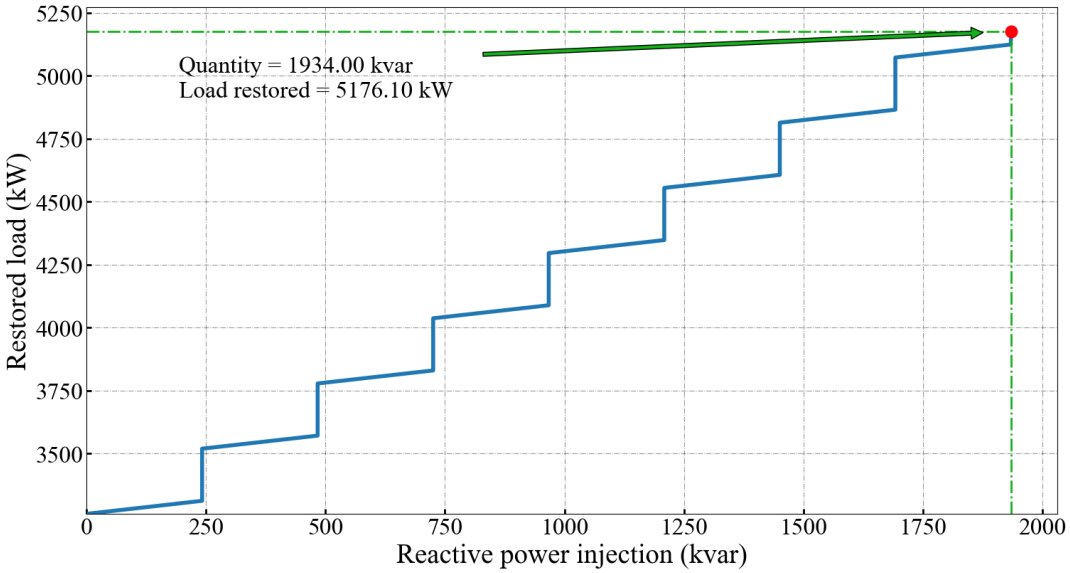

Figure 10.15: Use-Case #2-S3 – additional load restored.

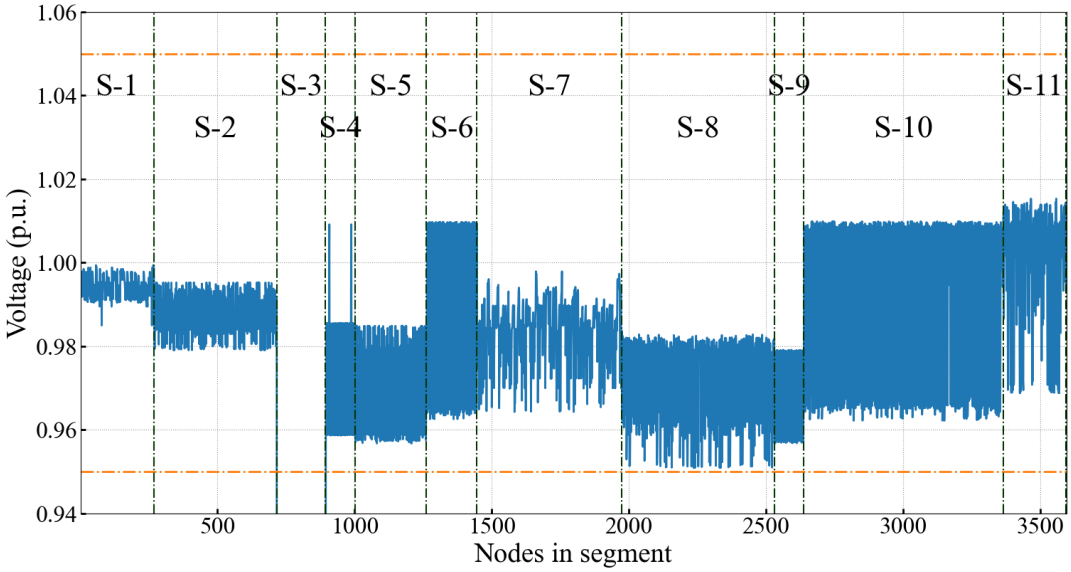

Figure 10.16: Use-Case #2-S3 – voltage magnitudes when TEA-1 is employed.

10.2.5 Co-simulation Results Use-Case #3-S1

In this use case scenario, as detailed in Section 6.3.1, segments lose power due to the two line-to-ground faults. While the self-healing system tries to reenergize the other segments, only 2,199 kW of load can be served without segment under-voltages (see Figure 10.17 through Figure 10.20).

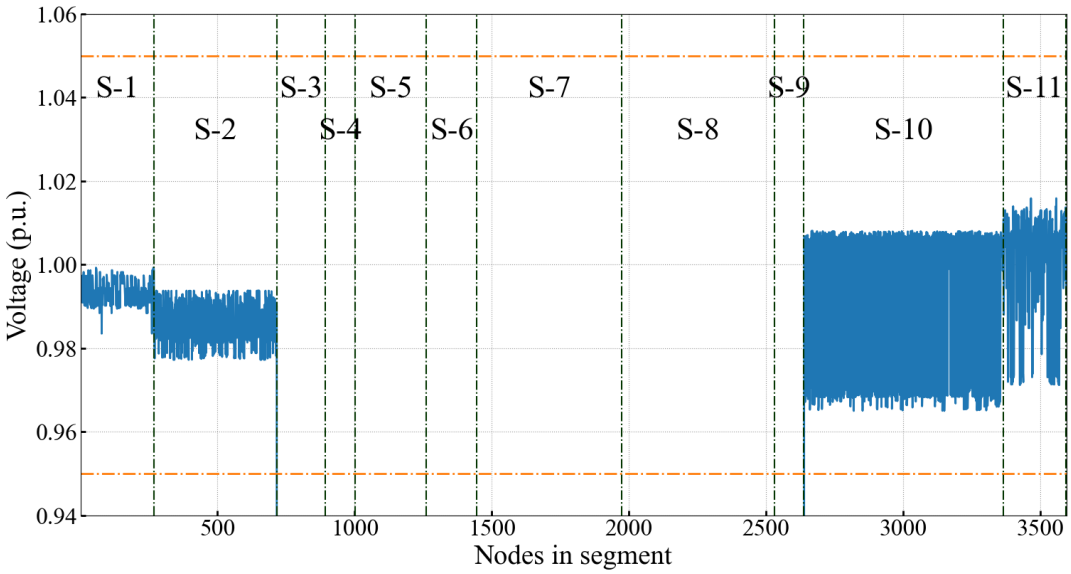

Figure 10.17: Use-Case #3-S1 – voltage magnitudes after opening RCL-3 and RCL-5.

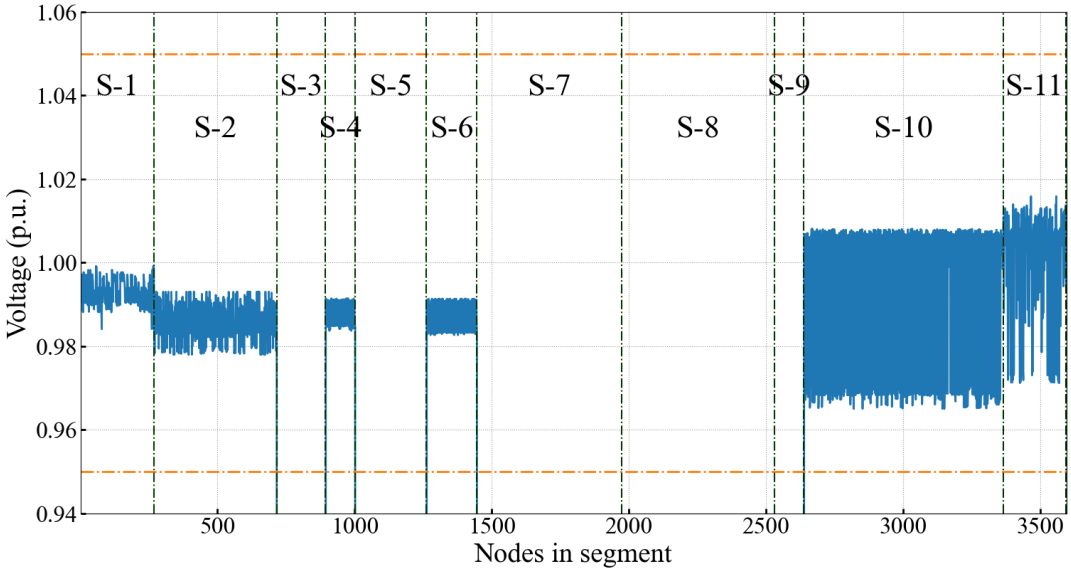

Figure 10.18: Use-Case #3-S1 – voltage magnitudes after closing RCL-2 and opening RCL-8.

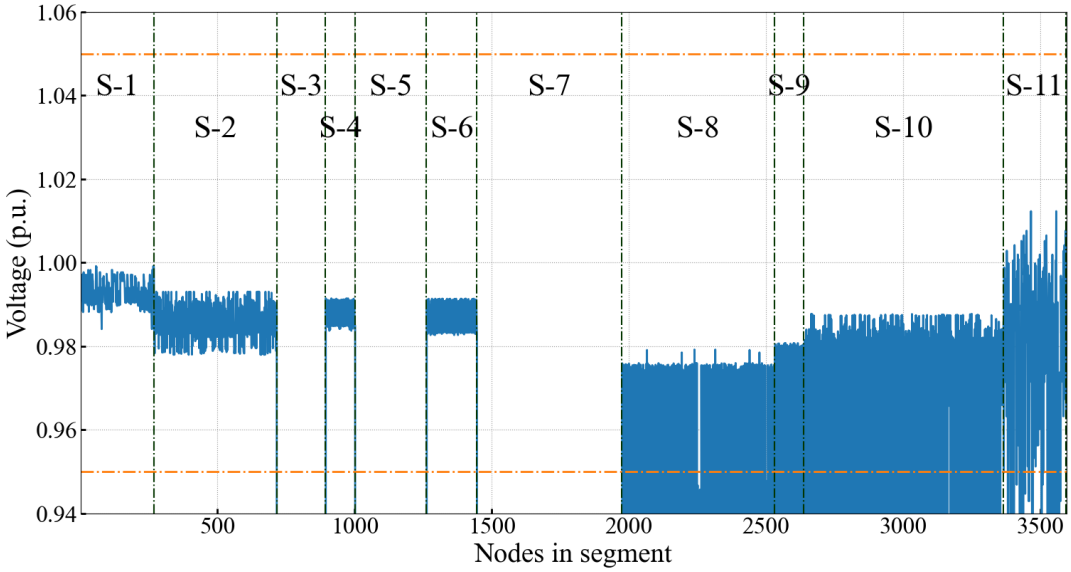

Figure 10.19: Use-Case #3-S1 – voltage magnitudes after closing RCL-11.

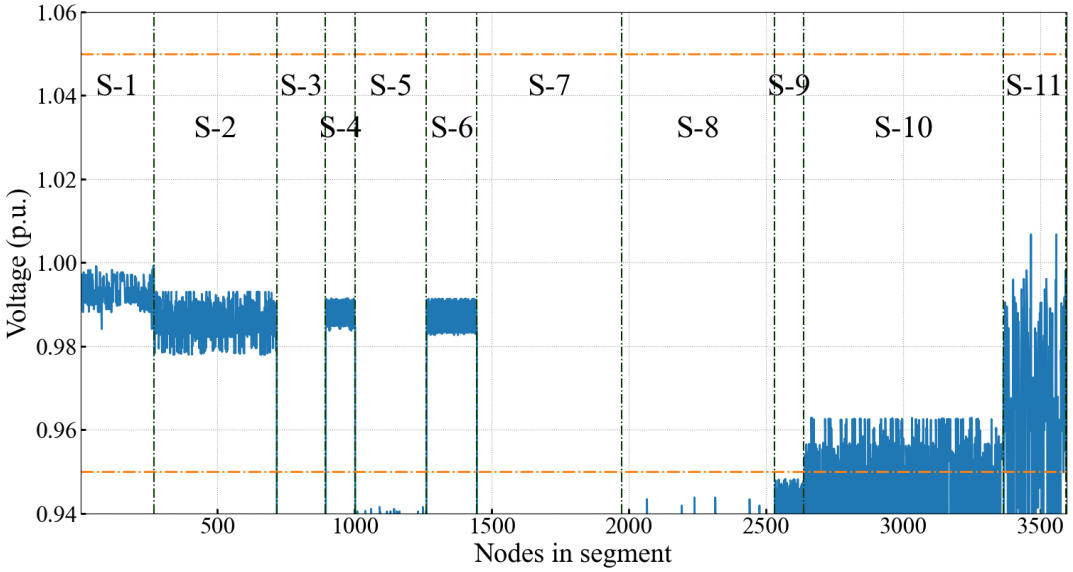

Figure 10.20: Use-Case #3-S1 – voltage magnitudes after closing RCL-9.

10.2.6 Co-simulation Results Use-Case #3-S3 using TEA-1

In this scenario, TEA-1 results in Figure 10.21 show that 15,713 kvar were cleared for 30.23 ¢/kvar. Mapped on the LRC in Figure 10.22, the reactive power injection allows for the restoration of a total 10,473 kW, while following the self-healing switching sequence. That means restoring an additional 8,273 kW (~79%) while ensuring voltages are kept within the limits (Figure 10.23).

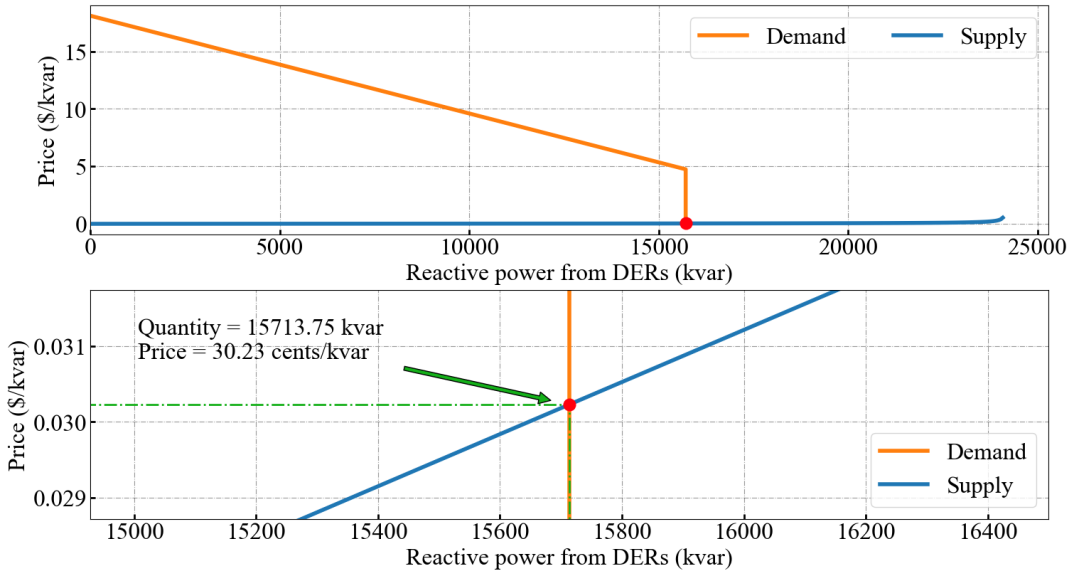

Figure 10.21: Use-Case #3-S3 – market clearing.

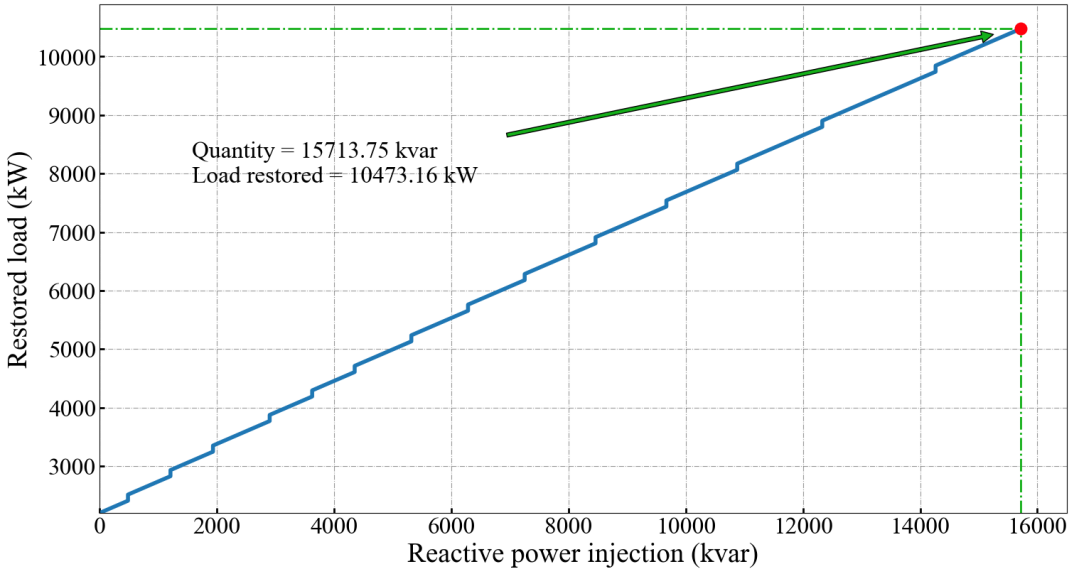

Figure 10.22: Use-Case #3-S3 – additional load restored.

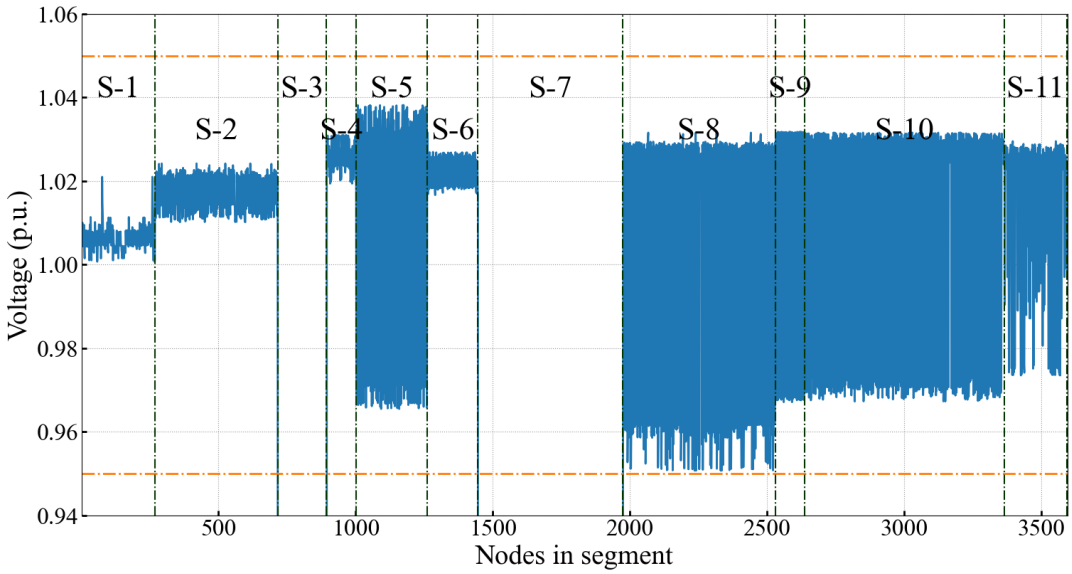

Figure 10.23: Use-Case #3-S3 – voltage magnitudes when TEA-1 is employed.

10.2.7 Co-simulation Results Use-Case #4-S1

This use case scenario is detailed in Section 6.4.1. With segments #3, #4, #5, #, #10, and #11 losing power because of the two line-to-ground faults on segments #3 and #10, the self-healing system decides a series of recloser switching. As seen in Figure 10.24 through Figure 10.26, the self-healing system would not be able to restore the entire load without causing under-voltage problems in some segments. Only 2,950 kW could be safely restored, before another switching would lead to voltage stability problems.

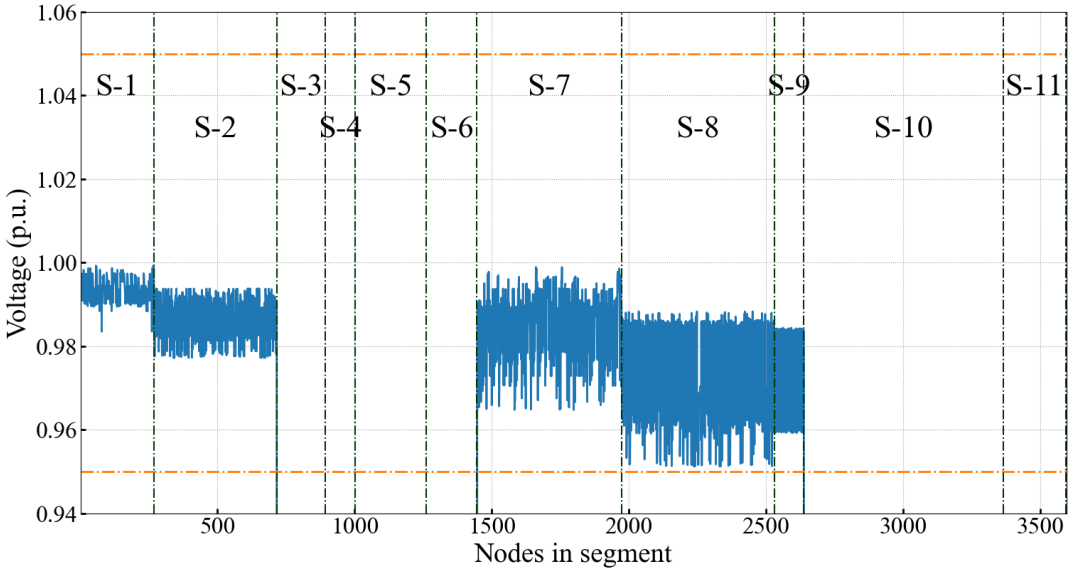

Figure 10.24: Use-Case #4-S1 – voltage magnitudes after opening RCL-3 and RCL-6.

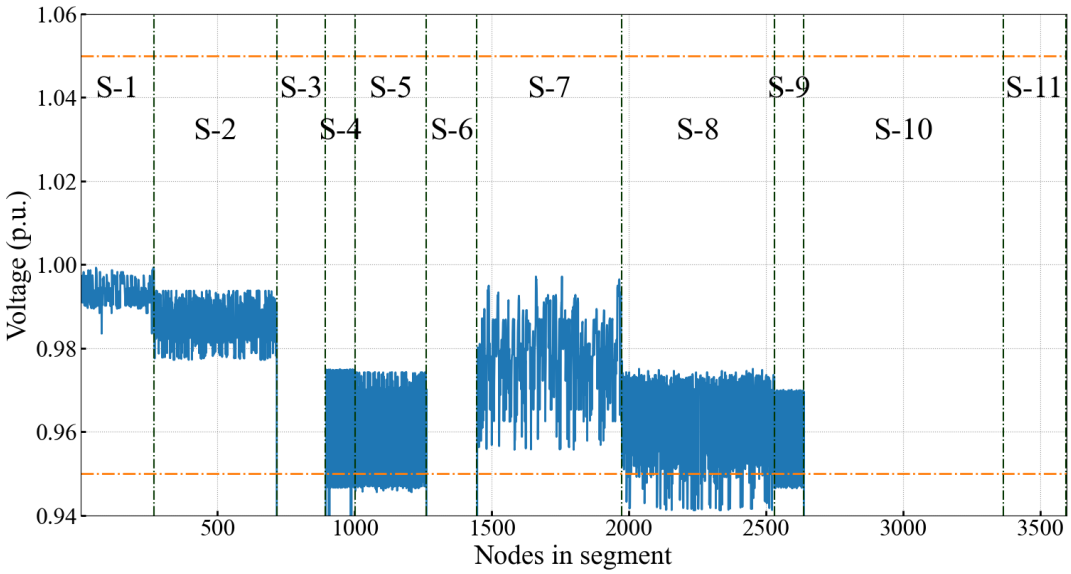

Figure 10.25: Use-Case #4-S1 – voltage magnitudes after closing RCL-9.

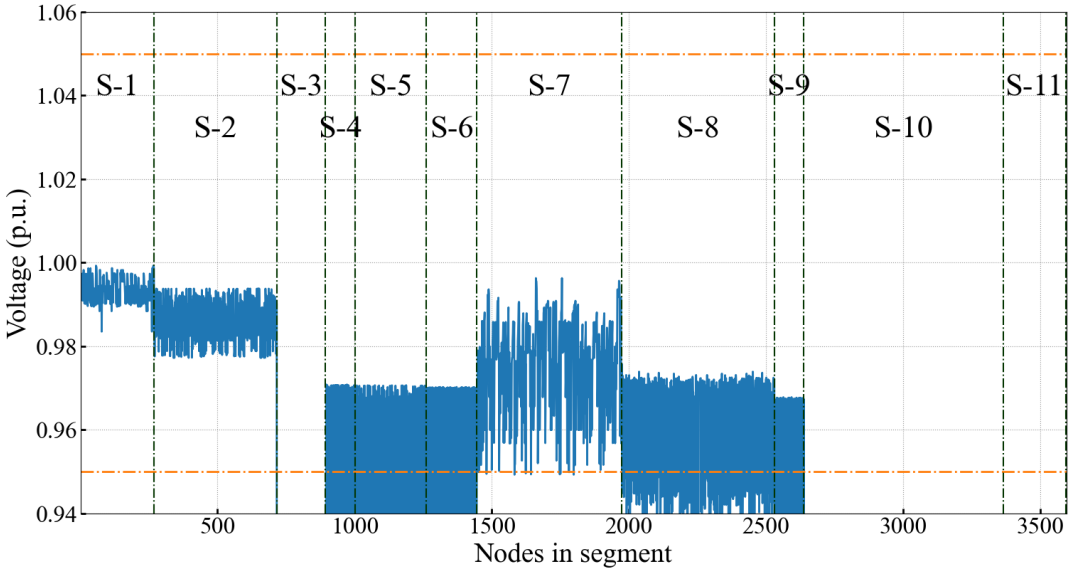

Figure 10.26: Use-Case #4-S1 – voltage magnitudes after closing RCL-6.

10.2.8 Co-simulation Results Use-Case #4-S3 using TEA-1

TEA-1 engages the PV resources to inject a total of 2,659 kvar at 4.20 ¢/kvar into the system (Figure 10.27). According to the LRC in Figure 10.28, this allows for an extra 2,225 kW of load to be restored, for a total of 5,176 kW, while ensuring voltage stability for all serviced segments as shown in Figure 10.29.

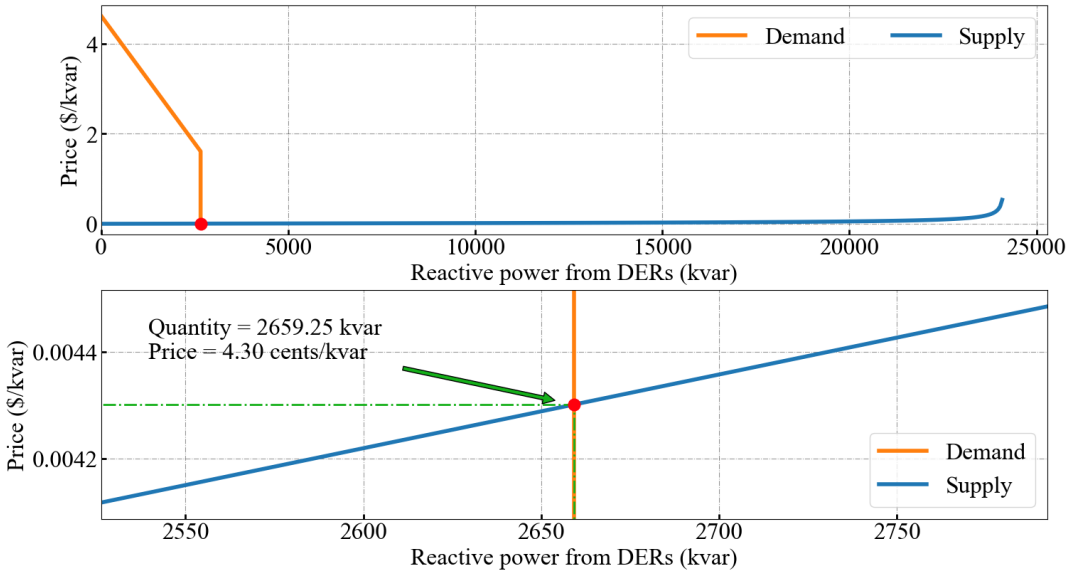

Figure 10.27: Use-Case #4-S3 – market clearing.

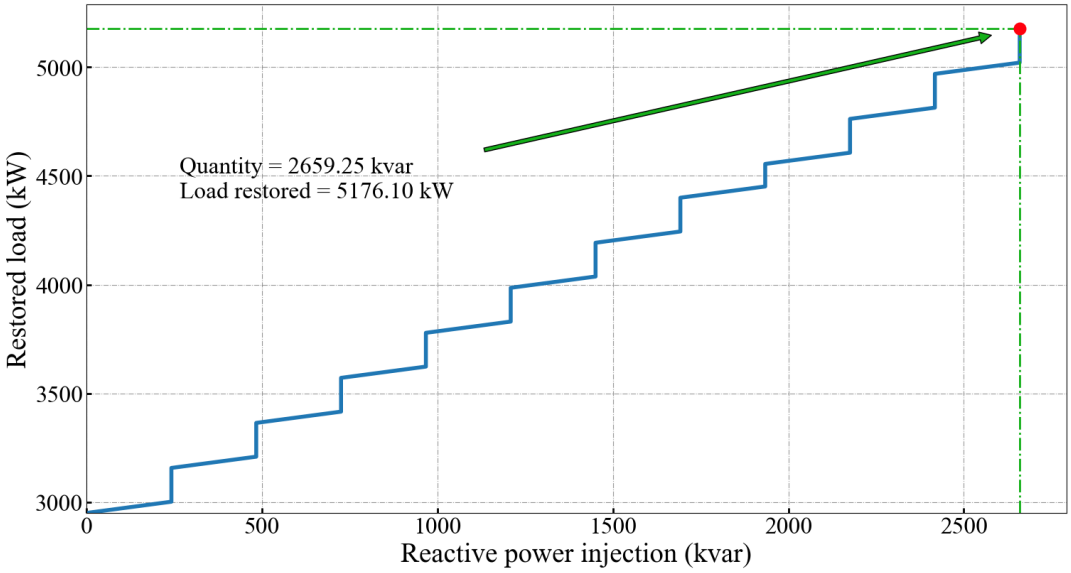

Figure 10.28: Use-Case #4-S3 – additional load restored.

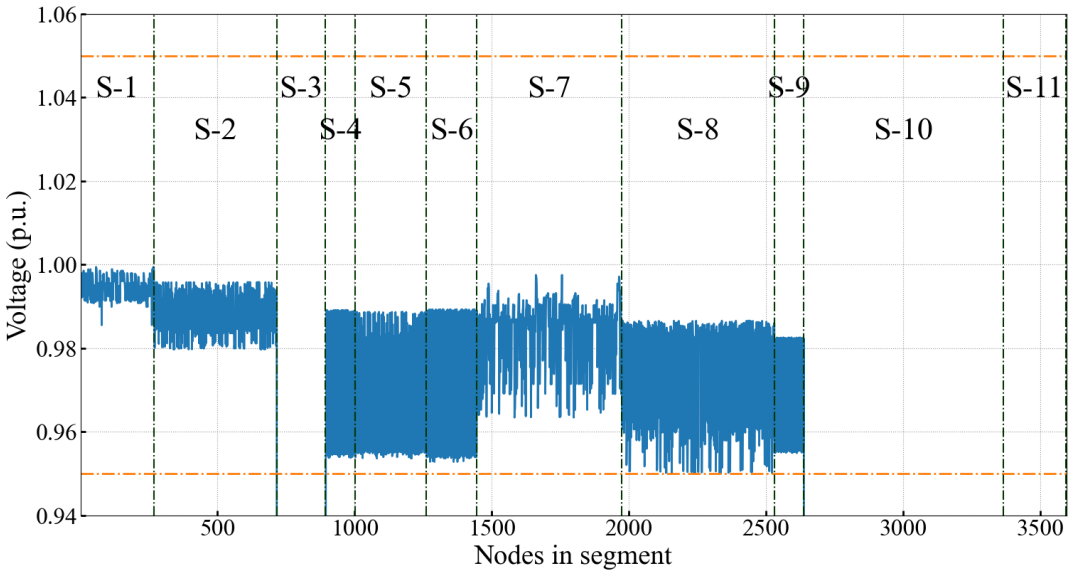

Figure 10.29: Use-Case #4-S3 – voltage magnitudes when TEA-1 is employed.

11.0 Controller Hardware in the Loop

In Section 10.0, the co-simulation of the transactive energy system examined the system level operation of a large number of devices. However, the co-simulation is conducted in a purely simulation environment. HIL simulations have an increased level of resolution and can provide a higher level of simulation accuracy. However, due to hardware constraints it is not always practical to model systems in full detail. For this reason, the project coordinated the co-simulations and HIL simulations to obtain the benefits of scale and accuracy. This section presents approaches for evaluating the ADMS application. A test case is included with HIL setups. The model development of distribution feeders and DERs is reported.

11.1 Approaches to Evaluate ADMS Applications

Different management systems under ADMS are emerging as a single integrated platform that supports grid optimization and management. Evaluation of these ADMS platforms before deployment is a critical step for utilities to investigate the applications for the intended operational objectives. Evaluation steps will de-risk the installation investment and other associated costs. Typically, ADMS evaluation needs models that reflect field settings effectively. ADMS test beds usually consist of software simulation and hardware elements that can create a distribution system and interface with ADMS SCADA using standard communication protocols. A block diagram of the ADMS machine with the different applications installed in the DMS and the model of the distribution system that can be simulated in the DMS tool is shown in Figure 11.1.

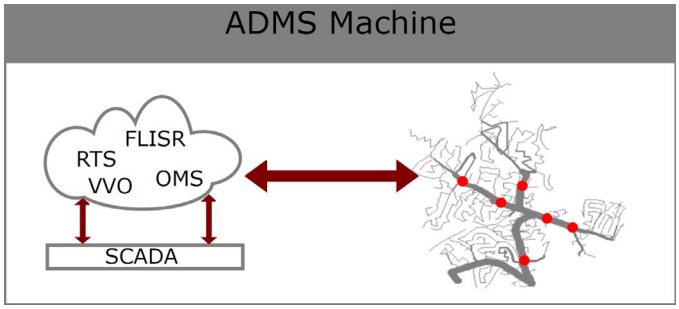

Figure 11.1: Block diagram of applications installed in distribution management system and the interaction with the simulation tool inside the distribution management system.

In the first scenario, experiments were conducted between the FLISR application in the system with the model simulated in the simulation tool available in the DMS. The simplified version of the distribution system modeled in the DMS's simulation tool is shown in Figure 11.2. For the first scenario, the evaluation is not the primary goal of this project, but the results from this SIL evaluation can be used to understand the FLISR actions that can be anticipated when using DNP3 and OpenFMB in the remote HIL experiments between NREL-ORNL and NREL-UNCC.

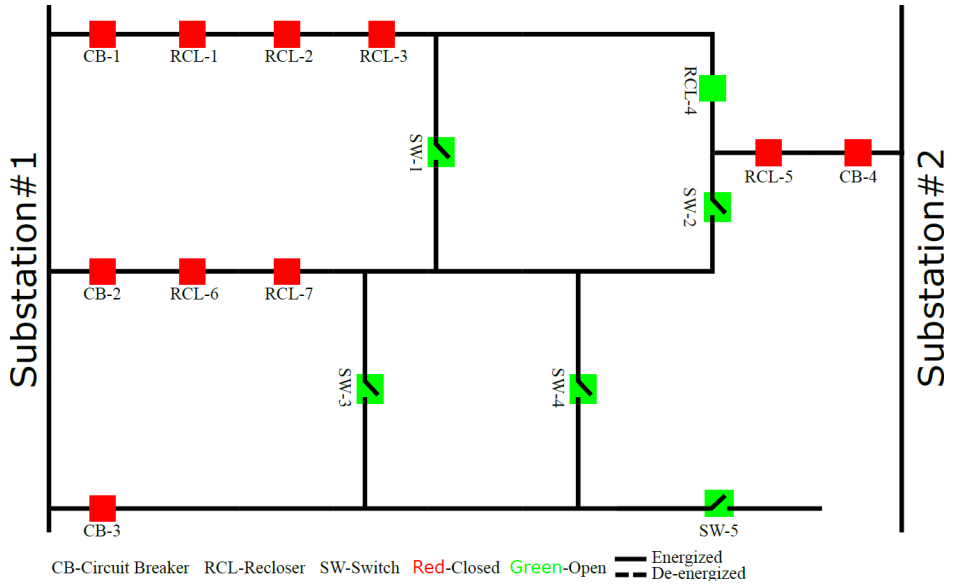

Figure 11.2: One-line diagram of the distribution system under study.

11.1.1 Test Case 1: Fault Between Recloser 2 and 3

The objective of this test case is to evaluate the ADMS FLISR application through the software simulation setup. The FLISR application makes the switching decisions based on predefined rules set by the operating utility. The utilities design the switching schemes to reduce the number of customers interrupted by outages. The one-line diagram shown in Figure 11.2 is part of a utility's larger medium-voltage (12.47 kV) distribution system. ADMS is programmed to sense and control this distribution system. The test system in Figure 11.2 has two substations with four feeders connected through reconfigurable switches (breakers, reclosers) and normally open switches. The low-voltage network containing loads are not shown in Figure 11.2.

Circuit breakers (CB-1, CB-2, CB-3, and CB-4) are feeder breakers located inside the substation. Reclosers (RCL-1, RCL-7) are used to detect the fault location, isolate the faulted section, and then reconfigure the network. Switches (SW-1 to SW-5) are used to manually reconfigure the network. In Figure 11.2, the status of the switches is indicated by the colors red and green. Red indicates normally closed, and green indicates normally open. The test system's normal configuration is shown in Figure 11.2.

For the test case 1, a three-phase permanent fault is placed between reclosers RCL-2 and RCL-3 in the simulated model of the test system, as shown in Figure 11.23. A fault in the system leads to a sudden increase in current, which is normally detected by the reclosers and breakers. RCL-2 and RCL-3 detects the fault current and opens the recloser to protect the line. Because of the high rate of temporary faults, utilities employ the three- or two-shot reclosing on to the disconnected network and restore power. It is important to remember that the FLISR application does not act until the recloser locks out after the final failed reclosing attempt.

In Figure 11.3, RCL- 2 and RCL-3 are open, and part of the network is de-energized, which is shown as a dashed line. The real-time graphical user interface (GUI) in ADMS shows the de-energized network as a white line in Figure 11.4. After the failed reclosing attempts, FLISR acts to close the normally opened recloser RCL-4 and energizes the network up to RCL-3 and SW-1. The planned reconfigured network through FLISR switching is shown in Figure 11.5. The planned actions are validated through the ADMS SIL setup. Figure 11.6 shows that the network from RCL-4 is energized up to RCL- 3 and SW-1.

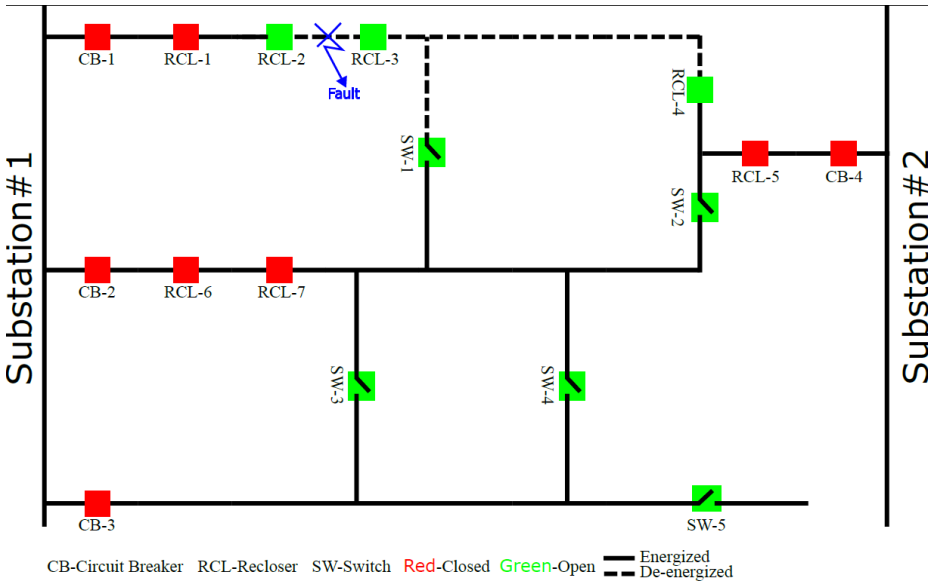

Figure 11.3: Test case 1 fault between recloser 2 and recloser 3.

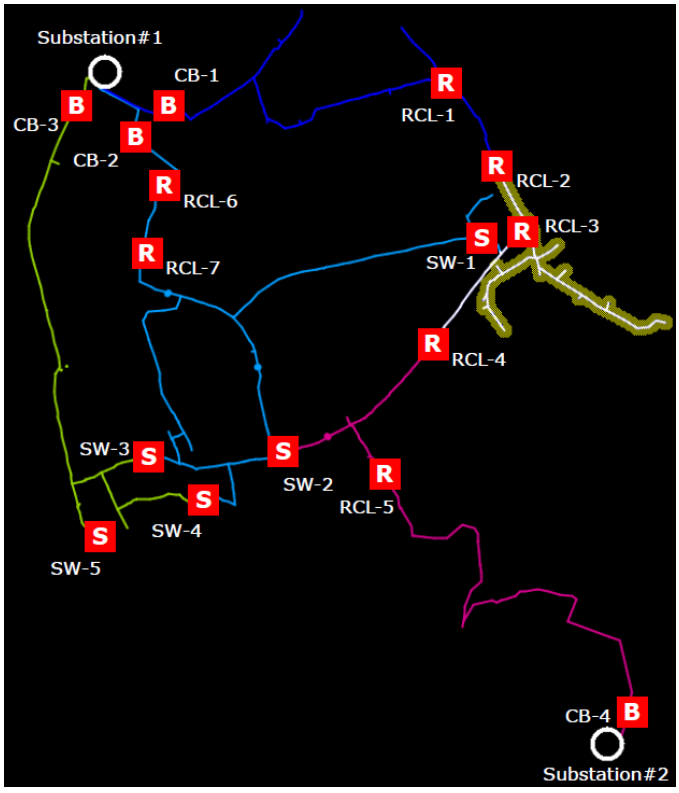

Figure 11.4: GUI of DMS indicating the faulted segment.

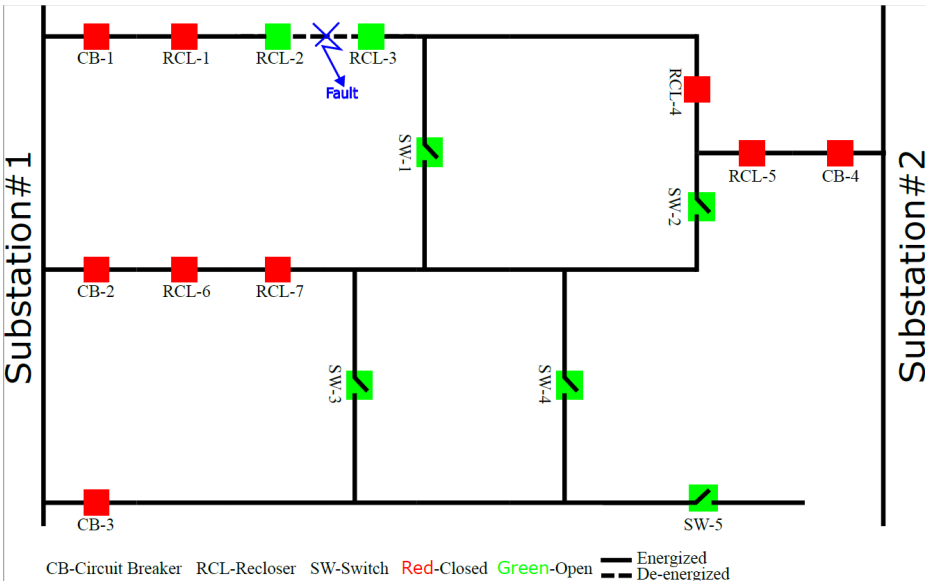

Figure 11.5: FLISR reconfigured circuit.

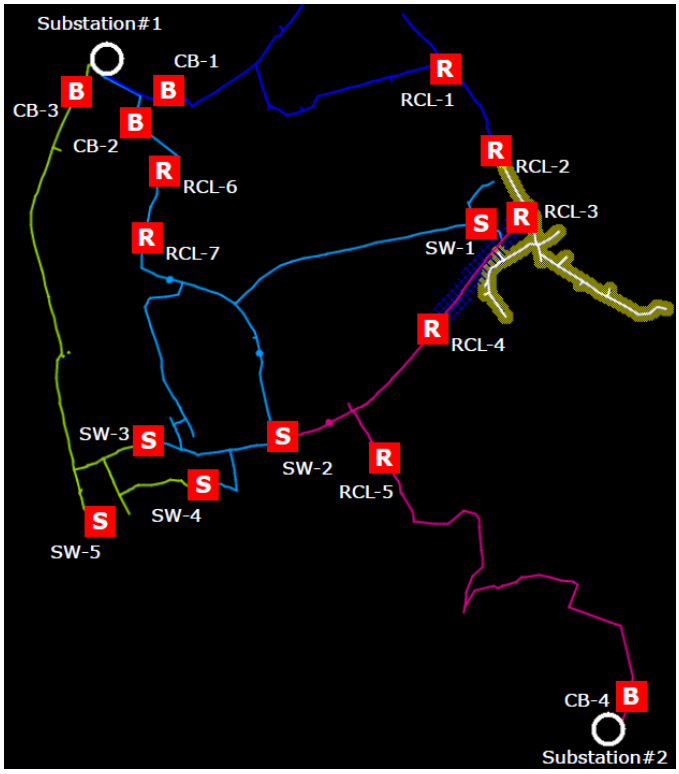

Figure 11.6: GUI of DMS indicating the reconfigured segment.

11.1.2 Remote Hardware-In-the-Loop

There are two remote hardware-in-the-loop (RHIL) setups used in this project. Two remote locations were used because it is uncommon for any one facility to have all of the necessary hardware. RHIL allows multiple locations to be interconnected in an HIL experiment, leveraging the resources of multiple locations

in a single HIL simulation. The first one connects the Distribution Management System installed at National Renewable Energy Laboratory's Energy Systems Integration Facility (ESIF) with the remote setup at Oak Ridge National Laboratory and at the University of North Carolina, Charlette. Figure 11.7 shows the RHIL setup between the different locations. The ADMS at NREL's ESIF is connected to the two different facilities through two data managers. The data managers can talk to each other through a dedicated VPN tunnel.

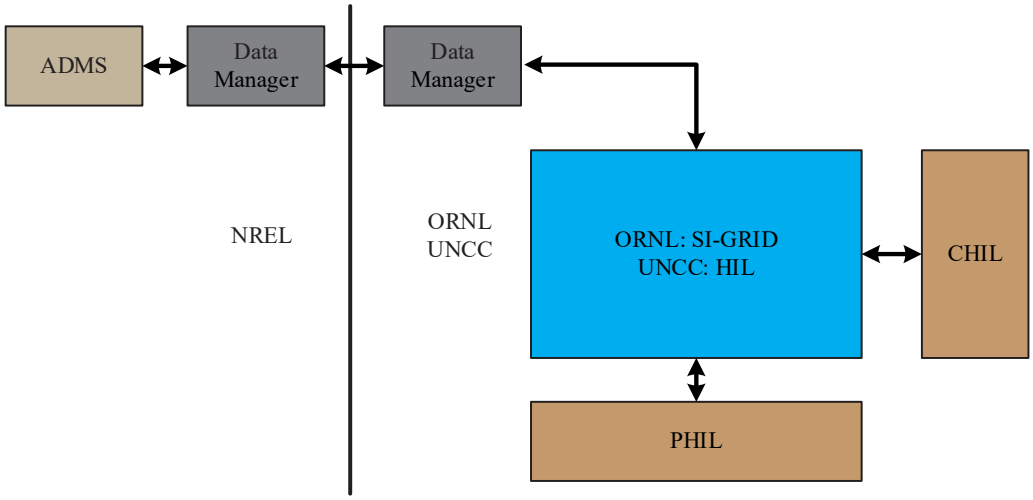

Figure 11.7: Remote Hardware-in-the-loop setup between NREL-UNCC and NREL-ORNL.

11.2 Model Development and Workflow Coordination

Multiple institutions performed the modeling, simulation, and emulation tasks in this project; hence a workflow coordination plan was enacted. This plan was intended to reduce duplicative work, manage data requests and storage, and to coordinate various modeling efforts. The project moved controls, algorithms, and methodologies from design to implementation over a series of development steps as shown in Figure 11.8 and Figure 11.9, culminating in laboratory evaluations. Initial design to deployment was informed by the CONOPS and IAP documents.

Figure 11.8: High level project workflow.

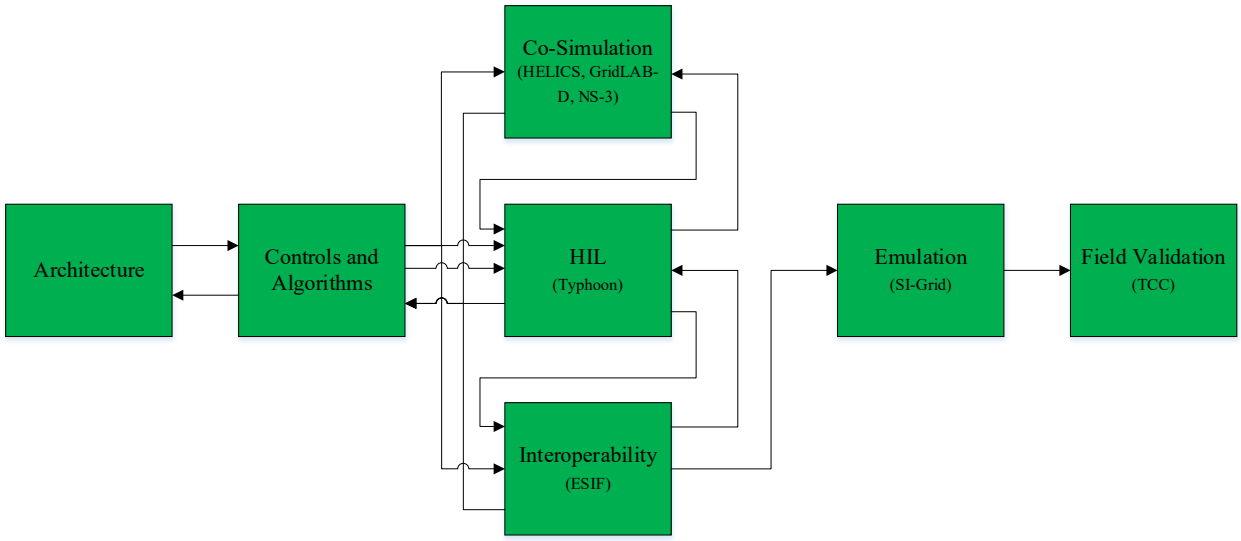

Figure 11.9: Modeling and simulation workflow and dependencies.

11.2.1 Dependency of Modeling Efforts

Recognizing the interdependency of the various modeling efforts with co-simulation being the initial step in the workflow, PNNL has led efforts to determine the relationship of the co-simulation piece on the subsequent modeling tasks. The primary goal of the exercise was to determine what data and methodologies other modeling tasks will be expecting from the co-simulation efforts. A number of key areas were identified, such as:

- Provide insight into communication implementation needs for HIL and emulation.
- Determine implementation techniques for methodologies such as self-healing and transactive control.
- Help verify model reduction adequacy.

Identifying these key areas will help project partners know where to prioritize simulation efforts. Similar exercises will be completed for both the HIL and emulation pieces of the project.

11.2.2 Model and Data Repository

To facilitate coordination between various partners, ORNL provided access to a Gitlab repository hosted at ORNL. The repository provides credential-based access to project data and resources such as models and validation results.

Project partners are using a variety of modeling tools including GridAPPS-D (PNNL), Typhoon HIL (UNCC and ORNL), SPOT (UTK), and operational DMS models (NREL) as examples. To ensure models are consistent, the project team agreed to use the Duke CYME model as a common starting point for model translation. This CYME model is stored on this repository along with validation results (discussed below).

11.2.3 Model Updates, Validation, and Consistency

Borrowing practices from software engineering, the project team is using the branch/merge technique for model management. When changes are proposed to the base model, a version of the currently accepted model is branched. Once changes are made and evaluated in this branched version of the model, the model is then re-submitted to the repository.

Upon submission of a branched model, the team evaluates and comes to a consensus on the proposed changes. If the team accepts the changes, the branched model is then merged into the main branch. At this point, project members update their individual translations of the model and re-validate them for adequacy. All translated models must meet an agreed upon set of criteria listed below:

- For models that are direct translations of the CYME model (e.g., CYME to GridAPPS-D for power flow), average bus voltages must be within 0.5% of the original model with no single bus voltage error larger than 1.0%.
- For models that are reduced translations of the CYME model (e.g., CYME to Typhoon), bus voltage at common points between models (e.g., reclosers) must be within 0.5% or the original model.

11.2.4 Team Coordination Examples

Some specific examples of team member coordination are as follows:

- ***Model verification and validation*** – As described above, the Duke CYME model will be the starting point for all modeling efforts in this project. Multiple project members including NREL, UTK, and PNNL evaluated the original CYME model to confirm the state of the model and to identify gaps in data.
- ***Recloser location in models*** – One of the gaps identified above was the location in the model of the reclosers to be used for reconfiguration. UTK and PNNL worked with Duke to identify locations for installed reclosers and to identify best-guess locations for reclosers that were not yet installed.
- ***Model reduction*** – The base CYME model must be reduced due to capacity limits of real-time simulators (such as the Typhoon HIL being used in this project) and hardware emulators (such as ORNL's Software-defined Intelligent Grid Research Integration and Development [SI-GRID]). Not only must the reduced model accurately represent the system, but is must also be compatible with the model's other team members are using, as well as the ADMS hosted at NREL. Lead by UNCC, initial model reductions efforts leveraged input and experience from team members to help ensure accuracy and compatibility are maintained.
- ***Laboratory interconnection*** – As part of this project, a direct network interconnection is being established between ORNL and NREL, and between UNCC and NREL. This interconnection will allow the GE ADMS system hosted at NREL to connect and control simulation and emulation assets located at ORNL and UNCC. Additionally, technical representatives from the project, cybersecurity groups from various parties collaborated to define and establish architecture and policies.
- ***OpenFMB Test Harness Development*** – ORNL has worked closely with Duke to design and implement a test harness for OpenFMB. This harness incorporates adapters developed by both Duke and ORNL, as well as commercial implementations of OpenFMB adaptors. Additionally, UTK, with support from ORNL and PNNL, is developing a VOLTTRON / OpenFMB adaptor intended to bridge the gap between customer and utility-owed assets.

- ***Development of CONOPS document*** – PNNL and Duke, with contributions and feedback from the rest of the project team, developed a Concept of Operations document designed to frame the project in a way that will be meaningful from a research perspective, as well as feasible from a utility operations perspective. This document outlines specific use-cases that will be considered in the simulation, emulation and implementation portions of the project.
- ***Implementation of reconfiguration algorithms*** – Since the exact reconfiguration algorithms implemented in the GE ADMS will not be known to the project team, PNNL developed reconfiguration algorithms internally. PNNL are working with other team members, including UTK and ORNL, to implement these algorithms on their own systems/models.
- ***Development of LVAT metrics*** – In support of the Laboratory Value Analysis Team (LVAT) development GMLC project, the project team evaluated existing proposed LVAT metrics and proposed additional metrics to accurately assess this and other distribution-focused projects. These metrics, developed by PNNL, NREL, and ORNL, were vetted by other project team members and submitted to the LVAT team for consideration.

11.3 Real-Time Hardware-in-the-Loop Models Development

The real-time hardware-in-the-loop simulations developed as part of HIL evaluation consist of two components: models for power electronics based distributed energy resources (DER) such as solar photovoltaic (PV) systems and battery energy storage systems (BESS); and models for distribution feeder components. The objective of the HIL modeling activity was to develop an integrated distribution system model of the Duke Energy feeder including the DERs (PV and BESS) which are interconnected to the feeder.

11.3.1 Distribution Feeder Model Development

The complete model of the Duke Energy feeder consists of more than 2,000 sections. A system of such a size is too large to be modeled unaggregated in a digital real-time simulator (RTDS) such as TyphoonHIL. As a result, the model was aggregated using the commercially-available CYME Power Engineering software to decrease the number of nodes to a computationally manageable number, while also preserving the model solutions. Specifically, the reduced order model yields the same power flow solution at key nodes, i.e., either side of the reclosers. The reduced model of the system contains less than 200 sections and was modeled in TyphoonHIL. The use of DRTS yields high time- resolution results in real-time that accurately represents device and system level interactions. The results of power flow analysis on the full model and the reduced or aggregated model showed less than 1.0% deviation in powerflow solutions at the substation nodes and on either side of the reclosers.

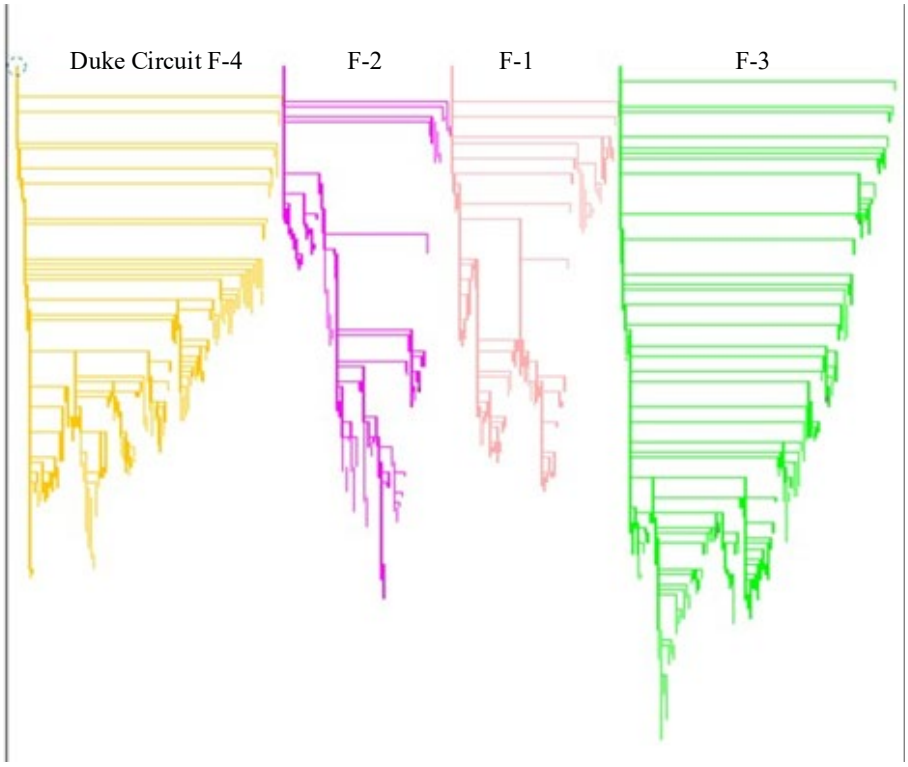

Figure 11.10: CYME one-line diagram of Duke Energy feeder prior to aggregation.

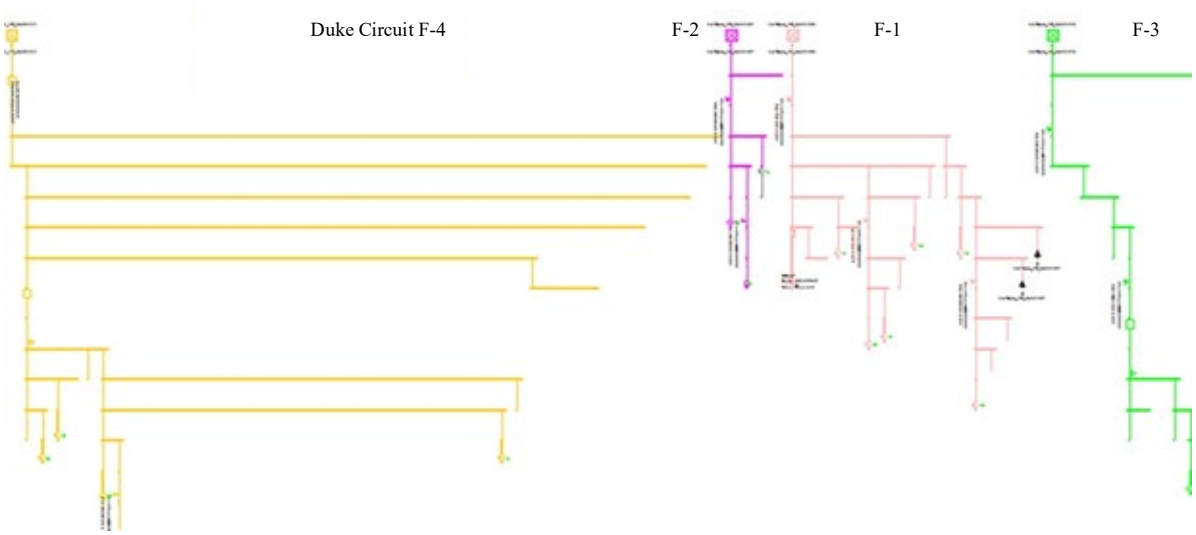

Figure 11.11: Reduced model one-line diagram of Duke Energy feeder (the aggregation exercise in CYME preserves the reclosers).

Table 11.1: Error (%) between Full Model and Aggregated Model (CYME Evaluation)

		ΔkW	Δkvar	ΔkVA
Circuit F-1	Total Generation	0.0012	-0.0076	0.0011
	Total Loads	-0.0571	-1.4635	-0.3211
Circuit F-2	Total Generation	0.0002	-0.0027	0.0000
	Total Loads	-0.0492	2.5582	0.0091
Circuit F-3	Total Generation	0.0041	0.0090	0.0046
	Total Loads	-0.0288	1.6135	0.1652
Circuit F-4	Total Generation	-0.0036	0.0130	-0.0008
	Total Loads	-0.0109	-2.2373	-0.4134

11.3.2 Distributed Energy Resources Model Development

The power electronic inverters used for integration of PV and BESS into the distribution feeder were modeled as two-level, three phase inverters as shown in Figure 11.12. These inverters can be operated in either grid following (current source) or grid forming (voltage source) modes.

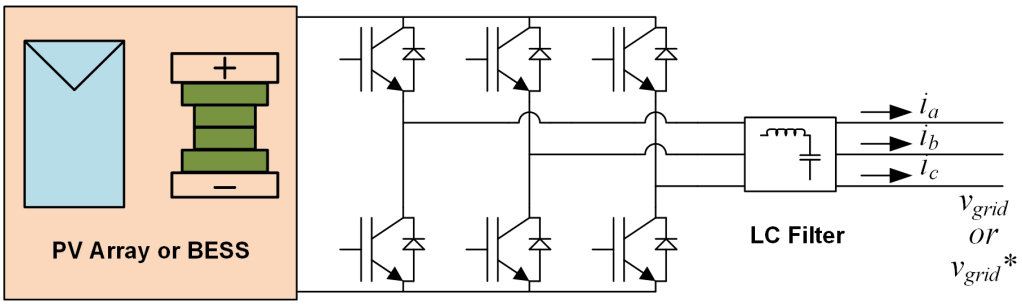

Figure 11.12: Three phase two level inverter topology for PV or BESS grid integration.

11.3.2.1 Control Scheme of PQ-SRF Controller for Grid Following Inverters

The synchronous reference frame (SRF) based PQ controller [92] termed as the PQ-SRF controller is shown in Figure 11.13. In the synchronous reference frame, the *DQ* voltage components (V_d and V_q) and the *DQ* current components (I_d and I_q) are determined using an *ABC-DQ* transformation [93]. The *DQ* components of voltage and current in the current analysis are obtained from the measured voltage (V_{PCC}) and current (I_{PCC}). A Phase Locked Loop (PLL) [94] is implemented to determine the phase angle (θ) of the voltage at PCC [95]. Using V_d and V_q, the reference currents along *d* and *q* control loops are calculated using the following equations:

$$I_d{}^* = \frac{V_d.P^* + V_q.Q^*}{V_d^2 + V_q^2} \tag{11-1}$$

$$I_q{}^* = \frac{V_d.P^* - V_q.Q^*}{V_d^2 + V_q^2} \tag{11-2}$$

P^* is the active power reference and Q^* is the reactive power reference determined from the algorithm described in Figure 11.13. The control loops along the *d*-axis and *q*-axis consist of PI controllers that generate reference voltages V_d^* and V_q^* respectively. The reference voltage is converted to the *ABC* frame from the *DQ* frame to get reference voltage, E_{ref} (E_a^*, E_b^* and E_c^*). E_a^*, E_b^* and E_c^* then from the input

to the sinusoidal pulse width modulation generators, with a switching frequency of 10 kHz. In the grid-following mode, since V_{PCC} is determined by the transmission grid itself, power flow through the inverter is controlled by the current magnitude and phase. Figure 11.14 shows the relationship between the current and voltage phasors in a grid-tied inverter. The phase angle of the inverter output current with respect to the grid voltage and its magnitude are controlled to produce the reference active and reactive powers.

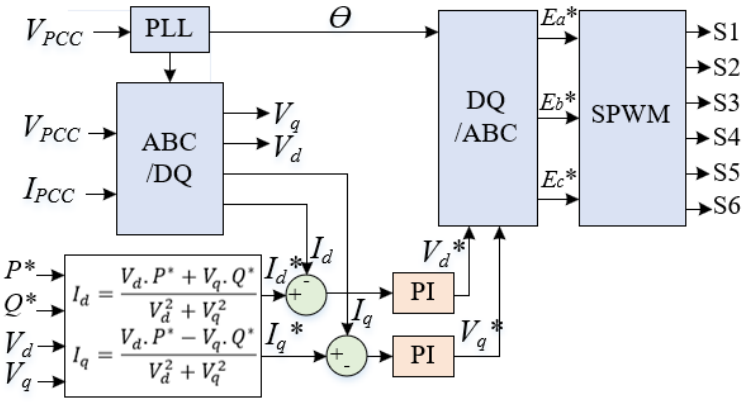

Figure 11.13: Simplified block diagram of the PQ-SRF controller.

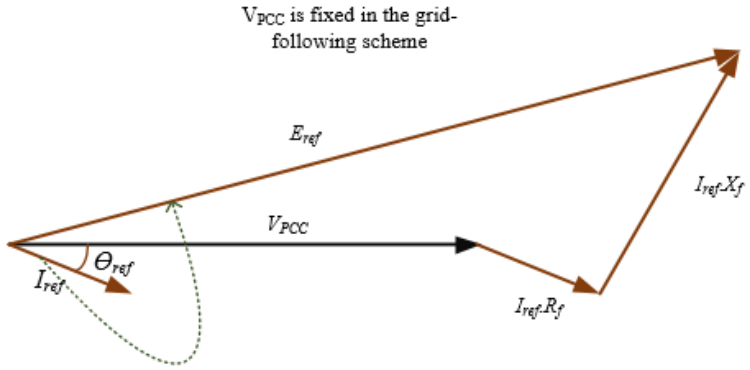

Figure 11.14: Phasor diagram showing the relationship between currents and voltages in a grid-tied inverter system.

11.3.2.2 Control Scheme of VF-SRF Controller for Grid Forming Inverters

The simplified diagram of the SRF based droop control scheme is shown in Figure 11.15. In this control scheme, I_{ref} (I_d* and I_q*) are calculated from active power-frequency (P-f) droop and reactive power-voltage (Q-V) droop control loops respectively. As the grid voltage and frequency are controlled by this droop control scheme [96], it has been named the VF-SRF controller. I_d* is generated from an outer frequency control loop. In this loop, the difference between the actual frequency and the reference frequency, (f*-f_{PCC}) is fed into a PI controller to generate the reference current along d-axis. Similarly, I_q* is generated from the outer voltage control loop. In this loop, the voltage error (V*-V_{PCC}) is fed into a PI controller to generate the reference current along q-axis. The inner current control loops are similar to the current control loop in the PQ-SRF controller. In this control strategy, P and Q from the inverter are generated depending on the load changes and the V* and f* given to the controller.

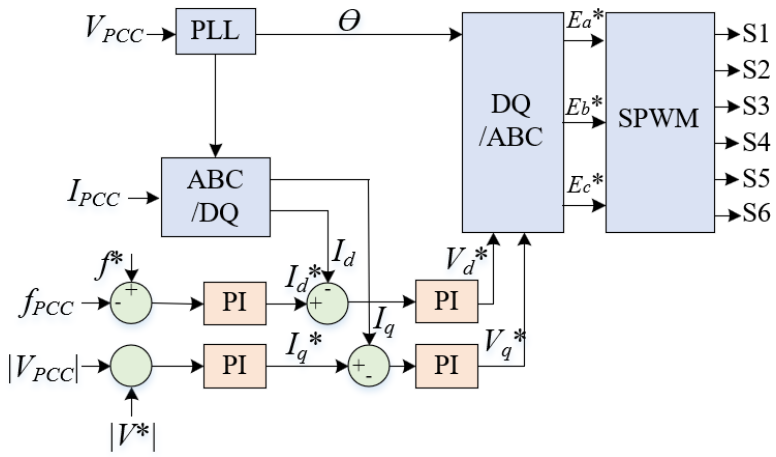

Figure 11.15: Simplified block diagram of the VF-SRF controller.

Active and reactive power droop control characteristics used in the grid-forming mode are shown in Figure 11.16. These droop control properties are programmable, and they mimic the behavior of synchronous generators with machine inertia. But for the test system in this paper, this simplified droop control is suitable and is expected to control the V and f as it is a grid-connected system. When the PCC node voltage decreases, the Q-V droop control loop is triggered and the Q output from the inverter is increased to force the V_{PCC} to remain within acceptable limits. Similarly, when the frequency drops, the P output from the inverter increases to force the f_{PCC} back into a stable band.

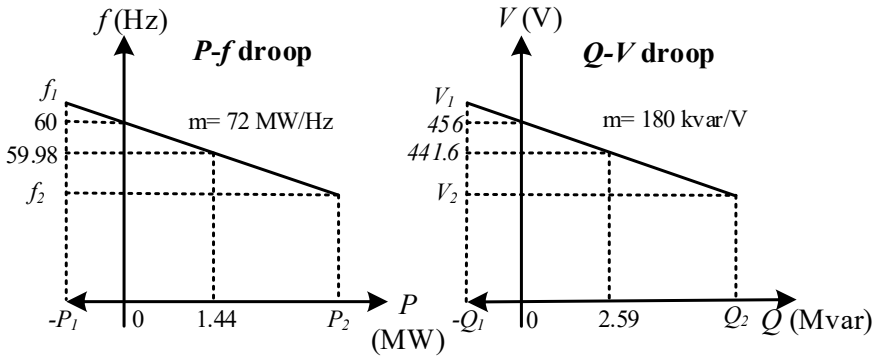

Figure 11.16: Traditional P-f and Q-V droop characteristics with slopes of programmable droop control.

11.3.3 Illustration of HIL Systems

The following sections discuss the HIL models of two systems in detail. The first system examines issues of power quality and the second system examines power coordination.

11.3.3.1 Illustration of HIL System 1: Power Quality in a Cluster of Microgrids

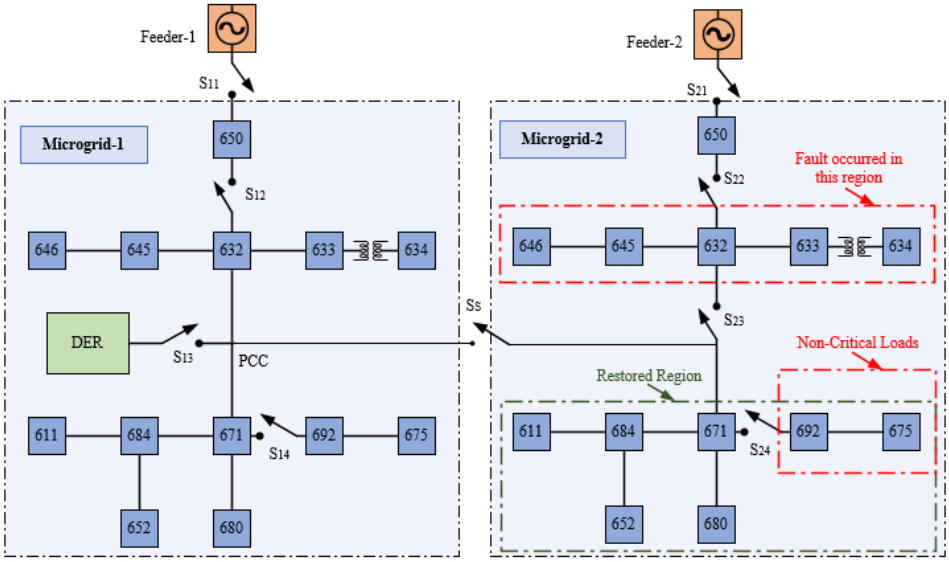

Figure 11.17: One-line diagram of two modified IEEE 13-node models representing microgrids that can be networked.

An illustrative distribution system is shown in Figure 11.17, which consists of two microgrids and each of them has 13 nodes. The model of the microgrid is inspired by a representative distribution system consisting of balanced and unbalanced loads, line impedances, a transformer, and meters. Each of these nodes is connected to one-line, two-line or three-line distribution buses and corresponding loads, as is commonly seen in North America Type distribution systems. For these reasons, voltages in the nodes are expected to be slightly unbalanced under normal operating conditions. In the modified 13-bus microgrid model, the loads at each node are assumed to be balanced. However, the node voltages are not still expected to be perfectly balanced because of the inherently unbalanced impedances in the IEEE 13-bus system.

A DER is connected to node-671 of the Microgrid-1 (PCC) via switch-S13 for P and Q injection. The DER consists of a PV inverter and a co-located BESS as shown in Figure 11.18. Each of them is connected to the PCC by a 3-phase inverter [97] and a transformer. The PV-inverter is controlled in grid-following mode whereas, the BESS can be controlled in grid-following as well as grid-forming [98] modes. At maximum irradiance, the PV array is rated at 3 MVA and the BESS is rated at 5 MVA. The battery voltage is rated at a nominal 800 V and it is assumed to have an initial State of Charge (SOC) of 80% for analysis purposes. A step-up transformer interfaces the 480V output of the inverter to the 4160V distribution PCC voltage. The 3-phase inverters are used to regulate P-Q or V-f depending on the operating mode [99], by the inverter controllers, which in turn receive reference setpoints from the supervisory controllers.

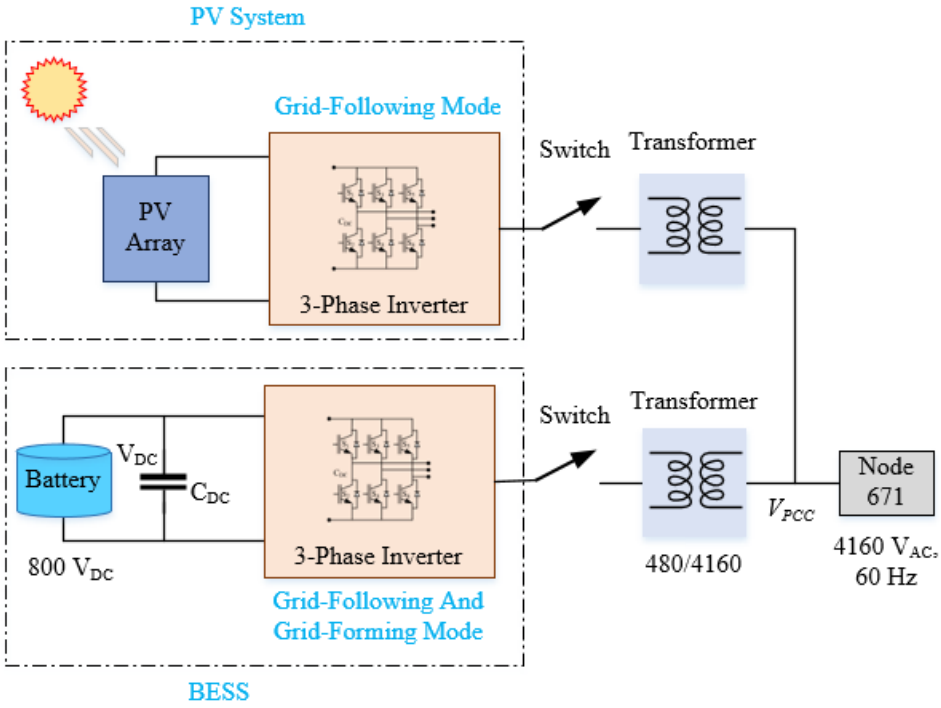

Figure 11.18: One-line diagram of the DER model with a PV system and a BESS.

In this analysis, node 632 of Microgrid-2 is assumed to have a fault, as shown in Figure 11.17 and consequently, a switch in Feeder-2, S21 is tripped for servicing. During the repair time, an attempt to supply power to the other healthy parts of Microgrid-2 will then be executed via node 675 from the active Microgrid-1. Firstly, switch S23 is opened to isolate the healthier sections of Microgrid-2 from the faulted section. To enable seamless power-flow from Microgrid-1 to Microgrid-2 without any voltage and frequency violations in the nodes, the DER in Microgrid-1 is controlled by modulating the reactive power output of the BESS as described in the logic in Figure 11.19.

Furthermore, a load shedding operation is performed by shedding a grouping of non-critical loads from the system by opening S24. During the load shedding operation, all the other control operations by the DER and status of the remaining switches have been kept unchanged.

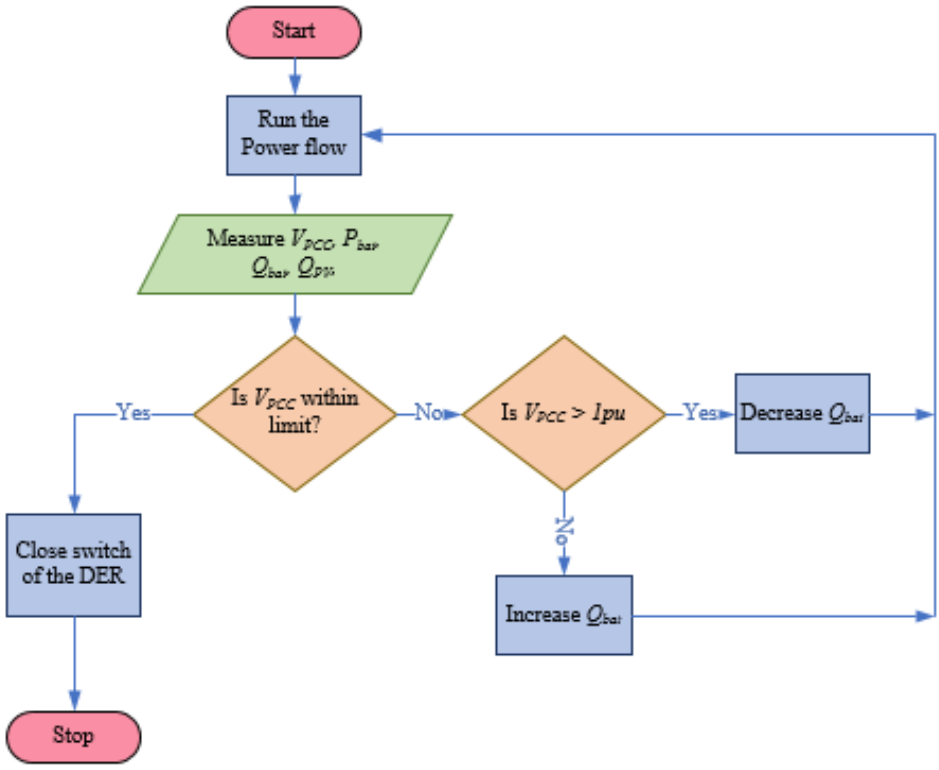

Figure 11.19: Flowchart of the BESS control by the PQ-SRF control scheme.

The power flow from the DER is commanded according to the algorithm shown in Figure 11.19. The node voltage improvements after DER deployment and shedding of non-critical loads is shown in Figure 11.20.

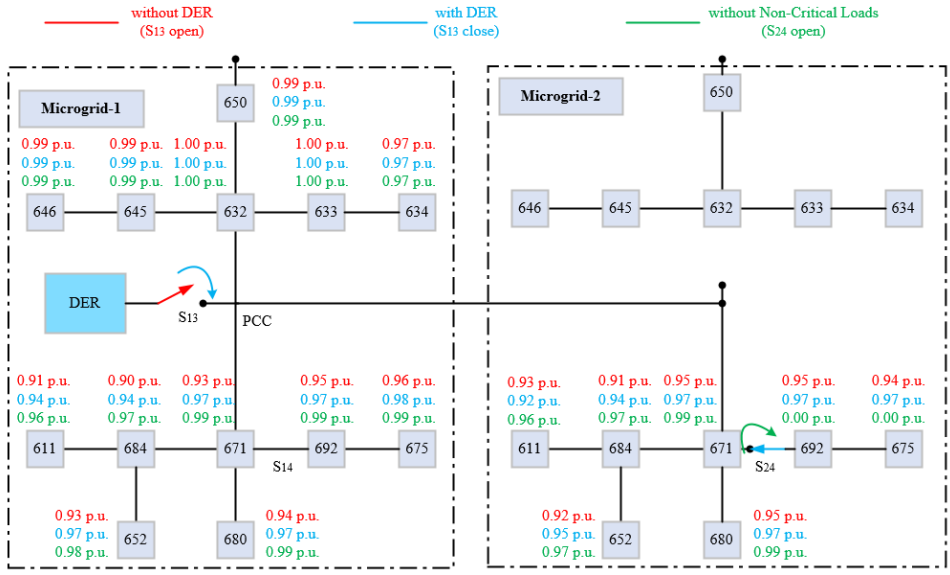

Figure 11.20: Node voltage improvements using DER deployment and shedding of non-critical loads.

11.3.3.2 Illustration of HIL System 2: Coordinated Power and Energy Management in a Cluster of Microgrids

Coordinated power and energy management between microgrids is agnostic to generator or energy storage types since coordination should happen at a supervisory controller level. The concept presented in this paper utilizes solar PV systems for localized power generation and BESS for localized energy storage. The power converters for DER grid integration are three phase two level inverters.

An illustrative microgrid cluster system containing two independent microgrids is shown in Figure 11.21. Each microgrid contains a solar PV plant and a BESS, allowing each distribution feeder to operate in grid-connected mode or in islanded mode. When there is a transmission system outage, the normally open (NO) recloser is closed to enable coordination between the two microgrids. The cluster was modeled in the real-time hardware-in-loop system TyphoonHIL and the operation of the system was verified using analog readouts of grid parameters. Each microgrid in the cluster capable of transitioning between grid-connected and islanded mode. When a transmission system outage is detected, the BESS inverter, which had been operating in the grid-following (current source) mode, transitions to grid-forming or islanded (voltage source) mode. When the microgrid enters islanded mode, the normally closed (NC) recloser is opened to isolate the microgrid from the transmission system. It is noted that prior to the transition, power from the BESS was supplied to local loads and also fed into the grid; and after transition to islanded mode, it only supplies power to the local loads, which manifests as a reduction in current output. The power flow, energy profiles and service availability are shown in Figure 11.22.

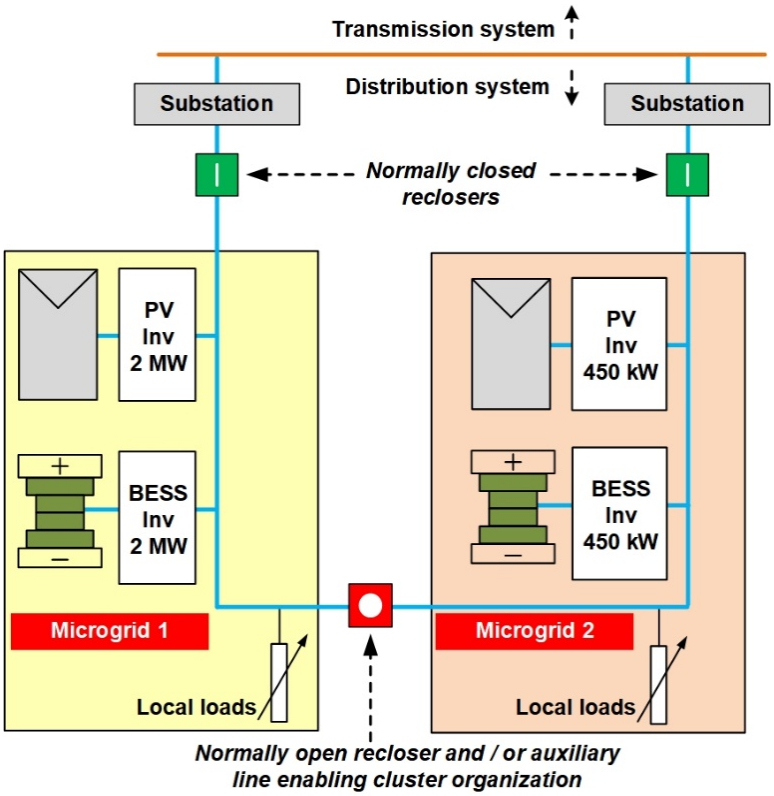

Figure 11.21: Demonstration of a microgrid cluster consisting of two microgrids.

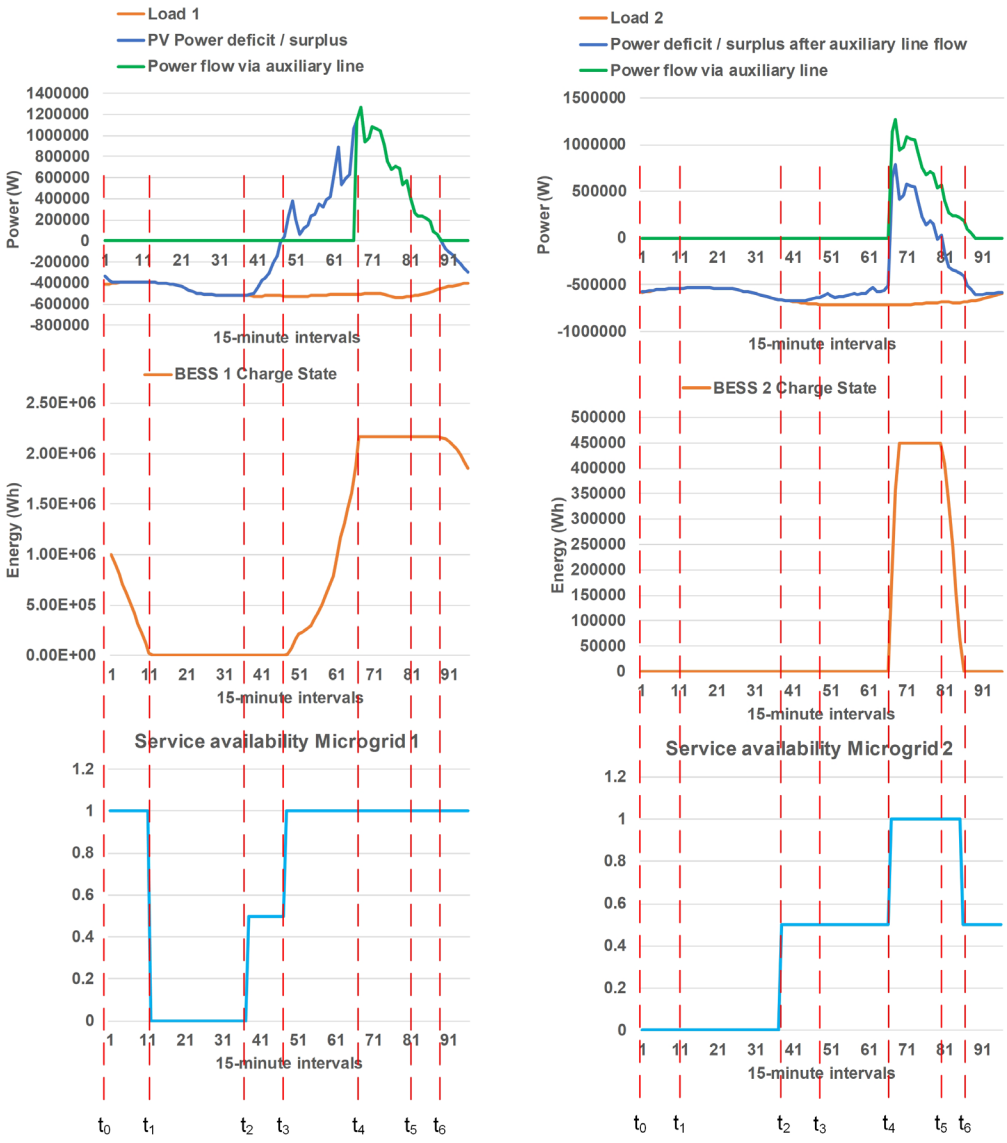

Figure 11.22: (a) Microgrid 1 operation: Power flows & BESS state of charge; (b) Microgrid 2 operation: Power flows & BESS state of charge. Service availability of 0.5 implies load demand being met partially.

The concept of microgrid clusters may be expanded to include a greater number of independent microgrids, connected by NO reclosers and auxiliary distribution networks, to improve grid availability and resiliency. By selective operation of the reclosers, and by assigning specific BESS inverters to grid-forming or islanded mode operation, power flow between independent microgrids can be achieved.

The illustration of an example architecture of an *n*-microgrid cluster is shown in Figure 11.23. The individual distribution feeders fed by the respective substations can operate independently as grid-connected or islanded microgrids. When the cluster coordination controller is enabled, it receives generation capacity and load demand in each microgrid and calculates the recloser settings and power generation set points for the DERs, in order to maximize service availability for the loads in the system. By categorizing

loads into critical and non-critical, and selectively disabling the non-critical loads, power availability for critical loads may be further improved. Through the operation of the appropriate NC and NO reclosers, any microgrid in the cluster could be switched between grid-connected and islanded mode independently.

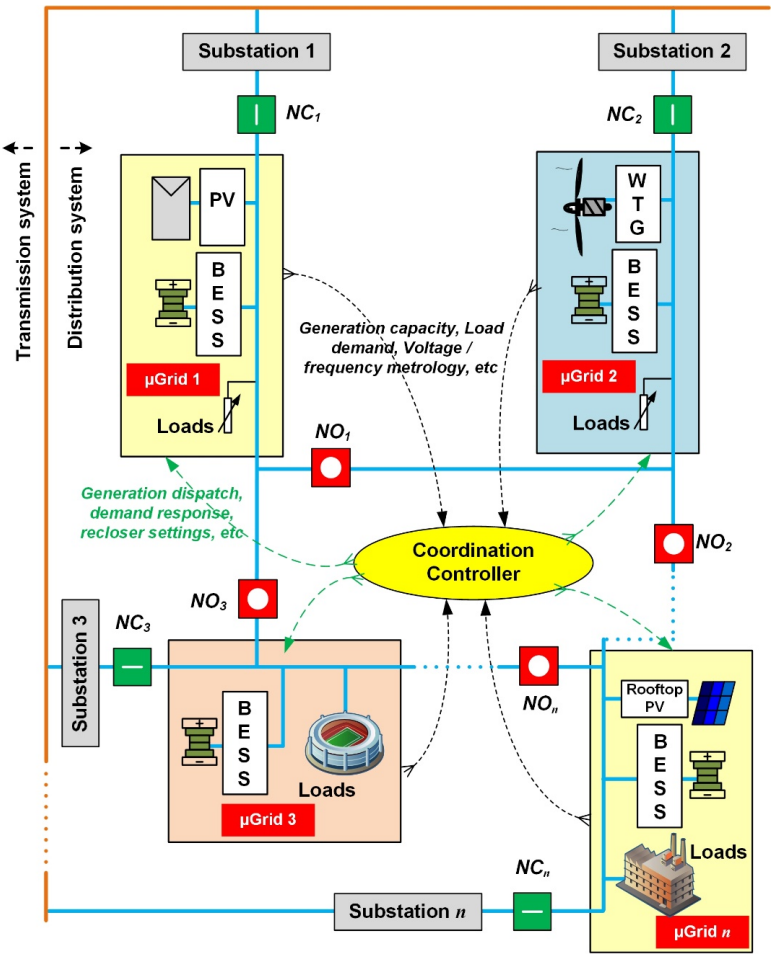

Figure 11.23: Architecture example of a microgrid cluster with n-microgrids.

Since the model assumes a centralized coordination controller, it is necessary for telemetry on generation capacity (from DERs), load demand, critical loads demand, and BESS SOCs from the individual microgrids to be transmitted to the central controller. Based on these inputs, the central coordination controller calculates the power dispatch commands for the individual microgrid. This logic provides the following salient operations: (1) when adequate generation capacity is present in a microgrid to meet local load demand, the local loads are served first and then the BESS is charged; (2) when there is inadequate generation capacity inside a microgrid, the logic attempts to meet critical load demand; (3) power sharing is enabled when there is excess capacity in a microgrid after serving local loads and charging local BESS; and (4) when all microgrid local loads are served and all BESS are fully charged, DER generation is curtailed.

12.0 Emulation and OpenFMB Harness for Development

The co-simulation techniques of Section 10.0 and hardware in the loop testing techniques of Section 11.0 are becoming increasingly commonplace in power system research. Simulation environments are used for easily modelled components where approximations are known and non-impactful; hardware provides higher fidelity data and performance. For this project, we combined these environments to leverage the benefits of both platforms to simulate how OpenFMB can be utilized in a field setting for FLISR operations.

ORNL and NREL have worked together to establish a data link between the two laboratories. This allows for DNP3 signals from an NREL DMS system to ORNL hardware, which then changes that DNP3 communication into OpenFMB and performs the requested control action in low-voltage hardware. Switch statuses are communicated back to NREL, for a full closed-loop control.

12.1 Emulation Methodology

For this set of experiments, the team set up to build a platform which could test end-to-end operations of FLISR systems when using OpenFMB. This includes using a DMS to send reconfiguration instructions to the switches on a known feeder. Those commands are converted from a traditional protocol, in this case DNP3, into OpenFMB to allow for standard, peer-to-peer communication amongst the affected switches. Those switches then use the reconfiguration instructions from the DMS to get into the correct configuration in the correct order. Switch statuses are reported back to the DMS, which confirms that the FLISR operation was successful. Note that this applies for operator-initiated reconfigurations. Reconfigurations due to faults can still be tested in this manner, however in this case we assume the FLISR does not operate in a distributed autonomous fashion, and that an operator is required to initiate reconfiguration.

Creating this entire process in a single simulation environment would be very complex and slow. Also, there is added value in observing how communication latency affects the effectiveness of the FLISR scheme. Considering these factors, and also the fidelity of the models, a methodology was formulated to test this scenario using a combination of communication, simulation, and hardware. An overview of the testing setup can be seen below.

Control actions are initiated by the DMS system at NREL and sent over fiber to the lab at ORNL, where the commands are received and interpreted by a local data manager. An HIL test system then acts upon the DMS commands and reports status information back to the DMS. The feeder model exists in a Typhoon RT simulation, while certain areas of interest of the feeder(s) are represented in hardware.

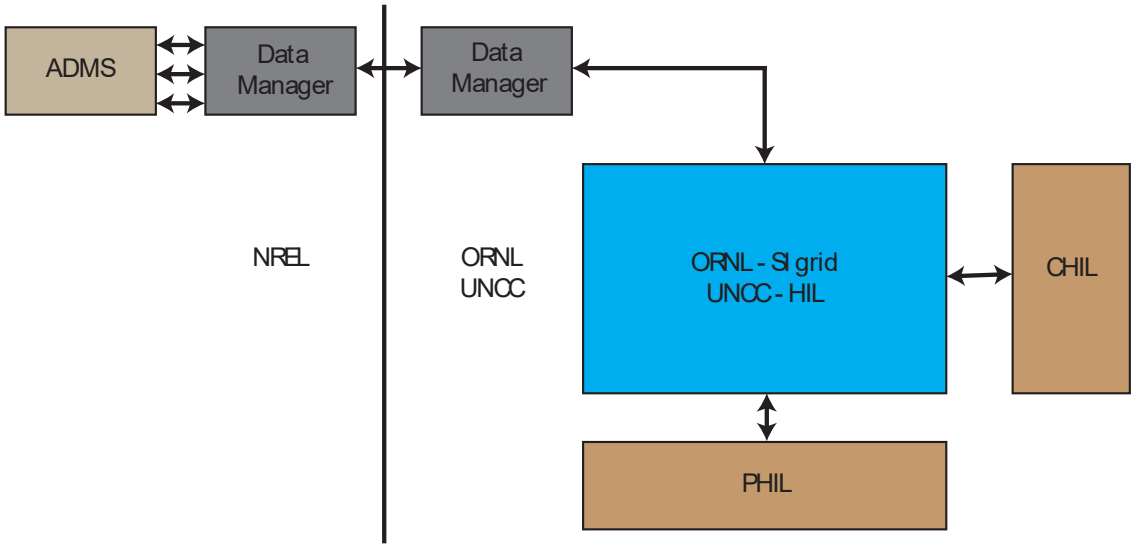

Figure 12.1: Multi-location HIL test setup.

The end goal for this setup is to demonstrate a viable, hardware-based implementation of OpenFMB which could realistically occur at a utility. Standard equipment is used to receive and translate utility standard protocols (DNP3) into OpenFMB for use in hardware.

12.2 Emulation Testing Setup

The following sections discus the communications and electrical hardware implemented at the OpenFMB Harness developed at ORNL and connected to the DMS at NREL.

12.2.1 Emulation Communications Setup

Using SEL RTACs, NREL is able to send DNP3 commands from its DMS system directly to an ORNL RTAC. Connected to that RTAC is an OpenFMB adapter, which is able to convert the DNP3 messages into the OpenFMB data model. This enables OpenFMB enabled devices on the feeder to use the DMS commands in a publish-subscribe protocol. Since most commercial devices are not yet OpenFMB capable out of the box, each device receives an adapter to convert back from OpenFMB to DNP3, which each device in the testbed speaks natively. This setup can be seen below.

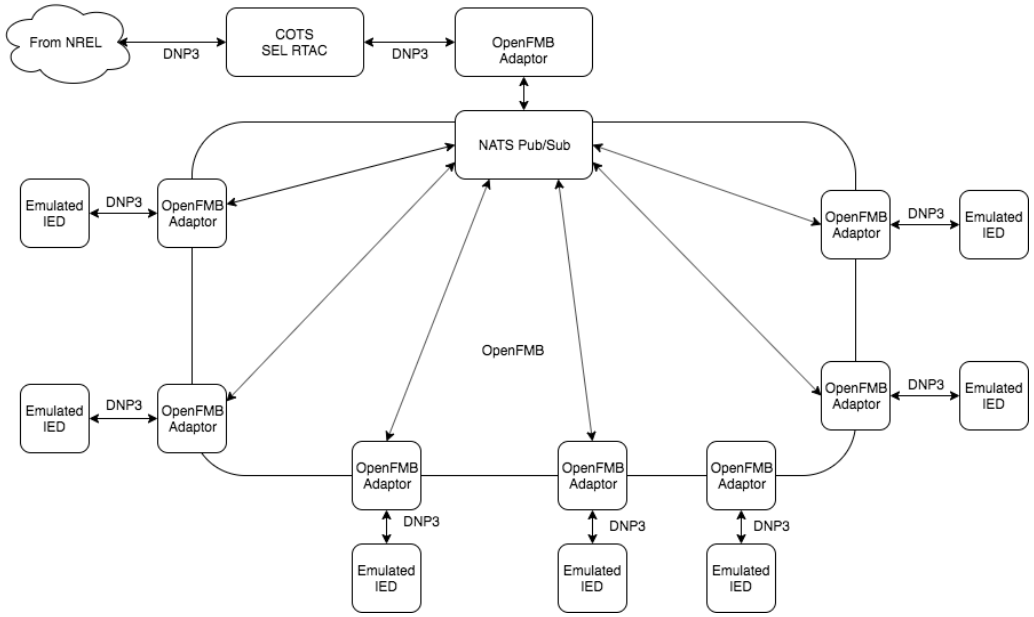

Figure 12.2: Multi-location HIL communication setup.

12.2.2 Emulation Hardware

This project utilizes the ORNL Software-defined Intelligent Grid Research Integration and Development (SI-GRID) platform. This test system consists of low-voltage, low-power generation and loads which can be reconfigured to represent varying feeder configurations. Initially designed to test multiple microgrid systems, SI-GRID is also able to test protecting settings at low powers, which makes testing of actual faults much lower risk, since the cost of components is much lower and the chance for injury or laboratory damage is small.

SI-GRID operates at 24Vrms, using a 3-phase 4 wire configuration. It is able to represent imbalanced systems, as well as harmonic content from certain types of loads and sources. To capture the effects of line impedance, sets of inductors and capacitors have been assembled to create a number of different impedance variations on a line. A user must simply use enough boards to represent the impedance at low voltage and bypass the remaining impedance on the board. SI-GRID can also represent various types of inverter-based generation including solar, energy storage, and certain types of wind turbines. Load imbalance and grid reconnection waveforms from SI-GRID can be seen below.

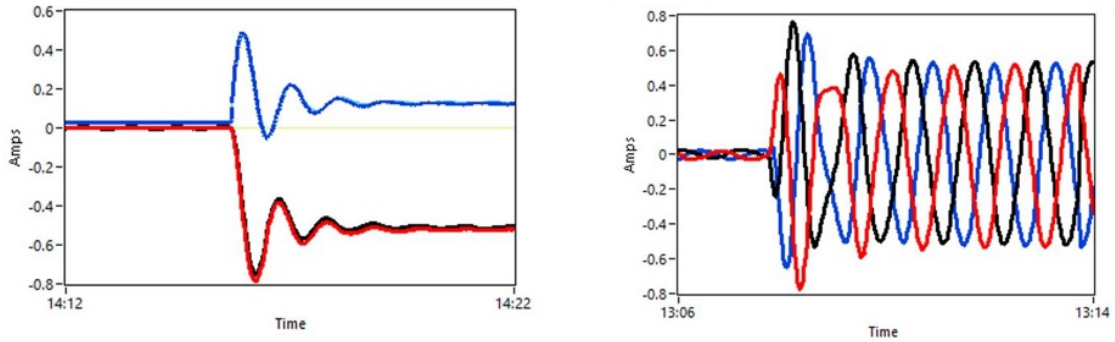

Figure 12.3: Load imbalance and grid reconnection waveforms from SI-GRID.

12.2.2.1 Experiment 1 – OpenFMB Demo

For this experiment, the SI-GRID was set up to demonstrate the capability of OpenFMB to enable peer-to-peer transactions between solar inverters. The experimental setup consisted of two SEL 651Rs, two OpenFMB adapters provided by Open Energy Solutions (OES), two SI-GRID inverters, a set of line impedance boards to separate the inverters, and software to store, visualize, and monitor the system. This communication architecture and test setup can be seen below.

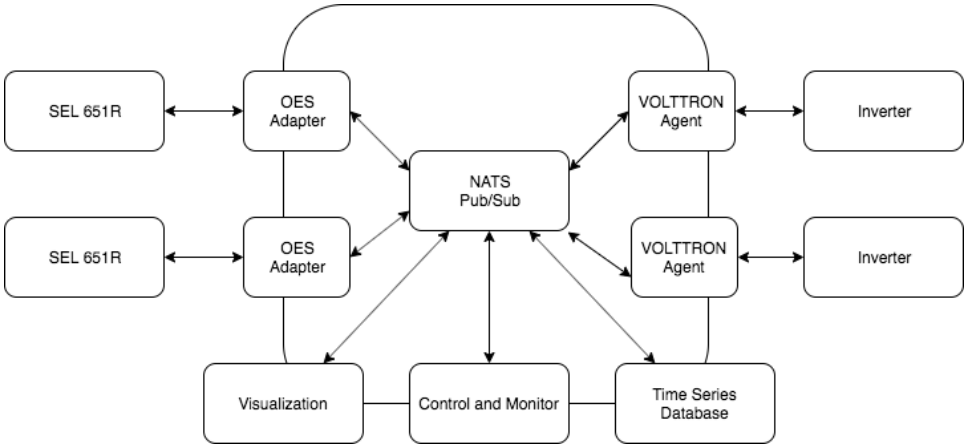

Figure 12.4: Multi-location HIL communication architecture.

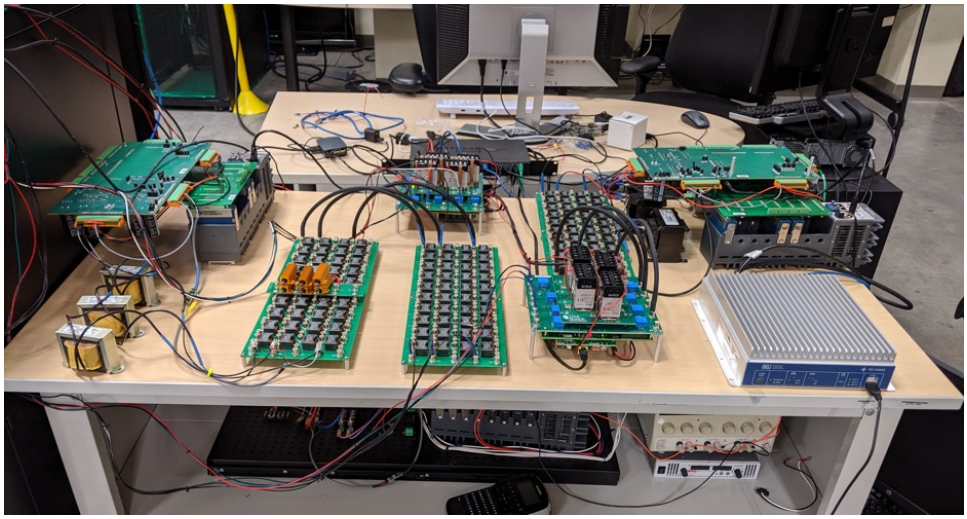

Figure 12.5: SI-Grid image showing COTS controllers and line emulators.

A detailed technical description of the test framework and results can be found in Sections 9 & 10. At a high level, the test setup allows for the impedance to be varied between PV inverters and observe how the transactive energy controllers adapt the price of electricity.

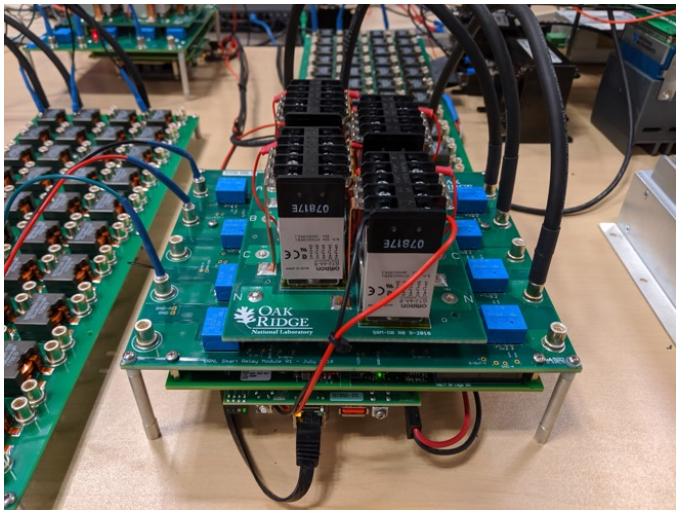

Figure 12.6: SI-Grid image showing smart relay boards.

Smart relay boards were designed to allow for an interface to SEL 651-Rs for operation of the breakers. This allows the team to use the protection capabilities of the SEL relay to change settings and send commands to be interpreted at low voltage and used to reconfigure the system. As the system is reconfigured, the OpenFMB adapters allow for the controllers to monitor the changing state of the grid and adapt their models to continue to produce optimal setpoints for a given use-case.

12.2.2.2 Experiment 2 – NREL / ORNL Remote FLISR Operation

This experiment uses the NREL DMS system to send reconfiguration commands to the ORNL testbed, where those commands are translated into OpenFMB and used to perform control actions on SI-GRID.

Similarly, to the first experiment, the SI-GRID was set up with some line impedances terminated with smart relay boards connected to SEL-651Rs. In this case, an inverter was used to represent the grid input to this system, which was determined by a Typhoon simulation. The Typhoon system outputs analog voltage waveforms, which the inverter read in on its control system and recreated on its output terminals as closely as possible.

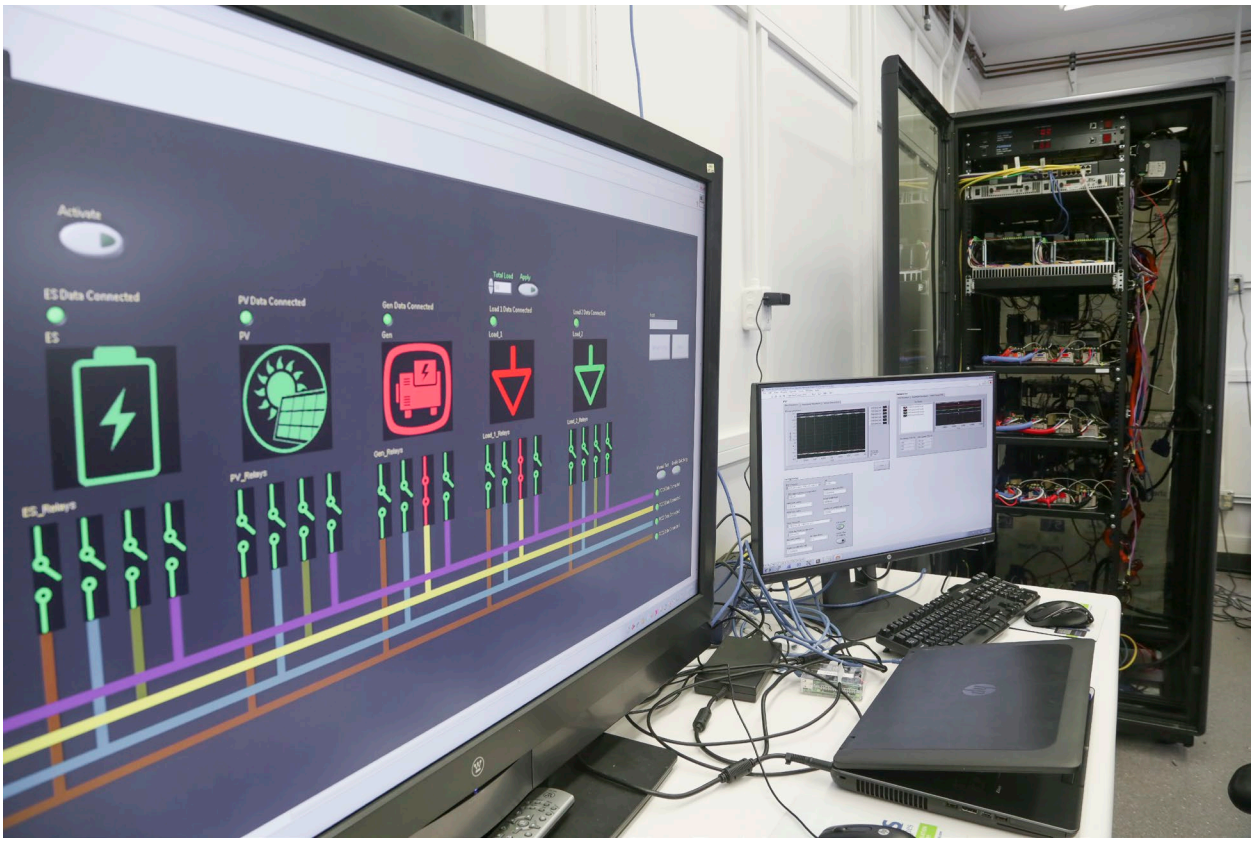

Figure 12.7: SI-Grid image showing GUI.

Each breaker within SI-GRID reports back its open/close status over OpenFMB. The OES adapter subscribes to the breaker information, such as voltage and current measurements and open/close status. The adapter translates the information into DNP3 messages which are sent to the SEL RTAC and then to the NREL DMS, creating a feedback loop for operators.

12.3 Emulation Results

The following sections contain the results of the emulation that was conducted at ORNL.

12.3.1 OpenFMB Demo

Section 9 of this report go into great detail about the transactive energy controllers and their implementation in software. For validation, the controllers were implemented in the testing setup described in Section 12.2.2.1.

12.3.2 DMS FLISR Operation

Communications and status points are shared between the ORNL hardware setup and the NREL DMS. That is, when the testbed at ORNL is active, the DMS at NREL can actively see changes in voltages, currents, and breaker statuses in near-real time. The latency between the two systems has not been fully evaluated and will be done at a later date. Simple protection curves have been programmed into the reclosers shown in Figure 12.8 to allow them to respond to a designed fault.

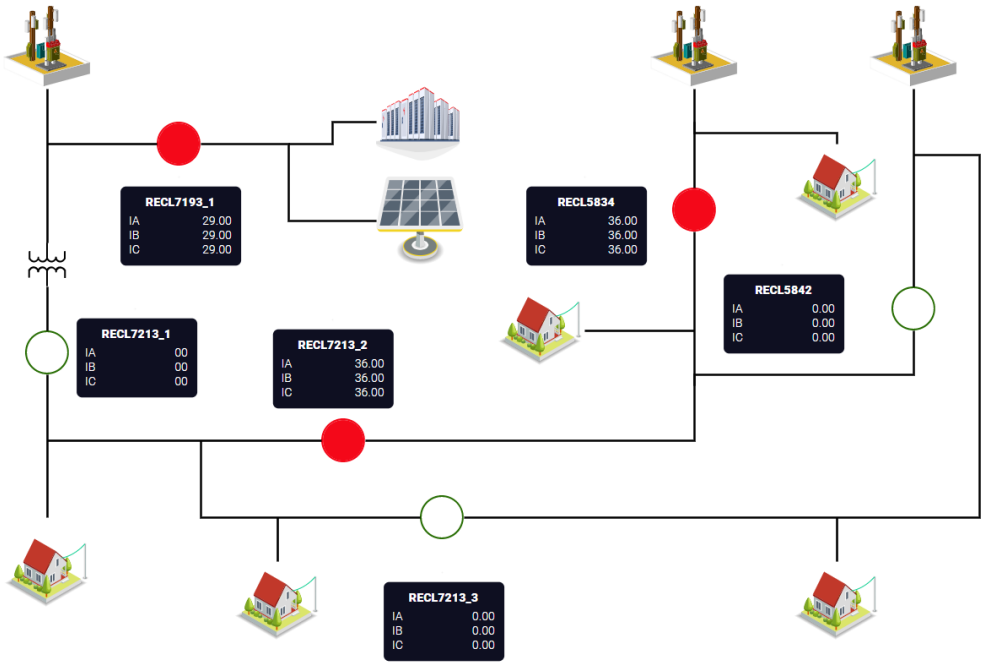

Figure 12.8: Normal emulated system pre-fault.

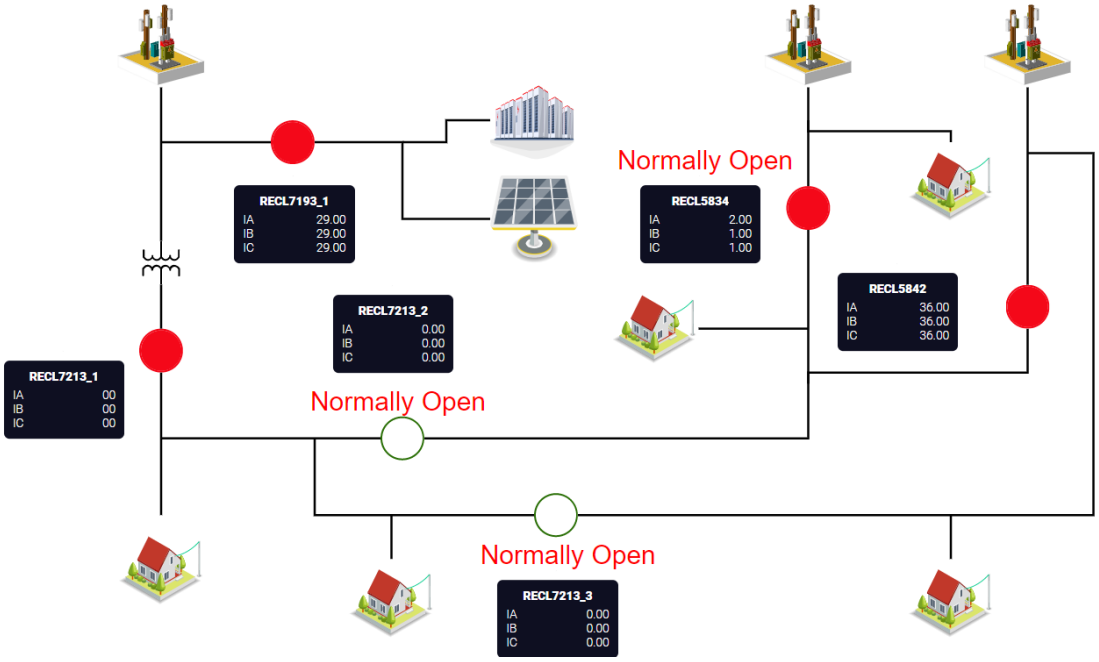

Figure 12.9: Reconfigured emulated system.

The reconfiguration of the system can happen locally and the change in configuration is sent to the DMS system.

13.0 Lessons Learned and Concluding Comments

Overall, this project was a success. Despite the lack of a formal field demonstration before the conclusion of the project, the major objectives of the project were achieved, and the work resulted in a persistent leave-behind capabilities. These included DOE follow-on projects and capabilities that are being incorporated/leveraged by industry. This section contains the lessons learned and final comments for the project.

13.1 Lessons Learned

Because the work in this project ranged from foundational research to applied engineering, there was an array of lessons learned.

- Model and simulation coordination
  - For any research project that will utilize multiple simulation types, there needs to be a consensus on the "source" for system model. For this project, the co-simulation model and the HIL models for this project both used the Duke Energy CYME model as the data source.
  - When a single source is being used for different models, there must a defined process for migrating from the source data to the individual model. For this project, there was a defined process for how to create the co-simulation, dynamic, and HIL models. This included rules for model reduction, validation, and comparison to ensure that results from different models could be compared. For example, nodes that were control points, such as a DER, could not be reduced.
  - Even though a project can have different simulation types, they must be cross-validated for consistency. For this project, co-simulation, dynamic, and HIL models were compared in steady-state to ensure fundamental agreements. This allows for cross-coordination for more complicated simulation results, and comparison. For example, electromechanical dynamic simulations were directly compared to HIL simulation to validate control performance. This enabled detailed high-fidelity HIL simulations to support larger scale co-simulation for transactive controls.
- Reliability and resiliency
  - Self-healing control can improve reliability of the whole system, since the deployment of smart switches and self-healing control can enable the capability of autonomous service restoration after an outage.
  - A microgrid can improve reliability of the critical load it serves because it provides a path to restore the critical load during an outage.
  - Additional customer loads can be restored by non-utility owned DERs using transactive energy based reactive power control, since the transacted reactive power from DERs can improve the voltage profile of a feeder to enable additional service restoration.
  - Reliability indices of both the whole system and the critical loads are improved using the combined self-healing control, microgrid, and transactive energy, and the engagement of non-utility owned DERs through transactive energy demonstrates great potential in improving the reliability and resilience of distribution systems.

- Today's distribution grid planning tools mainly focus on self-healing control (i.e., optimal recloser placement) by considering reliability improvement. There is a need to upgrade the tools to fully consider the impacts of DERs, microgrids, and transactable reactive power of non-utility owned DERs on both reliability and resilience for future distribution grid planning.

- Engaging non-utility assets:
  - While OpenFMB works well for utility assets, it is not ideal for behind the meter assets. VOLTTRON is well suited for behind the meter assets and can be connected to an OpenFMB Harness.
  - To provide reactive power support based on the transactive energy approach, the locations of the DERs should be considered as well as the reactive power capacities of the DERs.
  - With reactive power support from non-utility DERs, the voltage in the system could possibly be improved. The amount of voltage that can be supported by the DERs depend on the reactive power capacities of the DERs (determined by inverter kVA rating and its kW power output) and the locations of the DERs. To ensure the voltage can be regulated within the nominal ranges, other reactive power resources should provide the support in addition to the support from the customer's DERs in case the support from the DERs is not sufficient.
  - Providing ancillary services will shorten the lifetime expectation of PV inverter semiconductors.
    - Providing reactive power support will increase the mean junction temperature and the junction temperature variation of the PV inverter diodes. This increased junction temperature will eventually lead to shorter diode lifetime.
    - The filtering inductor associated with a PV inverter can increase the conduction loss variation of diodes when the load is inductive. The extra power losses in diodes lead to shorter lifetime expectation of PV inverter diodes.
    - PV inverter manufacturers will need to account for the provision of ancillary services, and in particular reactive power support, in the design of future products in order to ensure that provision of ancillary services does not negatively impact the lifetime of their products.
  - Low frequency thermal cycling (caused by solar angle change, cloud cover, or temporary bird shading) is the leading factor of PV inverter semiconductor aging. The 60-Hz thermal cycling (caused by 60-Hz line currents) only contributes to a minor aging effect.

- Sustainability of deployment
  - Fundamentally, utilities today are still reliant a hub and spoke architecture with tertiary systems (e.g., DMS) dispatching set points primary systems (e.g., RTUs). This project demonstrated how a properly configured, and coordinated, secondary system can provide operational flexibility.
  - Any system must align with current operational practice and equipment used. To ensure sustainability and further adoption a project must use equipment that current utility staff are familiar with. Limit the changes to the operational workflow.
  - Operationally, the work must align with operational practices. Additionally, operational staff should be consulted during the development phase to ensure that developed solutions are practical.
  - Configuration management of firmware must be considered and supported. This is essential for coordination of centralized tertiary systems (e.g., DMS) with secondary systems in the field (e.g., microgrids).

- Coordinated configuration management is necessary for proper coordination and cyber-security.
- Time-stamping at the secondary level is essential and is lacking from DNP3. This is essential for protection and for many advanced functions.
- Any type of grid-forming battery requires multiple group settings for protection.
- Cyber security must be transport, just like controls. Operators must be able to

13.2 Concluding Comments and Specific Outcomes

As stated in the introduction, the primary goal of this project was to increase the resiliency of distribution systems at utilities around the nation by deploying flexible operating strategies that engage end-use assets as a resource. The primary goal was divided into three areas as shown below, each of which was accomplished.

- Develop the architectures and controls to accelerate the deployment of resilient and secure distribution concepts through the flexible operation of traditional assets, DERs, and Microgrids;
- Integrate the operations of switching devices, DERs, and microgrids to implement a flexible segment-based approach for operating distribution systems;
- Develop a scheme of flexible operations that will be applicable to a wide range of technology combinations.

Specific tasks within the project developed the architectural design for a layered control structure that enables the coordinated operation of centralized and distributed assets. Simulations were conducted in various platforms (including co-simulation, steady-state, HIL, and emulation) that examined various operational use-cases under normal and abnormal conditions. This included evaluations of system reconfiguration, transactive control signals, and evaluations of reliability and resiliency. A physical instantiation of the OpenFMB framework was created in the OpenFMB Harness, which allowed for the evaluate of interoperability and cyber security issues. This work was coordinated with Duke Energy's deployment of an inverter-based microgrid, centralized self-optimizing grid, and the deployment of new switching equipment that included OpenFMB adaptors. An integrated assessment plan was developed for a final field validation but was not conducted due to a backlog in the DER interconnection queue. However, Duke Energy plans to execute this as part of the field commissioning. Despite the lack of a field demonstration, specific outcomes of the project included:

- The Duke-RDS project was a proof of concept that successfully demonstrated that-coordination of distributed assets, using existing commercially off-the-shelf relays and open-source software, can produce a more flexible system.
- Using distributed control, via OpenFMB, it is possible to coordinate the operation of centralized and distributed systems so that all operational requirements are met; with the RDS project focusing specifically on ensuring protection coordination.
    - Peer-to-peer synchronization: The project was able to measure the variance across vendor devices to determine the potential accuracy of peer-to-peer in a heterogeneous environment.
    - Over the air firmware update: By establishing proxies within RTACs, the project was able to initiate upgrades of firmware for downstream reclosers from the back office, which eliminates truck rolls.

    - Cyber: Demonstrated encryption using OpenFMB from gateway devices to the RTACs (up to the last foot).
    - Recloser Integration: Established a recloser template for deploying and configuring OpenFMB.
- The work performed in the RDS project provided Duke Energy additional confidence to move forward with future SOG technologies in regions with moderate to high penetration of grid-tied distributed energy resources.
- Work from this project is directly supporting the follow-on GMLC project titled "Citadels", which is using the same OpenFMB Harness concept, but applying it to network microgrid operations on the Electric Power Board of Chattanooga (EPB) system.
- As described by Duke Energy in their 2020 Sustainability Report: "an innovative microgrid setup is being planned at the Anderson County Civic Center. A 5-MW battery will be grid-connected and will provide backup power at the facility, which supports several emergency service agencies and serves as the state's largest hurricane evacuation shelter."
- Pursuant to docket no. E-2 sub 1219 and 1193, Duke Energy will spend $302 million on expanding the deployment of self-optimized grid (SOG). As quoted in the PUC filing, the new SOG system must address the fact that "…when privately owned roof-top solar becomes widespread, a dynamic, automated, capacity-enabled two-way power flow grid will be essential". The Duke-RDS project, and the concepts developed as part of it, provides Duke-Energy with new technical capabilities to complement and enhance the coordination of SOG in regions with medium to high penetration of grid-tied distributed energy resources.

14.0 References

[1] K. P. Schneider, S. Laval, J. Hansen, R. Melton, L. Ponder, L. Fox, J. Hart, J. Hambrick, M. Buckner, M. Baggu, K. Prabakar, M. Manjrekar, S. Essakiappan, L. Tolbert, Y. Liu, J. Dong, L. Zhu, A. Smallwood, A. Jayantilal, C. Irwin, G. Yuan, "A Distributed Power System Control Architecture for Improved Distribution System Resiliency," *IEEE Access*, vol. 7 no. 1, pp. 9957-9970, Jan. 2019.

[2] OpenFMB Repository. Accessed: Jan. 2019. [Online]: https://openfmb.gitlab.io/

[3] S. Vadari, Electric System Operations: Evolving to the Modern Grid. Norwood, MA, USA: Artech House, 2013.

[4] A. Smallwood, S. Laval, J. Gibson, and F. Goodman, "Managing renewables and DERs with open field message bus," *Proc. DistribuTECH*, 2018, pp. 1–6.

[5] Anderson Sports and Entertainment Center. [Online]: http://www.andersonevents.com/

[6] EATON Industries. Yukon Feeder Automation Software. [Online]: http://www.cooperindustries.com/content/public/en/power_systems/solutions/self-healing/yukon_feeder_automation.html

[7] S. Katipamula, J. Haack, G. Hernandez, B. Akyol, and J. Hagerman, "VOLTTRON: An open-source software platform of the future," *IEEE Electrification Magazine*, vol. 4, no. 4, pp. 15–22, Dec. 2016.

[8] K. P. Schneider, F. K. Tuffner, M. Elizondo, J. Hansen, J. Fuller, and D. Chassin, "Adaptive dynamic simulations for distribution systems using multi-state load models," *IEEE Trans. on Smart Grid*, vol. 10, no. 2, pp. 2257-2266, Jan. 2019.

[9] J. Haack *et al.*, "VOLTTRON™: Using distributed control and sensing to integrate buildings and the grid," in *IEEE 3rd World Forum on Internet of Things (WF-IoT)*, 2016, pp. 228–232.

[10] P. Kritprajun *et al.*, "VOLTTRON™ agent development for enabling reactive power support of non-utility ders by integrating transactive energy approach," *IEEE Power and Energy Society General Meeting*, 2020.

[11] J. Xie and C.-C. Liu, "Multi-agent systems and their applications," *Journal of International Council on Electrical Engineering*, vol. 7, no. 1, pp. 188–197, Jul. 2017.

[12] "PyModbus", [Online]: https://pyModbus.readthedocs.io/en/latest/readme.html.

[13] J. Dong, L. Zhu, Y. Liu, and D. T. Rizy, "Enhancing distribution system monitoring and resiliency: A sensor placement optimization tool (SPOT)," *IEEE Power & Energy Society General Meeting (PESGM)*, 4-8 Aug. 2019, Atlanta, GA, USA.

[14] A. Garces, "A linear three-phase load flow for power distribution systems," *IEEE Transactions on Power Systems*, vol. 31, no. 1, pp. 827-828, Jan. 2016.

[15] F. Li, and N. Sabir, "Monte Carlo simulation to evaluate the reliability improvement with DG connected to distribution systems," in *Proceedings of the 8th WSEAS International Conference on Electric Power Systems, High Voltages, Electric Machines*, 2008, pp. 21-23.

[16] F. Shen, Q. Wu, and Y. Xue, "Review of service restoration for distribution networks," *Journal of Modern Power Systems and Clean Energy,* vol. 8, no. 1, pp. 1-14, 2020.

[17] IEEE Guide for Electric Power Distribution Reliability Indices, *IEEE Standard 1366*, 2004.

[18] P. Gautam, P. Piya, and R. Karki, "Resilience assessment of distribution systems integrated with distributed energy resources," *IEEE Trans. Sustainable Energy*, vol. 12, no. 1, pp. 338-348, Jan. 2021.

[19] Q. Dong, J. Dong, L. Zhu, Y. Liu, P. Kritprajun, *L. M. Tolbert*, S. Laval, K. Schneider, and Y. Liu "Resilience evaluation of advanced distribution grids with self-healing control, microgrid and transactable reactive power", accepted by *2021 IEEE Power and Energy Society General Meeting*.

[20] J. Dong, L. Zhu, P. Kritprajun, Y. Liu, L. M. Tolbert, J. Hambrick, K. Schneider, and S. Laval, "Quantitative evaluation of reliability improvement: case study on a self-healing distribution system," in *Proc. 2020 IEEE Power & Energy Society Innovative Smart Grid Technologies Conference (ISGT)*, 2020, pp. 1-5.

[21] Q. Dong, J. Dong, L. Zhu, P. Kritprajun, Y. Liu, Y. Liu, L. M. Tolbert, J. Hambrick, K. Schneider, and S. Laval, "Impact of self-healing control on reliability evaluation in distribution system with microgrid", *IEEE ISGT Europe 2021*, under review.

[22] J. Dong, L. Zhu, Q. Dong, P. Kritprajun, Y. Liu, L. M. Tolbert, J. Hambrick, Y. Xue, B. Ollis, B. Bhattarai, K. Schneider, and S. Laval, "Integrating transactive energy into reliability evaluation for a self-healing distribution system with microgrid", *IEEE Transactions on Sustainable Energy*, under revision.

[23] M. Woodhouse, R. Jones-Albertus, D. Feldman, R. Fu, K. Horowitz, D. Chung, D. Jordan, and S. Kurtz, "On the path to sun shot: the role of advancements in solar photovoltaic efficiency, reliability, and costs," *Natl. Renew. Energy Lab.*, NREL/TP-6A20-65872. May, 2016.

[24] A. Golnas, "PV system reliability: An operator's perspective," *IEEE J. Photovoltaics*, vol. 3, no. 1, pp. 416–421, 2013.

[25] L. M. Moore and H. N. Post, "Five years of operating experience at a large, utility-scale photovoltaic generating plant," *Prog. Photovoltaics Res. Appl.*, vol. 16, pp. 249–259, 2008.

[26] S. Yang, A. Bryant, P. Mawby, D. Xiang, L. Ran, and P. Tavner, "An industry-based survey of reliability in power electronic converters," *IEEE Trans. Ind. Appl.*, vol. 47, no. 3, pp. 1441–1451, 2011.

[27] W. Gunther, "Understanding and managing the effects of battery charger and inverter aging," *Brookhaven Natl. Lab.*, BNL-NUREG-47472, 1992.

[28] J. W. McPherson, Reliability Physics and Engineering Time-to-Failure Modeling. Springer, 2013.

[29] H. Wang, K. Ma, and F. Blaabjerg, "Design for reliability of power electronic systems," *Annu. Conf. IEEE Ind. Electron. Soc.*, pp. 33–44, 2012.

[30] Q. Yuan, R. Endoh, T. Ima, Y. Kajita and Y. Luo, "Failure mode verification of power IGBT under different thermal stress application conditions in power cycling test environment," *International Conference on Electronics Packaging and iMAPS All Asia Conference (ICEP-IAAC)*, Mie, 2018, pp. 367-370.

[31] B. P. Bhattarai *et al.*, "Enhancing distribution system resiliency through a novel transactive energy systems framework," in *IEEE Power and Energy Soc. Gen. Meet.*, Atlanta, GA, USA, 2019, pp. 1-5.

[32] J. Alam, R. Melton, A. Somani, and T. McDermott, "Transactive approach for engaging distribution network assets for voltage management in Southern California Edison distribution feeders," Pacific Northwest Natl. Lab., PNNL- 27650, Richland, WA, United States, 2018.

[33] Z. Liu, Q. Wu, S. Huang, and H. Zhao, "Transactive energy: A review of state of the art and implementation," in *IEEE PowerTech,* Manchester, UK, 2017, pp. 1–6.

[34] T. Broeer, J. Fuller, F. Tuffner, D. Chassin, and N. Djilali, "Modeling framework and validation of a smart grid and demand response system for wind power integration," *Appl. Energy*, vol. 113, pp. 199–207, 2014.

[35] S. Widergren, C. Marinovici, T. Berliner, and A. Graves, "Real-time pricing demand response in operations," *IEEE Power Energy Soc. Gen. Meet.*, pp. 1–5, 2012.

[36] S. Chen, J. Ping, X. Le, Z. Yan, X. Xu, L. Yao, and J. Xi, "Forming bidding curves for a distribution system operator," *IEEE Trans. Power Syst.*, vol. 33, no. 5, pp. 5389–5400, 2018.

[37] Z. Liu, Q. Wu, K. Ma, M. Shahidehpour, Y. Xue, and S. Huang, "Two-stage optimal scheduling of electric vehicle charging based on transactive control," *IEEE Trans. Smart Grid*, vol. 10, no. 3, pp. 2948–2958, 2019.

[38] H. Hao, C. D. Corbin, K. Kalsi, and R. G. Pratt, "Transactive control of commercial buildings for demand response," *IEEE Trans. Power Syst.*, vol. 32, no. 1, pp. 774–783, 2017.

[39] J. Lian, H. Ren, Y. Sun, and D. Hammerstrom, "Performance evaluation for transactive energy systems using double-auction market," *IEEE Trans. Power Syst.*, vol. 34, no. 5, pp. 4128–4137, 2019.

[40] J. C. Fuller, K. P. Schneider, and D. Chassin, "Analysis of residential demand response and double-auction markets," *IEEE Power Energy Soc. Gen. Meet.*, pp. 1–7, 2011.

[41] R. Adhikari, M. Pipattanasomporn, M. Kuzlu, and S. R. Bradley, "Simulation study of transactive control strategies for residential HVAC systems," *IEEE PES Innov. Smart Grid Technol. Conf. Eur.*, pp. 1–5, 2017.

[42] D. J. Olsen, M. R. Sarker, and M. A. Ortega-vazquez, "Optimal penetration of home energy management systems in distribution networks considering transformer aging," *IEEE Trans. Smart Grid*, vol. 9, no. 4, pp. 3330–3340, 2018.

[43] D. J. Hammerstrom, R. Ambrosio, J. Brous, T. A. Carlon, D. P. Chassin, J. G. DeSteese, R. T. Guttromson, G. R. Horst, O. M. Jarvegren, R. Kiesling, N. T. Le, P. Michie, T. V. Oliver, R. G. Pratt, S. E. Thompson, and M. Yao, "Pacific Northwest gridwise testbed demonstration projects, Part I Olympic Peninsula project," *Pacific Northwest Natl. Lab.*, PNNL- 17167, Richland, WA, 2007.

[44] K. P. Schneider, S. Member, J. C. Fuller, D. Chassin, and S. Member, "Analysis of distribution level residential demand response," *IEEE/PES Power Syst. Conf. Expo.*, pp. 1–6, 2011.

[45] A. Anurag, Y. Yang, and F. Blaabjerg, "Reliability analysis of single-phase PV inverters with reactive power injection at night considering mission profiles," in *IEEE Energy Convers. Congr. Expo.*, pp. 2132–2139, 2015.

[46] A. Anurag, Y. Yang, and F. Blaabjerg, "Thermal performance and reliability analysis of single-phase PV inverters with reactive power injection outside feed-in operating hours," *IEEE J. Emerg. Sel. Top. Power Electron.*, vol. 3, no. 4, pp. 870–880, 2015.

[47] M. Andresen, G. Buticchi, and M. Liserre, "Thermal stress analysis and MPPT optimization of photovoltaic systems," *IEEE Trans. Ind. Electron.*, vol. 63, no. 8, pp. 4889–4898, 2016.

[48] Y. Yang, H. Wang, and F. Blaabjerg, "Improved reliability of single-phase PV inverters by limiting the maximum feed-in power," *IEEE Energy Convers. Congr. Expo.* , pp. 128–135, 2014.

[49] Y. Yang, E. Koutroulis, A. Sangwongwanich, and F. Blaabjerg, "Pursuing photovoltaic cost-effectiveness: absolute active power control offers hope in single-phase PV systems," *IEEE Ind. Appl. Mag.*, vol. 23, no. 5, pp. 40–49, 2017.

[50] Victron Energy, "Technical notes on output rating, operating temperature and efficiency," 2018. [Online]. Available: https://www.victronenergy.com/upload/documents/Output-rating-operating-temperature-and-efficiency.pdf

[51] Guangzhou Sanjing Electric, "Sunfree solar inverter datasheet." [Online]. Available: https://www.lizard.cl/_PDF/invh400048/Sunfree_Hybrid_Solar_Inerter_4K5K.pdf

[52] Solaredge, "Temperature de-rating - technical note (Europe & APAC)," 2019. [Online]. Available: https://www.solaredge.com/sites/default/files/se-temperature-derating-note-na.pdf

[53] Y. Liu et al., "Aging effect analysis of PV inverter semiconductors for ancillary services support," in *IEEE Open Journal of Industry Applications*, vol. 1, pp. 157-170, 2020.

[54] Y. Liu, P. Kritprajun, L. M. Tolbert, J. Dong, L. Zhu, J. C. Hambrick, K. Schneider, B. P. Bhattarai, "Modeling of marginal cost for PV inverter ancillary services considering inverter aging under transactive energy framework," *IEEE PES General Meeting*, 2020.

[55] A. Sangwongwanich, Y. Yang, D. Sera, and F. Blaabjerg, "Lifetime evaluation of grid-connected PV inverters considering panel degradation rates and installation sites," *IEEE Trans. Power Electron.*, vol. 33, no. 2, pp. 1225–1236, 2018.

[56] C. Blake, and C. Bull, "IGBT or MOSFET: Choose wisely", *International Rectifier*. [Online]. Available: https://www.infineon.com/dgdl/Infineon-IGBT_or_MOSFET_Choose_Wisely-Article-v01_00-EN.pdf?fileId=5546d462533600a40153574048b73edc

[57] Semikron, "Thermal resistance of IGBT modules - specification and modelling," 2014. [Online]. Available: https://www.semikron.com/dl/service-support/downloads/download/semikron-application-note-thermal-resistances-of-igbt-modules-en-2014-11-30-rev-01/

[58] G. Lakkas, "MOSFET power losses and how they affect power-supply efficiency," *Analog Appl. J.*, Texas Instrument, AAJ 1Q 2016, pp. 22–26, 2016. [Online]. Available: http://www.ti.com/lit/an/slyt664/slyt664.pdf

[59] J. Guo, "Modeling and design of inverters using novel power loss calculation and dc-link current/voltage ripple estimation methods and bus bar analysis," Ph.D. dissertation, Dept. Electr., Comput. Eng., McMaster Univ., 2017.

[60] J. Alam, R. Melton, A. Somani, and T. DcDermott, "Transactive approach for engaging distribution network assets for voltage management in southern california edison distribution feeders," Pacific Northwest National Laboratory (PNNL), Richland, WA, United States, Tech. Rep., Jan. 2019.

[61] P. D. Reigosa, H. Wang, Y. Yang, and F. Blaabjerg, "Prediction of bond wire fatigue of IGBTs in a PV inverter under a long-term operation," *IEEE Trans. Power Electron.*, vol. 31, no. 10, pp. 7171–7182, 2016.

[62] H. Wang, K. Ma, and F. Blaabjerg, "Design for reliability of power electronic systems," *38th Annu. Conf. IEEE Ind. Electron. Soc.*, Montreal, QC, Canada, 2012, pp. 33-44.

[63] M. Andresen, G. Buticchi, and M. Liserre, "Thermal stress analysis and MPPT optimization of photovoltaic systems," *IEEE Trans. Ind. Electron.*, vol. 63, no. 8, pp. 4889–4898, 2016.

[64] Y. Yang, H. Wang, and F. Blaabjerg, "Improved reliability of single-phase PV inverters by limiting the maximum feed-in power," *IEEE Energy Convers. Congr. Expo.*, Pittsburgh, PA, USA, 2014, pp. 128-135.

[65] K. Givaki, M. Parker, and P. Jamieson, "Estimation of the power electronic converter lifetime in fully rated converter wind turbine for onshore and offshore wind farms," *7th IET Int. Conf. Power Electron. Mach. Drives,* Manchester, UK, 2014, pp. 1-6.

[66] A. Sangwongwanich, H. Wang, and F. Blaabjerg, "Reduced-order thermal modeling for photovoltaic inverters considering mission profile dynamics," *IEEE Open J. Power Electron.*, vol. 1, no. August, pp. 407–419, 2020.

[67] A. T. Bryant, P. A. Mawby, P. R. Palmer, E. Santi, and J. L. Hudgins, "Exploration of power device reliability using compact device models and fast electrothermal simulation," *IEEE Trans. Ind. Appl.*, vol. 44, no. 3, pp. 894–903, 2008.

[68] X. Ma, Y. Guo, L. Wang, and W. Ji, "Exploration of the reliability of automotive electronic power steering system using device junction electrothermal profile cycle," *IEEE Access*, vol. 4, pp. 7054–7062, 2016.

[69] L. Ceccarelli, R. M. Kotecha, A. S. Bahman, F. Iannuzzo, and H. A. Mantooth, "Mission-profile-based lifetime prediction for a SiC mosfet power module using a multi-step condition-mapping simulation strategy," *IEEE Trans. Power Electron.*, vol. 34, no. 10, pp. 9698–9708, 2019.

[70] G. Lv, W. Lei, M. Wang, C. Lv, and J. Zhao, "Reliability analysis and design of MMC based on mission profile for the components degradation," *IEEE Access*, vol. 8, pp. 149940–149951, 2020.

[71] Z. Shen and V. Dinavahi, "Real-time device-level transient electrothermal model for modular multilevel converter on FPGA," *IEEE Trans. Power Electron.*, vol. 31, no. 9, pp. 6155–6168, 2016.

[72] W. Wei, G. Xu, and X. Qiu, "A novel assessment method of gate oxide degradation based on IGBT turn-on losses for on-line reliability monitoring," *Int. Conf. Intell. Comput. Autom. Syst.*, Chongqing, China, 2019, pp. 243-248.

[73] Z. Wang, B. Tian, W. Qiao, and L. Qu, "Real-time aging monitoring for IGBT modules using case temperature," *IEEE Trans. Ind. Electron.*, vol. 63, no. 2, pp. 1168–1178, 2016.

[74] B. A. Mather, "Quasi-static time-series test feeder for PV integration analysis on distribution systems," *IEEE Power Energy Soc. Gen. Meet.*, San Diego, CA, USA, 2012, pp. 1-8.

[75] R. Dugan, T. Short, and K. Forsten, "Modeling energy efficiency alternatives for distribution system power delivery," *IET Conf. Publ.*, no. 550 CP, pp. 8–11, 2009.

[76] K. P. Schneider and J. C. Fuller, "Voltage control devices on the IEEE 8500 node test feeder," *IEEE PES Transm. Distrib. Conf. Expo. Smart Solut. a Chang. World*, pp. 1–6, 2010.

[77] Y. Liu *et al.* , "Quasi-static time series fatigue simulation for PV inverter semiconductors with long-term solar profile," *IEEE Open Journal of Power Electron.*, 2021

[78] Y. Liu *et al.* , "Quasi-static time series fatigue simulation for PV inverter semiconductors with long-term solar profile," *IEEE Power & Energy Society General Meeting (PESGM)*, 2021

[79] C. Blake, and C. Bull, "IGBT or MOSFET: Choose Wisely," *International Rectifier*. El Segundo, CA, USA, [Online]. Available: https://www.infineon.com/dgdl/Infineon-IGBT_or_MOSFET_Choose_Wisely-Article-v01_00-EN.pdf?fileId=5546d462533600a40153574048b73edc

[80] A. Anurag, Y. Yang, and F. Blaabjerg, "Thermal performance and reliability analysis of single-phase PV inverters with reactive power injection outside feed-in operating hours," *IEEE J. Emerg. Sel. Top. Power Electron.*, vol. 3, no. 4, pp. 870–880, 2015.

[81] Z. Wang, "Real-time internal temperature estimation and health monitoring for IGBT modules," Ph.D. dissertation, Dept. Electr., Comput. Eng., Univ. Nebraska-Lincoln, 2017.

[82] ASTM E1049, "Standard practices for cycle counting in fatigue analysis," *ASTM Stand.*, 2017.

[83] J. W. McPherson and E. T. Ogawa, *Reliability physics and engineering time-to-failure modeling*, 2nd ed. Springer, 2007.

[84] W. Lai, M. Chen, L. Ran, O. Alatise, S. Xu, and P. Mawby, "Low Δtj stress cycle effect in IGBT power module die-attach lifetime modeling," *IEEE Trans. Power Electron.*, vol. 31, no. 9, pp. 6575–6585, 2016.

[85] L. L. Schluter and H. J. Sutherland, "User's guide for LIFE2's rainflow counting algorithm," *Sandia Natl. Lab.*, SAND90-2259, 1991.

[86] A. Sangwongwanich, Y. Yang, D. Sera, and F. Blaabjerg, "Lifetime evaluation of grid-connected PV inverters considering panel degradation rates and installation sites," *IEEE Trans. Power Electron.*, vol. 33, no. 2, pp. 1225–1236, 2018.

[87] M. A. Miner, "Cumulative fatigue damage conference," *J. Appl. Mech.*, vol. 67, pp. A159–A164, 1945.

[88] M. F. Ashby and D. R. H. Jones, Engineering Materials 1—An Intro-duction to Properties, Applications and Design, 3rd ed. Oxford, U.K.: Butterworth-Heinemann, 2005, p. 228.

[89] H. Huang and P. Mawby, "A lifetime estimation technique for voltage source inverters," *IEEE Trans. Power Electron*., vol. 28, no. 8, pp. 4113– 4119, Aug. 2013.

[90] B. Palmintier, D. Krishnamurthy, P. Top, S. Smith, J Daily, J. Fuller, Jason, "Design of the HELICS high-performance transmission-distribution-communication-market co-simulation framework", 2017 Workshop on Modeling and Simulation of Cyber-Physical Energy Systems (MSCPES), Pittsburgh, PA, 2017.

[91] The California Energy Commission (CEC), "Inverter performance test summaries." https://www.gosolarcalifornia.ca.gov/.

[92] D. K. Setiawan, Y. Megantara and B. N. Syah, "Three phase inverter of UPS control system for harmonic compensator and power factor correction using modified synchronous reference frame," *2015 International Electronics Symposium*, Surabaya, 2015, pp. 15-19.

[93] M. Faisal, M. S. Alam, M. I. M. Arafat, M. M. Rahman and S. M. G. Mostafa, "PI controller and park's transformation based control of dynamic voltage restorer for voltage sag minimization," *2014 9th International Forum on Strategic Technology (IFOST)*, Cox's Bazar, 2014, pp. 276-279.

[94] E. Bogalecka, "Stability analysis of a double fed induction generator with the PLL controller," *Proceedings of IECON'94 - 20th Annual Conference of IEEE Industrial Electronics*, Bologna, Italy, 1994, pp. 67-72 vol.1.

[95] W. Du, F. K. Tuffner, K. P. Schneider, R. H. Lasseter, J. Xie, Z. Chen, and B. P. Bhattarai "Modeling of Grid-Forming and Grid-Following Inverters for Dynamic Simulation of Large-Scale Distribution Systems," *Accepted* IEEE Transactions on Power Delivery.

[96] X. Lu, K. Sun, J. M. Guerrero, J. C. Vasquez and L. Huang, "State-of-charge balance using adaptive droop control for distributed energy storage systems in dc microgrid applications," *IEEE Transactions on Industrial Electronics*, vol. 61, no. 6, pp. 2804-2815, June 2014.

[97] K. Oguchi and T. Osawa, "A simple digitally controlled three-phase PWM inverter using turn-off thyristors," *IEEE Transactions on Industrial Electronics and Control Instrumentation*, vol. IECI-28, no. 4, pp. 256-259, Nov. 1981.

[98] D. Pattabiraman, R. H. Lasseter. and T. M. Jahns, "Comparison of grid following and grid forming control for a high inverter penetration power system," *2018 IEEE Power & Energy Society General Meeting*, Portland, OR, 2018.

[99] O. Sugimoto, T. Koga, S. Sugawara, H. Hayashi and T. Nozaki, "High frequency carrier PWM inverter by static induction (SI) thyristor," *PESC '88 Record., 19th Annual IEEE Power Electronics Specialists Conference*, 1988, pp. 455-461 vol.1

Appendix A: Detailed Steps of Closing a Recloser for Load Transfer

This appendix contains the detailed descriptions on individual actions described in the use-case section of the report.

A.1 Steps to Manually Close a Recloser through the DMS

- Grid Engineer checks the voltage and phase angle difference across the recloser to be closed.
- If ΔV and $\Delta\theta$ are within limits, the Distribution Operator (DO) closes the recloser using the Distribution Management System (DMS).
- Signal to close from DMS is sent to the recloser via D-SCADA (currently DNP3 but may be DNP3/OpenFMB/GOOSE for field validation).
- Recloser closes.
- Information of a topology change is shared among all reclosers and substation RTU/Gateway in the community of interest via OpenFMB. (Currently this information is coordinated manually by Grid Engineer and Distribution Protection and Controls Engineer. The set points are then changed via DMS/D-SCADA).
- All reclosers in the community of interest evaluate if there is a need to change the set point group and do so if necessary (if less than a second, no reboot is required.) NOTE: Circuit breakers are transmission controlled devices and will not change set point groups in this manner.
- DMS is notified via D-SCADA of set point changes.

A.2 Steps to Manually Open a Recloser through the DMS

- The Grid Engineer checks that the operation of the recloser will not result in an unintentional outage.
- The DO opens the recloser via the DMS.
- A signal to open from DMS/D-SCADA is sent to the recloser (currently DNP3 but may be DNP3/OpenFMB/GOOSE for field validation).
- The recloser opens.
- Information of a topology change is shared among all reclosers and substation RTU/Gateway in the community of interest via OpenFMB. (Currently this information is coordinated through the DMS.)
- All reclosers in the community of interest evaluate if there is a need to change the set point group and do so if necessary (if less than a second, no reboot is required). NOTE: Circuit breakers are transmission controlled devices and will not change set point groups in this manner.
- DMS is notified via D-SCADA of set point changes.

A.3 Steps to Automatically Open a Recloser through the DMS

- The DMS verifies that the breaker needs to be opened as part of self-healing scheme. (Foundational work on how the segment-based self-healing scheme works still needs to be conducted.)
- The DMS generates an open signal.

- A signal to open from DMS is sent to the recloser (currently DNP3 but may be DNP3/OpenFMB/GOOSE for field validation).
- The recloser opens.
- Information of a topology change is shared among all reclosers in the community of interest via OpenFMB. (Currently this information is coordinated through the DMS.)

A.4 Steps to Automatically Open a Recloser via Protection

- The recloser senses one or more phase currents that indicates a potential fault.
- Local values for inverse-time curves are used to determine if the recloser should open on over-current.
- If inverse-time curves indicate that the recloser should open, it does so.
- After a preset time, the recloser automatically closes.
- If there is no longer a fault, then the recloser remains closed.
- If the fault current is still present, then the recloser will reopen.
- The reclosing operation will repeat depending on if the unit is a three-shot or five-shot unit.
- On the final shot, the reclose locks out.
- Information of a topology change is shared among all reclosers in the community of interest via OpenFMB. (Currently this information is coordinated through the DMS.)
- All reclosers in the community of interest evaluate if there is a need to change the set point group and does so if necessary (if less than a second, no reboot is required).

Appendix B: Simulation Results of TEA-2 in Use-Case #1-S3

TEA-2 is validated using the same Blue-sky scenario described in Section 6.1.3 and Section 10.2.2. There are two switch closing operations. The voltage magnitude differences in three phases of RCL-11 and RCL-9 are [63.89, 134.36, 278.70] (V) and [-133.64, 146.30, -128.77] (V), respectively. With respect to the 7.2 kV base voltage and 2% p.u. limit, the upper limit can be calculated as 144 V. Therefore, both voltage magnitude differences across RCL-11 and RCL-9 should be reduced for the safe switching operations.

The marginal supply curves ($/kvar vs kvar) submitted by DERs are shown in Figure B.1 (a). DSO converts these into the marginal supply curves ($ vs V), shown in Figure B.1 (b), using the voltage sensitivity at the node, to which these DERs are connected. In Figure B.2, the aggregated supply curve for market clearing is shown.

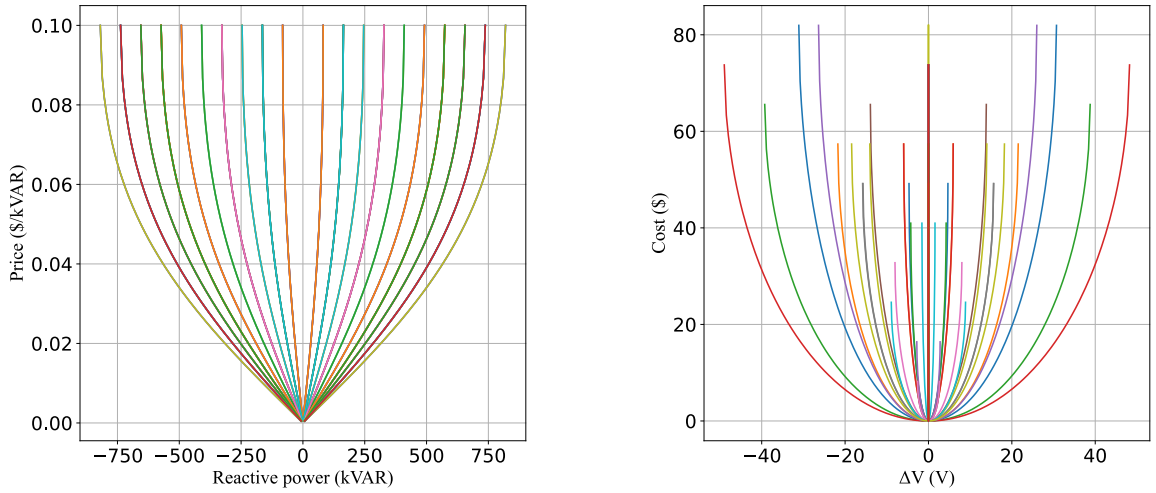

(a) (b)

Figure B.1: Individual supply curve.

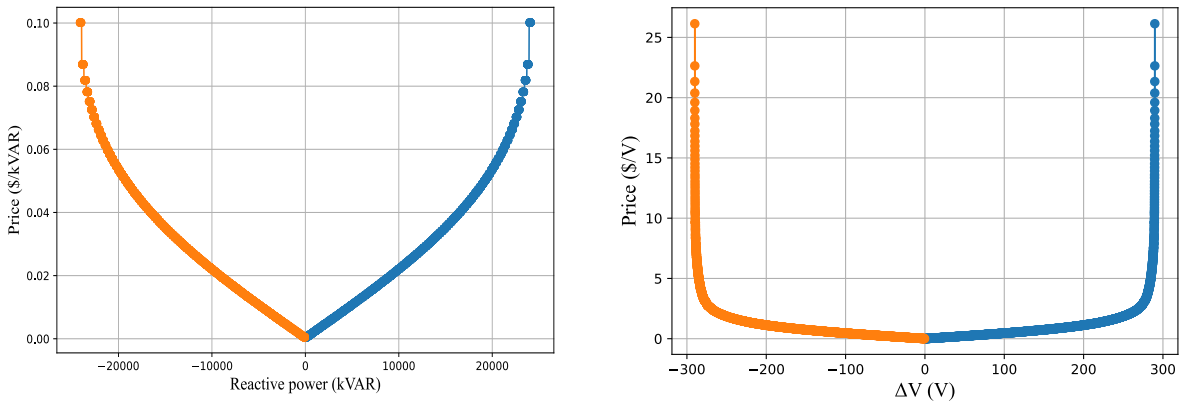

(a) (b)

Figure B.2: Aggregated supply curve.

DSO decides to increase the voltage magnitude of the S9-side node of RCL-11 (between S9 and S10) by 150V (i.e., 2.08% pu). With this the target ΔV (set as +150 V) and supply curve, the market clearing can be performed, as in Figure B.3. The settled price is 0.2442 ($/V). The reactive power contributions of DERs are shown in Figure B.4. As a result, the voltage magnitude difference across RCL-11 is reduced to [-95.37, -1.27, 131.65] (V) (i.e., [-1.32%, -0.02%, 1.83%] p.u.). The 2% p.u. limit is satisfied, and RCL-11 is closed.

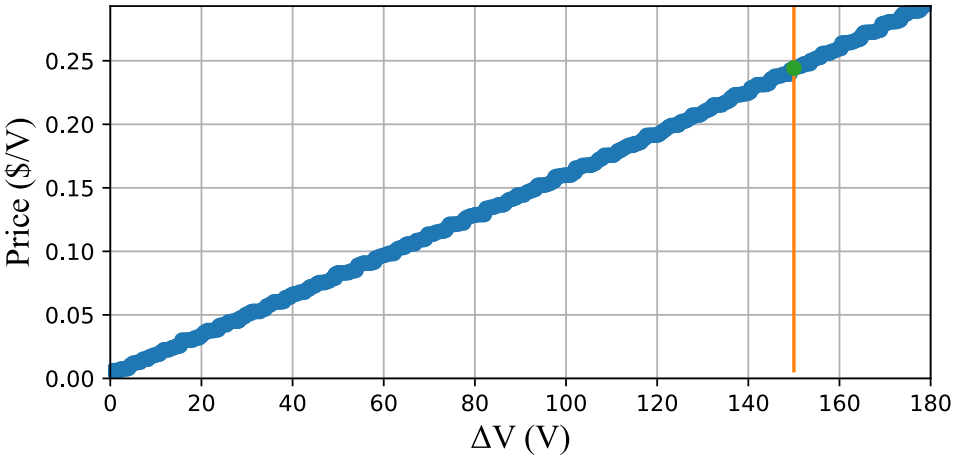

Figure B.3: TEA-2 RCL-11 - Market clearing.

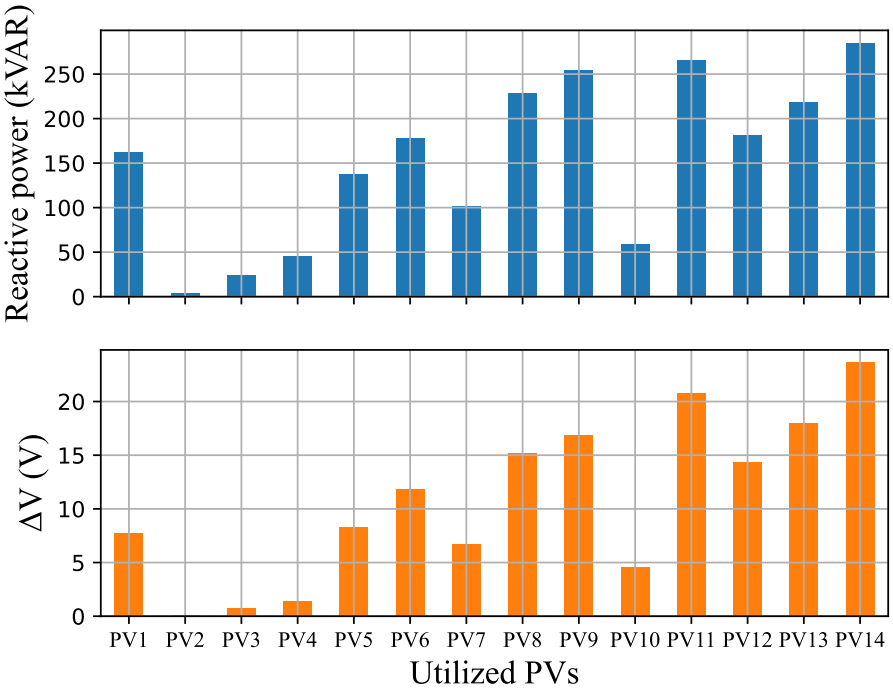

Figure B.4: TEA-2 RCL-11 - Reactive power from PVs.

Similarly, the voltage magnitude difference across RCL-9 should be checked before the closing operation. The values before and after applying TEA-2 are [-133.64, 146.30, -128.77] (V) (i.e., [-1.86%, 2.03%, -1.79%] p.u.) and [-138.59, 141.16, -133.66] (V) (i.e., [-1.92%, 1.96%, -1.86%]), respectively. DSO decides to increase the voltage magnitude of the S5-side node of RCL-9 (between S5 and S8) by 5 V. The aggregated supply curve is regenerated using the power flow results under updated topology (i.e., after closing RCL-11 and opening RCL-10). The market clearing and reactive power contributions of DERs are shown in Figure B.5 and Figure B.6, respectively. The settled price is 0.0275 ($/V). The 2% p.u. limit is satisfied, and RCL-9 is closed. TEA-2 resulted in closing two reclosers RCL-11 and RCL-9 which the utility was not able to close due to larger than acceptable voltage differential across their terminals. This demonstrates that DSO can use TEA-2 to address the local voltage constraints to support the additional switching operations.

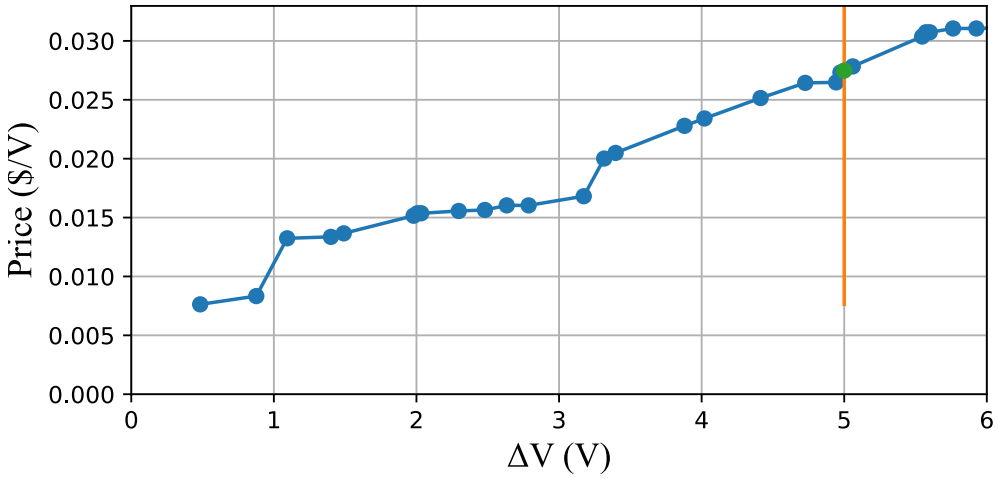

Figure B.5: TEA-2 RCL-9 - Market clearing.

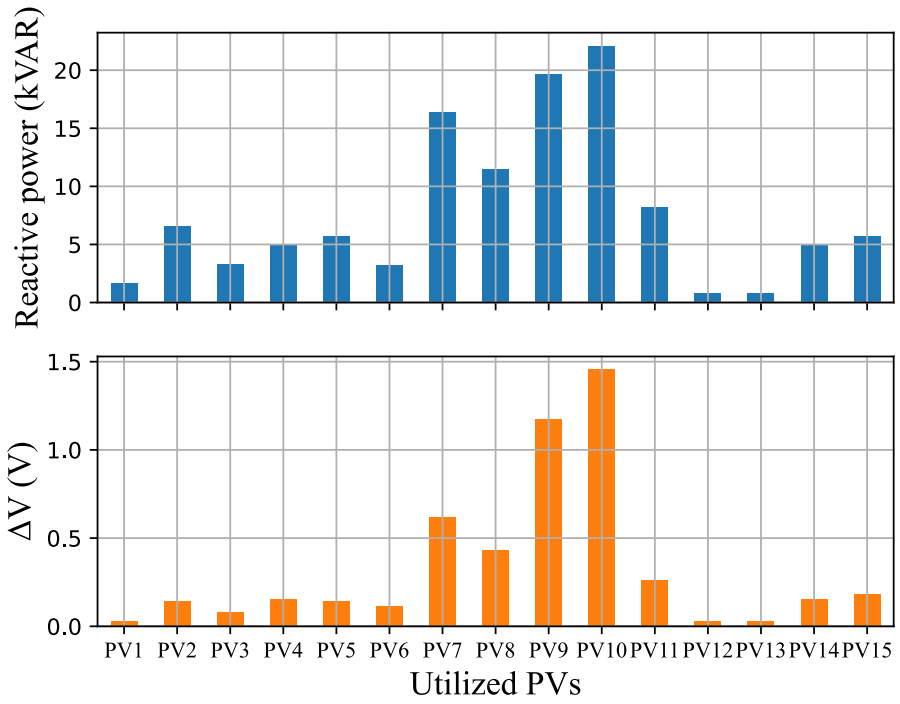

Figure B.6: TEA-2 RCL-9 - Reactive power from PVs.

Appendix C: Simulation Results of S2 for all Use-Cases

In this appendix, the S2 of each use-case is run using GridLAB-D only without the co-simulation framework. The power flow is solved with respect to each switching operation and the time dependent status values of switching devices and selected nodes are presented.

C.1 Simulation Results for Use-Case #1-S2

The scenario description is reported in 6.1.2. The status of switching devices and voltage magnitudes are shown in Figure C.1 and Figure C.2, respectively.

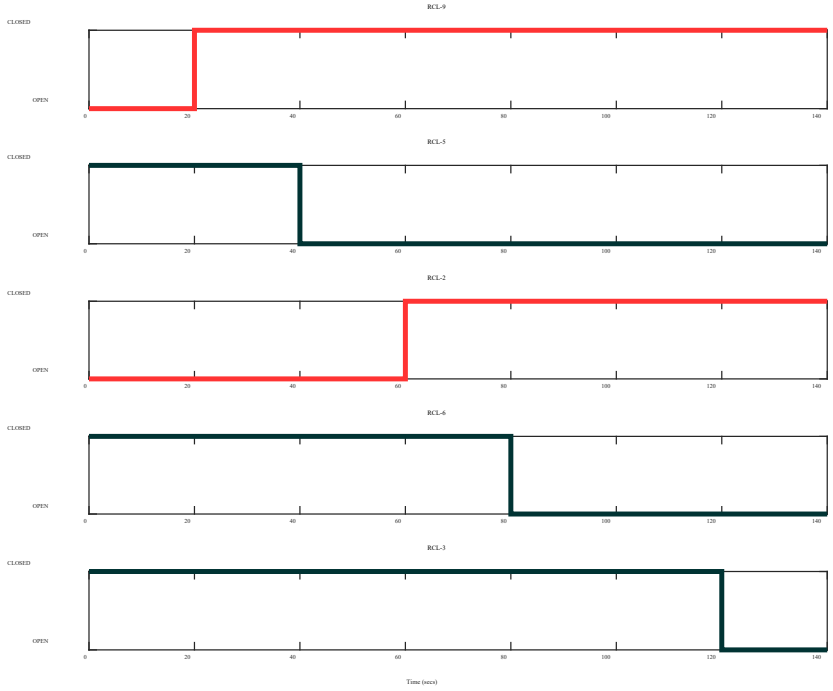

Figure C.1: Status of switching devices (UC#1-S2).

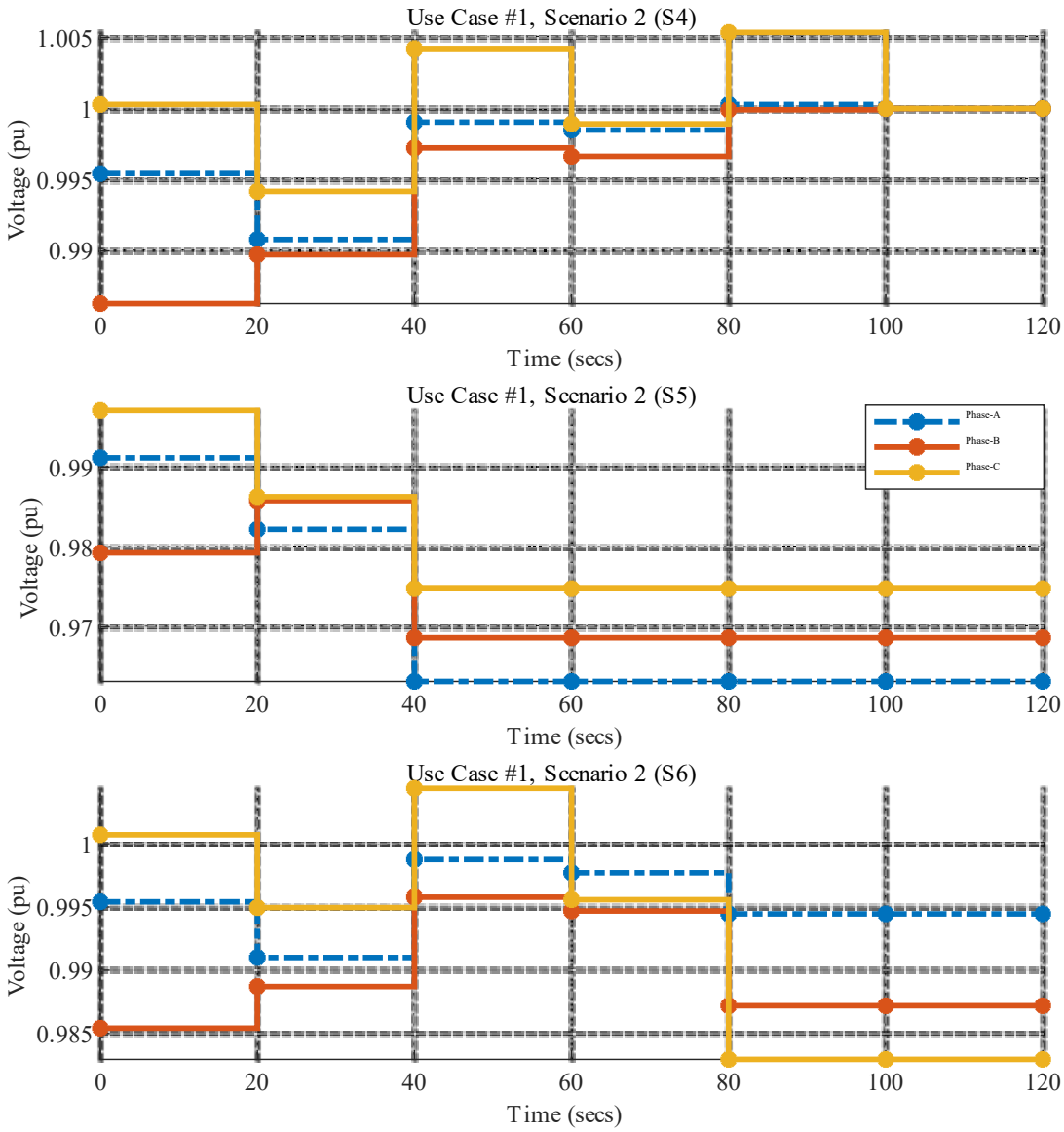

Figure C.2: Voltage Magnitude of selected nodes of interested segments (UC#1-S2).

C.2 Simulation Results for Use-Case #2-S2

The scenario description is reported in 6.2.2. The status of switching devices and voltage magnitudes are shown in Figure C.3 and Figure C.4, respectively.

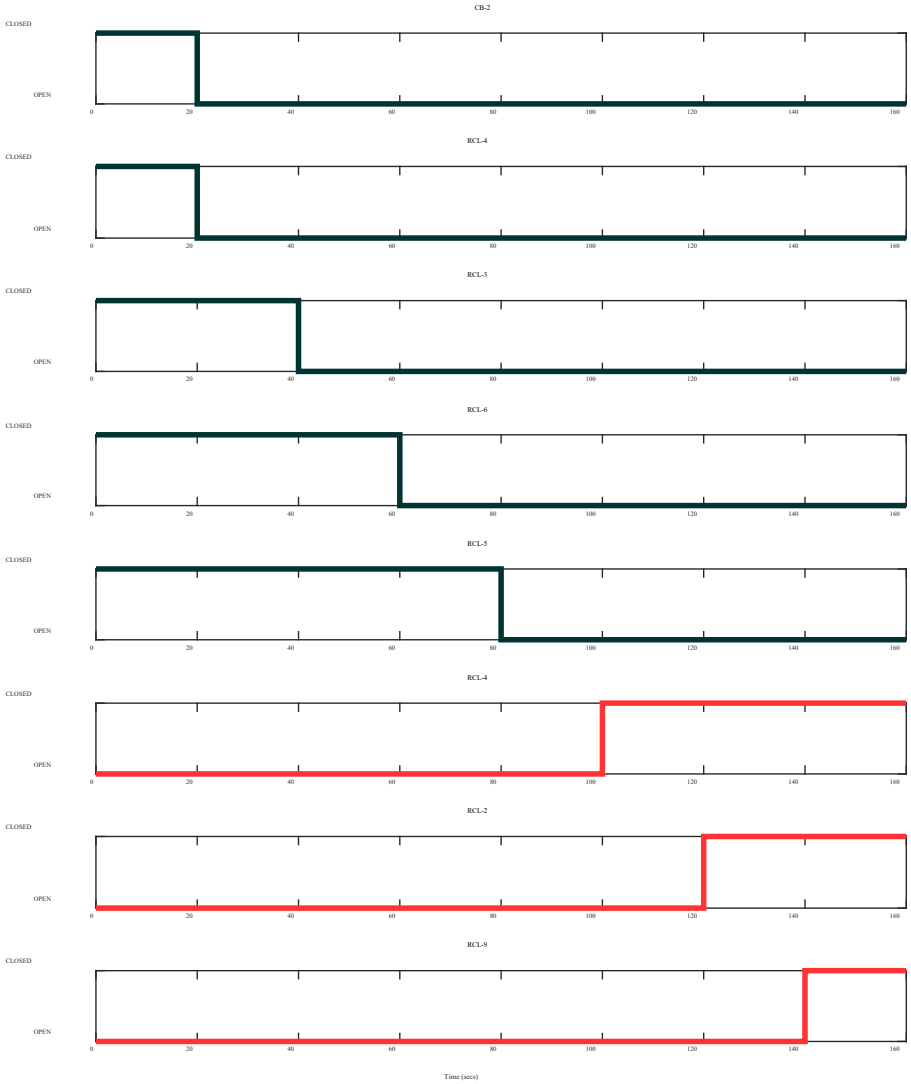

Figure C.3: Status of switching devices (UC#2-S2).

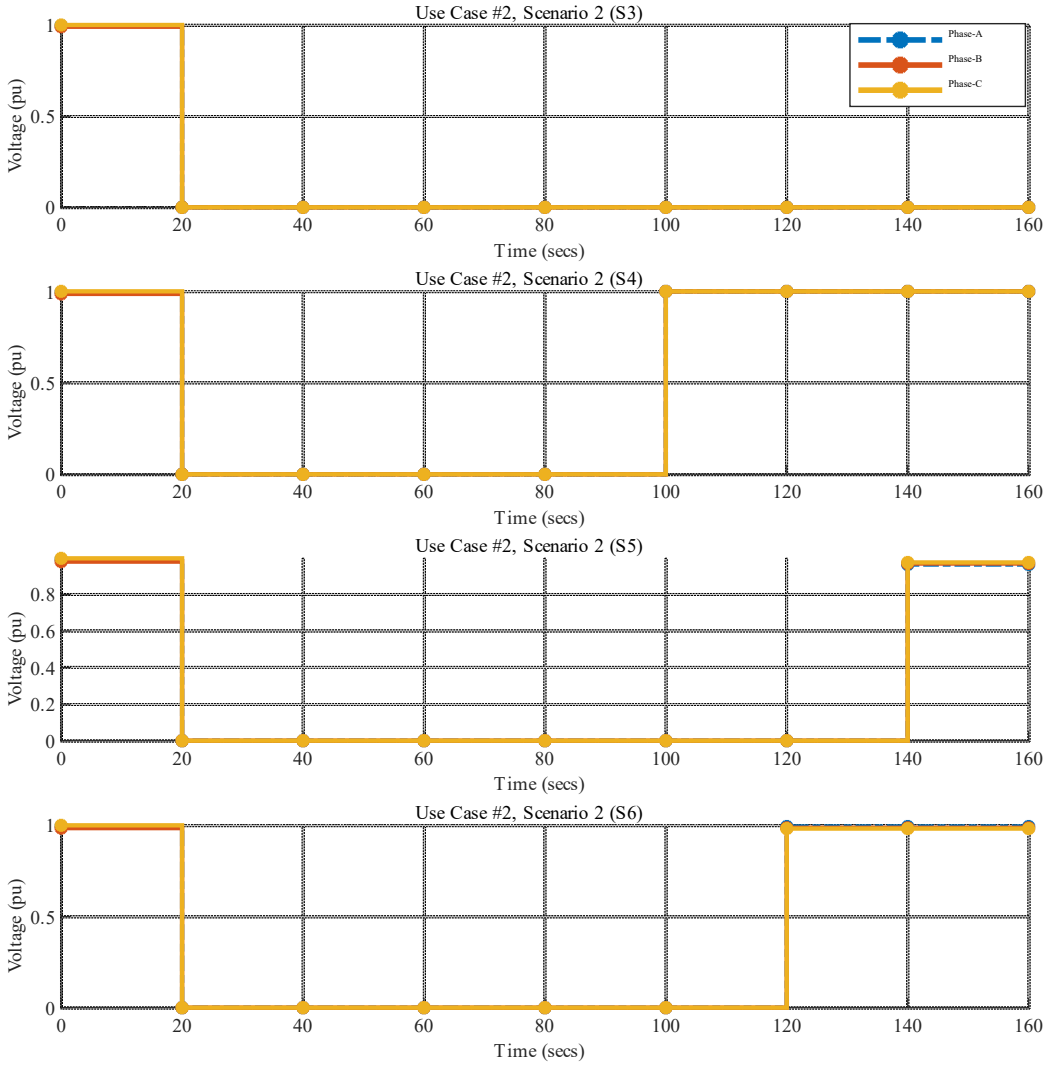

Figure C.4: Voltage magnitudes of selected nodes of interested segments (UC#2-S2).

C.3 Simulation Results for Use-Case #3-S2

The scenario description is reported in 6.3.2. The status of switching devices and voltage magnitudes are shown in Figure C.5 and Figure C.6, respectively.

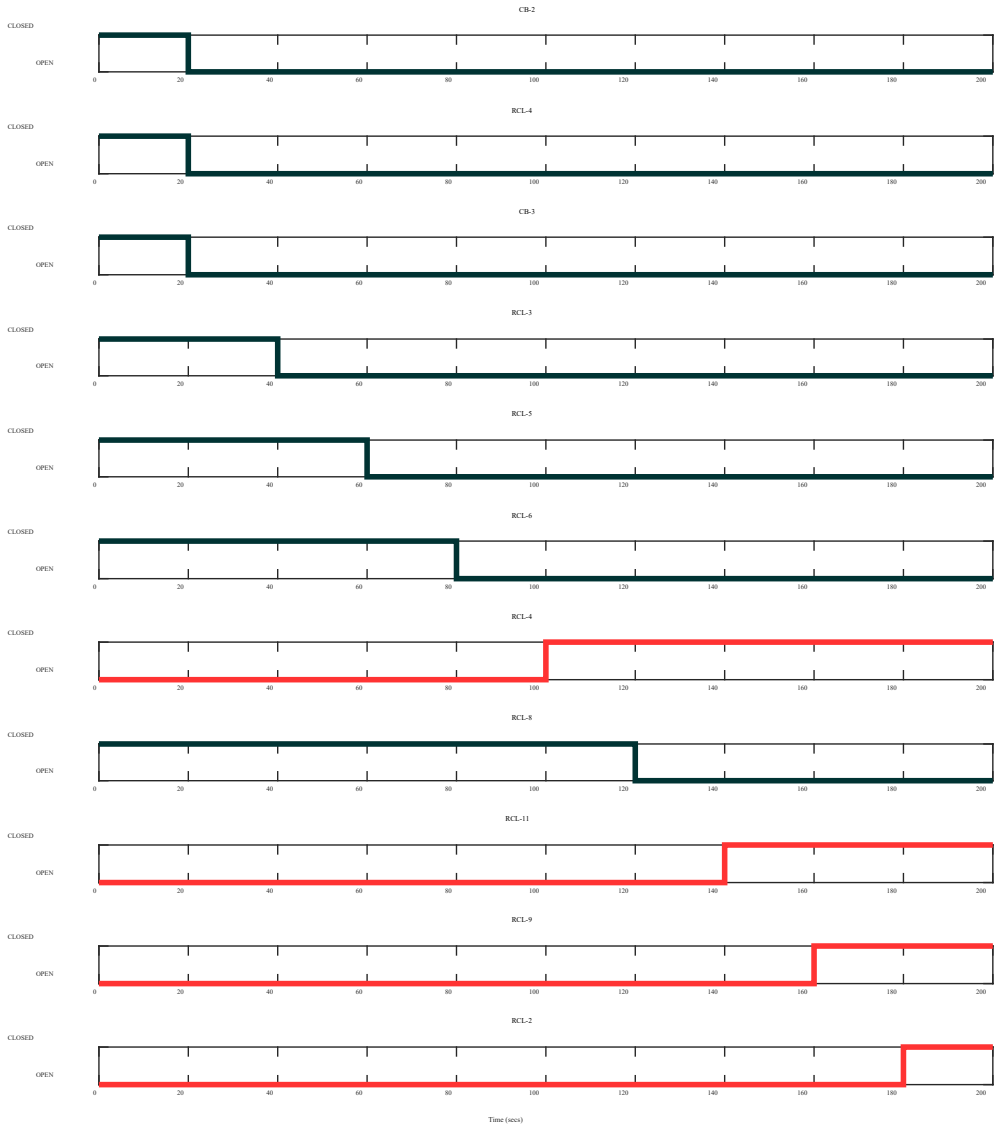

Figure C.5: Status of switching devices (UC#3-S2).

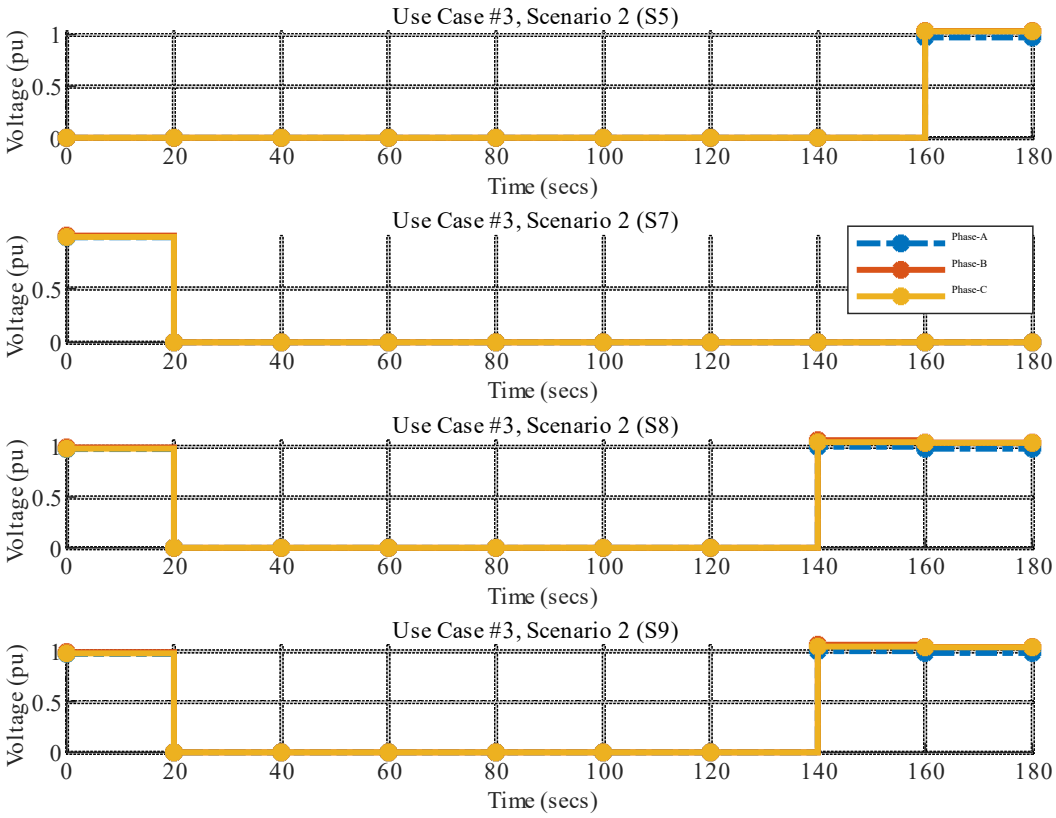

Figure C.6: Voltage magnitudes of selected nodes of interested segments (UC#3-S2).

C.4 Simulation Results for Use-Case #4-S2

The scenario description is reported in 6.4.2. The status of switching devices and voltage magnitudes are shown in Figure C.7 and Figure C.8, respectively.

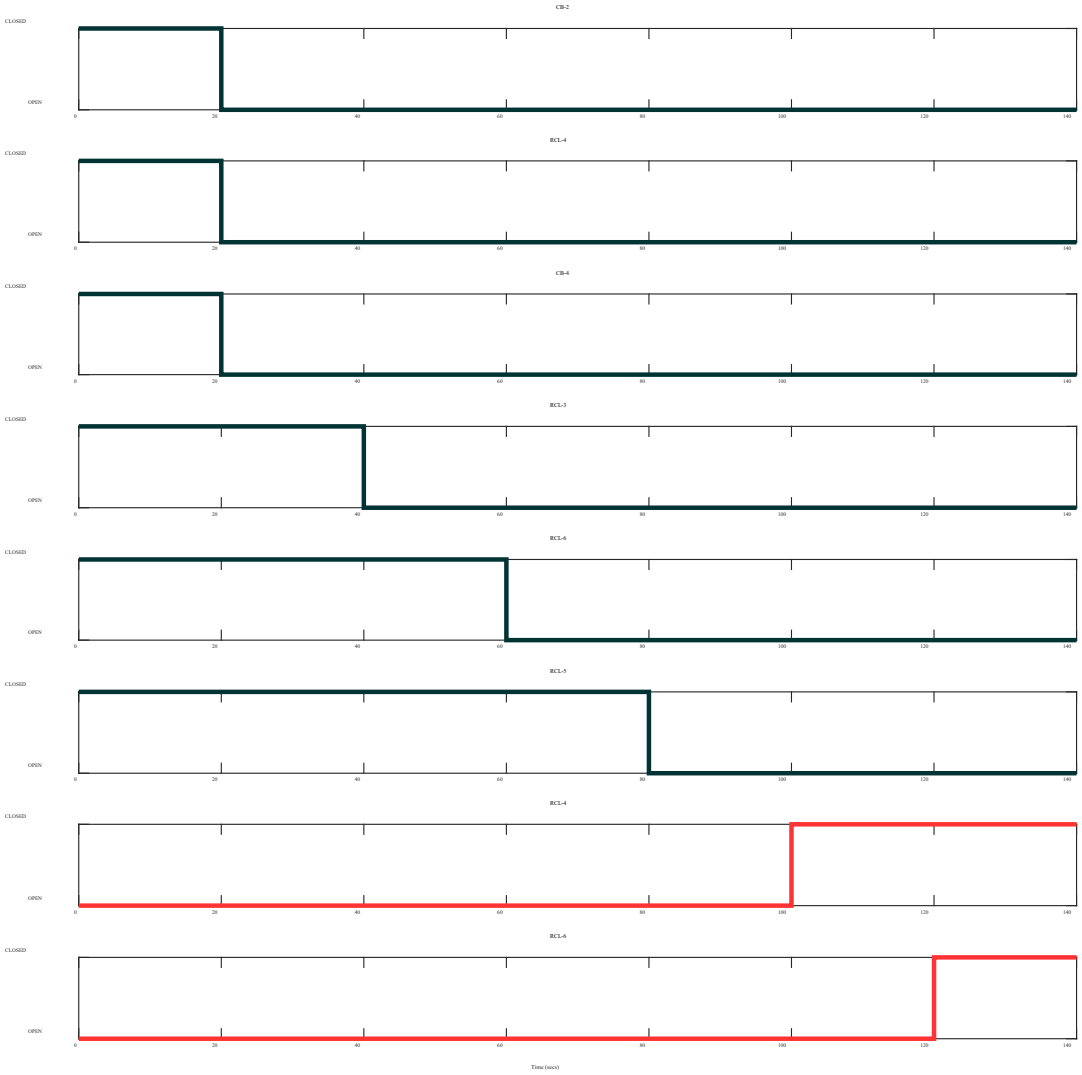

Figure C.7: Status of switching devices (UC#4-S2).

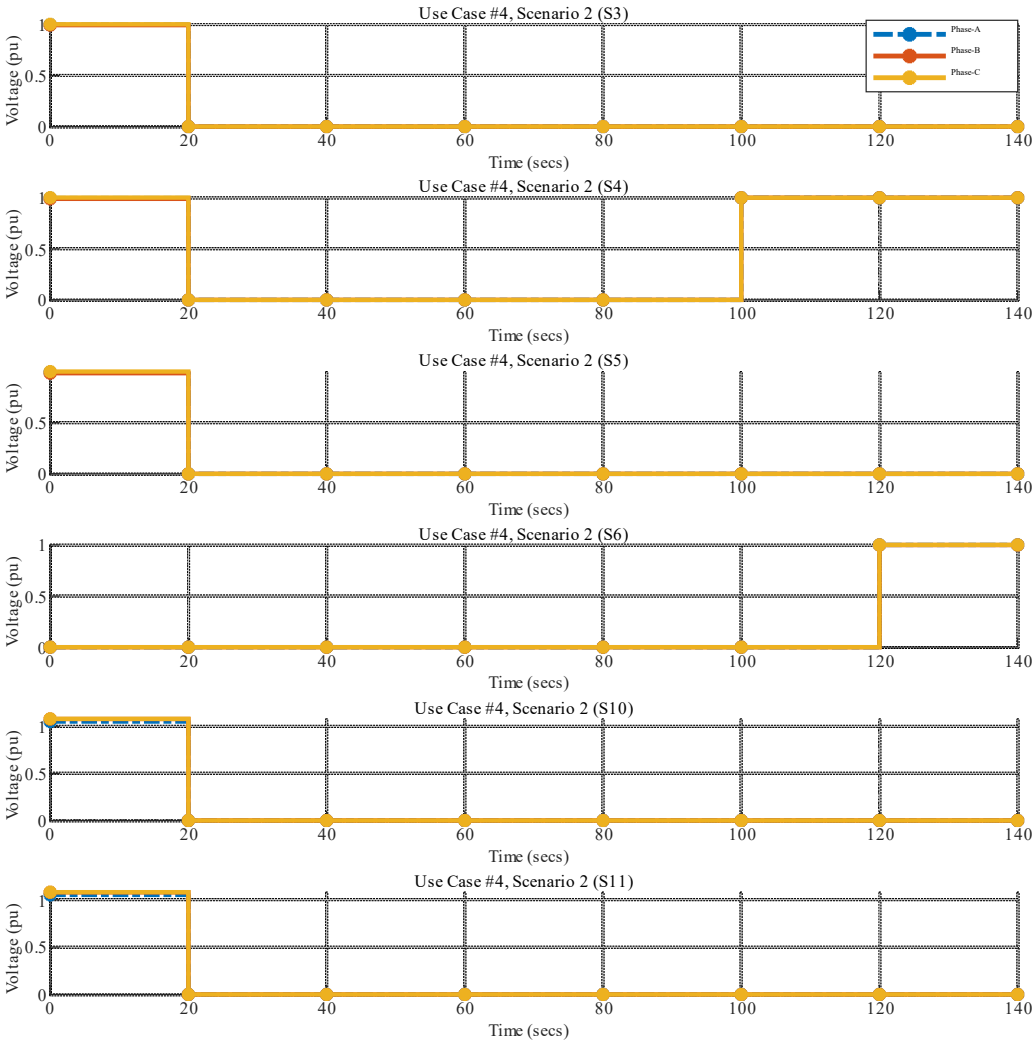

Figure C.8: Voltage magnitudes of selected nodes of interested segments (UC#4-S2).

Appendix D: Valuation Analysis for the Full Technology Suite

To support the broader RDS effort, representatives of a separate Laboratory Valuation Analysis Team estimated the relevant benefits that the RDS demonstration project could generate for the grid and society as a whole. The broader valuation effort will be presented in a separate report, which will include a wider range of value streams and sensitivity analysis related to the uncertain magnitude of performance and monetary benefits. This appendix section presents a subset of the results from that valuation analysis, including two dominant sources of societal value.

First, we estimate the value associated with the outcomes of the project's reliability simulations (Section 7.0), which reflect how the demonstrated technologies could improve reliability metrics for the local distribution network customers. This source of value is rooted in avoided outage costs for customers, based on reductions in both the frequency and length of short-duration power interruptions for residential, commercial, and industrial customers.

Second, we estimate the resilience benefits associated with the 5-MW microgrid providing backup power to TCC, which supports several emergency service agencies and serves as the state's largest hurricane evacuation shelter. This analysis quantifies the likelihood of TCC surviving power interruptions of different duration.

D.1 Valuing Reliability Benefits Through Avoided Outage Costs

Reliability benefits include the value of avoiding or reducing the impacts of routine faults that lead to short-duration outages (momentary to hours long) on the distribution network. The benefits of avoided outages are measured in dollars and depend on the number of outages prevented, the outage duration reduced, and the cost of outages to customers. Our process for valuing reliability benefits consists of three steps:

1) Determining expected reductions in the average frequency (SAIFI) and duration (SAIDI) of short-duration outages on an annual basis due to the RDS technologies;
2) Using customer composition to determine SAIFI and SAIDI reductions by customer type; and
3) Using damage functions for each customer type to convert SAIFI and SAIDI reductions into dollar savings.

The first step in our process was completed by the University of Tennessee at Knoxville, as described in Section 7.0 of this report. The results of their reliability simulations served as an input to this portion of our valuation analysis.

Table 7.6 (in the body of this report) shows SAIFI and SAIDI values across a range of scenarios. The Base Case assumes no RDS technologies, so the change in reliability indices across scenarios allows for the isolation of the reliability benefits associated with the RDS technologies. However, the three additional scenarios are cumulative, so the microgrid SAIFI and SAIDI numbers include the self-healing upgrades as well as the microgrid.

For the second step in our process, it is necessary to distinguish between the different customer types, each of which will experience different costs associated with a power interruption. In general, residential customers report lower costs (or damages) associated with power interruptions compared to commercial and industrial customers. For our estimates of the reliability benefits, we assume that 15% of the relevant customers are residential customers, 12% are small commercial and industrial (C&I) customers, and the

remainder are medium-to-large C&I customer. These customer types align with those defined in the ICE calculator, which estimates outage costs by state and customer type.

For the third step of our process, we develop an appropriate customer damage function for each customer type based on the ICE calculator for the state of South Carolina.[1] Table D.1 presents the resulting fixed and variable outage costs by customer type, which differentiate between outage costs that depend on outage duration versus those that do not (i.e., the latter are incurred immediately at the start of the outage). For example, damage to machinery from a loss of power is largely independent of outage duration, whereas lost productivity scales (or grows) with outage duration.

To reflect these different damage categories, we model outage costs as consisting of a fixed component (FC, which does not vary with outage duration) and a variable component (VC, which increases linearly with outage duration).[2,3] Fixed costs are given by the ICE calculator cost of a one-minute outage and variable costs are given by the ICE calculator cost of a one-hour outage minus fixed costs.

Table D.1: Fixed and Variable Costs Estimated from ICE Calculator

Customer Type	Fixed Costs $/kW	Variable Cost $/kW-hour
Residential	3.63	0.81
Small C&I	130.71	73.14
Med + Large C&I	22.68	8.94
Weighted Average	**32.55**	**15.29**

Total annual reliability benefits are then estimated based on the following equation:

$$Reliability\ Benefits = (\Delta\ SAIFI \times FC + \Delta\ SAIDI \times VC) \times (1 - T) \times PWF.$$

Beyond the monetary value associated with improvements in SAIFI and SAIDI (captured in parentheses in the equation above), the total reliability benefits are reported on a present value basis. In particular, we assume a tax rate (T) of 25.7% and a present worth factor (PWF) of 14.88, derived from assuming a 3% discount rate and a 20-year project life. All values are then converted to 2021 dollars using the consumer price index.

Table D.2 displays the estimated present value of reliability benefits per MW of customer load covered, where customer load is average load throughout the year. In addition, it shows the incremental value of each RDS technology. Applying the incremental savings per MW of each component to the total average system load (85MW), the value of reliability associated with the self-healing upgrades is approximately $48,975,000. Layering on the microgrid unlocks a relatively modest amount of incremental reliability value ($979,000) because it only covers a subset of the loads on the system. Finally, the addition of transactive energy services generates the greatest incremental reliability value. It is on the order of $113,383,000, which is beyond the value enabled by combination of the self-healing and microgrid upgrades.

[1] https://icecalculator.com

[2] Ericson and Lisell, A Flexible Framework for Modeling Customer Damage Functions for Power Outages (2018) *Energy Systems*

[3] Sullivan et. al., Updated Value of Service Reliability Estimates for Electric Utility Customers in the United States (2015) *LBNL.*

Table D.2: Estimated Present Value of Reliability Savings per MW of Load Covered

Scenario	Self-Healing	With Microgrid	With TES (60%)
Savings per MW Avg. Load	$576,173	$587,694	$1,921,618
Incremental Savings per MW	$576,173	$11,521	$1,333,924

D.2 Valuing of Resiliency Benefits

In contrast to the reliability benefits described in the previous section, the "resilience value" of the demonstrated technologies is rooted in the extent to which they improve the electricity distribution system's ability to prepare for, absorb, adapt to, and/or recover from major disruptive events. Estimating improvements in resilience (and the resulting value) is complex, in part, because different strategies can contribute to the mitigation of major disruptive events. For example, the self-healing grid technologies can increase the flexibility of the grid, thus providing resilience through the increased ability to absorb and adapt to a major disruption.

In this section, we adopt a definition of resilience that addresses the ability to recover and absorb major disruptive events by providing backup power to a facility that supports several emergency service agencies and serves as the state's largest hurricane evacuation shelter. In particular, the focus of this analysis is on the resilience value of the project's microgrid component, which was designed to provide approximately 30 hours of backup power to TCC. The resulting societal benefits may be quite substantial, but it is challenging to assign a dollar associated with command post for service providers and an emergency shelter to citizens who have been displaced by an extreme weather event. Therefore, this analysis culminates at the determination of a system performance metric—hours that critical load can be met by the microgrid. Future work will attempt to translate this performance metric into a corresponding societal value.

To begin quantifying the resilience benefits of the 5-MW microgrid, we utilize the Renewable Energy Integration & Optimization (REopt) platform.[1,2,3] REopt is a mixed-integer linear program that optimizes energy asset system size and dispatch. In this case, we developed an instance of REopt Lite that reflects the microgrid's battery size (5-MW/5-MWh) and historical hourly electricity demand.[4] We then performed the REopt Lite optimization—augmented with novel outage uncertainty and resilience valuation capabilities—over the course of a typical year.[5]

The critical load is assumed to be equal to the hourly load profile for TCC. Although the planned battery for the actual microgrid is rated at 5-MW/5-MWh, we imposed limits on how much of the battery can be used based on preferred (or required) state of charge bounds and uncertain auxiliary loads associated with the battery itself.[6] The resulting effective battery sizes explored include 4-MWh, 3-MWh, and 2-MWh. These battery sizes are not meant to be realistic; instead, they are designed to explore how sensitive the

[1] National Renewable Energy Laboratory, "REopt: A Platform for Energy System Integration and Optimization", [Online]: https://www.nrel.gov/docs/fy17osti/70022.pdf

[2] National Renewable Energy Laboratory, "REopt Energy Integration & Optimization Homepage", [Online]: https://reopt.nrel.gov/ (accessed May 27, 2020)

[3] E. Elgqvist, "REopt Lite Web Tool: Capabilities and Features," p. 30.

[4] REopt is designed to determine optimal investments that maximize net present value, including considering of a value of resilience; however, for the present analysis, we set existing PV and the potential for additional PV or battery capacity to zero, so the system being evaluated is restricted to the planned microgrid for TCC.

[5] National Renewable Energy Laboratory, "NREL/REoptLite", [Online]: https://github.com/NREL/REoptLite (accessed May 26, 2021).

[6] F. M. Gatta, A. Geri, S. Lauria, M. Maccioni and F. Palone, "Battery energy storage efficiency calculation including auxiliary losses: Technology comparison and operating strategies," *2015 IEEE Eindhoven PowerTech*, Eindhoven, Netherlands, 2015

survivability duration is to the magnitude of battery auxiliary loads and state of charging restrictions (the latter of which may be relaxed in the case of a major disruptive event).

Building off of these input assumptions, the REopt Lite web optimization tool seeks to maximize economic benefits, accounting for grid services and the value of resilience. Most often, REopt is configured to determine the optimal battery dispatch to maximize economic benefits, with resilience value being addressed through post-processing. Because the evaluated microgrid is primarily being built to provide backup power, we optimize the battery dispatch to prioritize resilience value; in other words, we assume that the battery is operated in such a way that it is fully charged prior to a grid outage event. Therefore, by comparing the available battery energy to the size of TCC's critical loads for all hours of the year, we can determine the outage duration that the evaluated microgrid could sustain.

Figure D.1 summarizes the outcomes of this analysis for all effective battery sizes explored. In general, the duration of outage that can be survived intuitively scales with the amount of available energy. The average outage duration that the evaluated microgrid can sustain exceeds 30 hours in all cases, but the ultimate resilience performance depends on the effective battery size and the hour of the year in which the outage begins. For an effective battery size of 4-MWh, the microgrid can meet typical TCC loads for at least one day (in the summer, when load is relatively high) and up to five days (for all other times of the year). For an effective battery size of 2-MWh (assuming higher auxiliary loads), the durations of outage over which critical loads could be sustained are reduced to a range of less than one day to up to three days.

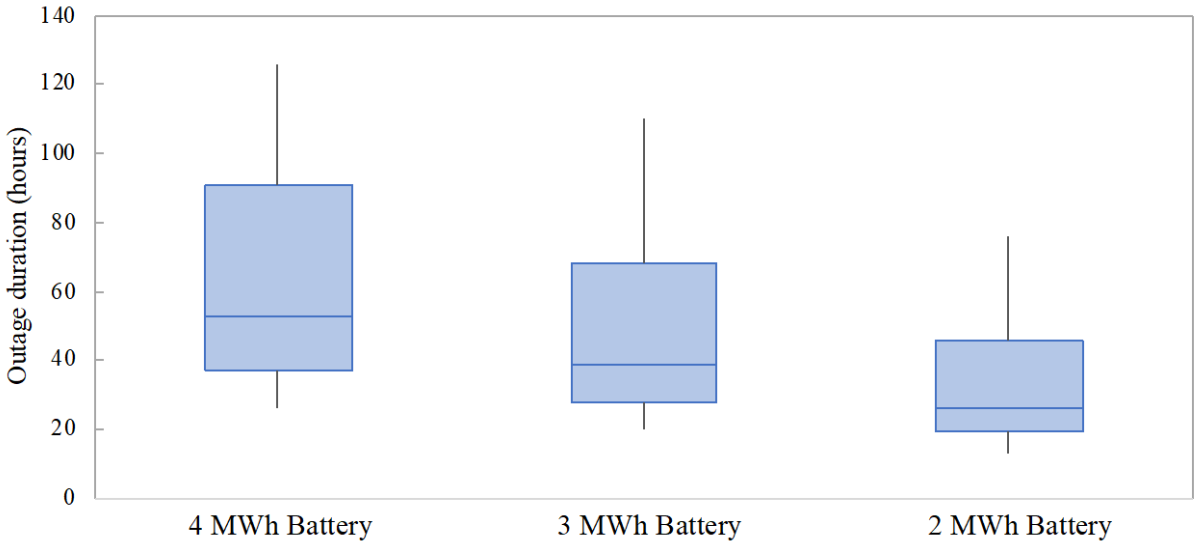

Figure D.1: Likelihood of surviving grid Interruptions of various durations

The simulated resilience benefits of the evaluated microgrid are specific to the inputs considered, including the effective battery size, the size (and shape) of TCC's critical loads, and the prioritization of resilience benefits over economic dispatch. Many other factors would influence the resilience performance of the microgrid but were not considered here:

- If TCC load increases when it serves as a hurricane shelter, then the outage durations that could be survived by the planned microgrid would be reduced.
- If the auxiliary loads associated with the battery component are weather-dependent, then the duration of outage that the microgrid could sustain would vary from the results presented here (which effectively assume a fixed auxiliary load throughout the year).

- If the battery component of the microgrid is used for higher-energy services (e.g., arbitrage), then it may not be appropriate to assume a full (or near-full) state of charge at the onset of a major disruptive event, particularly if the event is unpredictable. However, given the forecast ability of hurricane events, the assumption of a full state of charge may be valid for the primary resilience use case of the microgrid.
- If PV were added to the microgrid and remained connected during a major disruption, then the battery could be re-charged each day and sustain longer-duration outages.

Appendix E: Complete List of Project Publications

Throughout the project there were numerous publications. The following sections contain the comprehensive list of conference papers, journal papers, and trade publications associated with the project. Theis list contains the published papers at time the project was completed, 9/30/21 It is expected that there will be additional publications completed as follow-on activities after the completion of the project, but those are not included here.

E.1 Conference Papers

[1] S. Essakiappan, R. Sarup, R. Mbacke, M. Manjrekar, S. Laval, and K. Schneider, "Coordinated Power and Energy Management Using Cluster of Microgrids to Improve Grid Availability and Resiliency", *in proc. IEEE Energy Conversion Congress and Exposition*, 2019.

[2] B. P. Bhattarai, J. Alam, J. Hansen, K. P. Schneider, N. Radhakrishnan, and W. Du, "Enhancing Distribution System Resiliency through a Novel Transactive Energy System Framework," *in proc. IEEE PES General Meeting*, 2019.

[3] Y. Liu, P. Kritprajun, L. M. Tolbert, J. Dong, L. Zhu, J. C. Hambrick, K. Schneider, B. P. Bhattarai, "Modeling of Marginal Cost for PV Inverter Ancillary Services Considering Inverter Aging under Transactive Energy Framework," *in proc. IEEE Power and Energy Society General Meeting*, 2020.

[4] P. Kritprajun, J. C. Hambrick , L. M. Tolbert, J. Dong, L. Zhu, Y. Liu, B. Bhattarai, K. Schneider, S. Laval, "VOLTTRON Agent Development for Enabling Reactive Power Support of Non-Utility DERs by Integrating Transactive Energy Approach," *in proc. IEEE Power and Energy Society General Meeting*, 2020.

[5] J. Dong, Lin Zhu, P. Kritprajun, Y. Liu, L. M Tolbert, J. C. Hambrick, K. Schneider, S. Laval, "Quantitative Evaluation of Reliability Improvement: Case Study on a Self-healing Distribution System," *in proc. IEEE Innovative Smart Grid Technologies*, 2020.

[6] P. R. Chowdhury, P. K. Sahu, S. Essakiappan, M. Manjrekar, K. P. Schneider, and S. Laval, "Power Quality and Stability in a Cluster of Microgrids with Coordinated Power and Energy Management" *in proc. IEEE Industry Applications Society Annual Meeting*, 2020.

[7] P. Kritprajun, J. C. Hambrick, L. M. Tolbert, Y. Liu, J. Dong, L. Zhu, Q. Dong, K. Schneider, "Reactive Power Allocation of PV Inverters for Voltage Support in Power Systems Based on Transactive Energy Approach," *in proc. IEEE Energy Conversion Congress and Exposition,* 2021.

[8] Q. Dong, J. Dong, L. Zhu, Y. Liu, P. Kritprajun, L. M. Tolbert, S. Laval, K. P. Schneider, Y. Liu, "Resilience Evaluation of Advanced Distribution Grids with Self-healing Control, Microgrid and Transactable Reactive Power," *in proc. IEEE Power and Energy General Meeting*, 2021.

[9] Y. Liu, L. M. Tolbert, P. Kritprajun, Q. Dong, L. Zhu, J. C. Hambrick, K. P. Schneider, K. Prabakar, "Quasi-Static Time Series Fatigue Simulation for PV Inverter Semiconductors with Long-Term Solar Profile," *in proc. IEEE Power and Energy General Meeting*, 2021.

[10] Q. Dong, J. Dong, L. Zhu, P. Kritprajun, Y. Liu, Y. Liu, L. M. Tolbert, J. C. Hambrick, K. P. Schneider, S. Laval, "Impact of Self-healing Control on Reliability Evaluation in Distribution System with Microgrid," IEEE PES Innovative Smart Grid Technologies Conference – Europe, Virtual, Oct. 18-21, 2021

[11] Y. N. Velaga, K. Prabakar, M. Baggu and K. P. Schneider, "Evaluation of Centralized Model based FLISR in a Lab Setup," *in proc. IEEE Rural Electric Power Conference*, 2021

[12] P. R. Chowdhury, S. Essakiappan, M. Manjrekar, K. Schneider, and S. Laval, "Optimized Dispatch of Distributed Energy Resources for Resiliency and Power Quality Improvements at the Grid-Edge," *in proc. IEEE Kansas Power and Energy Conference*, April 2021.

E.2 Journal Papers

[1] K. P. Schneider, S. Laval, J. Hansen, R. Melton, L. Ponder, L. Fox, J. Hart, J. Hambrick, M. Buckner, M. Baggu, K. Prabakar, M. Manjrekar, S. Essakiappan, L. Tolbert, Y. Liu, J. Dong, L. Zhu, A. Smallwood, A.

Jayantilal, C. Irwin, G. Yuan, “A Distributed Power System Control Architecture for Improved Distribution System Resiliency,” IEEE Access, vol. 7 no. 1, pp. 9957-9970, Jan. 2019.

[2] Y. Liu, L. M. Tolbert, P. Kritprajun, J. Dong, L. Zhu, J. Hambrick, K. P. Schneider, K. Prabakar, “Aging Effect Analysis of PV Inverter Semiconductors for Ancillary Services Support,” *IEEE Open Journal of Industry Applications*, vol. 1, pp. 157-170, October 2020.

[3] J. Dong, L. Zhu, Q. Dong, P. Kritprajun, Y. Liu, Y. Liu, L. M. Tolbert, J. C. Hambrick, Y. Xue, T. B. Ollis, B. P. Bhattarai, K. Schneider, S. Laval, “Integrating Transactive Energy into Reliability Evaluation for a Self-healing Distribution System with Microgrid,” *Accepted IEEE Transactions on Sustainable Energy*, 2021.

[4] S. Essakiappan, P. Cowdrey, K. P. Schneider, S. Laval, K. Prabakar, M. Manjrekar, Y. Velaga, N. Shepard, J. Hambrick, and B. Ollis, “A Multi-Site Networked Hardware-in-Loop Platform for Evaluation of Interoperability and Distributed Intelligence at Grid-Edge,” *Accepted IEEE Open Access journal of Power and Energy*, 2021.

E.3 Blog Posts and Trade Publications

[1] N. Lanyi, “A USB port for the grid: OpenFMB will provide plug-and-play interoperability and communications for grid-edge DERs,” SEPA Blog, December 2018

[2] K. Schneider, S. Laval, A. Smallwood, “Flexibility and Resilience as Outcomes with Open Field Message Bus,” Power Grid International, Nov 2019

[3] R. Tucker, K. Schneider, S. Laval, “Grid Edge Innovation Transitioning from Lab to Field,” T&D World Article, Dec 2020

[4] R. Tucker, K. Schneider, S. Laval, “Moving Distributed Intelligence and Device Interoperability from Lab to Reality,” SEPA Blog, October 2020

[5] R. Tucker, B. Ollis, K. Prabakar, “Centralized and Distributed Controls for Increasing Resilience,” SEPA Blog, March 2021

[6] R. Tucker, B. Bhattarai, K. Schneider, “Increasing Grid Resilience with Transactive Energy,” SEPA Blog, June 2021

[7] R.Tucker, K. Schneider, “Increasing Grid Resilience under Differing Distributed Control Architectures,” SEPA Blog, August 2021

https://gridmod.labworks.org/